INFORMATION TO USERS

The most advanced technology has been used to photograph and reproduce this manuscript from the microfilm master. UMI films the text directly from the original or copy submitted. Thus, some thesis and dissertation copies are in typewriter face, while others may be from any type of computer printer.

The quality of this reproduction is dependent upon the quality of the copy submitted. Broken or indistinct print, colored or poor quality illustrations and photographs, print bleedthrough, substandard margins, and improper alignment can adversely affect reproduction.

In the unlikely event that the author did not send UMI a complete manuscript and there are missing pages, these will be noted. Also, if unauthorized copyright material had to be removed, a note will indicate the deletion.

Oversize materials (e.g., maps, drawings, charts) are reproduced by sectioning the original, beginning at the upper left-hand corner and continuing from left to right in equal sections with small overlaps. Each original is also photographed in one exposure and is included in reduced form at the back of the book. These are also available as one exposure on a standard 35mm slide or as a 17" x 23" black and white photographic print for an additional charge.

Photographs included in the original manuscript have been reproduced xerographically in this copy. Higher quality 6" x 9" black and white photographic prints are available for any photographs or illustrations appearing in this copy for an additional charge. Contact UMI directly to order.

U·M·I

University Microfilms International
A Bell & Howell Information Company
300 North Zeeb Road, Ann Arbor, MI 48106-1346 USA
313/761-4700 800/521-0600

Order Number 9000036

Subpicosecond time-resolved absorption and transient gratings in GaAs

Katz, Alvin I., Ph.D.

City University of New York, 1989

U·M·I
300 N. Zeeb Rd.
Ann Arbor, MI 48106

SUBPICOSECOND TIME RESOLVED ABSORPTION AND TRANSIENT GRATINGS IN GaAs

By

ALVIN KATZ

A dissertation submitted to the Graduate Faculty in Physics in partial fulfillment of the requirements for the degree of Doctor of Philosophy, the City University of New York.

1989

This manuscript has been read and accepted for the Graduate Faculty in Physics in satisfaction of the dissertation requirement for the degree of Doctor of Philosophy.

11/28/88
Date

Professor R. R. Alfano
Chair of Examining Committee

11/28/88
Date

Executive Officer

Prof. Roger Dorsinville

Prof. Joel Gersten

Prof. Ping-Pei Ho

Prof. Mel Lax

Dr. Frank Pelligrino
Supervisory Committee

The City University of New York

Abstract

SUBPICOSECOND TIME RESOLVED ABSORPTION

AND TRANSIENT GRATINGS IN GaAs

by

Alvin Katz

Advisor: Professor Robert R. Alfano

Carrier-carrier and intervalley scattering has been studied in submicron thick GaAs under intense photoexcitation by time resolved absorption and four wave mixing techniques using a femtosecond laser and amplifier system which was constructed as part of this thesis.

The laser oscillator is a colliding pulse ring cavity passively modelocked (cpm) Rhodamine 6G dye laser. The saturable absorber is DODCI (3,3'- diethyloxodicarbocyanine iodide). The oscillator produces pulses of 100 femtosecond duration and pulse energies of 50 picojoules at 620 nm and 115 megahertz repetition rate. The oscillator is pumped by a cw argon ion laser operating at a single line (514.5 nm). The amplifier system is a four stage amplifier pumped by a frequency doubled Q-switch Nd Yag laser. The electronics were constructed so as to allow the dye laser to trigger the pockel's cell of the Nd:Yag laser. The amplifier has a gain of 5×10^6; with an output pulse energy of 500 microjoules and a pulse width of 450 fs at a 20 hertz repetition rate.

Pump and probe absorption techniques were used to measure the

time evolution of the photoexcited carrier distribution function in GaAs. These measurements show that the electrons and holes do not achieve a Fermi-Dirac distribution until 800 femtoseconds after excitation.

Time resolved four wave mixing techniques were used to study intervalley scattering in GaAs. Both the dispersive (real part of n) and absorption saturation (imaginary part of n) of the free carrier contributions to the dielectric function is included to correctly explain the data. For energies high above the band gap, the interband (bleaching) contribution is strongly dependent on the distribution of electrons among the different valleys (Γ, L or X) of the conduction band and is opposite in sign from the intraband (dispersive) term. By using a three pulse transient grating experiment under the conditions of high pump intensity and probe energy (2.0 eV) much greater than the band gap (1.424 eV at room temperature), the effective time for intervalley scattering of electrons from the L-valleys back to the Γ-valley is directly measured. From the grating decay time of $\approx$ 9 picoseconds, a L $\rightarrow$ Γ time of 3 ps is estimated which is in good agreement with other recent work using time resolved photoluminescence.

This thesis is dedicated to

Silvia, Joshua and Eve

ACKNOWLEDGEMENTS

Many people have helped me with various aspects of this thesis and I wish to thank these people. First of all, I wish to thank my family who have given tremendous support during these past years, especially my wife Silvia, who has made many sacrifices in order to help me complete this thesis. I wish to thank my thesis advisor, Professor Robert R. Alfano, Professor Roger Dorsinville and Professor Ping Pei Ho for assistance and advise in the construction of the femtosecond laser system. I wish to thank Prof. Alfano for assistance in defining a thesis project, technical discussions and for financial support during this thesis work. I wish to thank Dr. Nathan Ockman, Dr. K. Arya and Dr. Mahesh Junnarkar for many helpful discussion on my thesis project as well as other areas of semiconductor physics. My many discussion with Dr. Ockman not only helped me clarify this thesis problem but opened many new questions that helped me increase my understanding of semiconductor physics. I wish to thank Professors Mel Lax, Joel Gersten and Dr. Frank Pellegrino for serving on my committee. I wish to thank the faculty members of the Physics Department of the City College of New York for teaching me physics. I also wish to thank Prof. L. Eastman of Cornell University for supplying the GaAs samples used in this thesis work. Last, but certainly not least, I wish to thank Mr. Yury Budansky, whose technical assistance was crucial in construction of the laser system.

This work was supported by the Air Force Office of Scientific Research and a Newport Research Award of the Optical Society of America.

TABLE OF CONTENTS

List of Tables

List of Figures

Chapter 2.

Chapter 3.

Chapter 1 Introduction

1.1. Background

There has been a long history of theoretical and experimental studies on carrier dynamics in GaAs, both for its technological value and for a greater understanding of the physics of polar semiconductors.[1-3] There has been extensive studies of the electron-LO-phonon interaction. Much experimental work has been done on measurements of carrier cooling rates from either photoluminescence[4-6] or absorption[7-9] spectroscopy. When this thesis work was begun, there were few optical measurements of the intervalley or e-e, e-h, h-e and h-h scattering rates on this time scale. Most of the measurements of electron transport gave results that varied over two orders of magnitude (from 10^{-14} to 10^{-12} seconds) and were at low carrier density where polar optical phonon emission dominates rather than carrier-carrier interactions.

The intervalley scattering rates have only recently been measured by optical methods. Taylor et al[10,11] using an equal pulse correlation method and a 90 fs pulse, measured the $\Gamma \rightarrow L$ intervalley time to be 40 fs in GaAs. Lin et al[12,13] using pump and probe absorption have measured the electron-electron scattering time in GaAs and found it to be on the order of 35 fs. Shah et al[14] using up-conversion, time-resolved the photoluminescence in GaAs. By comparing the photoluminescence rise time to similar semiconductors

(without intervalley scattering at the excitation frequency), they determined the effective L → Γ intervalley return time to be 9 ps. Deveaud et al[15] then used Ensemble Monte Carlo calculations to determine that the L → Γ scattering time is 2.7 ps with an electron making an average of 3 Γ → L scatters before relaxing to the bottom of the band.

Oudar et al [16] using pump and probe absorption, determined the momentum relaxation time for electrons in GaAs to be 190 fs. They excited the GaAs less then one LO-phonon energy above the band edge and measured the rotation of the polarization of the transmitted probe as a function of delay time. By this technique they were able to measure the momentum relaxation time by electron-electron scattering without intervalley scattering or LO-phonon emission.

Scattering process	Time
Electron - electron[12,13] scattering time	35 fs
Unscreen LO-phonon[8] emission time (holes) (electrons)	130 fs 110 fs
Momentum relaxation time[16]	140 - 190 fs
$\Gamma \rightarrow X$ intervalley[23] scattering time	55 fs
$\Gamma \rightarrow L$ intervalley[10,11] scattering time	80 fs
$L \rightarrow \Gamma$ intervalley[14] scattering time	3 ps
$X \rightarrow \Gamma$ intervalley[24] scattering time	0.5 ps
Electron-hole recombination time (low density) (high density $\approx 10^{19}$ cm^{-3}	10^{-9} sec 10^{-10} sec

Table 1.2.1. Summary of excited carrier scattering times in GaAs.

1.2. Thesis objectives

There are three objectives of this thesis work. The first is to study the time evolution of the carrier distribution function. The second is to study the effective L → Γ scattering times by time resolved four-wave mixing. The third objective is to measure the electron momentum relaxation time.

In chapter 2 of this thesis, I will review some of the band structure and carrier statistics of GaAs at high carrier density including band non-parabolicity. Conduction band non-parabolicity must be included in any attempted to calculate a quasi-Fermi level from the carrier density and temperature at the densities involved in the thesis work.

At the time this work was begun, femtosecond laser systems were not readily available. It was necessary to construct most of the laser and amplifier system used for this thesis work. The modelocked laser was a colliding pulse passively modelocked ring cavity dye laser with Rhodamine 6G as the lasing dye and DODCI as the modelocking dye. The amplifier is a four stage system pumped by a Q-switch Nd:YAG laser. This system was modelled on a design developed by Fork et al.[17] Chapter 3 will contain a discussion of passively modelocked dye lasers, and a description of the laser system with a discussion of those parameters important to the operation of this laser system.

As part of this thesis, I measured the time evolution of the carrier distribution function within the first picosecond of optical excitation. It was necessary to construct the entire optical experimental setup for this experiment as part of this thesis. These are the first measurements to directly measure the carrier distribution function with sub-picosecond resolution. Recently, theorists, using Ensemble Monte Carlo calculations[18-22] have been able to calculate the time evolution of the distribution function. Their results show that it does not evolve into a thermalized (Fermi-Dirac or Maxwellian) distribution until 2 ps after excitation. In chapter 4, I will describe the experimental apparatus constructed for the pump and probe absorption experiment and present the results of the absorption measurements which show a non-thermalized distribution in the first 800 fs after excitation.

The transient grating technique for doing time resolved four-wave mixing is discussed in chapter 5. In this chapter, I calculate the interband and intraband contributions to $\delta\varepsilon_1$ for free carriers in GaAs and show how $\delta\varepsilon_1$ depends on the distribution of electrons between the Γ and L valleys of the conduction band. Although, I was not able to time resolve the $\Gamma \rightarrow$ L intervalley scattering time, I was able to measure the L $\rightarrow \Gamma$ return time. In chapter 5, the transient grating data will be discussed. From these measurements, I have determined the effective L $\rightarrow \Gamma$ scattering in GaAs to be 9 ps. As part of this thesis, it was also necessary to

construct the entire experimental apparatus.

The last part of this thesis will discuss the results of the orientation grating measurements of the momentum relaxation time in GaAs. Although the temporal resolution of the laser system was not short enough to accurately measure this time, estimates of the momentum relaxation time have been made from the data taken in the 2θ and $-\theta$ directions from a two pulse grating experiment. From these results, the momentum relaxation time in GaAs is measured to be 150 fs.

1.3. Notes

[1]E. M. Conwell, **Solid State Physics Supplement 9,** Academic, New York (1967)

[2]R. R. Alfano, ed. **Semiconductors Probed by Ultrafast Spectroscopy,** Academic, New York (1984).

[3]Proceedings of the Fifth International Conference on Hot Carriers in Semiconductors. Boston Ma. (1987).

[4]1J. Shah, Solid State Electron. **21**, 43 (1978).

[5]S. Tanaka, Kobayashi, H. Saito and S. Shionoya, J. Phys. Soc. Japan **49**, 1051 (1980).

[6]R. J. Seymour, M. R. Junnakar and R. R. Alfano, Solid State Commun. **41**, 657 (1982).

[7]C. V. Shank, R. L. Fork, R. F. Leheny, and J. Shah, Phys. Rev. Lett. **42**, 112 (1979).

[8]R. F. Leheny, J. Shah, R. L. Fork, C. V. Shank and A. Migus, Solid State Commun. **31**, 809 (1979).

[9]D. von der Linde and R. Lambrich, Phys. Rev. Lett. **42**, 1090 (1979).

[10]A. J. Taylor, D. J. Erskine, and C. L. Tang, J. Opt. Soc Am. B **2**, 663, (1985).

[11]A. J. Taylor, D. J. Erskine and C. L. Tang, Appl. Phys. Lett.**43**, 989 (1983).

[12]W. Z. Lin, L. G. Fujimoto, E. P. Ippen and R. A. Logan, Appl. Phys. Lett. **50**, 124 (1987).

[13]W. Z. Lin, L. G. Fujimoto, E. P. Ippen and R. A. Logan, Appl. Phys. Lett. **51**, 161 (1987).

[14]J. Shah, B. Deveaud, T. C. Damen, W. T. Tsang, A. C. Gossard and P. Lugli, Phys. Rev. Lett. **59**, 2222 (1987).

[15]B. Deveaud, J. Shah, T. C. Damen, A. C. Gossard and P. Lugli, Solid State Electron. **31**, 436 (1988).

[16]J. L. Oudar, A. Migus, D. Hulin, G. Grillon, J. Etchepare and A. Antonetti, Phys. Rev. Lett. **53**, 384 (1984).

[17]R. L. Fork, B. I. Greene and C. V. Shank, Appl. Phys. Lett. **38**, 671 (1981).

[18]J. Zimmerman, P. Lugli, and D. K. Ferry, Solid State Electron. **26**, 233 (1986).

[19]P. Lugli and D. K. Ferry, Physica **117B**, 251 (1983).

[20]M. A. Osman and D. K. Ferry, Phys. Rev. B **36**, 6018 (1987).

[21]M. A. Osman and H. L. Grubin, Solid State Electron, **31**, 471 (1988).

[22]M. A. Osman, H. L. Grubin, J. P. Kreskovsky and D. L. Ferry, SPIE PROC. **793**, 94 (1987).

[23]P. C. Becker, H. L. Fragnito, C. H. Brito Cruz, J. Shah, R. L. Fork, J. E. Cunningham, J. E. Henry and C. V. Shank, Appl. Phys. Lett. **53**, 2089 (1988).

[24]W. B. Wang, N. Ockman, M. Yan and R. R. Alfano, Submitted for publication.

Chapter 2. Review of electron and hole statistics and band non-parabolicity in highly excited GaAs

2.1 Review of GaAs lattice

The following material lays the background for my research. The GaAs lattice has cubic sphalerite structure.[1] The unit cell is face centered cubic with a basis of one Gallium atom at (0,0,0) and one Arsenic atom at $(\frac{1}{4},\frac{1}{4},\frac{1}{4})$. The length of a side of the unit cell is 5.65325 Å and the nearest neighbor distance is 2.44793 Å at 300 K.[2] The reciprocal lattice is body centered cubic and thus has inversion symmetry. The distance from the center to the edge of the first Brilluoin zone in the (1,0,0) direction is 1.111×10^{8} cm^{-1} and in the (1,1,1) direction is 0.962×10^{8} cm^{-1}. The band structure[2] of GaAs is shown in figure 2.1.1.

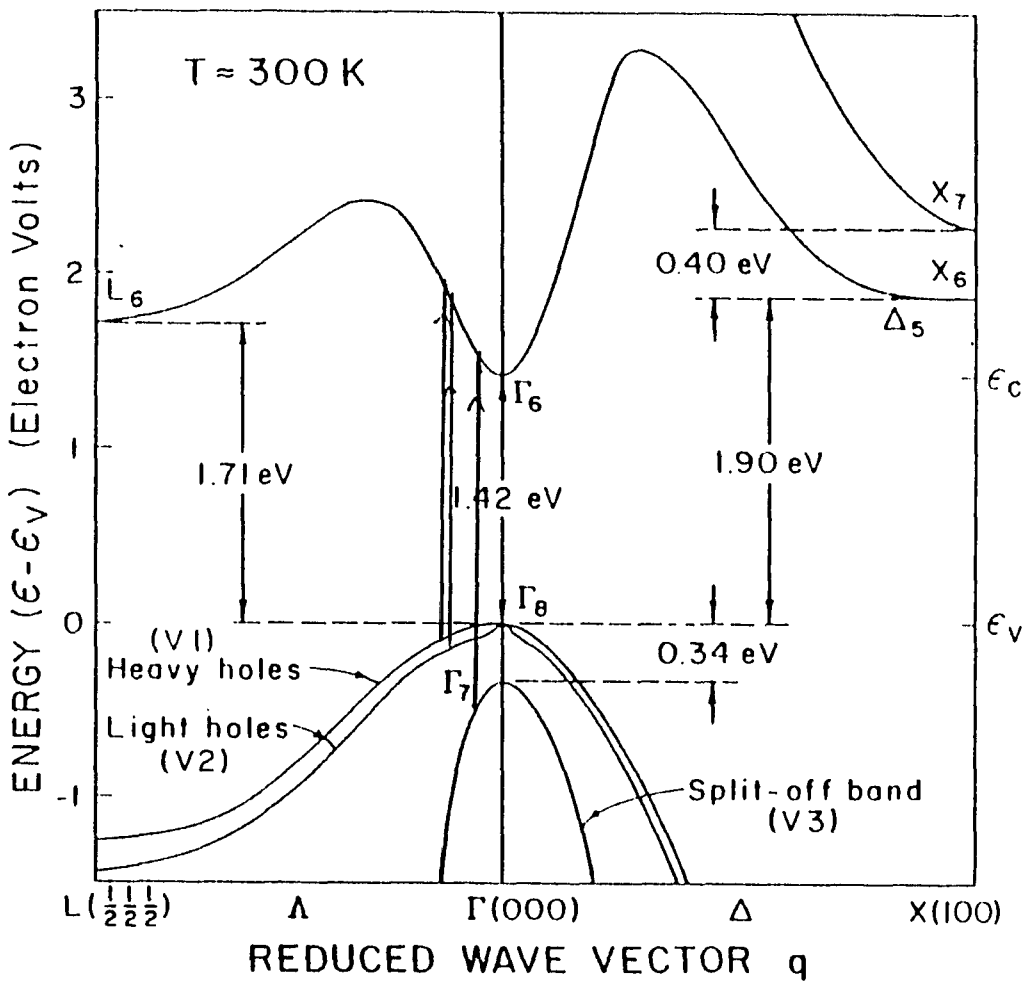

Figure 2.1.1. Band structure of GaAs (taken from reference 13).

2.2 Conduction band

The lowest conduction band and the three highest valence bands are the most significant ones in most optical experiments involving photoexcitation in the visible and near infrared wavelength region. The conduction band has a minimum at the zone center (Γ point), four secondary minima at the zone edge in the (1,1,1) direction (L_6 point) and three secondary minima in the (1,0,0) direction (X_6 point). Since the valence band maximum is also at the zone center, GaAs is a direct gap semiconductor. The temperature dependent band gap can be described by[3,4]

$$E_g = 1.519 - \frac{5.406 \times 10^{-4}\ T^2}{(T + 204)} \quad \text{eV.} \qquad (2.2.1)$$

At room temperature the band gap is 1.424 eV. The two lowest temperature dependent indirect band gaps, from the uppermost valence band to the L_6 and X_6 conduction band minima were determined by Aspnes from UV electroreflectance measurements to be modeled by[2,5-8]

$$E_L = 1.815 - \frac{6.05 \times 10^{-4}\ T^2}{(T + 204)} \quad \text{eV} \qquad (2.2.2)$$

$$E_X = 1.981 - \frac{4.60 \times 10^{-4}\ T^2}{(T + 204)} \quad \text{eV.} \qquad (2.2.3)$$

and the energy difference is

$$\Delta_{\Gamma L} = E_L - E_\Gamma = 0.296 - \frac{6.45 \times 10^{-5}\ T^2}{(T + 204)} \quad \text{eV} \qquad (2.2.4)$$

$$\Delta_{\Gamma X} = E_X - E_\Gamma = 0.462 - \frac{8.05 \times 10^{-5}\ T^2}{(T + 204)} \quad \text{eV.} \qquad (2.2.5)$$

At room temperature, the L minima are 0.285 eV and the X minima, 0.476 eV above the Γ minimum. The direct gaps to the L_6 and X_6 points are both in the ultraviolet (3.1 eV and ≈ 5 eV) and will not be observed at the probe energies involved in the experimental part of this thesis work.

The room temperature effective mass at the Γ point is given by

$$m_e = 0.063\ m_o \quad . \tag{2.2.6}$$

See references 2 and 9 for a review of measurements of the conduction band-edge effective mass. The Γ-valley deviates significantly from being parabolic for k not equal to zero. At the high carrier densities and temperatures in this work, conduction band non-parabolicity must be considered in any effort to fit an electron density from a measured quasi-fermi level and carrier temperature. The relationship between carrier density, quasi-Fermi level and carrier temperature is

$$N_e = 2 \int_0^{\infty} \frac{d^3\mathbf{k}}{(2\pi)^3} \frac{1}{\left(1 + \exp\left[\frac{E - \mu}{K_B T_e}\right]\right)} \tag{2.2.7}$$

where N_e is the carrier density, E is the energy of electrons at state $\mathbf{k}$, μ_e is the electron quasi-Fermi level and T is the carrier Temperature. For a parabolic band, $(E - E_g) = \frac{\hbar^2 k^2}{2m_e^*}$ and by changing the variable of integration from momentum to energy in Eq. 2.2.7, the relationship between electron density, temperature and Fermi level is

$$N_e = \frac{1}{2\pi^2}\left(\frac{2m_e^*}{\hbar^2}\right)^{\frac{3}{2}} \int_{E_g}^{\infty} \frac{(E - E_g)^{1/2}\, dE}{\left(1 + \exp\left[\frac{E - \mu_e}{K_B T}\right]\right)} \quad . \tag{2.2.8}$$

A change in variables to $\xi = \frac{E}{K_B T}$ and defining $\eta \equiv \frac{\mu_e - E_g}{K_B T}$, gives

$$N_e = \frac{1}{2\pi^2}\left[\frac{2m_e^* K_B T}{\hbar^2}\right]^{\frac{3}{2}} \int_0^{\infty} \frac{\xi^{1/2}\, d\xi}{1 + \exp(\xi - \eta)} = 2\left[\frac{m_e K_B^* T}{2\pi\hbar^2}\right]^{\frac{3}{2}} \mathcal{F}_{1/2}(\eta) \tag{2.2.9}$$

where $\mathcal{F}_{1/2}(\eta)$ is the Fermi Integral of order $^1/_2$.

Blakemore[2] has included non-parabolicity by expanding E(k) to terms in k^4 in a k•p perturbation model,[10,11] and gets a band non-parabolicity factor given by

$$\alpha = -\ (0.824 + 2.0 \times 10^{-5}\ T) \tag{2.2.10}$$

In this case, the energy - momentum relation is

$$E = E_g + \frac{\hbar^2 k^2}{2m_e^*} + \frac{\alpha}{E_g}\left(\frac{\hbar^2 k^2}{2m_e^*}\right)^2 \tag{2.2.11}$$

The relationship between carrier density, temperature and quasi-Fermi level then becomes

$$N_e = 2\left[\frac{m_e^* K_B T}{2\pi\hbar^2}\right]^{\frac{3}{2}} \left\{\mathcal{F}_{1/2}(\eta) - \left[\frac{15\alpha K_B T}{4E_g}\right]\mathcal{F}_{3/2}(\eta)\right\} \tag{2.2.12}$$

where $\mathcal{F}_{3/2}(\eta)$ is the Fermi function of order $\frac{3}{2}$.

$\mathcal{F}_{1/2}(\eta)$ can be approximated reasonable well by[23]

$$\mathcal{F}_{1/2}(\eta) = \frac{\exp(\eta)}{1 + \exp(\eta)} \qquad \eta < 1 \qquad (2.2.13a)$$

and

$$\mathcal{F}_{1/2}(\eta) = \frac{4}{3\sqrt{\pi}}\left[\eta^2 + 1.7\right]^{3/4} \qquad \eta > 1 \quad . \qquad (2.2.13b)$$

An approximation for the Fermi function of order $^3/_2$ can be derived from the relationship

$$\mathcal{F}_{1/2}(\eta) = \frac{d\{\mathcal{F}_{3/2}(\eta)\}}{d\eta} \quad . \qquad (2.2.14)$$

Using Eqs. 2.2.13a,b and 2.2.14, $\mathcal{F}_{3/2}(\eta)$ can be approximated by

$$\mathcal{F}_{3/2}(\eta) = 3.70 \ln (1.+0.27\exp(\eta)) \qquad n < 1 \qquad (2.2.15a)$$

and

$$\mathcal{F}_{3/2}(\eta) = 0.30 \left(\eta^{5/2} + 6.18 \sqrt{\eta}\right) \qquad \eta > 1 \ . \qquad (2.2.15b)$$

The quasi-Fermi levels for a parabolic and non-parabolic conduction band are calculated as a function of electron temperature at a density of 1.2×10^{19} cm^{-3} and are shown in figure 2.2.1. The quasi-Fermi levels as a function of electron density at carrier temperatures of 600 K and 1400 K are calculated and shown in figures 2.2.2a and 2.2.2b. These calculations only consider the Γ-valley population. In a non-parabolic band, as the electron density increases, the increase in μ_e is much less than for a parabolic band.

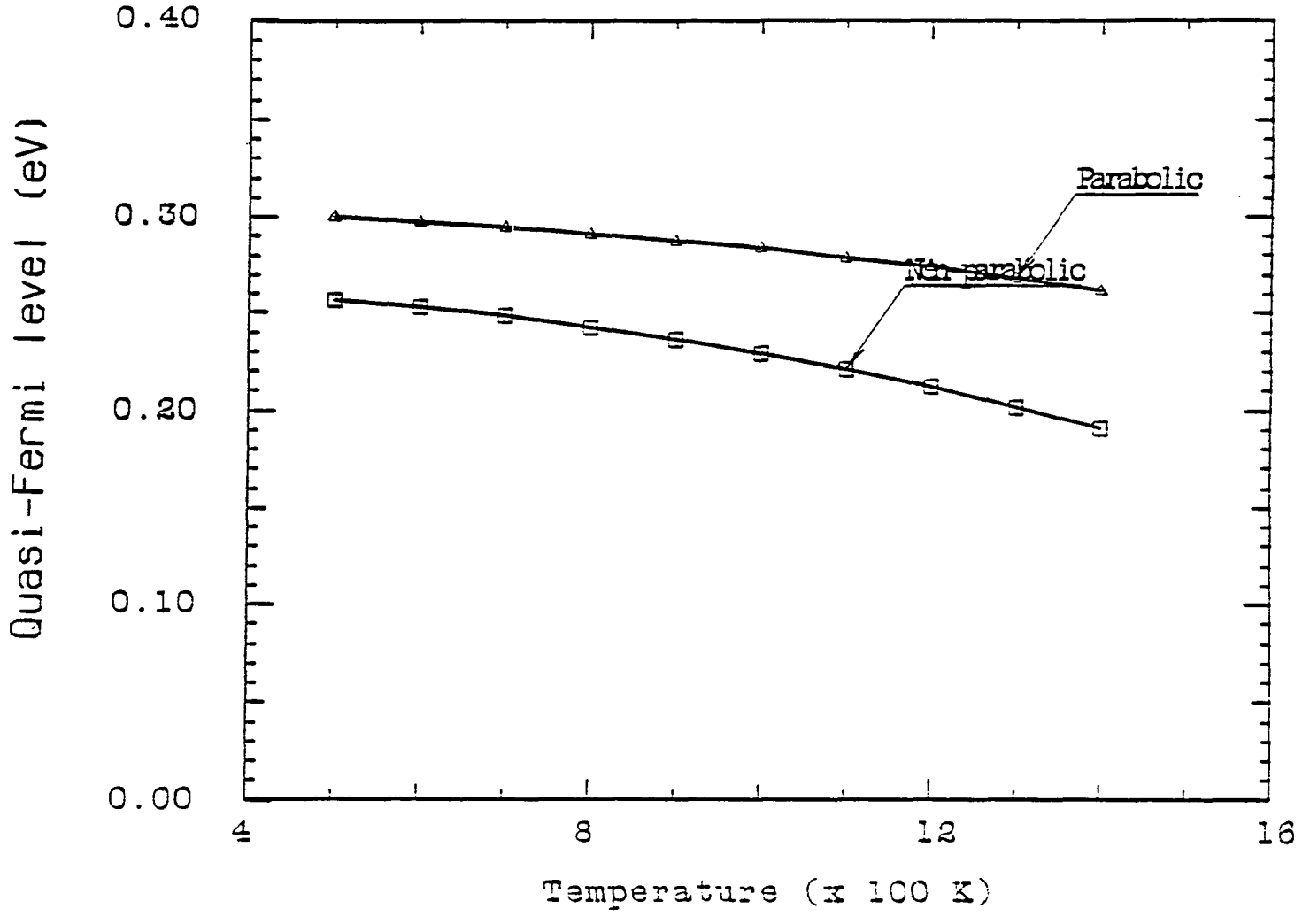

Figure 2.2.1. Electron quasi-Fermi levels calculated for a parabolic and non-parabolic conduction band as a function of carrier temperature at a carrier density of 1.2×10^{19} cm^{-3}.

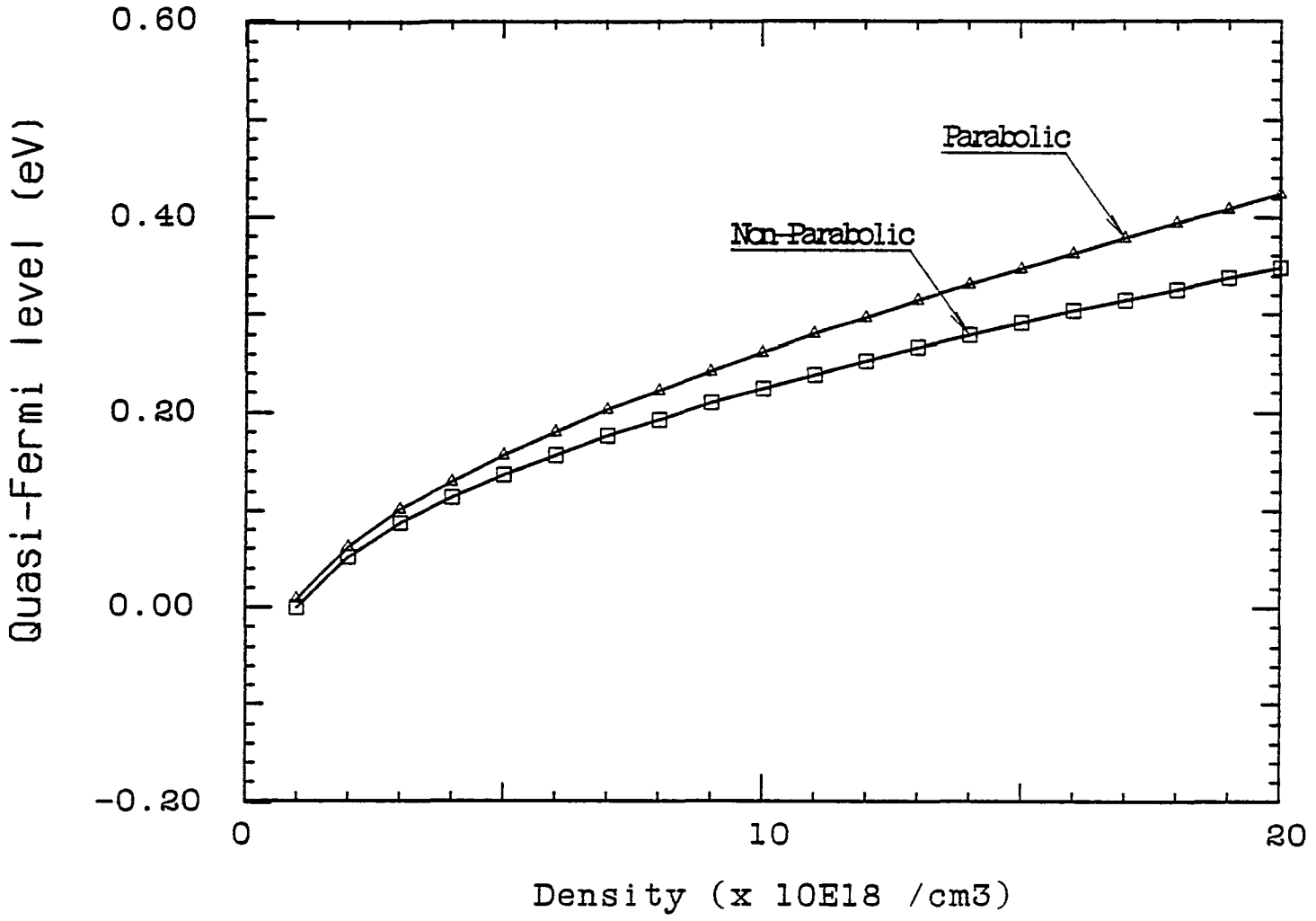

Figure 2.2.2a. Electron quasi-Fermi levels for parabolic and non-parabolic conduction band as a function of carrier density for a carrier temperature of 600 K.

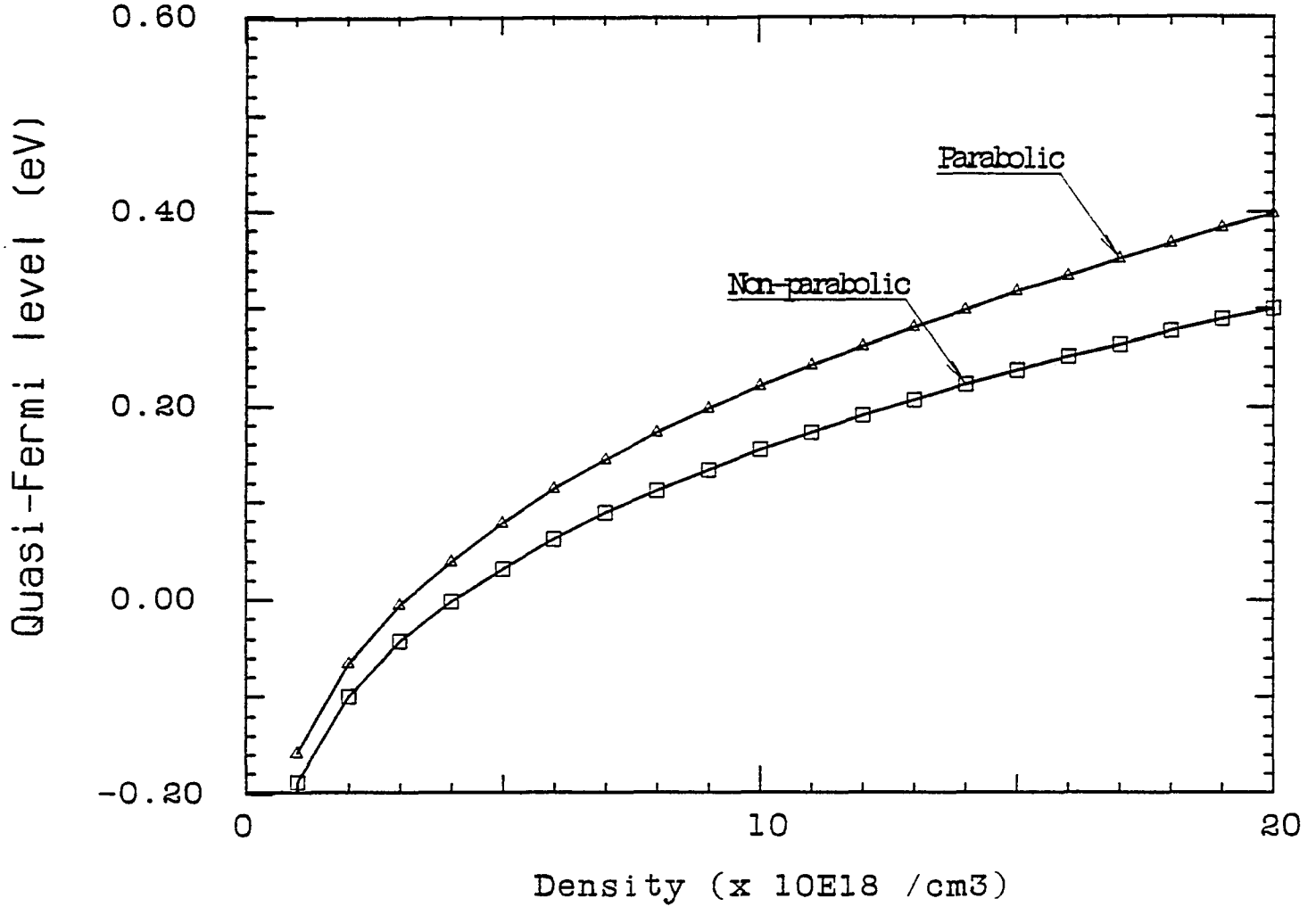

Figure 2.2.2b. Electron quasi-Fermi levels for parabolic and non-parabolic conduction band as a function of carrier density for a carrier temperature of 1400 K.

The position of the Fermi level is important in interpreting the near band edge transient grating data in chapter 5.

The effective mass for the four L-valleys can be described by transverse and longitudinal components[6]

$$m_l \approx 1.9\ m_o \qquad (2.2.16)$$

and

$$m_t \approx 0.075\ m_o\ , \qquad (2.2.17)$$

respectively. The density of states effective mass for the four L-valleys is

$$m_L = (16\ m_l\ m_t^2\ )^{1/3} \approx\ 0.56\ m_o\ . \qquad (2.2.18)$$

The factor of 16 is to account for the 4 L-valleys. The density of states at the L-valley minima is about 26 times greater then the density of states of the Γ-valley minimum.

Similarly for the three X valleys, the longitudinal and transverse components of the effective mass are[5,13]

$$m_l = 1.9\ m_o \qquad (2.2.19)$$

and

$$m_t = 0.19\ m_o\ . \qquad (2.2.20)$$

The density of states effective mass for the three X-valleys is

$$m_X = (9\, m_l\, m_t^2)^{1/3} \approx 0.85\, m_o \quad . \qquad (2.2.21)$$

The density of states at the X-valley minima is about 50 times greater than the Γ-valley minimum. The factor of 9 is to account for the 3 X-valleys.

Non-parabolicity in X and L-valleys can be neglected in this work because of the large density of states and the higher energy of these valleys.

The total electron population is the sum of the population in the Γ, X and L valleys:

$$N = N_\Gamma + N_L + N_X \quad . \qquad (2.2.22)$$

When the Γ, X and L-valleys are in thermal equilibrium with each other (which occurs a couple of picoseconds after excitation), the electrons reach a common temperature and quasi-Fermi level. In this case, the total electron population in the conduction band is given by

$$N_e = 2\left[\frac{m_\Gamma K_B T}{2\pi\hbar^2}\right]^{\frac{3}{2}} \left\{\mathcal{F}_{1/2}\left[\frac{\mu_e - E_\Gamma}{K_B T}\right] - \left[\frac{15\alpha K_B T}{4E_g}\right] \mathcal{F}_{3/2}\left[\frac{\mu_e - E_\Gamma}{K_B T}\right]\right\} +$$

$$2\left[\frac{m_L K_B T}{2\pi\hbar^2}\right]^{\frac{3}{2}} \mathcal{F}_{1/2}\left[\frac{\mu_e - E_L}{K_B T}\right] + 2\left[\frac{m_X K_B T}{2\pi\hbar^2}\right]^{\frac{3}{2}} \mathcal{F}_{1/2}\left[\frac{\mu_e - E_X}{K_B T}\right] \qquad (2.2.23)$$

where m_Γ, m_L and m_X are the density of states effective masses in the

Γ, L and X valleys, E_Γ, E_L and E_X are the energies at the bottom of Γ, L and X valleys, respectively, μ_e is the quasi-Fermi level and T is the carrier temperature. The fraction of electrons in the Γ, L and X valleys, as function of carrier temperature is shown in figure 2.2.3 for a total density of 1.2×10^{19} cm^{-3}.

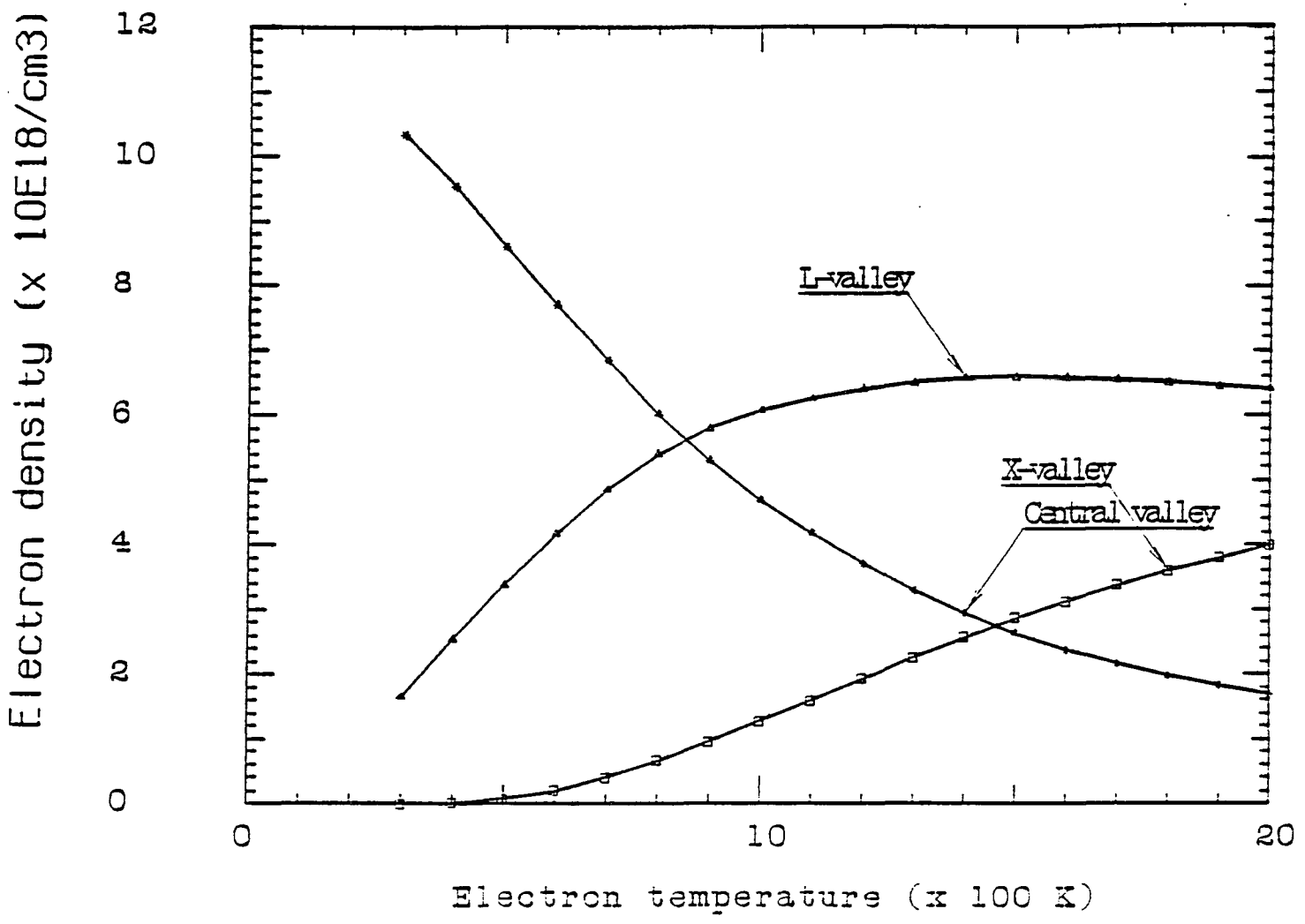

Figure 2.2.3. The fraction of electrons in the Γ, L and X-valleys as a function of carrier temperature. The total density is 1.2×10^{19} cm^{-3}. The three valleys are assumed to be in thermal equilibrium.

2.3 Review of valence bands statistics

Holes from the three uppermost valence bands can make transitions to the conduction band under the range of photon excitation and/or probe energies used in this thesis work and therefore the heavy-hole, light-hole and splitoff bands must be considered in the interpretation of the data. The heavy-hole and light-hole valence bands have a degenerate maximum at k = 0. The splitoff band has a maximum at k = 0, and is 0.341 eV below the heavy-hole and light-hole bands.

The heavy-hole band can be considered parabolic with a room temperature effective mass given by[14]

$$m_h^* = 0.5\ m_o \quad . \tag{2.3.1}$$

The light-hole and splitoff bands both deviate considerably from being parabolic and are strongly anisotropic (the effective mass is a function of direction in k-space).[2] The room temperature band-edge effective mass for the light-hole band is given by[2,14]

$$m_l = 0.076\ m_o \quad . \tag{2.3.2}$$

The dimensionless non-parabolicity parameter is given by[2]

$$\beta = -(3.87 - .001\ T) \quad . \tag{2.3.3}$$

For measurements taken at band edge, the effect of the light-hole band

is small and can be included by a small correction to the heavy-hole effective mass and neglecting its non-parabolicity. As soon as one moves a few tens of millivolts below the band-edge, the light-hole band is generally parallel to the heavy-hole band and displaced about 80 to 100 meV below the heavy-hole band.

The band-edge effective mass of the splitoff band at room temperature is given by[15]

$$m_{so} = 0.145\ m_o \qquad (2.3.4)$$

and the non-parabolicity factor is[2]

$$\gamma = +10.8 \quad . \qquad (2.3.5)$$

Note that γ is positive, the density of states decreases as one moves away from k = 0. The splitoff band has a small effect on the hole statistics but transitions from the splitoff to the conduction band are clearly evident in the pump and probe absorption measurements of chapter 4.

The relationship between hole density, temperature and quasi-Fermi level is derived in a similar way as the conduction band. With $\zeta \equiv \frac{E_v - \mu_h}{K\,T}$ for the heavy-hole band, this relationship is given by

$$N_h = 2\left[\frac{m_h K_B^* T}{2\pi\hbar^2}\right]^{\frac{3}{2}} \mathcal{F}_{1/2}(\zeta) \qquad (2.3.6)$$

For the heavy-hole and light-hole bands (including light-hole non-parabolicity) the relationship between carrier density, temperature and quasi-Fermi level is given by[2]

$$N_h = 2\left[\frac{K_B T}{2\pi\hbar^2}\right]^{\frac{3}{2}} \left\{\left[(m_h^*)^{\frac{3}{2}}+(m_l^*)^{\frac{3}{2}}\right]\mathcal{F}_{1/2}(\zeta) - (m_l^*)^{\frac{3}{2}}\left[\frac{15\beta K_B T}{4E_g}\right]\mathcal{F}_{3/2}(\zeta)\right\} . \qquad (2.3.7)$$

The hole quasi-Fermi levels have been calculated for a single parabolic heavy-hole band and for a heavy-hole and non-parabolic light-hole bands for the range of temperatures and densities corresponding to the experimental conditions of this thesis. The temperature dependence of μ_h is shown in figure 2.3.1 for a hole density of 1.2×10^{19} cm^{-3}. The density dependence of μ_h for a hole temperature of 1000 K is shown in figure 2.3.2. The influence of the light-hole non-parabolicity on hole statistics is less significant since the holes are not degenerate under the experimental conditions.

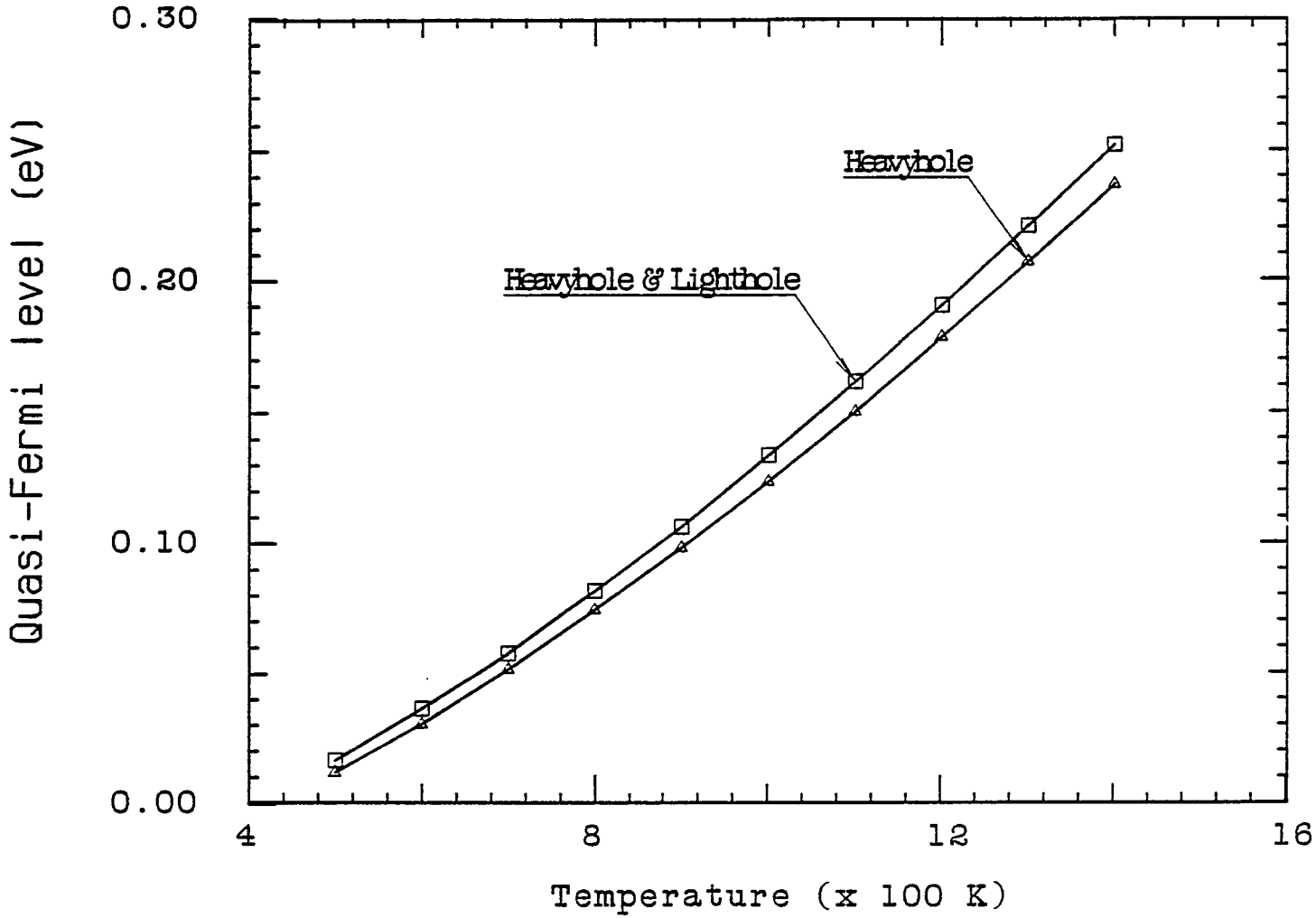

Figure 2.3.1. Hole quasi-Fermi levels as a function of carrier temperature for $n = 1.2 \times 10^{19}$ cm^{-3}, calculated for a single parabolic heavy-hole band and for a parabolic heavy-hole and non-parabolic light hole band.

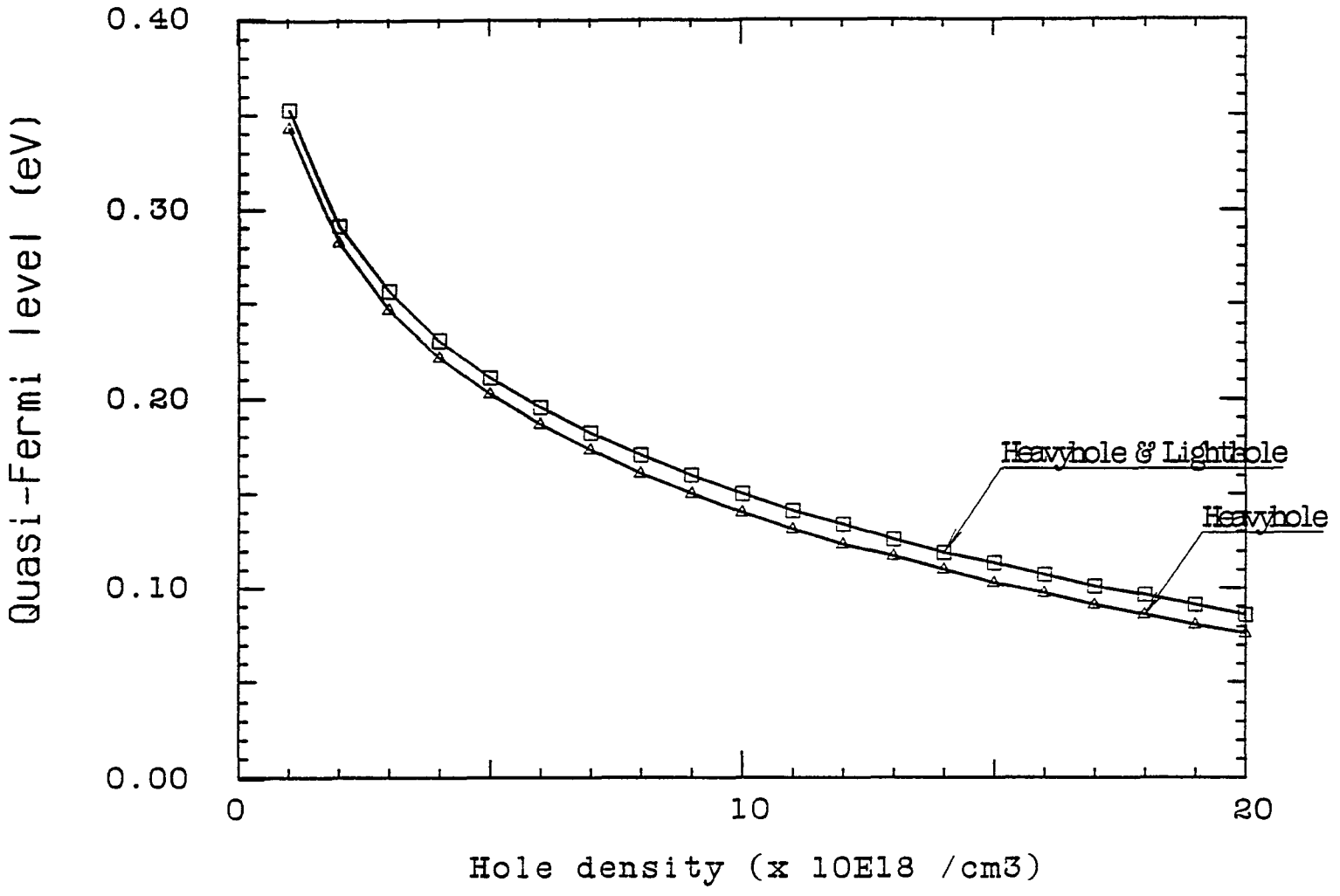

Figure 2.3.2. Hole quasi-fermi levels as a function of density, Tc = 1000 K. The calculations are for a single parabolic heavy-hole band and for a parabolic heavy-hole and nonparabolic light-hole band.

2.4 Description of GaAs samples studied in this thesis

The GaAs samples studied in this thesis were grown by molecular beam epitaxy by Paul Enquist of Professor Eastman's group at Cornell University. The samples were of 0.25 and 0.75 micron thickness. Each sample was grown with an $Al_xGa_{1-x}As$ cover layer to reduce the number of surface states. The front cover layer is 2 micron thick and the back cover layer is 1 micron thick. The mole fraction of Al is 0.5 for the 0.75 micron samples and 0.5 for the 0.25 micron samples. The samples were grown on a GaAs substrate which was subsequently etched off and then mounted on glass cover slips. The $Al_xGa_{1-x}As$ direct band gap at 293 K is given by[16]

$$E_g = 1.424 + 1.247x \qquad (0 \le x \le 0.45) \qquad (2.4.1a)$$

$$E_g = 1.424 + 1.247x + 1.147(x-0.45)^2 \qquad (0.45 \le x \le 1) . \qquad (2.4.1b)$$

For $x \ge 0.45$, the Γ minimum (and also the L minima) is above the X minima and the $Al_xGa_{1-x}As$ band gap is indirect. The indirect gap is given by[16]

$$E_g = 1.900 + 0.125x + 0.143\ x^2 \qquad (0.45 \le x \le 1) . \qquad (2.4.2)$$

The indirect and direct band gaps for $x = 0.5$ (0.7) is 2.0 eV (2.06 eV) and 2.05 eV (2.37 eV) respectively. In either case the absorption edge of the $Al_xGa_{1-x}As$ is greater than the excitation laser photon energy of 2.01 eV used in this thesis. The samples were doped

	GaAs thickness	dopant	concentration	$Al_xGa_{1-x}As$ cover layer
#1	0.75 μ	Be	5×10^{18} cm^{-3}	x = 0.5
#2	0.75 μ	Be	5×10^{17} cm^{-3}	x = 0.5
#3	0.75 μ	Be	5×10^{16} cm^{-3}	x = 0.5
#4	0.25 μ	Si	1×10^{18} cm^{-3}	x = 0.7
#5	0.25 μ	Si	1×10^{16} cm^{-3}	x = 0.7
#6	0.25 μ	Be	$1.5 \times 10^{18} cm^{-3}$	x = 0.7
#7	0.25 μ	Si	1×10^{17} cm^{-3}	x = 0.7

Table 2.4.1. GaAs samples studied in this thesis work.

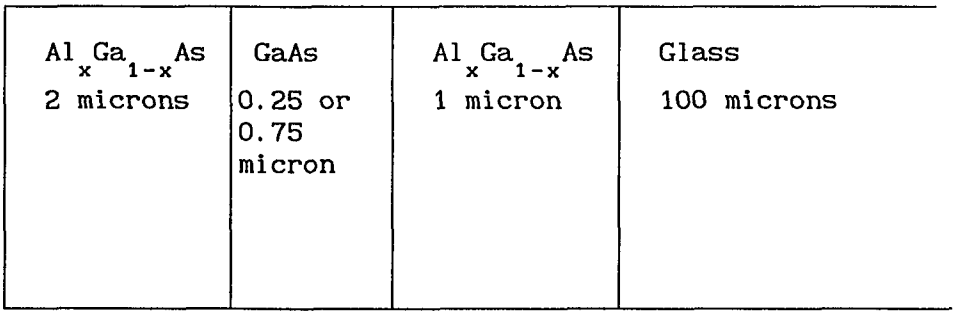

Figure 2.4.1. Structure of GaAs samples used in this thesis. The thickness of the GaAs was either 0.25 microns with x = 0.7 or 0.75 microns with x = 0.5.

intentionally with either silicon (n-type) or beryllium (p-type). The dopant concentration is much less than the density of the photoexcited carriers. The sample characteristics are summarized in table 2.4.1 and the samples are drawn schematically in figure 2.4.1.

The absorption curve for one of the 0.75 micron thick GaAs samples (#2) is shown in figure 2.4.2. The data is uncorrected for sample reflectivity. The index of refraction of GaAs is 3.3 and for $Al_xGa_{1-x}As$ is 3.6. The reflectance at the $Al_xGa_{1-x}As$-air interface is 32% and the $Al_xGa_{1-x}As$-glass interface is 17%. The reflectance at the glass-air interface is 4%. The reflectance at the GaAs-$Al_xGa_{1-x}As$ interface is << 1%. The 400 cm^{-1} oscillations in the below band gap region of the spectrum is caused by an etalon effect in the sample. The etalon effect is also evident in the photoluminescence spectrum. The sharp rise in the absorption at 2.06 eV is the onset of absorption by the cover layer. Absorption from the splitoff band is observed at energies greater than 1.765 eV. In the experimental part of this thesis, the excitation wavelength is 6170 Å (2.01 eV) and the probe wavelengths are in the range of 8000 Å to 6170 Å (1.55 to 2.01 eV).

The absorption coefficient, α, of this sample can be calculated from the uncorrected optical density by equations 2.4.3 and 2.4.4. The O.D. (uncorrected for reflection) is given by

$$I_t = I_o \, 10^{-O.D.} \quad . \qquad (2.4.3)$$

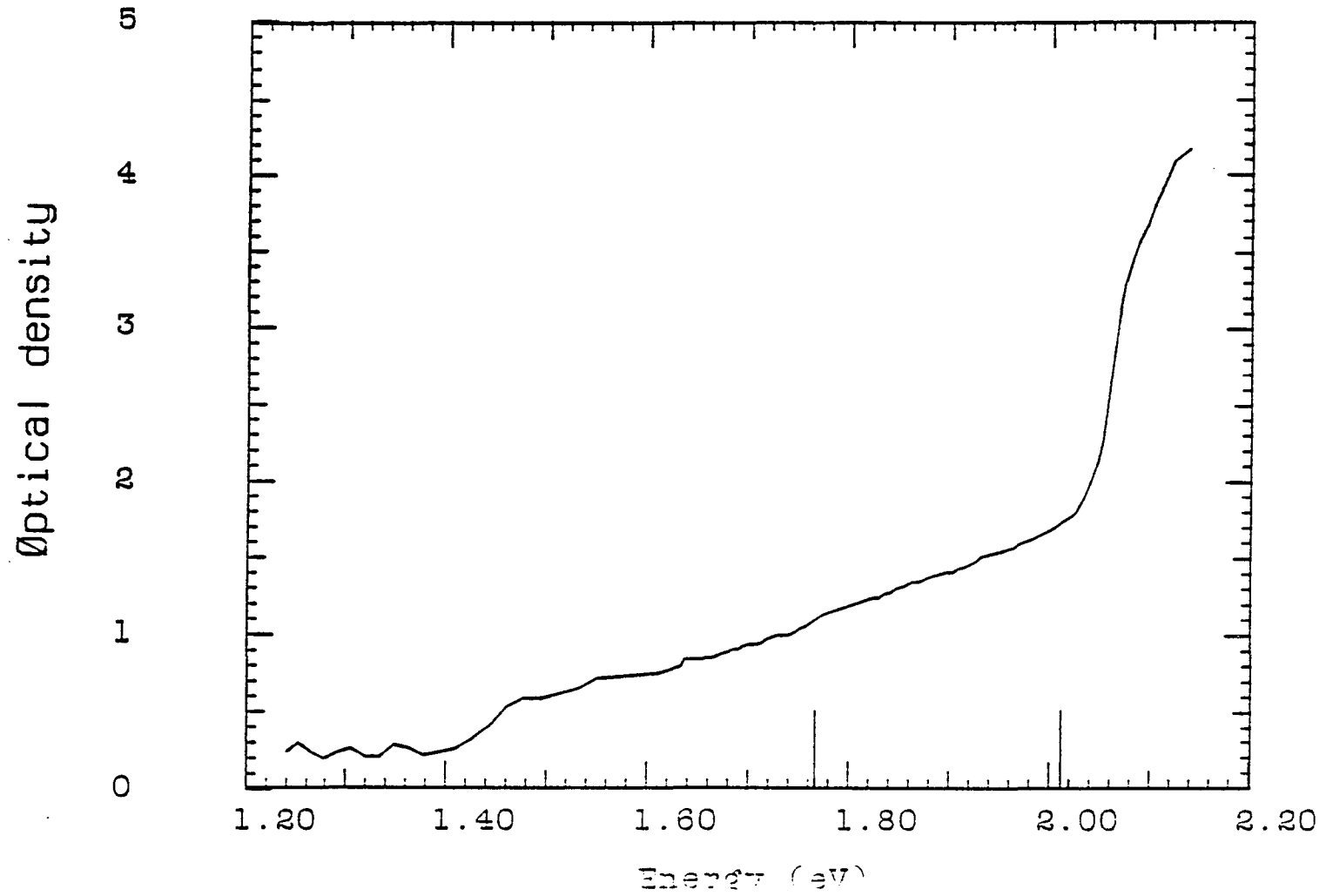

Figure 2.4.2. Optical density of GaAs sample #2 (0.75 μ thickness), uncorrected for sample reflectivity. The cover layer is 2 μ of $Al_{.5}Ga_{.5}As$ in front and 1 μ in back.

While the absorption coefficient is given by

$$I_t = I_o(1-R_1)(1-R_2)^2(1-R_3)(1-R_4)\exp(-\alpha\ell) \qquad (2.4.4)$$

where R_1, R_2, R_3, and R_4 are the reflection coefficients at the Air-AlGaAs, AlGaAs-GaAs, AlGaAs-glass and glass-air interfaces respectively and ℓ is the sample thickness (0.75 μ). Combining eqs 2.4.3 and 2.4.4 gives

$$\alpha = \{\ln[(1-R_1)(1-R_2)^2(1-R_3)(1-R_4)] + O.D.\ \ln(10)\}/\ell \qquad (2.4.5)$$

and using the appropriate values for the reflectivities and sample thickness gives

$$\alpha = 8.2 \times 10^3 + 3.07 \times 10^4\ (O.D) \quad cm^{-1}\ . \qquad (2.4.6)$$

The absorption coefficient is plotted in figure 2.4.3 over the energy range of 1.424 to 2.05 eV. Above 2.05 eV, the different contributions from the GaAs and the $Al_{.5}Ga_{.5}As$ would have to be separated to correctly determine α.

In pump and probe absorption experiments, one measures the change in the intensity of the transmitted beam. The change in transmission depends on $\Delta\alpha\ell$. For a given change in absorption, a thicker sample gives a greater change in transmission but the absolute transmitted intensity is reduced. In absorption experiments the optical thickness of the sample should be thin in order to allow the

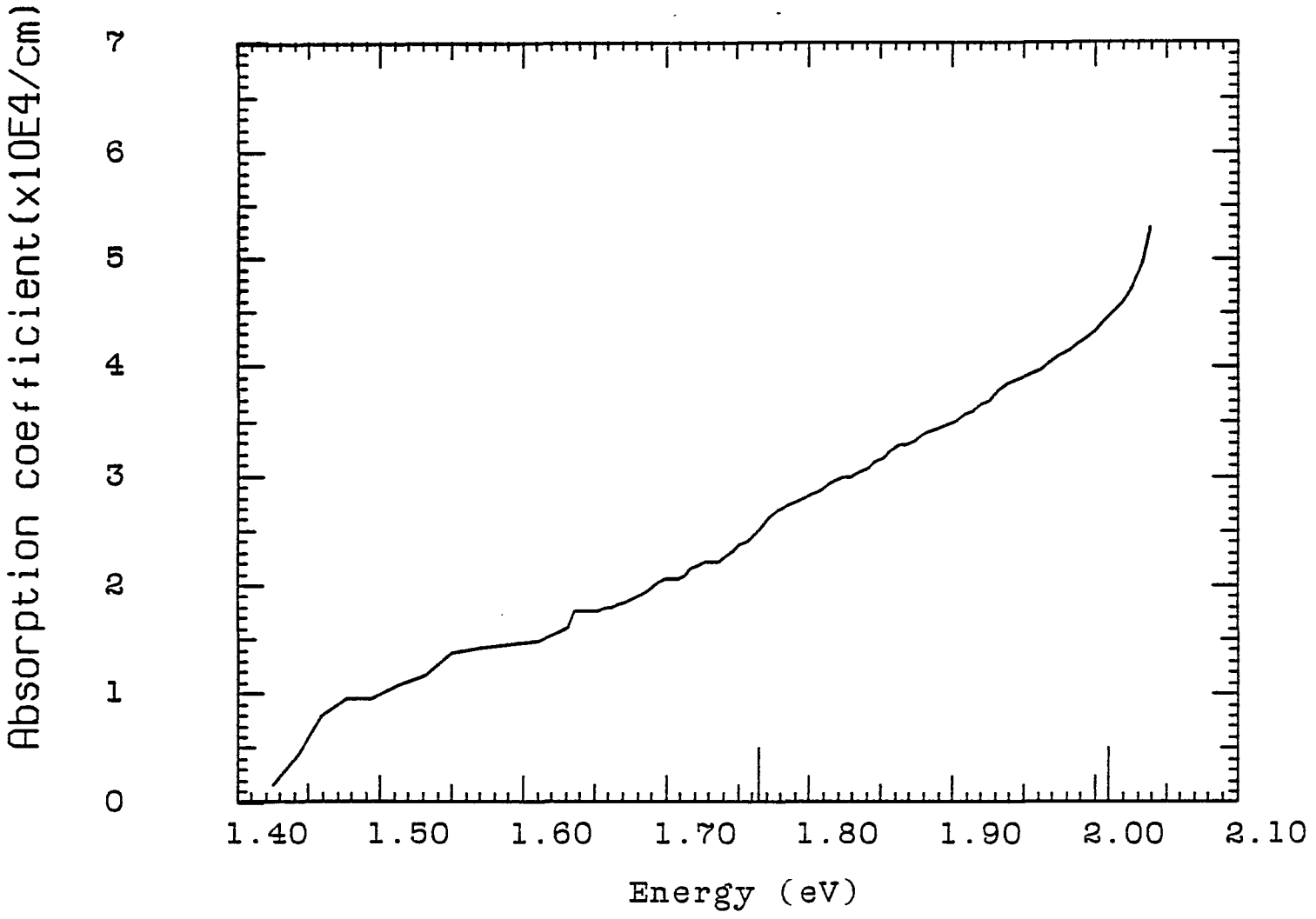

Figure 2.4.3. Absorption coefficient of GaAs sample #2 (0.75 μ thickness). The cover layer is 2 μ of $Al_{.5}Ga_{.5}As$ in front and 1 μ in back.

detected transmitted signal to be greater than the background light and detector noise level but thick enough so that there is a detectable change is transmission. Most of the absorption data was taken with the 0.75 micron thick sample ($\alpha\ell$ = 3.0 at 2.01 eV).

In the transient grating experiments, the signal is detected in the background free direction and thus in a thinner sample there will be less absorption of the diffracted signal by the sample. For this reason most of the transient grating data was taken with the 0.25 micron thick samples although data was taken on all samples.

2.4 Notes

[1]V. M. Goldschmidt, Trans. Faraday Soc. **25**, 1253 (1929).

[2]J. S. Blackemore, J. Appl. Phys. **53**, R123 (1982).

[3]M. B. Panish and H. C. Casey, J. Appl. Phys. **40**, 162 (1969).

[4]C. D. Thurmond, J. Electrochem. Soc. **122**, 1133 (1975).

[5]D. E. Aspnes, Phys. Rev. B **14**, 5331 (1976).

[6]D. E. Aspnes and A. A. Studna, Phys. Rev. B **47**, 4605 (1973).

[7]D. E. Aspnes, C. G. Olson and D. W. Lynch, Phys. Rev. B **12**, 2527 (1975).

[8]D. E. Aspnes, C. G. Olson and D. W. Lynch, Phys. Rev. Lett. **378**, 766 (1976).

[9]G. E. Stillman, C. M. Wolfe and J. O. Dimmock in Vol 12 of **Semiconductors and Semimetals**, edited by R. K. Willardson and A. C. Beer (Academic, New York) p. 169 (1977).

[10]E. O. Kane, J. Phys. Chem. Solids **1**, 249 (1957).

[11]H. Ehrenreich, Phys. Rev. **120**, 1951 (1960).

[12]J. S. Blakemore, **Semiconductor Statistics,** (Dover, New York 1983).

[13]D. E. Aspnes in **Gallium Arsenide and related Compounds,** (No. 33b, Institute of Physics, London) p110.

[14]M. S. Skolnick, A. K. Jain, R. A. Stradling, J. Leotin, J. C. Ousset, and S. Askenazy, J. Phys. C **9**, 2809 (1976).

[15]M. Reine, R. L. Agrawal and B. Lax, Phys. Rev. B **51**, 3033 (1972).

[16]H. C. Casey, Jr. and M. B. Panish, **Heterostructure Lasers,** (Academic New York, 1978) Part A.

Chapter 3 Femtosecond laser system

3.1 Oscillator

3.1.1 Introduction

Organic dyes make an excellent broadband gain medium for passively modelocked lasers.[1] Typical dye emission bands span 300 nm. Dyes have a large quantum efficiency. CW rhodamine 6G (Rh6G) dye lasers can be made to lase from 560 nm to 640 nm.

The first modelocked dye lasers[2,3] used a modelocked Nd:glass or argon laser to synchronously pump Rh6G. The first passive modelocking[4,5] of an organic dye used Rh6G as the gain medium and 3,3'-diethyloxadicarbocyanine iodide (DODCI) as the modelocking dye. These systems were flash lamp pumped and produced 6 ps pulses although pulse width measurements indicated incomplete modelocking.[5] The first cw passively modelocked Rh6G dye lasers[6-8] used the 514.5 nm output of a continuous argon ion laser to pump Rh6G. DODCI was the modelocking dye. The cavity consisted of the Rh6G flowing in one cell and the DODCI in another cell. This allowed tighter focusing in the saturable absorber. A prism was inserted in the cavity for tunability of the dye laser over the range of 590 to 620 nm.

A simple cavity design for passively modelocking this system was a 2 dye cell, 5 mirror linear cavity consisting of the lasing dye flowing in one cell and the saturable absorber in the other cell.[6] A prism was inserted in the cavity for tunability. Two curved mirrors

were used to focus and recollimate the pulse at each dye cell. One of the focusing mirrors served as the output mirror (typical reflectivity ≈ 95 - 99%, the other mirrors had 100% reflectivity over the gain bandwidth of the laser). This arrangement allows independent control of the laser intensity at the Rh6G and the DODCI by using mirrors with different radii of curvature. This configuration also allows for astigmatic compensation in the cavity by controlling the angle of incidence at the focusing mirrors.[9] Variations on the cavity design included: mounting the saturable absorber cell on an end mirror;[10] inserting an acousto-optical cavity dumper in the laser cavity[11,12] (this increased the output pulse energy but the repetition rate was reduced to 10^5 Hz); and extending the cavity design to 6 mirrors. An Astigmatically compensated design was later extended to a six mirror ring cavity.[13] Other improvements consisting of replacing the dye cells with free flowing jet streams. This reduced group velocity dispersion effects by decreasing the optical path length in the gain and absorbing media. The jet stream thickness can be reduced to 10^{-2} to 10^{-3} cm. These systems typically produced pulses that were about 1 ps in duration but highly chirped and unstable. Using external pulse compression[14] or by mixing malachite green into the DODCI[15] the pulses could be compressed to 0.3 ps. In 1981, the colliding pulse modelocked (CPM) ring cavity laser was developed.[16] The output pulses from this system were about 100 fs in duration and very stable. This cavity design is the one used in this thesis work and will be discussed in detail in section 3.1.4.

3.1.2 Modelocking and ultrashort pulse generation

Unlike modelocked solid state lasers, where the pulse width is determined by the recovery time of the saturable absorber, the pulse width of passively modelocked dye lasers is considerably faster than the recovery time of the DODCI;[1,17-22] which was measured to be 0.3 ns[17,23] to 1.2 ns.[1] The passive modelocking of this system is accomplished by a combination of bleaching of the absorption of the DODCI and gain saturation in the Rh6G. The absorption and fluorescence spectra of Rh6G and the absorption spectra of DODCI are shown in fig. 3.1.1, 3.1.2 and 3.1.3 respectively. The absorption peak of the DODCI (585 nm) is close to the emission peak of the Rh6G (560 nm). The gain curve of this combination is flat over a broad range of wavelengths allowing the laser pulses to have a bandwidth of ≥ 6 nm (corresponding to 70 femtoseconds for a transform limited $sech^2$ pulse envelope centered at 620 nm).[24]

That the Rh6G - DODCI combination can only modelock in the red and not near the absorption peak of the DODCI is strong experimental evidence that a photoisomer exists in the DODCI with an absorption peak at 620 nm.[1,17,23,25,26] The photoisomer has been observed in the fluorescence[17,27] and absorption[1] spectra of DODCI and is believed to play an important role in the bleaching of the DODCI by increasing the longer wavelength absorption in the DODCI. It is the cause of an observed bistable mode in the laser cavity. It has been observed that the laser system can operate completely modelocked in the red (615-630) or lase cw in the yellow (560-570 nm).[28-30] Minor changes in alignment or pumping power can cause the system to switch modes.

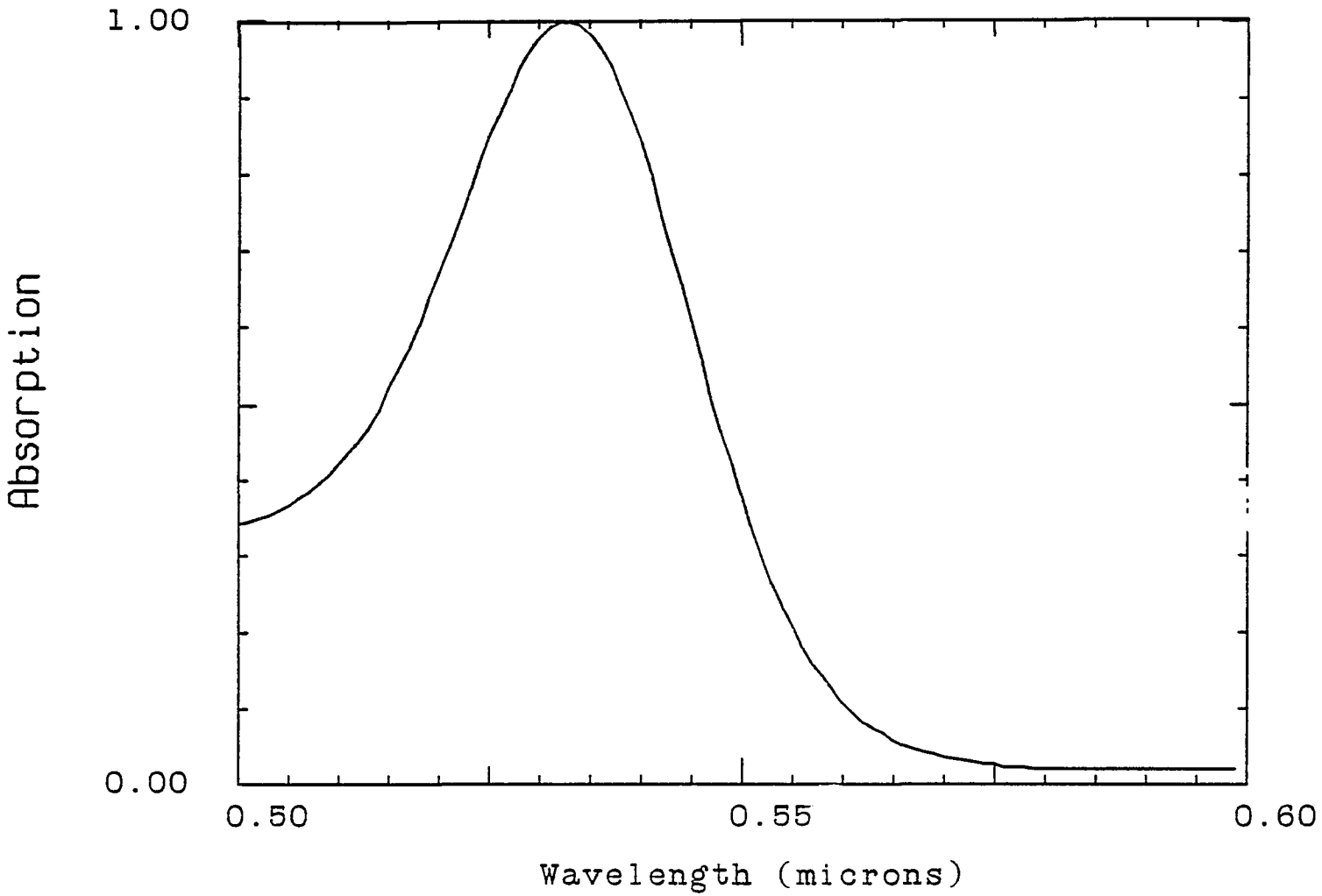

Figure 3.1.1. Absorption spectrum of the oscillator gain dye (Rhodamine 6G). The concentration is 1.5×10^{-3} molar in ethylene glycol.

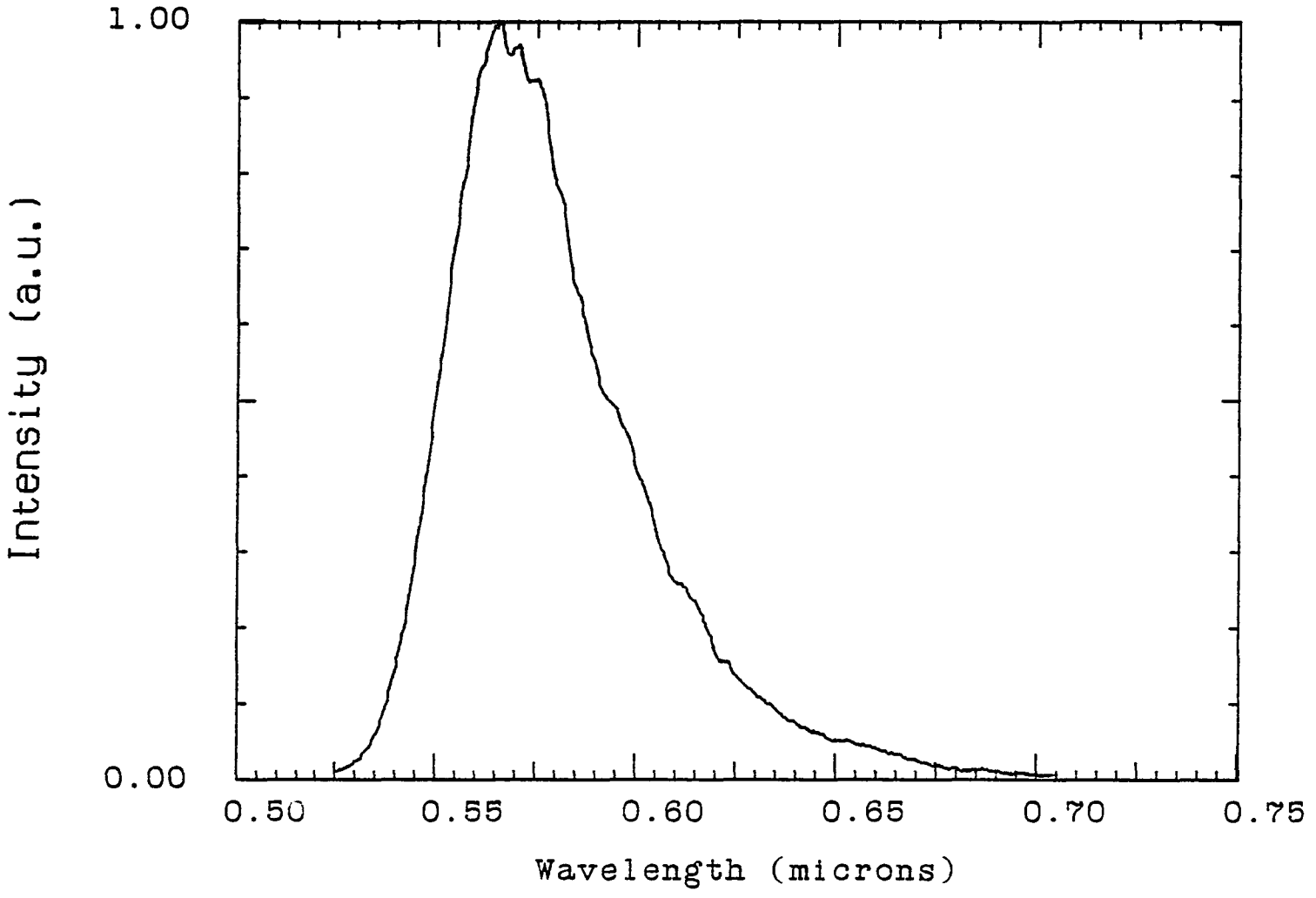

Figure 3.1.2. Fluorescence spectrum of Rhodamine 6G. The fluorescence curves, for Rh 6G and the other gain dyes, are not corrected for self-absorption or detector response.

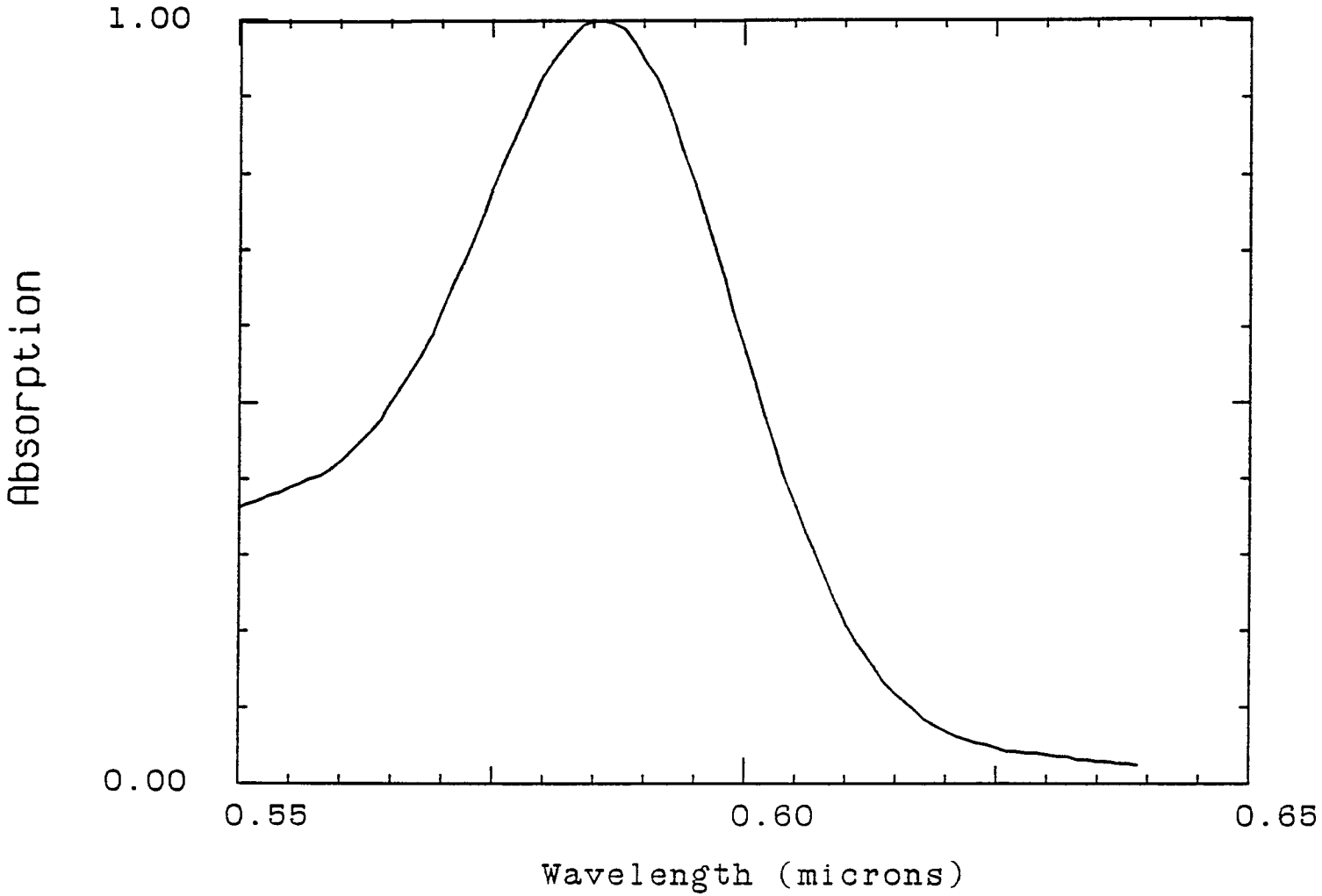

Figure 3.1.3. Absorption spectrum of the modelocking dye, DODCI. The modelocking dye is a 10^{-4} molar solution of DODCI in ethylene glycol.

The formation of ultrashort pulses in a passively modelocked Rh6G, DODCI combination can only be explained in terms of both gain saturation and a saturable absorber. Streak camera measurements show that a well modelocked laser pulse evolves from intensity fluctuations over the course of a few cavity round trips and is not limited by the relaxation time of the saturable absorber.[15] When a pulse enters the saturable absorber the leading edge of the pulse is absorbed but the center part of the pulse where the intensity is greater bleaches the dye and is transmitted with less loss. This steepens the leading edge of the pulse. The pulse is now amplified in the Rh6G jet. However, the leading edge of the pulse depletes the excited states of the dye and the trailing edge of the pulse in not amplified.[21] Other cavity losses contribute to reducing the trailing edge. It has been shown that if the saturable absorber cross section is much larger than the gain cross section, pulse shortening will occur, independent of input pulse shape.[21,31] This process is sensitive to the relative gain of the Rh6G and the absorption in the DODCI, therefore the dye concentrations, pumping power and laser spot sizes must be carefully controlled.

3.1.3 Laser cavity and frequency chirp

The ultimate limit on the output pulses of this dye laser system is determined by the gain bandwidth of the Rh6G and DODCI combination and is $\approx$ 20-25 fs.[32] That this pulse width is not achieved is the result of dispersion inside the laser cavity, and in order to minimize the pulse width, the number of dispersive elements in the cavity must be minimized. The sources of dispersion in the laser

cavity are the saturation of the absorbing dye, self-phase modulation in the dye solvent,[33-37] group velocity dispersion in the dye solvent[36] the dielectric coatings of the cavity mirrors,[36-41] as well as any glass or other passive dispersive elements in the optical path. All of these sources of frequency chirp serve to broaden the pulse. Since the gain and the absorption saturation is not linear throughout the pulse duration, chirp can also reduce the bandwidth. The extent of pulse chirping is determined by the actual cavity configuration. Slightly different cavity designs can have different degrees of pulse chirp. Fontaine et al[37] report a cavity with negative chirp (i.e. shorter wavelengths lead) while Shank et al[14,42] report a cavity with positive chirp. In my laser cavity, the chirp was found to be a function of DODCI concentration. At low DODCI concentrations, the chirp is negative and insertion of the proper length of glass in the laser (external to the cavity) results in a narrower pulse. At higher DODCI concentrations the chirp is positive and the glass only serves to broaden the pulse; while a grating pair (as described in section 3.2.3) shortens the pulse width.

The role of the saturable absorber jet stream is complicated by the fact that frequency chirp is produced by saturation of absorption in the DODCI and self-phase modulation (SPM) in the solvent as well as group velocity dispersion in both.[35,36] The different contributions to the frequency chirp in the DODCI jet have been discussed in references 35 and 36. De Silvestri et al[36] calculate the chirp due to the normal absorption of the DODCI as well as the photoisomer. They find that the two contributions are opposite in sign; the normal

absorption gives negative chirp and the photoisomer gives positive chirp at their laser wavelength of 610 nm. For a laser operating at 620 nm (which is the absorption peak of the photoisomer) the photoisomer contribution would be significantly less. They also find that the contribution from the Rh6G to be considerably less than the DODCI.

Miranda et al[35] have calculated the chirp produced in the DODCI jet stream for different DODCI concentrations, pulse energy and pulse width; examining both self-phase modulation in the solvent as well as the absorption saturation of the dye. Their results are summarized below.

The high peak intensity produced in the DODCI causes large changes in the solvent contribution to the index of refraction through self phase modulation (SPM). The solvent contribution to the index of refraction is given by

$$n_s = n_o + n_2 I^2 \quad . \tag{3.1.1}$$

The contribution to the index of refraction due to resonant absorption of the DODCI is given by

$$n_r = \frac{\pi}{2}(\omega_o - \omega) \quad \frac{c}{\omega_o} \alpha g(\omega) \tag{3.1.2}$$

where α is the saturated absorption coefficient given by

$$\alpha(t) = \alpha_o \exp\left[\frac{-\int_{-\infty}^{t} I(\xi)d\xi}{E_s}\right] \qquad (3.1.3)$$

E_s is the absorber saturation energy density, and $g(\omega)$ is the absorption line shape given by

$$g(\omega) = 2\left\{\pi\Delta\omega\left[1+\frac{4(\omega_o-\omega)^2}{\Delta\omega^2}\right]\right\}^{-1} . \qquad (3.1.4)$$

The time dependent phase delay is given by

$$\Phi(t) = -\frac{n_2\omega l}{c} I(t) - G(\omega)\frac{\omega l}{c}\alpha(t) . \qquad (3.1.5)$$

Where $G(\omega) = \frac{n_r}{\alpha(\omega)}$. The frequency shift is $\delta\omega = \frac{d\Phi}{dt}$ and is given by

$$\delta\omega = -\frac{n_2\omega l}{c}\frac{dI}{dt} - G(\omega)\frac{\omega l}{c}\frac{d\alpha(t)}{dt} \qquad (3.1.6)$$

and the pulse chirp, defined as $C \equiv \frac{d^2\phi}{dt^2} = \frac{d(\delta\omega)}{dt}$ is given by

$$C = -\frac{n_2\omega l}{c}\frac{d^2I}{dt^2} - G(\omega)\frac{\omega l}{c}\frac{d^2\alpha(t)}{dt^2} . \qquad (3.1.7)$$

The extent of the pulse chirp depends on the pulse width, pulse energy and the absorber concentration. If we consider a gaussian pulse, $I(t) = I_o \exp\left[-\frac{t^2}{\tau^2}\right]$; the chirp is given by

$$C = \frac{4\pi n_2 l I_o}{\lambda\tau^2}\left[1-\frac{2t^2}{\tau^2}\right]\exp\left[\frac{-t^2}{\tau^2}\right] - \frac{2\pi I_o G(\omega)\alpha}{\lambda E_s}\left[\frac{I_o}{E_s} - \frac{2t}{\tau^2}\right]\exp\left[\frac{-t^2}{\tau^2}\right] . \qquad (3.1.8)$$

The solvent contribution to the chirp is positive in the central part of the pulse ($|t| <$ half width at half maximum) and negative and small in the wings of the pulse where the pulse intensity is considerably less. The amount of chirp from the solvent increases with shorter pulse widths or greater pulse intensity. The absorber dye contribution to the chirp is always negative except in the extreme wings of the pulse where the pulse intensity is small. The amount of negative chirp generated by the dye increases as the pulse energy increases relative to the saturation energy. At lower dye concentrations, the threshold for bleaching is less and the amount of negative contribution to the chirp is greater. The optimum concentration of DODCI is when the two terms cancel. This concentration depends on the intracavity pulse energy, focused spot size in the jet and the thickness of the jet stream. Experimentally the absorber dye concentration for minimum pulse width was determined by measuring the pulse width as the concentration was slowly increased. At each concentration, glass rods of varying lengths were inserted in the laser path to determine when the chirp changed from negative to positive.

In the cavity design used in this thesis work, where there are no prisms or other transmission optics, the other significant source of chirp is the cavity mirrors. High reflectivity dielectric coated mirrors are made of alternate layers of high and low index of refraction material with a thickness of $\lambda/_4$. A typical narrow band reflection coating consists of about 19 layers. A broadband reflection coating consists of many different layers and can add

considerably to the chirp. The calculations in references 36 and 38, show the phase shift of a narrow band dielectric coating to be zero at the center frequency of the coating, the phase shift rapidly becomes positive (negative) as one moves to shorter (longer) wavelengths. The phase shift varies much more rapidly if the reflectivity of the mirror is smaller or if the angle of incidence is different than the intended angle of the coating. Bourkoff et al[41] calculate changes in pulse shape due to dispersive mirrors. Considerable pulse distortion and broadening has been shown for a variety of commercially available broadband dielectric mirrors.[40]

3.1.4 Colliding pulse modelocked ring cavity dye laser

To reduce the pulse width and improve the stability of the laser, a ring cavity design was developed by Fork et al.[16,43] This cavity supports two counter propagating pulses. The cavity losses are a minimum when the two pulses overlap in the DODCI jet stream. The position of the rhodamine jet stream is one quarter of the cavity length from the DODCI. This insures that excited population in the rhodamine has equal time to build up between the counter propagating pulses and each pulse experiences equal gain. This colliding pulse modelocking (CPM) laser, without any additional dispersion correcting devices, can produce pulses of as short as 60 fs duration.[43]

The oscillator design constructed for this thesis work is shown in figure 3.1.4. The oscillator is pumped by the 514.5 nm line of a Spectra Physics model 171 Argon Ion laser operating at 2.5 watts output power. The Argon laser is rotated to P polarization to match

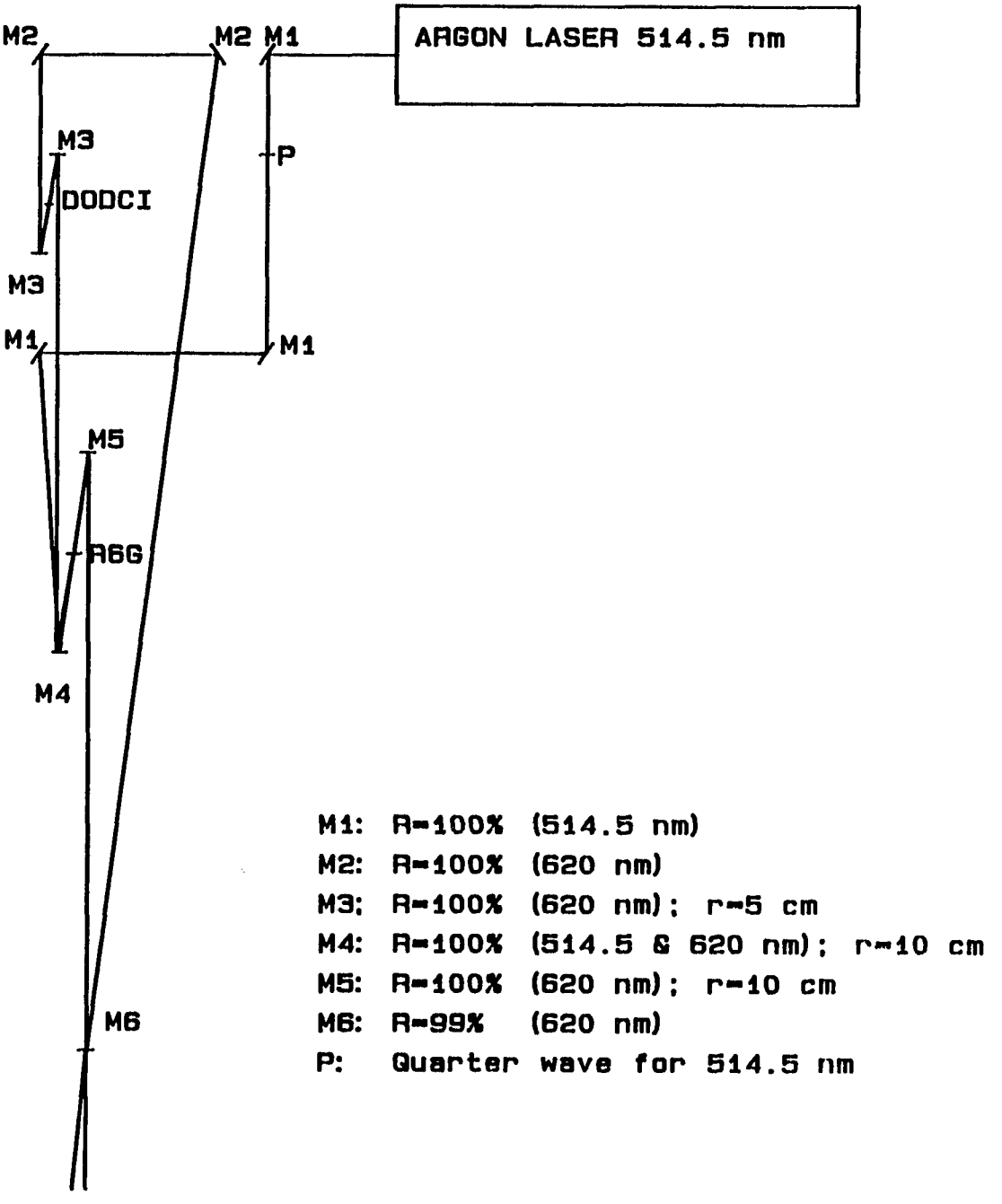

Figure 3.1.4. Femtosecond colliding pulse mode-locking ring cavity dye laser oscillator. The dye concentrations are 1.5 x 10^{-3} molar for the Rhodamine 6G and 10^{-4} for the DODCI.

the polarization of the dye laser. The cavity consists of seven mirrors and two jet streams plus three mirrors and a rotator for aligning the pump. Two curved mirrors of 5 cm radius of curvature (M3 in figure 3.1.4) are used to focus the beam into the DODCI. The mirrors labeled M4 and M5, of 10 cm radius of curvature, focus the beam into the Rh6G. M4 also focuses the Argon laser into the Rh6G. M6 and M2 are flat mirrors used to complete the ring. M6 is also the output mirror with a transmission of 1%. All the other mirrors are 100% reflectors. The jet streams are aligned at Brewster's angle to the laser path, eliminating reflection losses for P polarized light. The DODCI concentration is 10^{-4} molar and the Rhodamine concentration is 1.5×10^{-3} molar. The center wavelength of the laser output is 620 nm. The temporal duration of the output of this laser is 100 - 150 fs. The pulse energy is 50 - 100 picojoules per pulse at a repetition rate equal to the cavity round trip time of 114 MHz. The average output power is 5 to 10 milliwatts.

The advantage of the ring cavity over the linear cavity is the result of the standing wave produced by the interference pattern of the counter propagating pulses in the saturable absorber jet stream. It has been shown that colliding pulse modelocking has a more favorable stability region and leads to increased pulse shortening when compared to a linear cavity arrangement.[44-48] When the pulses spatially overlap in the jet stream, the electric fields of the pulses are in phase over the coherence length of the pulse. In this case the intensity is 4 times that of a single pulse and the bleaching is greatly enhanced. Additionally, if the absorber jet is thinner than

the pulse width, the spatial wings of the chirped pulse will be out of phase and therefore the effective bleaching will be less than the bleaching for the coherent portion of the pulse. This will dechirp the pulse and eliminate the spatial wings of the pulse.

It is possible to improve the stability and shorten the pulse width of the CPM laser by the insertion of tuneable dispersion correcting elements in the cavity. Although not incorporated into the laser system used for this thesis, the addition of four Brewster angle prisms in the laser cavity give an adjustable source of negative dispersion which can be used to balance the other dispersive elements of the cavity and give pulses as short as 25 fs.[49-51]

3.2 Pulse measurement and compression

3.2.1 Pulse measurement by second harmonic generation

Subpicosecond laser pulses are too short to be measured by electronics but must be measured by nonlinear optical methods. Autocorrelation measurements by non-collinear second harmonic generation (SHG) is an effective method to measure the pulse width of ultrashort, high repetition rate lasers.[52,53]

When a laser beam is incident on a uniaxial crystal a polarization at twice the laser frequency is produced. If the indices of refraction of the crystal axes, crystal orientation and laser polarization are such as to satisfy conservation of energy and momentum, a significant fraction of the laser beam can be converted to its second harmonic. This condition is known as phase-matching and the requirements are

$$\begin{aligned} k_\omega + k_\omega &= k_{2\omega} \\ \omega + \omega &= 2\omega \end{aligned} \qquad (3.2.1)$$

For a light wave propagating at an arbitrary angle θ to the optic axis the index of refraction is given by[54]

$$\frac{1}{n_e^2(\theta)} = \frac{\cos^2\theta}{n_o^2} + \frac{\sin^2\theta}{n_o^2} \quad . \qquad (3.2.2)$$

where n_o is the index of refraction along the ordinary axes and n_e is the index along the extraordinary (optic) axis. Eqs. 3.2.1 becomes

$$\frac{c}{n(\omega,k)} + \frac{c}{n(\omega,k)} = \frac{c}{n(2\omega,K)} \qquad (3.2.3)$$

$$n_\omega = n_{2\omega} \quad . \qquad (3.2.4)$$

For most crystals with normal dispersion, phase matching requires the fundamental and second harmonic waves must be of a different type. In a KDP (Potassium diHydrogen Phosphate) crystal, two types of phase matching are possible.[55-57] Type I phase-matching consists of two ordinary waves summing to produce an extraordinary wave at twice the frequency. Type I is also designated o-o-e. Type II phase matching consists of an ordinary wave and an extraordinary wave summing to produce an extraordinary wave at twice the frequency. Type II is also designated o-e-e. The phase matching angle for type I SHG can be calculated by Eqs. 3.2.2 and 3.2.3 and is given by

$$\sin^2\theta = \frac{n_e^2(2\omega)\,\{n_o^2(2\omega) - n_o^2(\omega)\}}{n_o^2(\omega)\,\{n_e^2(2\omega) - n_o^2(2\omega)\}} \quad . \qquad (3.2.5)$$

For 6200 Å the type I phase matching angle is 57.7° in KDP. The indices of refraction were taken from the **CRC Handbook of Lasers.**[58]

The non-collinear type I phase-matching geometry (fig. 3.2.1) is background free, relatively easy to align and does not require a half-wave plate in one of the pulse trains. For a non-collinear

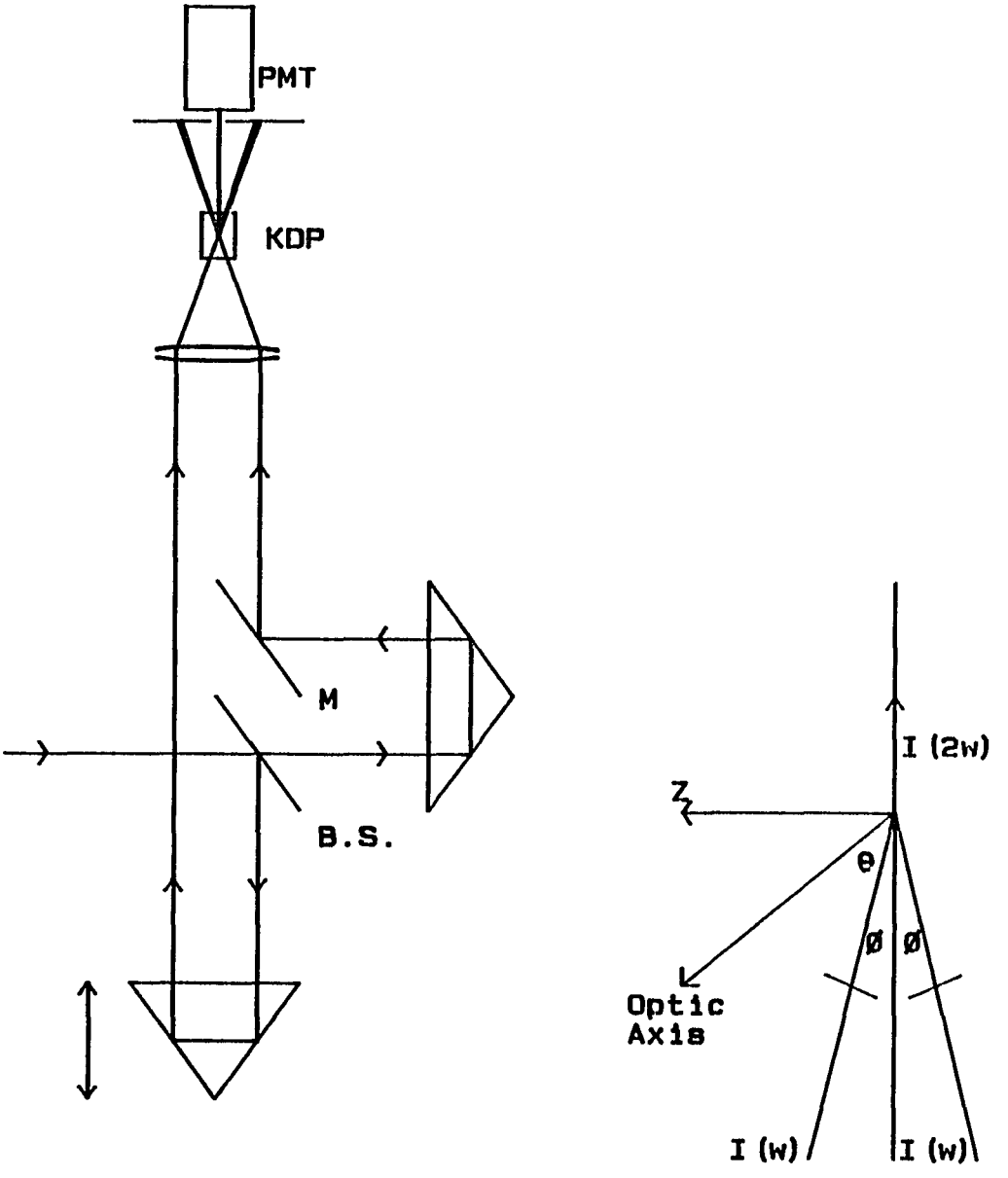

Figure 3.2.1. Second harmonic correlator for monitoring the laser pulse width. The KDP crystal is cut for type I phasematching. The input beams are P-polarized and the second harmonic is S-polarized.

geometry, the fundamental waves do not propagate as a true o-wave but at a slight angle to the ordinary axes and therefore the phase matching angle for the non-collinear geometry is slightly different than for single beam SHG. The propagation direction is also different for the mixing signal than for the individual beam second harmonic. Apertures can reduce the single pulse SHG to below the detector noise level. By using the proper geometry, almost all transmission optics can be removed from the apparatus, eliminating pulse broadening due to dispersion. The temporal resolution of this system is then limited only by the phase matched bandwidth of the nonlinear material.[59-64] The phase matched bandwidth is given by

$$\delta\lambda = \pm \left[\frac{1.39\ \lambda_1}{2\pi l} \frac{dn_o^{\omega}}{d\lambda_1} - \frac{1}{2} \frac{dn_e^{2\omega}}{d\lambda_2} \right] . \qquad (3.2.6)$$

In KDP, for a 6200 Å fundamental wavelength and a 50 Å bandwidth, the maximum interaction length in the crystal is 0.2 mm. A non-collinear geometry with tight focusing limits the interaction length in the crystal to

$$l = d \frac{\cos(\theta)}{\sin(2\theta)} \qquad (3.2.7)$$

where d is the focused spot diameter and 2θ is the angle between the beams in the nonlinear crystal. If the two beams are separated by 1 cm and focused by a 5 cm lens to a 25 micron spot size, the interaction length is 0.180 mm.

For pulses less than 100 fs, group velocity mismatch as well as phase velocity mismatch must be considered.[61-65] A calculation of the group velocity dispersion of the fundamental pulse shows that broadening is negligible. Using the value of the index given in reference 58 for an ordinary wave, the broadening of a 50 fs gaussian pulse in 200 microns of KDP is about 1 fs. However, the group velocity mismatch between the fundamental and the second harmonic must be considered. If phase-matched, the fundamental and second harmonic have the same phase velocity but not necessarily the same group velocity. The broadening of the second harmonic pulse has been considered in ref. 60-64. The resultant effects on SHG pulse measurements is considered in ref. 65. The measured autocorrelation will, in general, be a function of the input pulse shape and chirp.

3.2.2 Pulse autocorrelation

If a variable delay is introduced to one of the pulse trains, the second harmonic intensity will change as a function of the delay. Let the envelope of the field of the pulses be $E_1(t)$ and $E_2(t+\tau)$. The polarization at 2ω is

$$P(t,\tau) = \chi^2 E_1(t) E_2(t+\tau) \quad . \tag{3.2.8}$$

A slow detector will integrate $P(t,\tau)$ over time and the detected signal is

$$G(\tau) = \int_{-\infty}^{\infty} E_1(t)E_2(t+\tau)E_1^*(t)E_2^*(t+\tau)\,dt \qquad (3.2.9)$$

$$G(\tau) = \int_{-\infty}^{\infty} I_1(t)I_2(t+\tau)dt \quad . \qquad (3.2.10)$$

The pulse convolution $G(\tau)$ is related to the pulse width but has lost knowledge of the pulse shape or chirp. To get the correct pulse width, the pulse shape must be determined independently, i.e. from the product of the pulse's spectral bandwidth and temporal width.

For a gaussian pulse, the ratio of the autocorrelation FWHM to the pulse FWHM, $\frac{\tau_G}{\tau_P}$, is 1.41 and $\delta\nu\delta t = 0.44$. The autocorrelation is also a gaussian. For a pulse with a hyperbolic secant squared intensity envelope, $\frac{\tau_G}{\tau_P} = 1.55$ and $\delta\nu\delta t = 0.315$.

Consider a sech^2 pulse with an intensity full width at half maximum, τ_p. The intensity profile is given by

$$I(t) = I_o\ \text{sech}^2\left[\frac{1.76\ t}{\tau_p}\right] \quad . \qquad (3.2.11)$$

The electric field of this pulse is given by

$$E(t) = \sqrt{I_o}\,\text{sech}\left[\frac{1.76\ t}{\tau_p}\right] \exp(-i\omega_L t) \qquad (3.2.12)$$

and the spectrum of the electric field is given by

$$\mathcal{E}(\omega) = \sqrt{\frac{\pi I_o}{2}}\frac{\tau_p}{1.76}\ \mathrm{sech}\left[\frac{\tau_p\pi(\omega-\omega_L)}{1.76}\right] \quad . \qquad (3.2.13)$$

The intensity spectrum is given by

$$I(\omega) = \frac{\pi I_o}{2}\left[\frac{\tau_p}{1.76}\right]^2 \mathrm{sech}^2\left[\frac{\tau_p\pi(\omega-\omega_L)}{2(1.76)}\right] \quad . \qquad (3.2.14)$$

The FWHM product of $I_{1/2}(t)\cdot I_{1/2}(\nu)$ is

$$\delta\nu\delta t = \frac{1}{2\pi}\ \frac{2(1.76)^2}{\pi\tau_p}\tau_p = 0.315 \qquad (3.2.15)$$

The pulse intensity autocorrelation given by Eq. 3.2.10 for a sech^2 pulse shape can be calculated by using the convolution theorem. The fourier transform of the intensity profile, given by Eq. 3.2.16, can be evaluated using the Cauchy Residue Theorem.

$$\mathcal{F}\,[I(t),\xi] = \int_{-\infty}^{\infty} I_o\,\mathrm{sech}^2\left[\frac{1.76\ t}{\tau_p}\right]e^{i\xi t}\ dt \qquad (3.2.16)$$

The contour of integration is a semicircle in the upper half plane with a radius equal to infinity. All the poles are of order two and located on the imaginary axis at the points given by

$$t = \frac{\tau_p}{1.76}(n + \frac{1}{2})\pi i; \qquad n = 0,1,2,3\ .\ .\ . \qquad (3.2.17)$$

and the residues are given by

$$C_n = \frac{i\xi\tau_p^2}{(1.76)^2} \exp\left[\frac{-\xi\tau_p}{1.76}(n+\frac{1}{2})\pi\right] \tag{3.2.18}$$

The sum of the residues, multiplied by $2\pi i$, is:

$$\mathcal{F}[I(t),\xi] = \frac{2\pi\xi\tau_p^2}{(1.76)^2} \exp\left[\frac{-\pi\xi\tau_p}{2(1.76)}\right] \sum_n \exp\left[\frac{-\pi\xi\tau_p}{1.76}\right]^n \tag{3.2.19}$$

$$\mathcal{F}[I(t),\xi] = \frac{2\pi\xi\tau_p^2}{(1.76)^2} \exp\left[\frac{-\pi\xi\tau_p}{2(1.76)}\right] \frac{1}{\left[1-\exp\left[\frac{-\pi\xi\tau_p}{1.76}\right]\right]} \tag{3.2.20}$$

$$\mathcal{F}[I(t),\xi] = \frac{2\pi\xi\tau_p^2}{(1.76)^2} \operatorname{csch}\left[\frac{-\pi\xi\tau_p}{1.76}\right] \quad . \tag{3.2.21}$$

Using the convolution theorem, the autocorrelation of the pulse is given by

$$G(\theta) = \int_{-\infty}^{\infty} \mathcal{F}(\xi)\ \mathcal{F}(\xi) e^{-i\xi\theta} d\xi \tag{3.2.22}$$

$$G(\theta) = \int_{-\infty}^{\infty} \frac{4t^4\xi^2}{\pi^2} \operatorname{csch}^2(\xi t) e^{-i\xi\theta}\ d\xi \tag{3.2.23}$$

where $t \equiv \frac{\pi\tau_p}{1.76}$. Again the contour is a semicircle of infinite radius in the upper half plane. The poles are of second order and located on the imaginary axis at the points $\xi t = 2n\pi i$; n=1,2,3 . . . . The residues are given by

$$C_n = \frac{4t^4}{\pi^2}\left[\frac{2n\pi i}{t^3} - \frac{n^2\pi^2 i\theta}{t^4}\right] \exp\left[\frac{-\pi\theta n}{t}\right] \quad . \tag{3.2.24}$$

In order to evaluate the sum of the residues, Eq. 3.2.24 is separated into two terms, which are:

$$2\pi i\sum_{n} C_n = -\sum_{n} 16nt \exp\left[\frac{-\pi\theta n}{t}\right] + \sum_{n} 8\pi n^2\theta \exp\left[\frac{-\pi\theta n}{t}\right] \quad . \qquad (3.2.25)$$

The first summation on the right hand side of Eq. 3.2.25 can be rewritten and summed to give:

$$16t \exp\left[\frac{-\pi\theta}{t}\right] \sum_{n} n\left[\exp\left[\frac{-\pi\theta}{t}\right]\right]^{n-1} = 16t \exp\left[\frac{-\pi\theta}{t}\right]\left\{-\exp\left[\frac{-\pi\theta}{t}\right]\right\}^{-2} . \quad (3.2.26)$$

The second summation in 3.2.25 can be evaluated by rewriting n^2 as $\frac{n(n+1)}{2} + \frac{n(n-1)}{2}$ and then the summation can be written as:

$$\sum_{n} 8\pi n^2\theta \exp\left[\frac{-\pi\theta n}{t}\right] = 8\pi\theta\left[\sum_{n}\frac{n(n+1)}{2}\exp\left[\frac{-\pi\theta}{t}\right]^n + \sum_{n}\frac{n(n-1)}{2}\exp\left[\frac{-\pi\theta}{t}\right]^n\right] . \quad (3.2.27)$$

The first summation on the right hand side of Eq. 3.2.27 is equal to:

$$8\pi\theta\sum \frac{n(n+1)}{2} \exp\left[\frac{-\pi\theta}{t}\right]^n = 8\pi\theta \exp\left[\frac{-\pi\theta}{t}\right] \sum \frac{n(n+1)}{2} \exp\left[\frac{-\pi\theta}{t}\right]^{n-1} \quad (3.2.28)$$

which is equal to:

$$8\pi\theta \exp\left[\frac{-\pi\theta}{t}\right]\left[1-\exp\left[\frac{-\pi\theta}{t}\right]\right]^{-3} \quad . \qquad (3.2.29)$$

Similarly, the second summation on the right hand side of Eq. 3.2.27 is given by

$$8\pi\theta\sum_{n}\frac{n(n-1)}{2}\exp\left[\frac{-\pi\theta}{t}\right]^{n} = 8\pi\theta\exp\left[\frac{-\pi\theta}{t}\right]^{2}\sum_{m}\frac{(m+1)m}{2}\exp\left[\frac{-\pi\theta}{t}\right]^{m-1} \qquad (3.2.30)$$

where the index is changed to m; m=n-1. Eq. 3.2.28 is summed to give:

$$8\pi\theta\exp\left[\frac{-\pi\theta}{t}\right]^{2}\left[1-\exp\left[\frac{-\pi\theta}{t}\right]\right]^{-3} \quad . \qquad (3.2.31)$$

The autocorrelation is the sum of the three terms (Eqs.3.2.26, 3.2.29 and 3.2.31) and is given by

$$G(\tau) = 3\left[\frac{\tau\cosh(\tau)}{\sinh^{3}(\tau)} - \frac{1}{\sinh^{2}(\tau)}\right] \qquad (3.2.32)$$

where $\tau = \frac{\pi\theta}{2t}$, and $G(\tau)$ is normalized such that $G(0) = 1$. The FWHM of $G(\tau)$, τ_g, is 2.7196. Therefore the ratio of the FWHM of the $sech^2$ pulse to the FWHM of the autocorrelation is $\frac{\tau_p}{\tau_g} = \frac{1.76}{2.72} = 0.648$.

One has the option of slowly varying the delay line by translating a stepping motor and recording $G(\tau)$ averaged over a long time period. Or one can rapidly vary the delay by mounting the corner cube on an acoustic modulator.[66,67] The second harmonic autocorrelation can be displayed on an oscilloscope in real time to assist in the laser alignment. An autocorrelator is permanently installed for monitoring the laser output. The voltage of the acoustic modulator (shaker) that drives the corner cube is also used to drive the time base (plug-in 7B50) of an oscilloscope (Tektronix model 7904). This insures that the time axis of the oscilloscope trace is linear although the shaker movement is sinusoidal. Normally, two pulses would be observed on the oscilloscope, corresponding to each

direction of the shaker travel. A square wave pulse, at the shaker frequency, is applied to the "z-axis" of the oscilloscope to reduce the intensity of the CRT during one half of the shaker cycle. Proper adjustment of the oscilloscope triggering level and relative phase of the oscilloscope and shaker will block one of the pulses on the CRT.

A typical pulse autocorrelation and spectrum are shown in figures 3.2.2 and 3.2.3. Assuming a $sech^2$ pulse envelope the FWHM is 140 fs and $\delta\lambda$ = 35 Å giving $\delta\nu\delta t$ = 0.38, indicating that the pulse is slightly chirped. The convolution of a $sech^2$ pulse shape of FWHM = 140 fs is shown for in fig. 3.2.2 for comparison. The laser pulse convolution looks like a $sech^2$ pulse with wings. The actual pulse shape is probably a combination of $sech^2$ and exponentials with some chirp. Note, for a two sided exponential pulse given by

$$I = I_o \exp\left[\frac{-2\ln 2|t|}{\tau_p}\right] \qquad (3.2.33)$$

the autocorrelation is given by

$$G(\tau) = (1+2|\tau|)e^{-2|\tau|} \qquad (3.2.34)$$

with $G_{1/2} = 0.413\ I_{1/2}$ and $\delta\nu\delta\tau_p = 0.142$. The two sided exponential autocorrelation exhibits much larger wings than either a gaussian or $sech^2$ pulse.

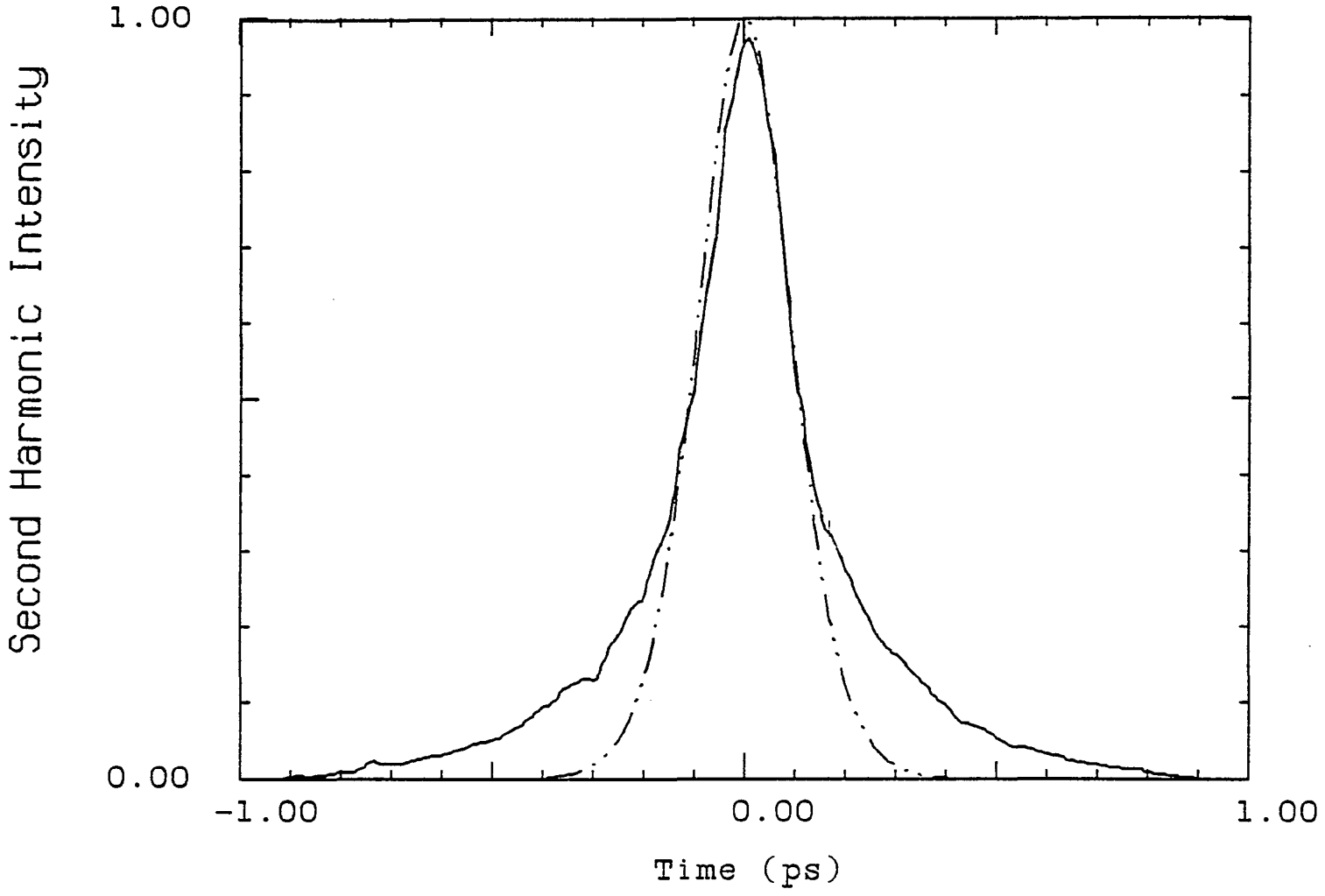

Figure 3.2.2. A typical oscillator autocorrelation. The autocorrelation FWHM is 220 fs. For a $sech^2$ pulse shape the FWHM of the pulse is 140 fs. The autocorrelation of a 140 fs $sech^2$ pulse is shown for comparison.

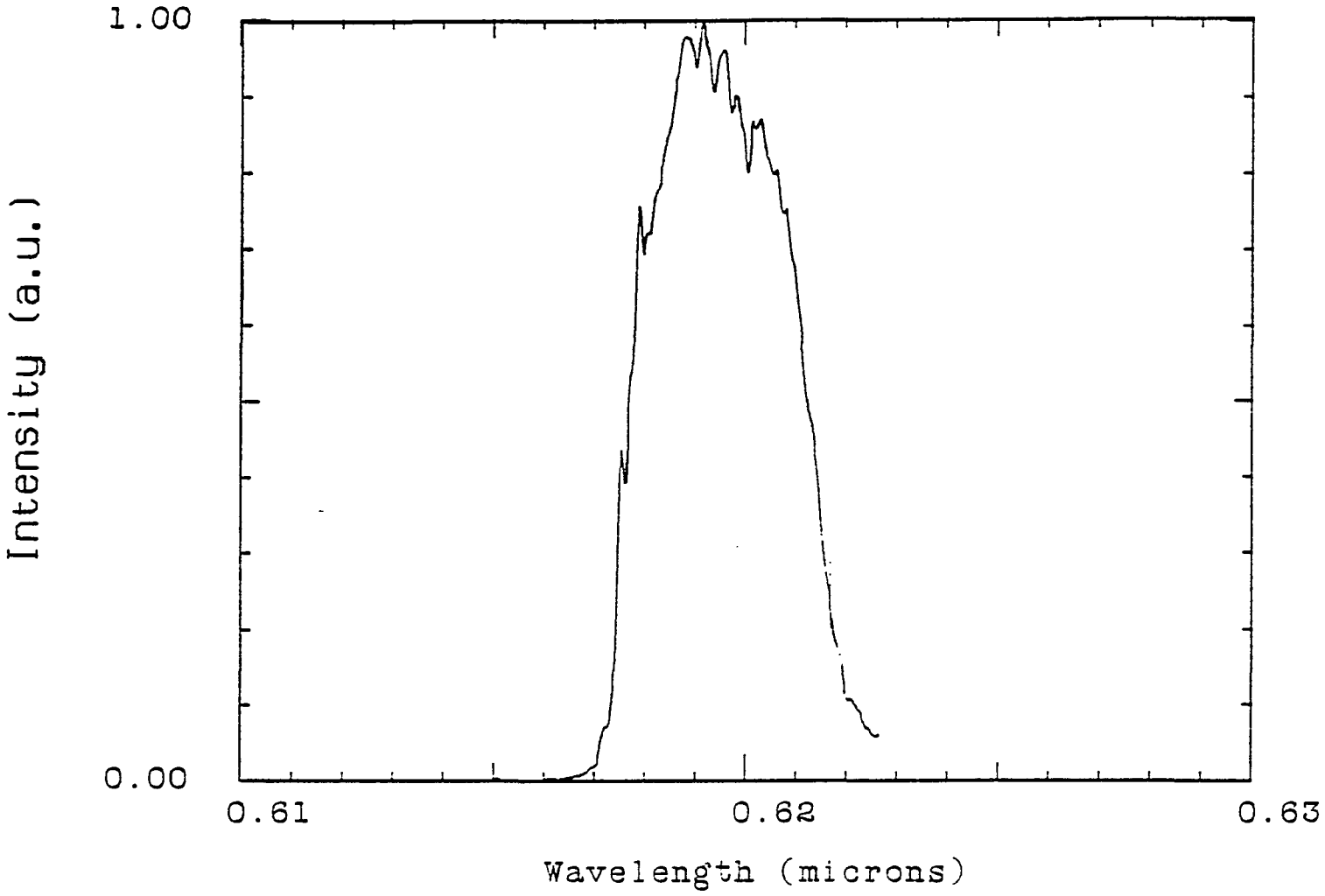

Figure 3.2.3. Typical oscillator spectrum. The laser is centered at 6195 Å and its bandwidth is δlambda = 35 Å => $\delta\nu = 2.73 \times 10^{12}$ sec^{-1}. For a 140 fs pulse, $\delta t \delta\nu = 0.38$. The amplified pulse spectrum has the same width. although the pulse broadens to 450 fs in the amplifier.

3.2.3 Pulse compression

As discussed in section 3.1.3, the output pulses of the CPM laser can have a frequency sweep (chirp) that can be either positive or negative depending on the actual cavity design. The linear component of the frequency sweep can be eliminated with the proper dispersive elements in the beam path (external to the cavity).

If the chirp is negative (i.e. the short wavelength components lead the pulse, that is, blue light is in the front and red is in the tail), the insertion of the proper length of a transparent material such as glass or water can compress the pulse. Most non-absorbing materials have normal dispersion, therefore, the group velocity in the material is faster for longer wavelengths and the red components of the pulse catch up with the blue, compensating for the negative chirp and compressing the pulse.

The index of refraction of a transparent medium can be described by the Cauchy formula[68]

$$n^2 = A_o + A_1 \lambda^{-2} + A_2 \lambda^{-4} + \ldots \qquad (3.2.33)$$

The group velocity, defined as

$$v_g = \frac{d\omega}{dk} \qquad (3.2.34)$$

is given by

$$\frac{1}{v_g} = \frac{n}{c} + \frac{\omega}{c}\frac{dn}{d\omega} \qquad (3.2.35)$$

If one is far from any absorption regions, n varies slowly with λ and from Eq. 3.2.12, the refractive index can be approximated by

$$n = A_o + \frac{A_1\omega^2}{8\pi^2c^2A_o} \qquad (3.2.36)$$

The frequency dependence of the relative time delay is $d(^1/v_g)/d\omega$;

$$\frac{d(^1/v_g)}{d\omega} = \frac{2}{c}\frac{dn}{d\omega} + \frac{\omega}{c}\frac{d^2n}{d\omega^2} \qquad (3.2.37)$$

$$\frac{d(^1/v_g)}{d\omega} = \frac{3A_1\omega}{4\pi^2A_oc^3} \qquad (3.2.38)$$

which, in first order, is linear in frequency.

This method of pulse compression has many drawbacks. The delay line is not easily adjustable. At high power densities non-linear optical effects can occur such as SPM or stimulated raman scattering. The most serious drawback to this technique is the laser pulses rarely have negative chirp. If the oscillator has a small negative chirp, it is usually cancelled by the normal dispersion of other optics in the beam such as lenses, dye amplifiers, beam splitters etc.

The more common case, is that the laser pulses have positive chirp, either from the cavity elements, amplifier system (see section

3.3) or experimental apparatus. A pair of gratings can be used to give a negative chirp to the pulse cancelling the linear positive chirp.[14,69-71] A pair of gratings aligned parallel to each other can give a quadratic phase correction (linear frequency sweep) to the pulse. Consider fig. 3.2.4, if two wavelengths, λ and $\lambda+\delta\lambda$ are incident on a grating at the blazing angle, the optical path length, P is given by

$$P = b(1+\cos\theta) = \frac{D(1+\cos(\theta)}{\cos(\theta-\Phi)} \qquad (3.2.39)$$

where Φ is the angle of incidence, θ is the diffracted angle, b is the slant distance and D is the normal distance between the two gratings. The spacing between grooves is d. The relationship between θ and λ is

$$\lambda = d\,[\sin(\theta-\Phi) + \sin(\theta)] \quad . \qquad (3.2.40)$$

The wavelength dependence of the optical path is

$$\frac{dP}{d\lambda} = -\left[\frac{\sin(\theta)}{\cos(\theta-\Phi)} + \frac{1+\cos(\theta)\sin(\theta-\Phi)}{\cos^2(\theta-\Phi)}\,\frac{d\theta}{d\lambda}\right] . \qquad (3.2.41)$$

The time delay is

$$\frac{dt}{d\lambda} = \frac{b\lambda}{cd^2[1-(\lambda/d - \sin\theta)^2]} \quad . \qquad (3.2.42)$$

The large losses in pulse energy (15 - 30%) at each grating) can be reduced by the use of holographic gratings[72] or by the use of

prisms made of Tellurium Oxide (TeO_2).[73] The high material dispersion of the TeO_2 allows a linear frequency correction as a reasonable separation distance between the prisms. Using Brewster angle prisms and P-polarized light, reduces losses to less than 1%.

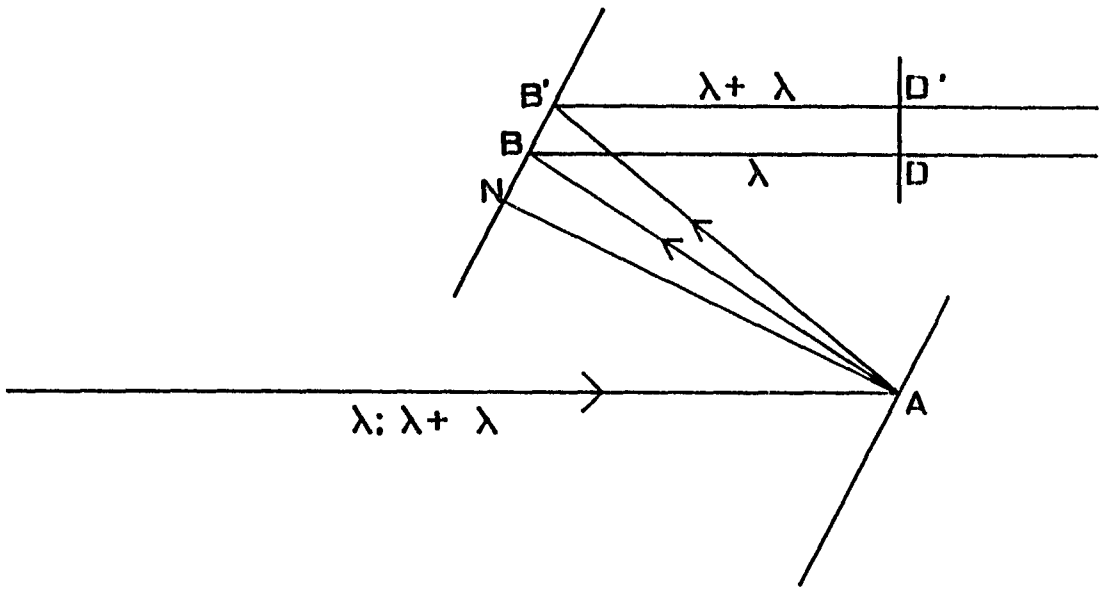

Figure 3.2.4. Geometry for pulse compression by a grating pair. The optical path difference between ABD and AB'D' is linear in $\delta\lambda$.

3.3 Femtosecond laser amplifier system

3.3.1 Introduction

To observe bleaching of the absorption or four-wave mixing in semiconductors it is necessary to increase the peak power of the laser output. Therefore a laser amplifier system was constructed.

In order to have uniform gain over the entire bandwidth of the laser pulse, the amplifier system must have a broad gain profile around the oscillator wavelength of 6200 Å. Any non-linear frequency gain in the system will distort and broaden the pulse. For this reason, the organic dyes, sulfarhodamine B (kiton red 620) and sulfarhodamine 640, dissolved in H_2O, were selected as the gain media for the amplifier system. A four-stage amplifier is used to prevent gain saturation, by successively increasing the pumping volume in each stage.

A dye laser amplifier system must be designed to deal with the short energy storage times, < 5 ns, and the high stimulated emission cross section leading to amplified spontaneous emission (ASE).[74-79] Since the excited state lifetime of the rhodamines is 3-5 ns, the ideal pump source for the amplifier should be less than 3 ns and high intensity near the absorption peak of the amplifier dyes. Longer pump sources would only add to the background fluorescence of the amplifier dyes without improving the gain. Also if the pump duration was longer than the oscillator pulse separation (the cavity round trip time, 8.8 ns) multiple pulses would be amplified. For this reason the second

harmonic of a Q-switched Nd:YAG laser was chosen as the pump for the amplifier. The Nd:YAG laser selected was manufactured by Quanta-Ray (Spectra Physics), model DCR-2A. The laser consists of a flashlamp pumped Nd:YAG rod as the oscillator and one flash lamp pumped Nd:YAG rod as an amplifier. The Nd:YAG laser is Q-switched by a KDP crystal used as a Pockels cell. A type II KDP crystal for second harmonic generation in a sealed housing is located at the output of the laser. When properly aligned and with the correct Q-switch voltage and delay, the laser outputs 750 millijoules of 1.06 micron light in a 4 ns pulse. The second harmonic pulse at 0.532 microns is 2 ns in duration and 250 millijoules of energy. Details of the amplifier cells are given later.

3.3.2 Synchronization of the dye and ND:YAG lasers

In order to insure temporal overlap of the Nd:YAG and dye lasers, it is necessary to control the firing of the YAG laser. The timing of the Nd:YAG is complicated and not easy to externally control.[80] The 8.8 ns spacing of the oscillator pulses is fixed by the cavity length. Three milliseconds before the Nd:YAG is fired, 3200 volts is applied to the Q-switch, preventing lasing action; approximately 210 microseconds before the Q-switch is fired, the flash lamps are fired. The voltage on the Q-switch is then rapidly reduced to zero and 75 nanoseconds later the laser pulse is emitted. The internal jitter between the discharging of the Q-switch voltage and the emission of the laser pulse is 250 ps.

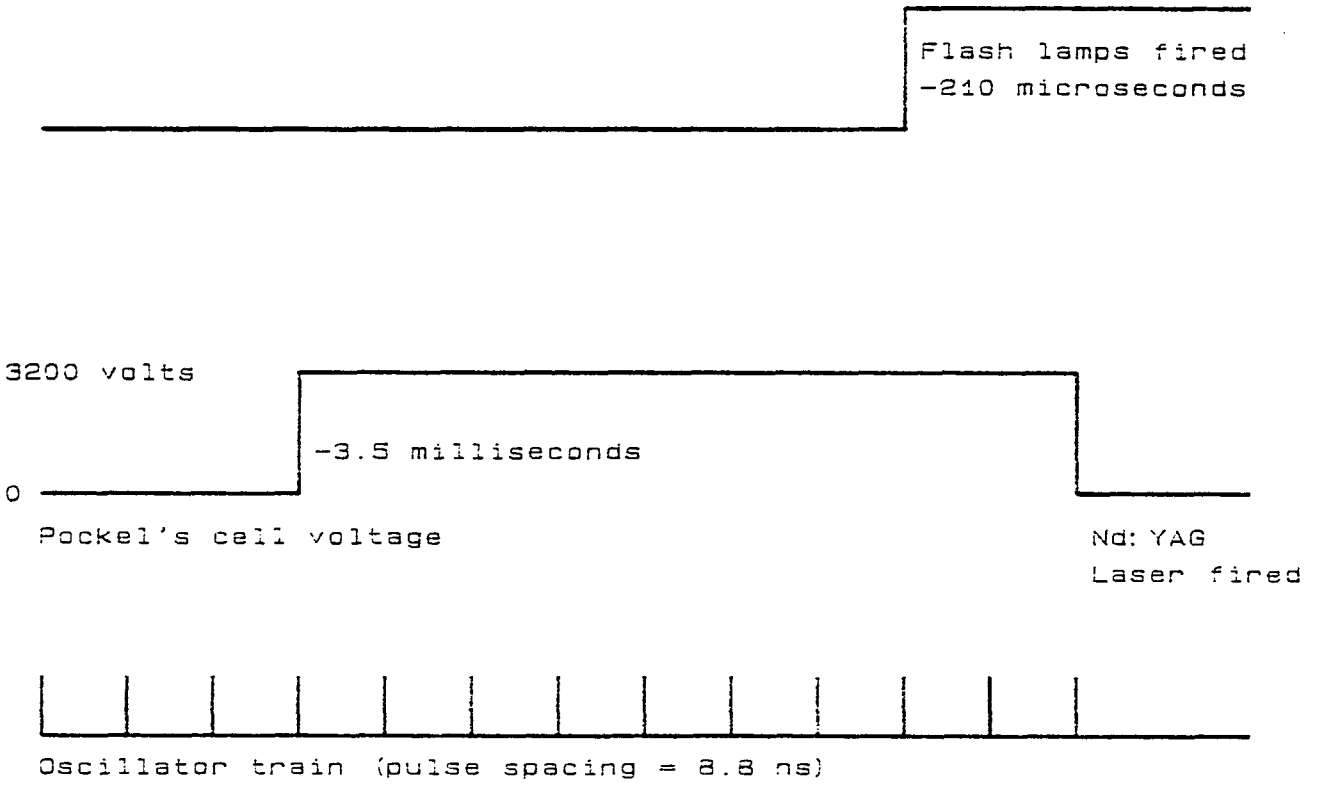

Figure 3.3.1. Timing sequence of the Nd:YAG laser. Voltage is applied to the Pockel's cell 3.5 milliseconds before the flash lamps are fired. The flash lamps are fired 210 μs before the Pockel's cell voltage is reduced to zero and the laser pulse is emitted.

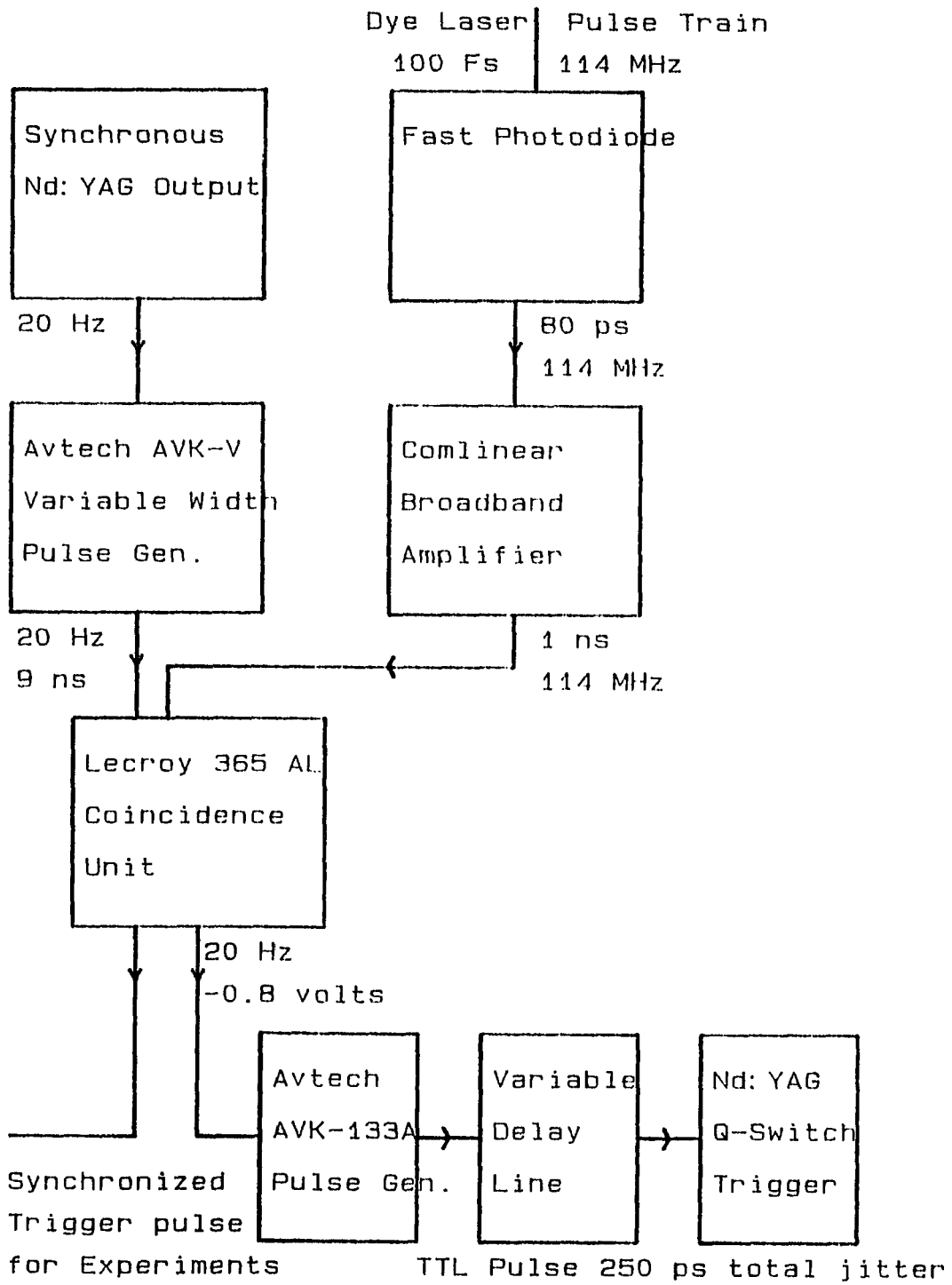

Figure 3.3.2. Triggering circuit for the firing of the Nd:YAG laser in synchronization with the dye laser. The jitter between the dye laser and the Nd:YAG is less than 500 ps.

The most effective way to control the firing of the Nd:YAG laser was to use the internal 20 Hz clock of the Nd:YAG to apply voltage to the Q-switch and fire the flashlamps while letting the dye laser pulse train control the discharging of the Q-switch and firing of the Nd:YAG laser. This is accomplished by the use of a coincidence counter, a variable delay line and various pulse generators and a broadband amplifier, shown schematically in fig. 3.3.1.

The Nd:YAG pulse that would ordinarily trigger the Q-switch is directed to a pulse generator (model AVK-V-N, manufactured by Avtech Inc.) whose output is a square pulse of -0.8 volts and duration adjusted to be 9 ns. The 9 ns width of the pulse generator was selected to insure an overlap with one of the dye laser pulses. The jitter of this pulse generator is not relevant to the laser synchronization. This pulse is applied to one input of a Lecroy coincidence unit, model 365 AL. Part of the oscillator pulse train is detected by a fast photodiode ($\approx$ 80 ps rise time) and amplified to -0.8 volts by a wide band amplifier, manufactured by Comlinear Inc., model CLC100 . This pulse is applied to the second input of the coincidence unit. When the oscillator pulse train and the Nd:YAG pulse overlap in the coincidence unit, the unit outputs a pulse of -1.6 volts and low jitter. Another low jitter pulse generator (Avtech model AVK-133A) triggers on the risetime of output pulse of the coincidence unit and emits a 5 volt TTL pulse. This pulse is passed through a passive, zero jitter variable delay line with 250 ps resolution and then triggers the discharging of the Q-switch. The total jitter of this system is less than 500 ps (see fig. 3.3.2). The

variable delay line is used to insure the Nd:YAG and dye laser pulses arrive at the amplifier cells at the same time.

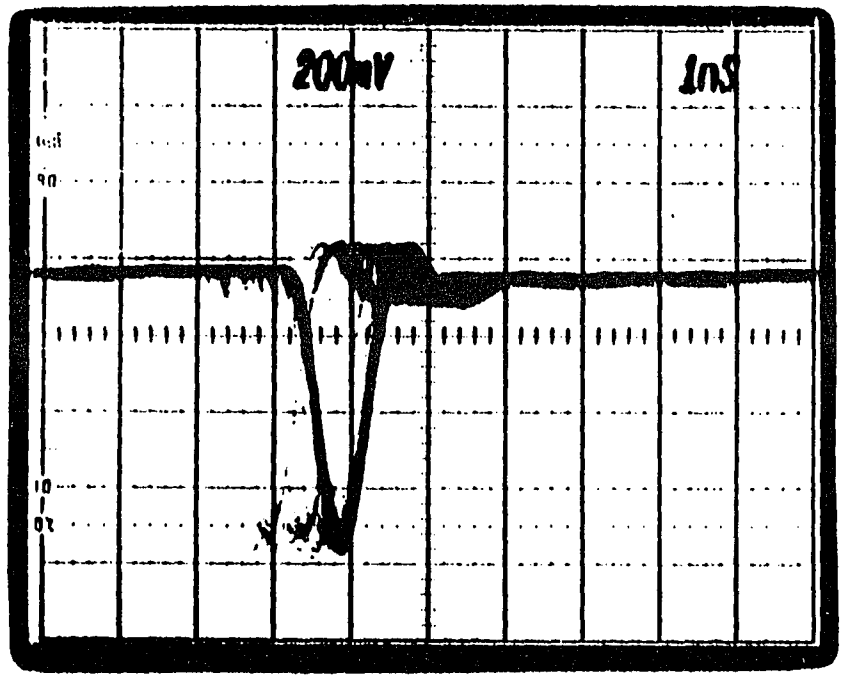

Figure 3.3.3. Jitter between the Nd:YAG and dye lasers. The dye laser pulse train, detected by a fast photodiode is displayed on a Techtronix 7104 oscilloscope, triggered by the output of the AVK-133A pulse generator. The exposure time is 30 seconds (300 pulses).

Cell	Dye	Conc.	Spot size	Length	Gain	Pump Energy	Output Energy
#1	SRB	5×10^{-4}	400 μ	3.5 cm	600	12 mJ	50 nj
#2	SR640	8×10^{-5}	2 mm	3.5 cm	50	25 mJ	2.5 μj
#3	SR640	5×10^{-5}	5 mm	3.5 cm	15	50 mJ	40 μj
#4	SR640	2×10^{-5}	1 cm	12 cm	12	160 mJ	0.5 mj

Table 3.3.1 Summary of Amplifier dye cells.

3.3.3 Amplifier cells and optics

The amplifier is a four stage system (see fig. 3.3.3 and table 3.3.1). The first three cells are pumped transversely. The polarization of the Dye laser and Nd:YAG are both P, although this gives less gain than if they were both S; there is less background emission in this configuration. Since the first three cells are pumped transversely, if both lasers are S polarized, their polarizations are parallel to each other but the Nd:YAG polarization is perpendicular to the propagation direction. If both lasers are P polarized, they are polarized perpendicular to each other but the Nd:YAG polarization is parallel to the direction of propagation.

The first stage amplifier consists of a concentrated (5×10^{-4} molar) solution of sulfarhodamine B (also known as Kiton Red 620) flowing in a 3.5 cm long quartz cell. The windows of the cell are tilted 8° with respect to the propagation direction to prevent the lasing of luminescence reflected from the cell windows. Sulfarhodamine B was selected as the first amplifier dye because its absorption peak (5640 Å) is close to the 5320 Å pump; and the absorption at 6200 Å is small in the 3.5 cm long cell. The absorption curve for sulfarhodamine B is shown in fig. 3.3.4. This allows a small laser spot size (400 microns) at the cell. Approximately 5% of the Nd:YAG (12.5 mj) is focused to a line by a 25 cm focal length cylindrical lens.

The first cell is the greatest source of background light in the amplifier system and the hardest to eliminate. The emission from

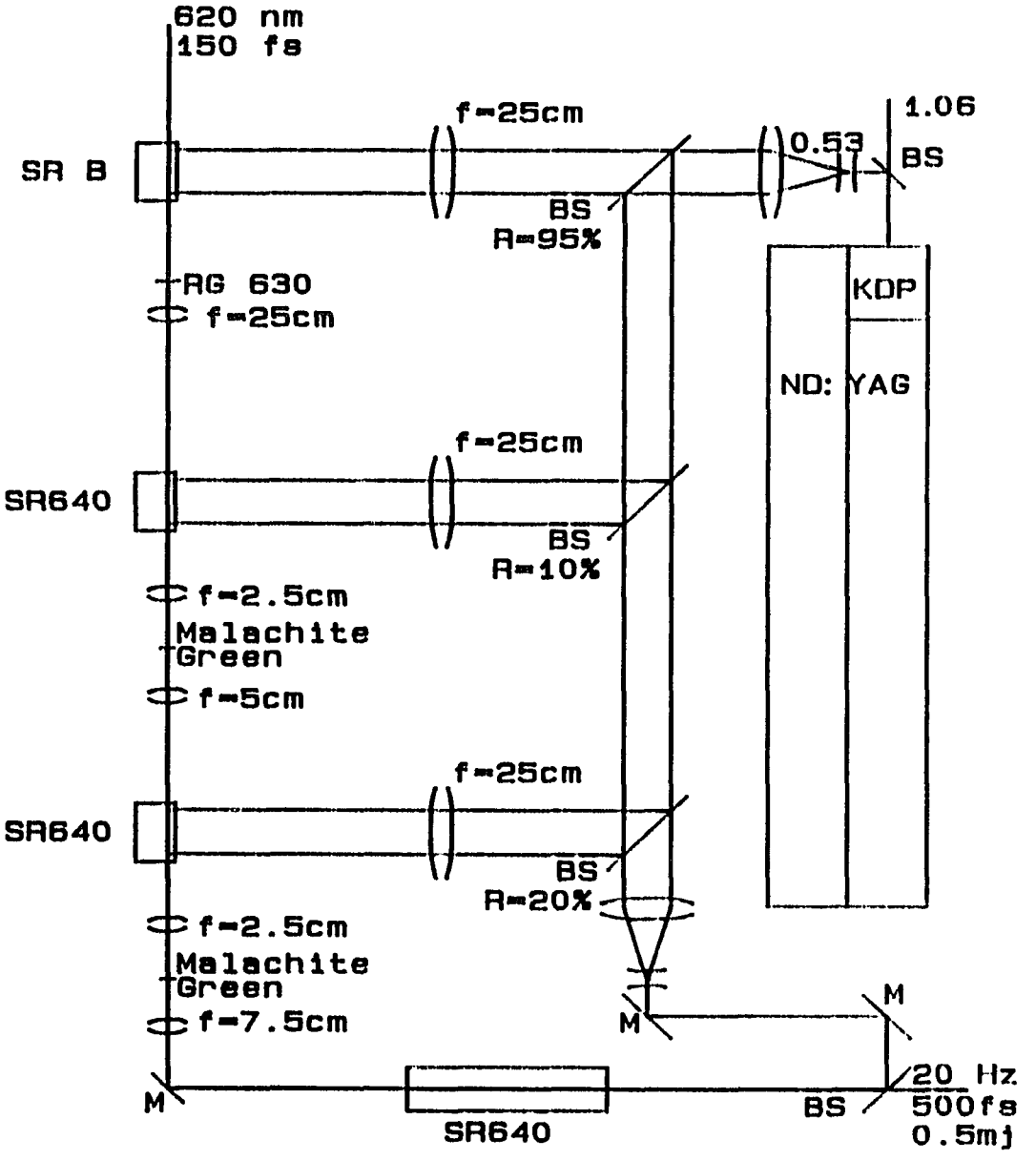

Figure 3.3.4. Schematic of the femtosecond amplifier system.

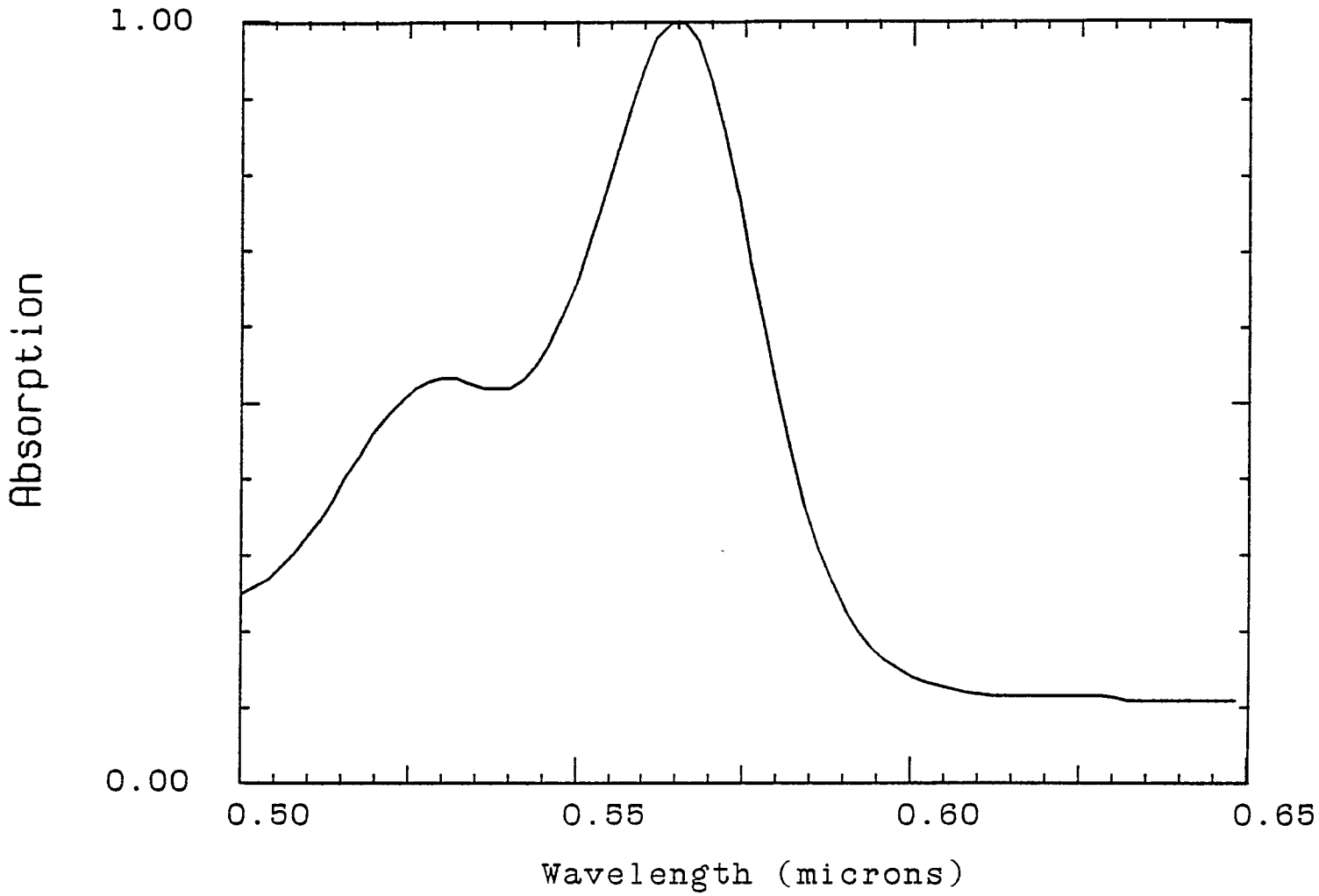

Figure 3.3.5. Absorption spectrum of the dye in the first amplifier stage. The concentration of the sulfarhodamine B solution is 5 x 10^{-4} molar dissolved in H_2O.

the first cell is also amplified by the later stages. The fluorescence peak of the sulfarhodamine B is at 5940 Å (see fig. 3.3.5). Although the emission cross section at 6200 Å is smaller for sulfarhodamine B than for sulfarhodamine 640, most of the ASE can be eliminated by the use of glass filters, R62 and RG630, and apertures to block the ASE of the first cell. Because of the low initial pulse energy and the high concentration of the dye, the first cell gives the highest gain, $\approx$ 600.

The second and third stages of the amplifier are also transversely pumped cells as in the first stage. The amplifier dye is sulfarhodamine 640 (8×10^{-5} molar in the second stage and 5×10^{-5} m in the third stage). The higher gain at 6200 Å and lower absorption at 5320 Å allows the use of larger beam sizes and lower concentrations without the problems of lasing in the cells. The absorption and emission spectra for sulfarhodamine 640 is shown is figures 3.3.6 and 3.3.7. The pump power and spot size for these stage are 25 mj, 2mm and 50 mj, 5 mm respectively. The gain is 50 and 15, respectively.

In order to prevent the amplification of the spontaneous emission (ASE), saturable absorbers are placed after the second and third stages. The saturable absorbers consist of two flowing jet streams of malachite green (1×10^{-3} m). The laser is tightly focused into the jet stream by a 2.5 cm lens. The concentration is the minimum needed to absorb the ASE. The collimating lenses were selected to give the proper spot size for the next amplifier stage. The absorption spectra of the malachite green is shown in figure 3.3.8. The fast

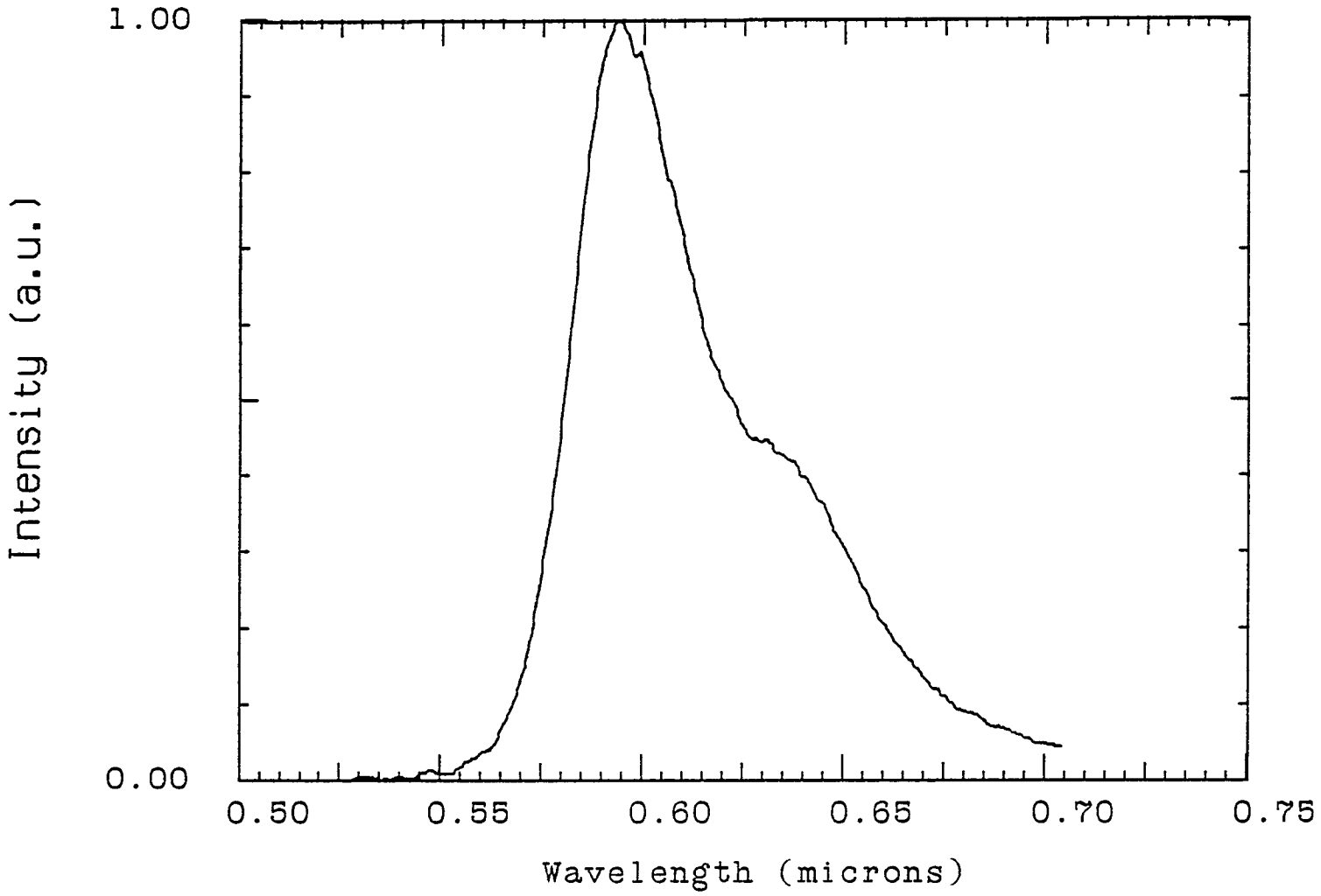

Figure 3.3.6. Fluorescence spectrum of Sulfarhodamine B.

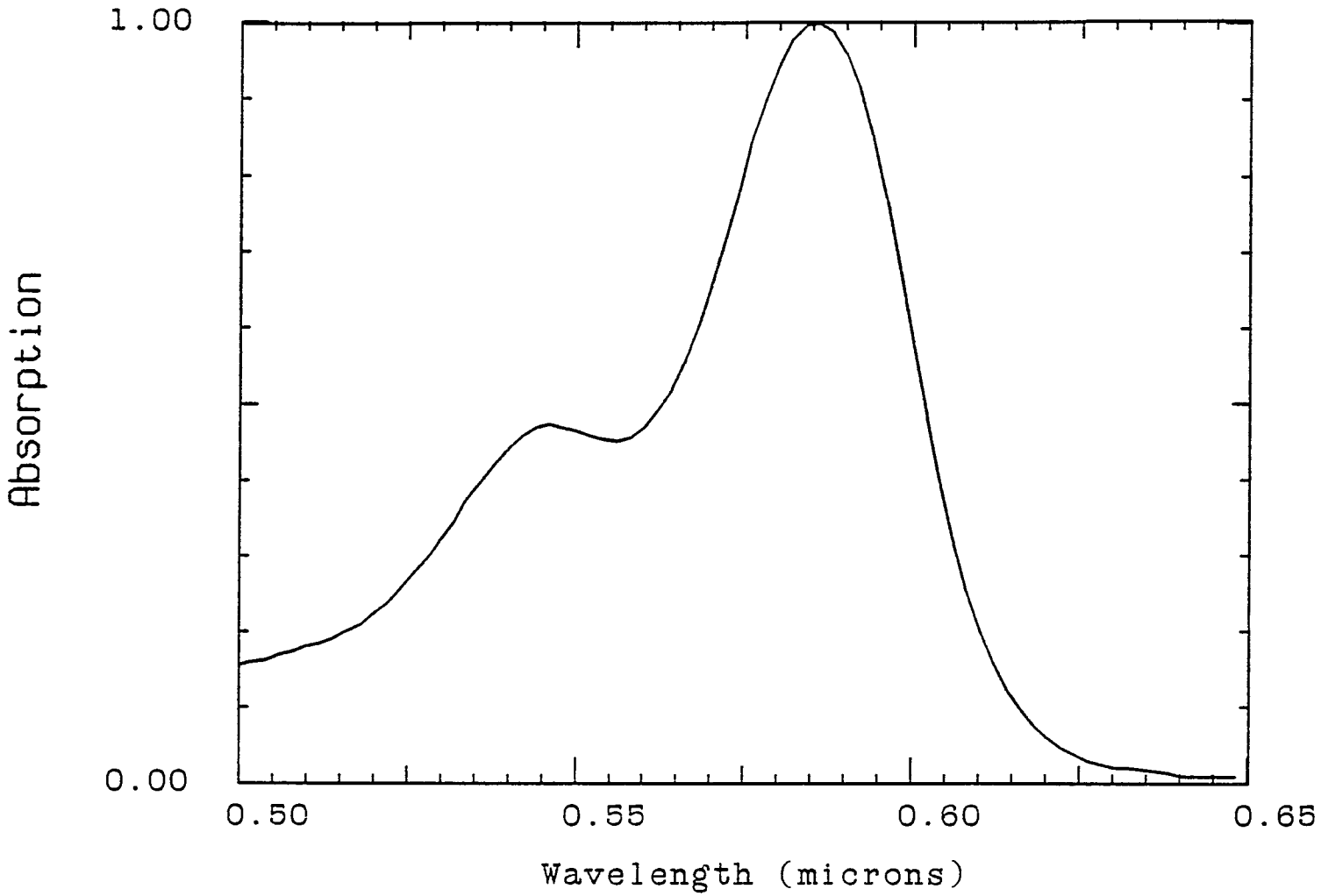

Figure 3.3.7. Absorption spectrum for Sulfarhodamine 640. The concentrations are 8×10^{-5}, 5×10^{-5}, 2×10^{-5}, molar in the second, third and fourth stages respectively. The solvent is H_2O.

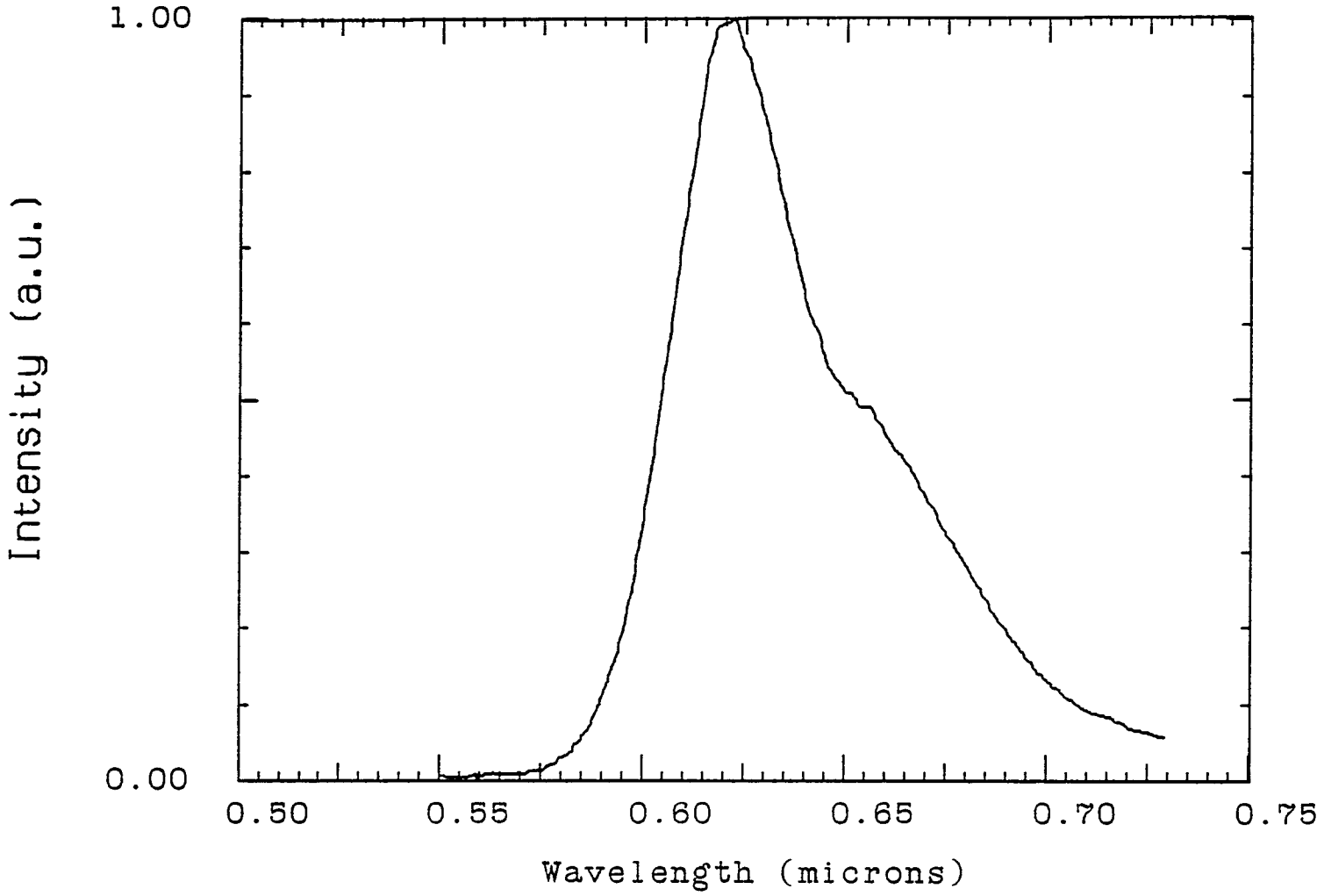

Figure 3.3.8. Fluorescence spectrum of sulfarhodamine 640.

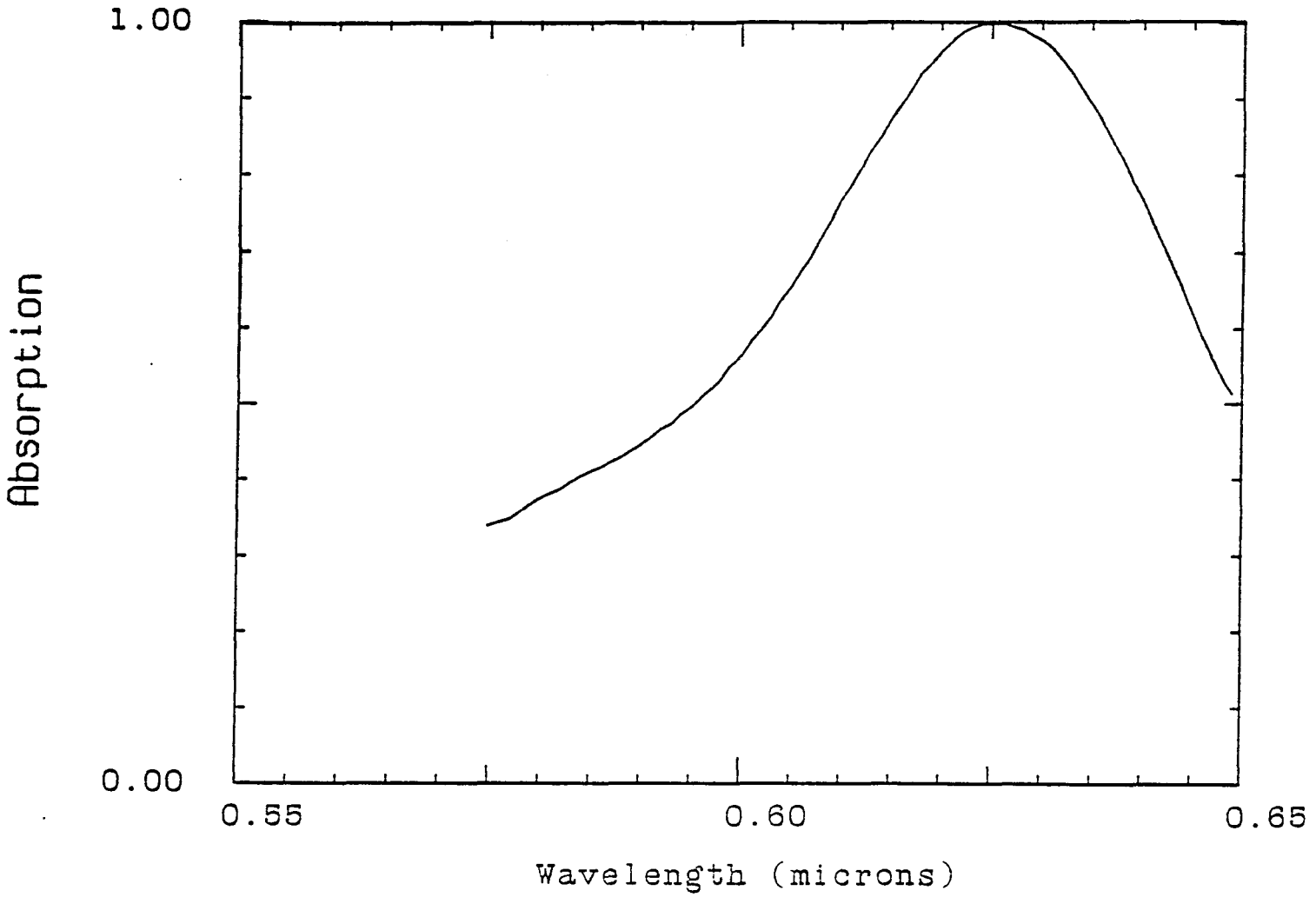

Figure 3.3.9. Absorption spectrum of the amplifier saturable absorbers. Both concentrations are 1 x 10^{-3} molar solutions of Malachite Green in ethylene glycol.

relaxation time of the malachite green[81] (10 ps.) makes it an effective shutter for blocking the nanosecond long emission from the amplifier dyes.

The final stage consists of a dilute solution of sulfarhodamine 640 (2×10^{-5} m) flowing in a 12 cm long cylindrical cell. The dye is longitudinally pumped by the remaining 160 mj of the Nd:YAG pulse. The pump pulse and dye laser are aligned parallel and counter propagating. This geometry helps even out the intensity variations in the laser cross section caused by transverse pumping. The gain in the last cell is 12. A dielectric beam splitter is used to separate the femtosecond laser pulse and the Nd:YAG pulse.

The total gain of this system is 5×10^{6}, giving a pulse energy of $\approx$ 0.5 mj. The gain of the system is very sensitive to the input wavelength and small changes in the oscillator wavelength due to realignment require major corrections to the amplifier dye concentrations for maximum gain. During alignment, the dye laser pulse width and spectra is measured after each stage of the amplifier. The pump intensity, spot size and alignment were adjusted to insure the spectral shape of laser pulse did not change during amplification, and the only pulse broadening was due to dispersion in the dye solvent ($\approx$ 22 cm of water), and to glass lenses and windows ($\approx$ 5 cm). Without the grating compressor, the output pulse width of the system is 460 fs and the pulse energy is 500 microjoules. An autocorrelation of the amplified pulse is shown in figure 3.3.9, the autocorrelation width is 720 fs which corresponds to a pulse width of 460 fs if one assumes a

$sech^2$ pulse. The output pulse width is not that strongly dependent on the oscillator pulse width; a narrower oscillator pulse has a larger bandwidth and therefore experiences more broadening in the amplifier system. The chirp is linear and the pulse can be compressed to under 100 fs by a grating pair as described in section 3.2.3. However the extend of pulse compression by the gratings is limited by the initial oscillator pulse width and spectra.

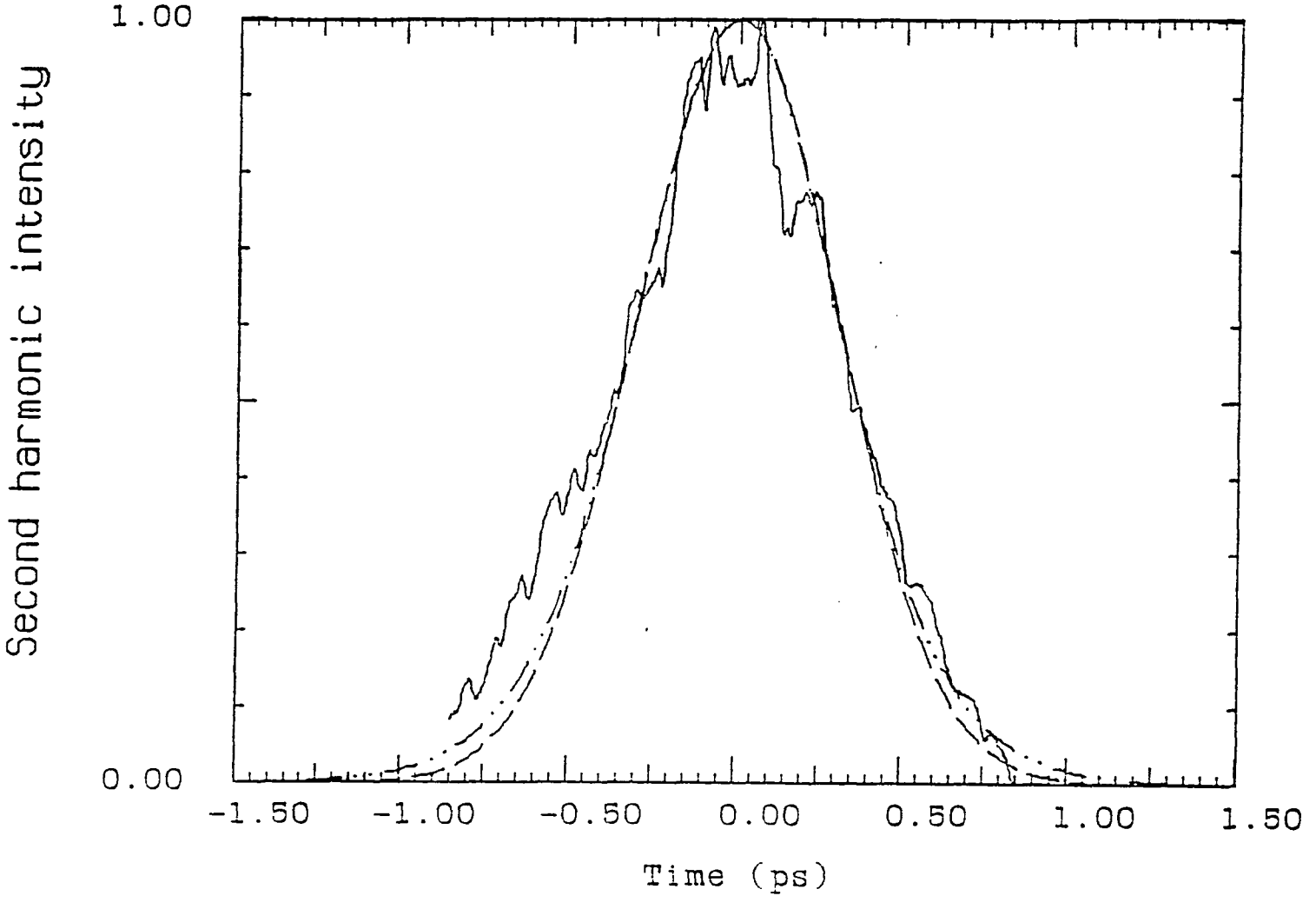

Figure 3.3.10. A typical amplified laser pulse autocorrelation. The autocorrelation FWHM is 720 fs. For a $sech^2$ envelope, the pulse FWHM is 460 fs. The autocorrelations for a gaussian and a $sech^2$ pulse are shown.

3.4 Notes

[1]C. V. Shank and E. P. Ippen, **Mode-locking of Dye Lasers** in Topics in Applied Physics, Vol 1. ed. by F. P. Schäfer (Springer-Verlag Berlin 1977).

[2]W. H. Glenn, M. J. Brienza, A. J. Demaria, Appl. Phys. Lett. **12**, 54 (1968).

[3]B. H. Soffer and J. W. Linn, J. Appl. Phys. **39**, 5859 (1968).

[4]W. Schmidt and F. P. Schäfer, Phys. Lett. **26** A, 558 (1968).

[5]D. J. Bradley and F. O. O'Neil, J. Opto-electron. **1**, 69 (1969).

[6]E. P. Ippen, C. V. Shank and A. Dienes, Appl. Phys. Lett. **21**, 348 (1972).

[7]C. V. Shank. E. P. Ippen and A. Dienes, Digest of Technical Papers, VII International Quant. Elect. Conf., Montreal 1972.

[8]F. O'Neill, Opt. Commun. **6**, 360 (1972).

[9]H. W. Kogelnik, E. P. Ippen, A. Dienes and C. V. Shank, IEEE J. Quantum Electron. **QE-8**, 373 (1972).

[10]I. S. Ruddock and D. J. Bradley, Appl. Phys. Lett. **29**, 296 (1976).

[11]C. V. Shank and E. P. Ippen, Appl. Phys. Lett. **24**, 374 (1974).

[12]C. V. Shank and E. P. Ippen, Laser Focus, Pg. 44, July 1977.

[13]K. K. Li, Appl. Optics, **21**, 967 (1982).

[14]E. P. Ippen and C. V. Shank, Appl. Phys. Lett., **27**, 488 (1975).

[15]E. G. Arthurs, D. J. Bradley and A. G. Roddie, Appl. Phys. Lett., **23**, 88 (1976).

[16]R. L. Fork, B. I. Greene and C. V. Shank, Appl. Phys. Lett. **38**, 671 (1981).

[17]D. J. Bradley, in **Methods of Generation** in topics in Applied Physics Vol. 18. ed. by S. L. Shapiro, (Springer-Verlag Berlin 1977).

[18]G. H. C. New, IEEE J. Quantum Electron., **QE-10**, 115 (1974).

[19]H. H. Haus, IEEE J. Quantum Electron., **QE-11**, 736 (1975).

[20]Z. A. Yasa, O. Teschke, L. W. Braverman and A. Diennes, Optics Commun., **15**, 354 (1975).

[21]Z. A. Yasa, O. Teschke, and L. W. Braverman, J. Appl. Phys., **47**, 174 (1976).

[22]N. J. Frigo, IEEE J. Quantum Electron., **QE-19**, 511 (1983).

[23]E. G. Arthurs, D. J. Bradley, A. G. Roddie, Chem. Phys. Lett. **22**, 230 (1973).

[24]At optimum alignment of the laser, the oscillator bandwidth was 60 Å, however the output pulse width was 100 fs, indicating that the pulses were chirped and not transform limited.

[25]D. N. Dempster, T. Morrow, R. Rankin, and G. F. Thompson, J.C.S. Faraday II **68**, 1479 (1972).

[26]E. G. Arthurs, D. J. Bradley, A. G. Roddie, Appl. Phys. Lett. **20**, 125 (172).

[27]E. G. Arthurs, D. J. Bradley, and A. G. Roddie, Opt. Commun., **8**, 118 (1973).

[28]E. P. Ippen and C. V. Shank, unpublished. This bistable mode is discussed in ref. 1.

[29]A. Katz and Y. Budansky, unpublished

[30]G. R. Jacobovitz, C. H. B. Cruz, N. P. Mansur and M. A. Scarparo, Optics Commun. **59**, 233 (1986).

[31]P. G. Kryukov and V.S. Letokhov, Sov. Phys. Uspekhi, **122**, 641 (1970).

[32]Mode-locking of this laser can be accomplished between 610 nm and 630 nm. If the laser output was a transform limited pulse with a bandwidth of 20 nm, the temporal pulse width would be 20 fs, assuming a sech^2 pulse envelope ($\delta\nu\ \delta t = 0.316$).

[33]W. Rudolph and B. Wilhelmi, Optics Commun., **49**, 371 (1984).

[34]J.-C. Diels, W. Dietel, J. J. Fontaine, W. Rudolph and B. Wilhelmi, J. Opt. SOc. Am B, **2**, 680 (1985).

[35]R. S. Miranda, G. R. Jacobovitz, C. H. B. Cruz and M. A. F. Scarparo, Optics Lett., **11**, 224 (1986).

[36]S. De Silvestri, P. Laporta and O. Svelto, IEEE J. Quantum Electron., **QE-20**, 533 (1984).

[37]J. J. Fontaine, W. Dietel and J.-C. Diels, IEEE J. Quantum Electron., **QE-19**, 1467 (1983).

[38]W. Dietel, E. Döpel, K. Hehl, W. Rudolph and E. Schmidt, Optics Commun., **50**, 179 (1984).

[39]S. De Silvestri, P. Laporta and O. Svelto, Optics Lett., **9**, 335 (1984).

[40]A. M. Weiner, J. G. Fujimoto and E. P. Ippen, Optics Lett., **10**, 71 (1985).

[41]D. N. Christodoulides, E. Bourkoff, R. J. Joseph and T. Simos, IEEE J. Quantum Electron., **QE-22**, 186 (1986).

[42]C. V. Shank, R. L. Fork and R. T. Yen, in **Picosecond Phenomena III**, edited by K. B. Eisenthal, R. M. Hochstrasser, W. Kaiser and A. Laubereau (Springer-Verlag, Heidleberg, 1982) P. 2.

[43]R. L. Fork, C. V. Shank, R. Yen and C. A. Hirlimann, IEEE J. Quantum Electron., **QE-19**, 500 (1983).

[44]W. Dietel, E. Döpel, D. Kühlke and B. Wilhelmi, Optics Commun., **43**, 433 (1982).

[45]D. Kühlke, W. Rudolph and B. Wilhelmi, Appl. Phys. Lett., **42**, 325 (1983).

[46]D. Kühlke, W. Rudolph and B. Wilhelmi, IEEE J. Quantum Electron., **QE-19**, 526 (1983).

[47]G. R. Jacobovitz, C. H. B. Cruz and M. A. Scarparo, Optics Commun. **57**, 133 (1986).

[48]M. S. Stix and E. P. Ippen, IEEE J. Quantum Electron., **QE-19**, 520 (1983).

[49]J. P. Gordon and R. L. Fork, Optics Lett., **9**, 153 (1984).

[50]J. A. Valdmanis, R. L. Fork and J. P. Gordon, Optics Lett., **10**, 131 (1985).

[51]J. A. Valdmanis and R. L. Fork, IEEE J. Quantum Electron., **QE-22**, 112 (1986).

[52]E. P. Ippen and C. V. Shank, in **Techniques for Measurements** in Topics in Applied Physics Vol. 18. ed. by S. L. Shapiro, (springer-Verlag Berlin 1977).

[53]M. Maier , W. Kaiser, J. A. Giordmaine, Phys. Rev. Lett., **17**, 1275 (1966).

[54]A. Yariv, **Quantum Electronics**, (John Wiley and Sons, New York, NY, (1975) P 88.

[55]J. A. Giordmaine, Phys. Rev. Lett., **8**, 19 (1962).

[56]P. D. Maker, R. W. Terhune, M. Nisenoff, C. M. Savage, Phys. Rev. Lett., **8**, 21 (1962).

[57]B. Green, J. C. Liu, R. R. Alfano and D. Anafi, Optics Commun., **22**, 119 (1977).

[58]**CRC Handbook of Lasers**, (Chemical Rubber Co. Cleveland Ohio, 1971) P 516.

[59]R. C. Miller, Phys. Lett., **26A**, 177 (1968).

[60]J. Comly, E. Garmine, Appl. Phys. Lett., **12**, 7 (1968).

[61]S. A. Akhmanov, A. P. Sukhorukov and A. S. Chirkin, Sov. Phys. JETP, **28**, 748 (1969).

[62]W. H. Glenn, IEEE J. Quantum Electron., **QE-5**, 284 (1969).

[63]R. Y. Orlov, T. Usmanov and A. S. Chirkin, Sov. Phys. JETP, **30**, 584 (1970).

[64]Y. N. Karamin and A. P. Sukharov, Sov. J. Quant. Electron., **5**, 496 (1975).

[65]A. M. Weiner, IEEE J. Quantum Electron., **QE-19**, 1276 (1983).

[66]R. L. Fork and F. A. Beisser, Appl. Optics, **17**, 3534 (1978).

[67]A. Kalpaxis, A. G. Doukas, Y. Budansky, D. L. Rosen, A. Katz and R. R. Alfano, Rev. Sci. Instrum., **53**, 960 (1982).

[68]Born and Wolf, **Principles of Optics**, 6th ed. (Pergamon Press, New York, NY 1980) Pg. 95.

[69]E. B. Treacy, Phys. Lett., **28A**, 34 (1968).

[70]E. B. Treacy, Appl. Phys. Lett., **14**, 112 (1969).

[71]E. B. Treacy, IEEE J. Quantum Electron., **QE-5**, 454 (1969).

[72]T.-Y. Yang, P. P. Ho, A. Katz, R. R. Alfano and R. A. Ferrante, Appl. Optics, **24**, 2021 (1985).

[73]M. Nakazawa, T. Nakashima, H. Kubota and S. Seikai, J. Opt. Soc. Am. B, **5**, 215 (1988).

[74]R. S. Adrain, E. G. Arthurs, D. J. Bradley, A. G. Roddie and J. R. Taylor, Optics Commun., **12**, 140 (1974).

[75]U. Ganiel, A. Hardy, G. Nuemann, D. Treves, IEEE J. Quantum Electron., **QE-11**, 881 (1975).

[76]G. Dujardin and P. Flamant, Optics Commun., **24**, 243 (1978).

[77]A. Migus, C. V. Shank, E. P. Ippen and R. L. Fork, IEEE J. Quantum Electron., **QE-18**, 101 (1982).

[78]T. Sizer, J. D. Kafka, I. N. Duling, C. W. Gabel and G. A. Mourou, IEEE J. Quantum Electron. **QE-19**, 506 (1983).

[79]A. A. Hilno, O. E. Martinez and E. J. Quel, IEEE J. Quantum Electron. **QE-22**, 20 (1986).

[80]The firing of the flash lamps and the discharging of the voltage on the Pockels cell can be externally controlled but the Nd:YAG laser has no provisions for externally applying the initial voltage to the Pockels cell before firing of the lamps. This must be done by the internal clock of the Nd:YAG.

[81]P. P. Ho, A. Katz, R. R. Alfano and N. Schiller, Optics Commun.,**54**, 57 (1985).

Chapter 4 Time resolved pump and probe absorption studies of carrier kinetics in GaAs

4.1 Introduction

4.1.1 Background

When a semiconductor is photoexcited by interband absorption from an ultrashort laser pulse, the carriers are excited into a narrow distribution of energies at different **k** states determined by the exciting laser's bandwidth and the band structure of the material. The well localized distribution of carriers at $\mathbf{k}_i$ immediately begins to change by carrier-carrier scattering and phonon emission.[1-16] Carrier-carrier scattering depends on the density of carriers and dominates at high density. Carrier-carrier scattering, while conserving the total energy of the carriers, evolves the distribution function into a Fermi-Dirac-like distribution at a carrier temperature hotter than the lattice temperature. The various transitions for 2.01 eV (6200 Å) photoexcitation of GaAs are shown in figure 4.1.1 and table 4.1.1.

Initially the electrons and holes can form separate distributions at different temperatures, the electrons being hotter than the holes. For direct transitions and parabolic bands the energy distribution between the excited electrons and holes is given by[17]

$$E_e = \frac{m_h(\hbar\omega - E_g)}{(m_e + m_h)} \qquad (4.1.1)$$

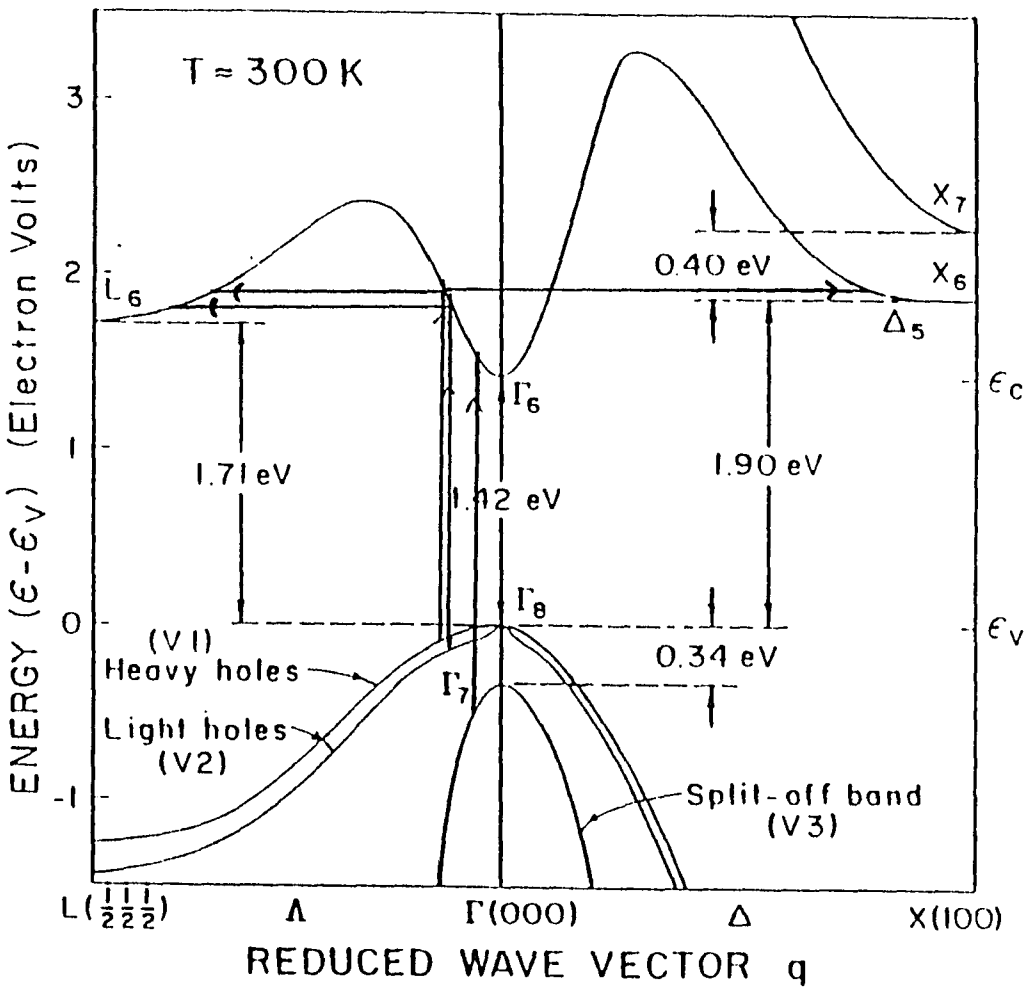

Figure 4.1.1. Band structure of GaAs with the three possible transitions at 2.01 eV shown. Electrons excited from the heavyhole can scatter to the L and X-valleys while electrons excited from the lighthole only have enough energy to scatter to the L-valleys.

transition	electron excess energy	hole excess energy	k (cm^{-1}) (parabolic)	k (cm^{-1}) (non-para)
HH - Cond	520 meV	-66 meV	9.3×10^6	1.5×10^7
LH - Cond	432 meV	-154 meV	8.5×10^6	1.4×10^7
SO - Cond	171 meV	-74 meV	5.3×10^6	5×10^6

Table 4.1.1. 2.01 eV transitions in GaAs. The excess energy is given relative to the band edge. The non-parabolic values for k are estimated from figure 4.1.1.

$$E_h = \frac{m_e(\hbar\omega - E_g)}{(m_e + m_h)} \qquad (4.1.2)$$

where m_e and m_h are the electron and hole effective masses and $\hbar\omega$ is the excitation photon energy. The larger effective mass for the holes results in most of the absorbed photon's energy being transferred to the electrons. In the case of GaAs, for heavy-hole to conduction band transitions, $m_e = 0.063\ m_o$ and $m_h = 0.50\ m_o$, therefore about 87% of the excess energy is given to the electrons and 13% to the holes. Electron - hole interactions then bring the electrons and holes to a common temperature, hotter than the lattice. The electron and hole quasi-Fermi levels are determined by the carrier density and temperature. Phonon emission is the mechanism for energy loss by the excited carriers to the lattice. At low carrier density, the electron-phonon interaction dominates resulting in a distribution function exhibiting peaks at energies displaced by an optical phonon energy. At high density, carrier-carrier scattering redistributes the energy among the carrier population and screening of the electron-phonon interaction becomes active. The electron and hole distributions are shown schematically in figures 4.1.2a-d.

The shape and time evolution of the non-equilibrium distribution depends on how the e-e, e-h, h-e, h-h, e-ph and h-ph interactions influence the form of the distribution function. The standard distributions: Fermi-Dirac or Maxwell-Boltzman can not be assumed until the system is thermalized. Osman and Ferry[13] using Ensemble Monte Carlo calculations find that a smooth but not standard distribution (Maxwellian or Fermi-Dirac) forms within 0.5 ps. They

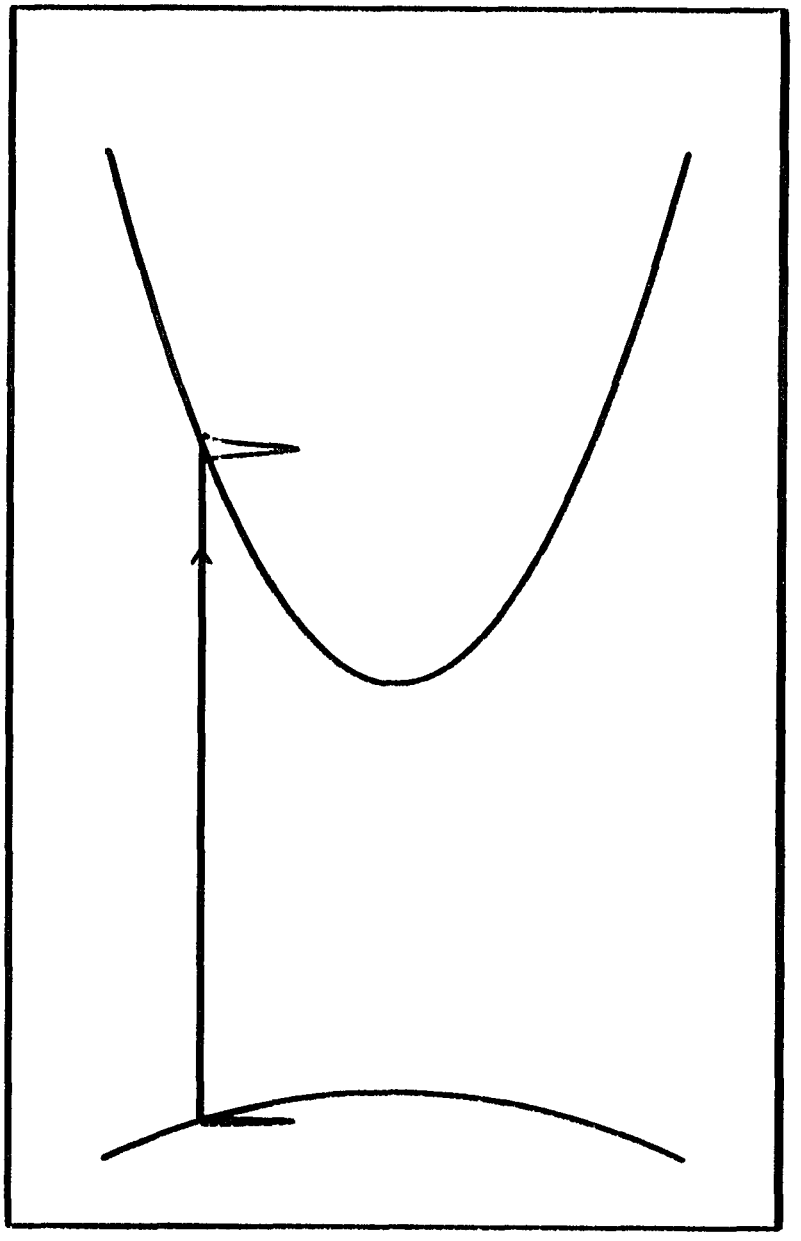

Figure 4.1.2a. For an ultrafast excitation pulse, at t = 0, the carriers are excited into a δ-function distribution. The initial energy of the electron and hole distributions is determined by the effective masses of the conduction and valence bands.

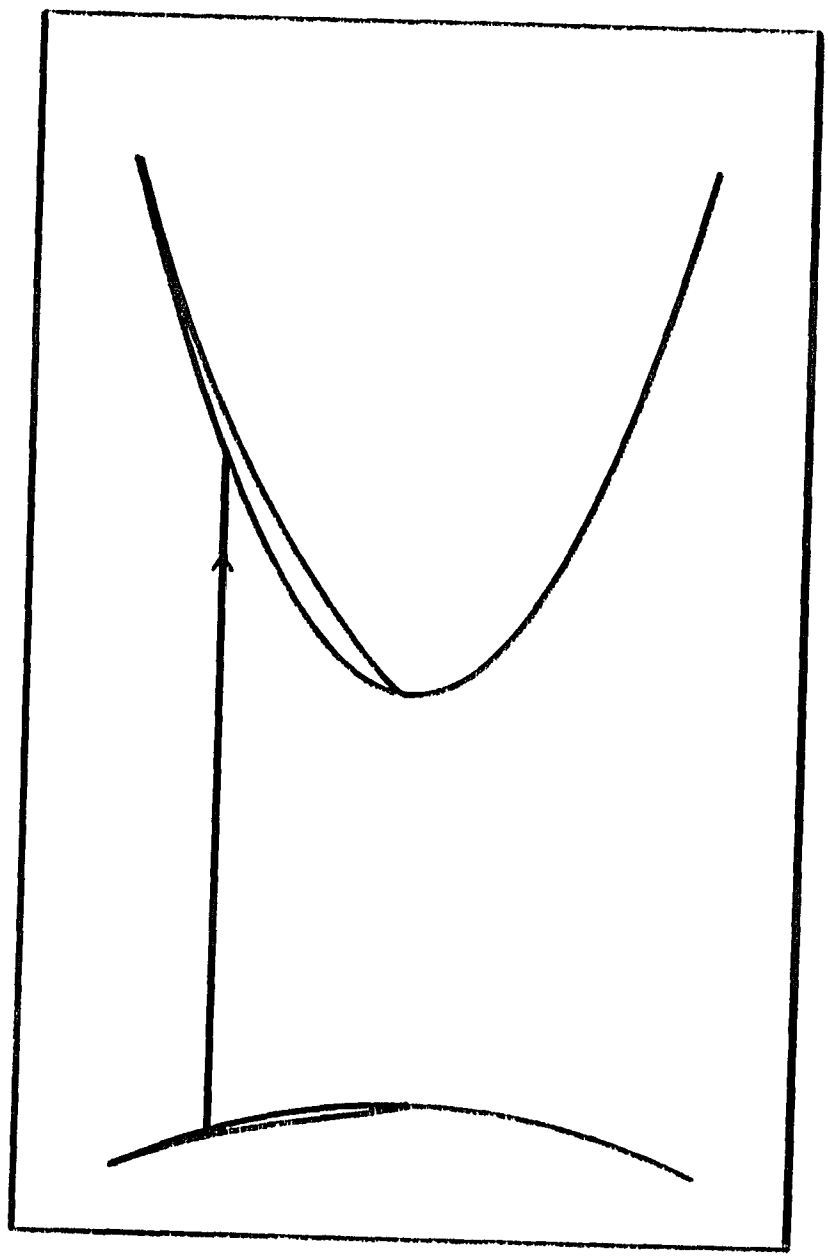

Figure 4.1.2b. In the case of high intensity excitation, $t_{LOPh} > t_{ee}, t_{hh}$ and t_{he}. The electrons and holes form thermalized distributions. When $t_{he} > t_{ee}, t_{hh}$, the electron distribution is much hotter than the hole distribution. The distribution is shown schematically for $t > t_{ee}, t_{hh}$ but $t < t_{he}$.

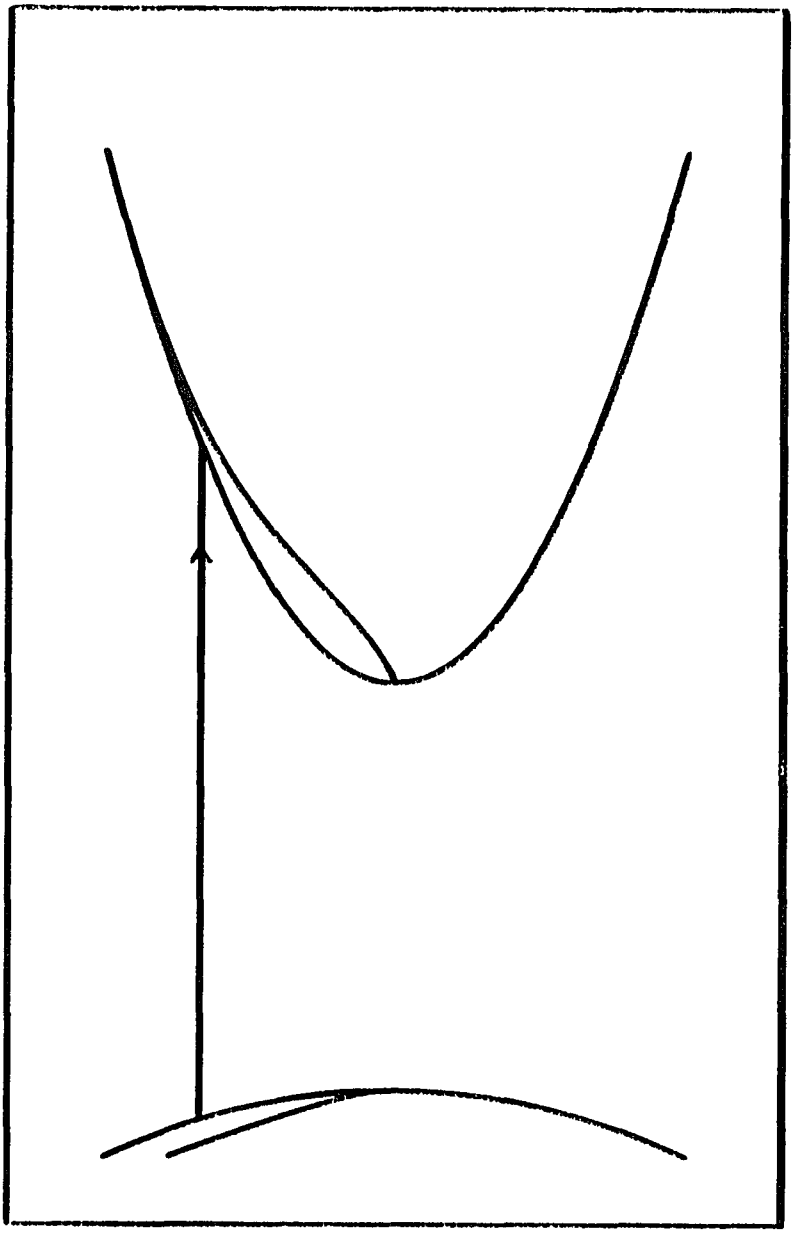

Figure 4.1.2c. In the case of high intensity excitation, $t_{LOPh} > t_{ee}$, t_{hh} and t_{he}. The electrons and holes form thermalized distributions. When $t_{he} < t_{ee}, t_{hh}$, the electrons and holes come to a common temperature as they thermalize.. The distribution is shown schematically for $t > t_{he}$.

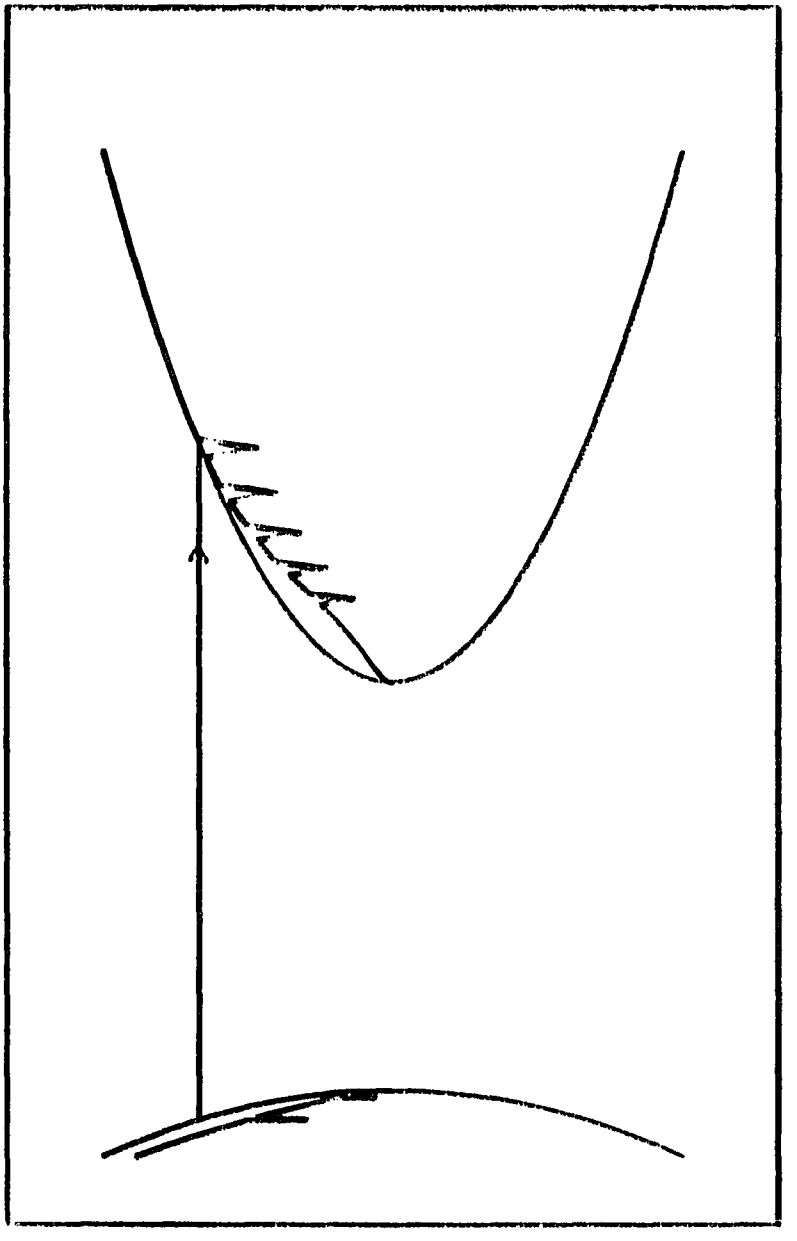

Figure 4.1.2d. In the case of low intensity excitation, $t_{LOPh} < t_{ee}$, t_{hh} and t_{he}. The electron and hole distributions show peaks at energies that are multiples of $\hbar\omega_{LOPh}$ below the excitation energy. The electrons and holes loose most of their initial energy to the lattice before the thermalize. The distribution is shown schematically for $t > t_{LOPh}$.

find that a standard form of the distribution function is obtained only after 2.0 ps. The work of Osman and Ferry show that at high concentrations the e-h interactions as well as the e-e interaction is an important factor in determining the thermalization rate of the carriers. The expressions for the e-h, h-e, e-e and h-h scattering rates are:[13]

$$\Gamma_{eh}(\mathbf{k}_o) = \frac{p\mu e^4}{2\pi\varepsilon^2\hbar^3}\int\frac{d^3k\, F_h(\mathbf{k})\, Q_{eh}}{\beta^2(Q_{eh}^2+\beta^2)} \tag{4.1.3}$$

$$\Gamma_{he}(\mathbf{k}_o) = \frac{n\mu e^4}{2\pi\varepsilon^2\hbar^3}\int\frac{d^3k\, F_e(\mathbf{k})\, Q_{eh}}{\beta^2(Q_{he}^2+\beta^2)} \tag{4.1.4}$$

$$\Gamma_{ee}(\mathbf{k}_o) = \frac{n\mu e^4}{2\pi\varepsilon^2\hbar^3}\int\frac{d^3k\, F_e(\mathbf{k})\, Q_{ee}}{\beta^2(Q_{ee}^2+\beta^2)} \tag{4.1.5}$$

$$\Gamma_{hh}(\mathbf{k}_o) = \frac{p\mu e^4}{2\pi\varepsilon^2\hbar^3}\int\frac{d^3k\, F_h(\mathbf{k})\, Q_{hh}}{\beta^2(Q_{hh}^2+\beta^2)} \tag{4.1.6}$$

where

$$Q_{eh} = 2\mu\left|\frac{\mathbf{k}_o}{m_e} - \frac{\mathbf{k}}{m_h}\right| \tag{4.1.7}$$

$$Q_{he} = 2\mu\left|\frac{\mathbf{k}_o}{m_h} - \frac{\mathbf{k}}{m_e}\right| \tag{4.1.8}$$

$$Q_{ee} = 2\mu\left|\frac{\mathbf{k}_o}{m_e} - \frac{\mathbf{k}}{m_e}\right| \tag{4.1.9}$$

$$Q_{hh} = 2\mu \left| \frac{k_o}{m_h} - \frac{k}{m_h} \right| \qquad (4.1.10)$$

and n and p are the electron and hole concentrations, μ is the reduced mass ($m_e m_h/[m_e+m_h]$ for Γ_{eh} and Γ_{he}, $\frac{m}{2}e$ for Γ_{ee} and $\frac{m}{2}h$ for Γ_{hh}) and β is the inverse screening length. Osman and Ferry used an ensemble Monte Carlo technique to calculate the different scattering rates assuming a Maxwellian distribution. Their results are shown in figures 4.1.3.a-c Because of the smaller density of states (and therefore the greater likelihood of a final state being occupied) of the conduction band the h-h and e-h scattering rates are faster than the e-e and h-e scattering rates.

From Eqs. 4.1.3 through 4.1.6, we see that the e-e, e-h, h-e and h-h scattering rates depend on the shape of the distribution function. The conventional methods using the Boltzman Transport Equation require the a priori knowledge of the form of the distribution function, which is not known for the non-equilibrium situation during the first few picoseconds. Ensemble Monte Carlo techniques do not assume a form for the distribution function and therefore are necessary to accurately calculate the time evolution of the non-equilibrium distribution function.[9] For an initial δ-function excitation, we see from eqs. 4.1.5 and 4.1.6, that e-e and h-h scattering can only occur within the bandwidth of the excitation and under these conditions e-h interactions dominate in the thermalization of the distribution, although the efficiency of energy transfer is weak due to the larger mass of the holes compared to the electrons.

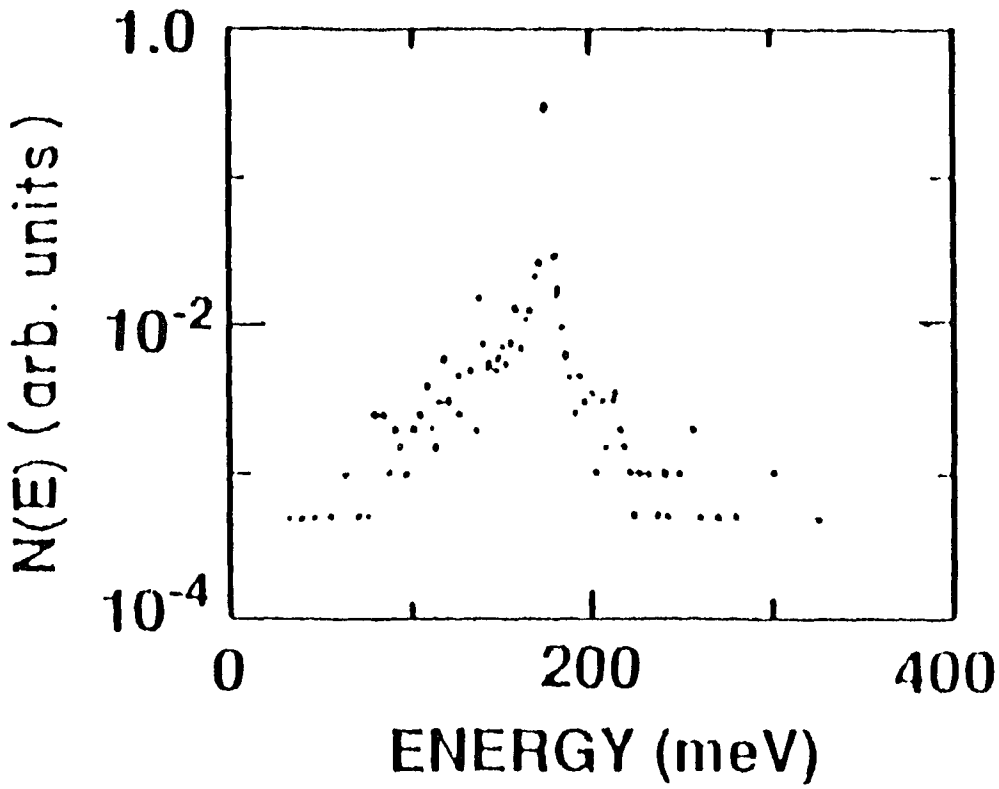

Figure 4.1.3a. Ensemble Monte Carlo calculations of Osman and Ferry of the electron distribution at 250 fs after excitation by a 1.71 eV laser. The density is 10^{18} cm^{-3}. Taken from reference 13.

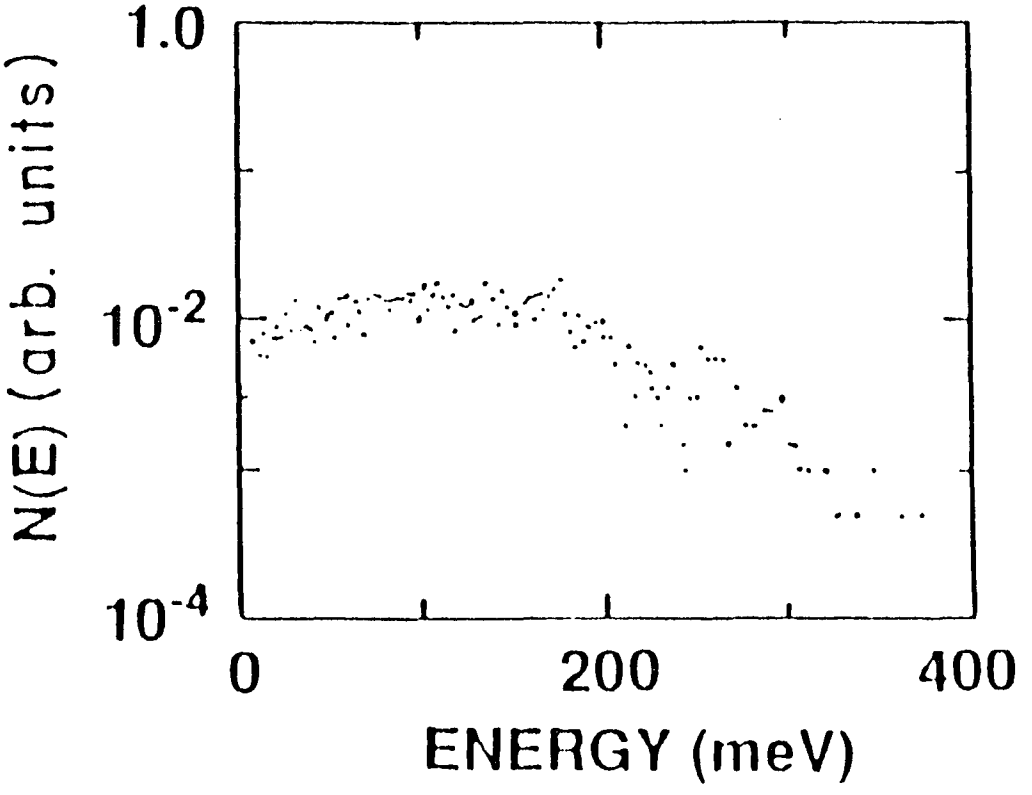

Figure 4.1.3b. Ensemble Monte Carlo calculations of Osman and Ferry of the electron distribution at 500 fs after excitation by a 1.71 eV laser. The density is 10^{18} cm^{-3}. Taken from reference 13.

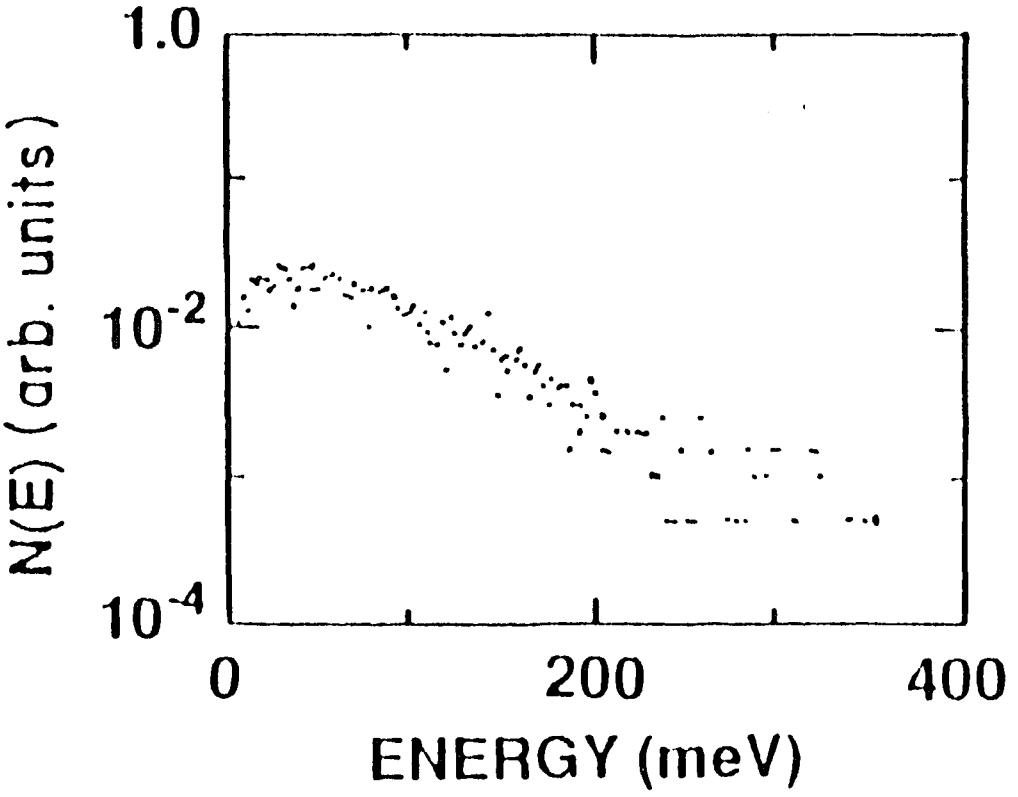

Figure 4.1.3c. Ensemble Monte Carlo calculations of Osman and Ferry of the electron distribution at 1000 fs after excitation by a 1.71 eV laser. The density is 10^{18} cm^{-3}. Taken from reference 13.

Experimental evidence has shown that under high excitation the rate of energy loss to the lattice is slowed due to screening.[18-25] At high concentrations ($>10^{18}$ cm^{-3}) e-e as well as e-h interactions are important factors which determine the cooling rates and electron thermalization. The electrons lose energy to the holes. The holes, because of their heavier effective mass, are less screened and lose energy to the lattice at a faster rate than the electrons. Furthermore, in a multi-valley semiconductor such as GaAs, electrons, with sufficient energy, can rapidly scatter to other valleys by deformation potential LO-phonon emission or absorption.[26,27] This process will reduce the electron population in the direct valley and complicate the dynamics. The electrons that scatter to the upper valleys lose kinetic energy when they scatter. Through e-e scattering, these electrons form a distribution in the side valleys at a lower temperature than the central valley. The LO-phonon interaction in these valleys is less screened because of their larger effective mass.[28] When these electrons scatter back to the central valley they gain kinetic energy and can reheat the electron in the Γ-valley. Under high photoexcitation, when the electron-polar LO phonon interaction is screened, more than 80% of the electrons can scatter to the L and X-valleys.[14] Previous work at lower densities using pump and probe absorption[29-32] or using pulse correlation techniques[33-36] have measured the time for electrons to scatter from their initial state of excitation by intervalley or electron-electron scattering. They have found these times to be on the order of less than 50 femtoseconds. The evolution of the distribution from a δ-function into a thermal distribution involves a large number of

carrier-carrier collisions and will occur on a slower time scale than the time for a single electron-electron scattering event. Experimental knowledge of the shape of the distribution function on a short time scale can then be compared with Ensemble Monte Carlo theory, taking in account the influences and activity of e-e, e-h, h-e, h-h and e-ph interactions on the shape of the distribution.

4.1.2 Transient absorption

Consider above band gap absorption in a semiconductor with parabolic bands. The absorption coefficient for allowed direct transitions is[17]

$$\alpha = \frac{\mu_o c^2 (2\mu_r)^{3/2} f_{vc} (\hbar\omega - E_g)^{1/2} (1 - F_e - F_h)}{4 m_o n \pi \hbar^2} \qquad (4.1.11)$$

where μ_r is the reduced effective mass, f_{vc} is the oscillator strength and F_e (F_h) is the occupation number for electrons (holes) in the conduction (valence) band at states separated by $\hbar\omega$. If the sample is not heavily doped then F_e and F_h are both zero for $\hbar\omega$ more than a few KT_L above bandgap. However intense optical excitation creates a large number of excited electrons (holes) in the conduction (valence) band at a temperature hotter than the lattice. The change in absorption is given by

$$\delta\alpha(\omega) = -\delta\alpha_{BL} + \delta\alpha_{FC} + \delta\alpha_{BR} \qquad (4.1.12)$$

where $-\delta\alpha_{BL}$ is the decrease in interband absorption due to the photoexcitation carriers; $\delta\alpha_{FC}$ is intraband free carrier absorption,

which is negligible compared to interband absorption; and $\delta\alpha_{BR}$ is the change in absorption due to band gap renormalization. A large excited population screens the coulomb interaction which reduces the band gap.[37] This increases the joint density of states resulting in an increase in absorption (a decrease in transmission). The change in the absorption coefficient due to band gap renormalization is given by

$$\delta\alpha_{BR} = \alpha_o \left[\frac{(\hbar\omega-(E_g+\delta E_g))^{1/2}}{(\hbar\omega - E_g)^{1/2}} - 1. \right] \qquad (4.1.13)$$

where δE_g is the change in band gap due to renormalization. The band gap change at high densities and low carrier temperature can be approximated by[25,38,39]

$$\delta E_g = - \Gamma (n^{1/3} + p^{1/3}) \qquad (4.1.14)$$

The measured value of Γ is 2.1×10^{-8} cm eV.[38] For carrier densities in the range of 1×10^{19} cm^{-3} to 2×10^{19} cm^{-3}, δE_g is in the range of -80 to -115 meV. At higher carrier temperatures the band gap shift will be less.[5] For $\hbar\omega - E_g >> \delta E_g$, $\delta\alpha_{BR}$ is approximately given by

$$\delta\alpha_{BR} = \frac{-\alpha_o \delta E_g}{2(\hbar\omega-E_g)} = \alpha_o \frac{\Gamma(n^{1/3} + p^{1/3})}{2(\hbar\omega-E_g)} \qquad (4.1.15)$$

The change in absorption due to bleaching is given by:

$$\delta\alpha_{BL} = -(\alpha_o+\delta\alpha_{BR}) (F_e + F_h) \quad . \qquad (4.1.16)$$

Pump and probe absorption techniques can be used to measure the changes in α (and thus $F_e + F_h$) as a function of delay time between the pump and probe pulses. If $\delta\alpha(\omega)$ is measured over a large range of energies at different delay times, information about the time evolution of the excited carrier distribution function can be obtained.

In practice one measures the change in transmission, which is related to the absorption by

$$T(t) = I_o(1-R)^2 \exp-[(\alpha_o + \delta\alpha_{BR})\ell(1-F_e(t)-F_h(t))] \qquad (4.1.17)$$

where R is the sample reflectivity, which is separately measured and ℓ is sample thickness. The reflectivity changes under photoexcitation are small compared to absorption changes. For my samples, with an AlGaAs cover layer, the reflectivity is dominated by the AlGaAs - air interface not the GaAs - AlGaAs interface.

By taking the ratio of the excited transmission to the unexcited transmission,

$$\frac{T(t)}{T} = \frac{I_o(1-R)^2 \exp-[(\alpha_o + \delta\alpha_{BR})\ell(1-F_e(t)-F_h(t))]}{I_o(1-R)^2 \exp-[\alpha_o \ell]} \qquad (4.1.18)$$

the relationship between the measured change in transmission and the occupation probability in the optically coupled region is

$$\frac{T(t)}{T_o} = \exp[(\alpha_o+\delta\alpha_{BR})\ell(F_e(t)+F_h(t)-\delta\alpha_{BR}\ell] \quad . \qquad (4.1.19)$$

Solving for $F_e + F_h$, gives

$$F_e + F_h = [\ln(T(t)/T_o)]/\{(\alpha_o + \delta\alpha_{BR})\ell\} - \delta\alpha_{BR}\ell \quad . \qquad (4.1.20)$$

The unexcited absorption, α_o, must be independently measured.

If more than one transition is allowed at a given probe frequency, as in GaAs, where absorption can occur from the heavy-hole, light-hole and splitoff valence bands, the absorption coefficient is the sum of the absorption coefficients for each transition. For each transition, the initial and final states have different Fermi factors. In order to correctly interpret the data, α for each transition must be known as well as the occupation number of all the states involved.

4.1.3 Electron and hole contributions to $\delta\alpha$

Both the excited electrons and holes contribute to the absorption changes. For a semiconductor, such as GaAs, with a much smaller conduction band effective mass than the valence band effective mass, the relative contribution of electrons and holes depends on the probe energy. The conduction band, with its smaller density of states will be degenerate under moderate or intense photoexcitation while the holes will be degenerate only at extremely intense excitation levels. At probe energies near band gap, the conduction band, being degenerate, will have a higher occupation number than the valence band

and the electron dynamics will dominate the transient absorption. If one probes with higher frequencies, the optically coupled states in the conduction band will be further from band edge than the coupled valence band states; therefore the Fermi factor for the electrons will decrease faster than the hole Fermi factor as the probe energy is increased.

The occupation probability for electrons and holes at a carrier density of $n_e = n_h = 2 \times 10^{19}$ cm^{-3} is shown in figures 4.1.4a and 4.1.4b for carrier temperatures of 1400 K and 600 K, respectively. Since, in GaAs, at high carrier temperatures, the electron population in the central valley can be considerably less than the hole population, the electron and hole occupation probabilities are also plotted for $n_h = 2 \times 10^{19}$ cm^{-3} and $n_e = 1 \times 10^{19}$ cm^{-3} in figures 4.1.5a and b for carrier temperatures of 1400 K and 600 K respectively. The conduction and valence bands are taken to be parabolic with effective masses $m_e^* = 0.063\ m_o$ and $m_h^* = 0.50\ m_o$. The x-axis (energy) in figures 4.1.4a,b and 4.1.5a,b is scaled to show the energy for vertical transitions (see Eq 4.1.1 and 4.1.2).

From figures 4.1.4a and b and 4.1.5a and b, we see that for probe energies less than 0.3 eV above gap, $F_e >> F_h$ and the induced absorption changes are dominated by the electrons. At higher energies, more than 0.8 eV above gap, $F_h >> F_e$ and the holes dominate the absorption changes. For energies in the range of 0.3 to 0.8 eV above band gap both the electrons and holes contribute. The relative contribution of electrons and holes will change as carriers cool and

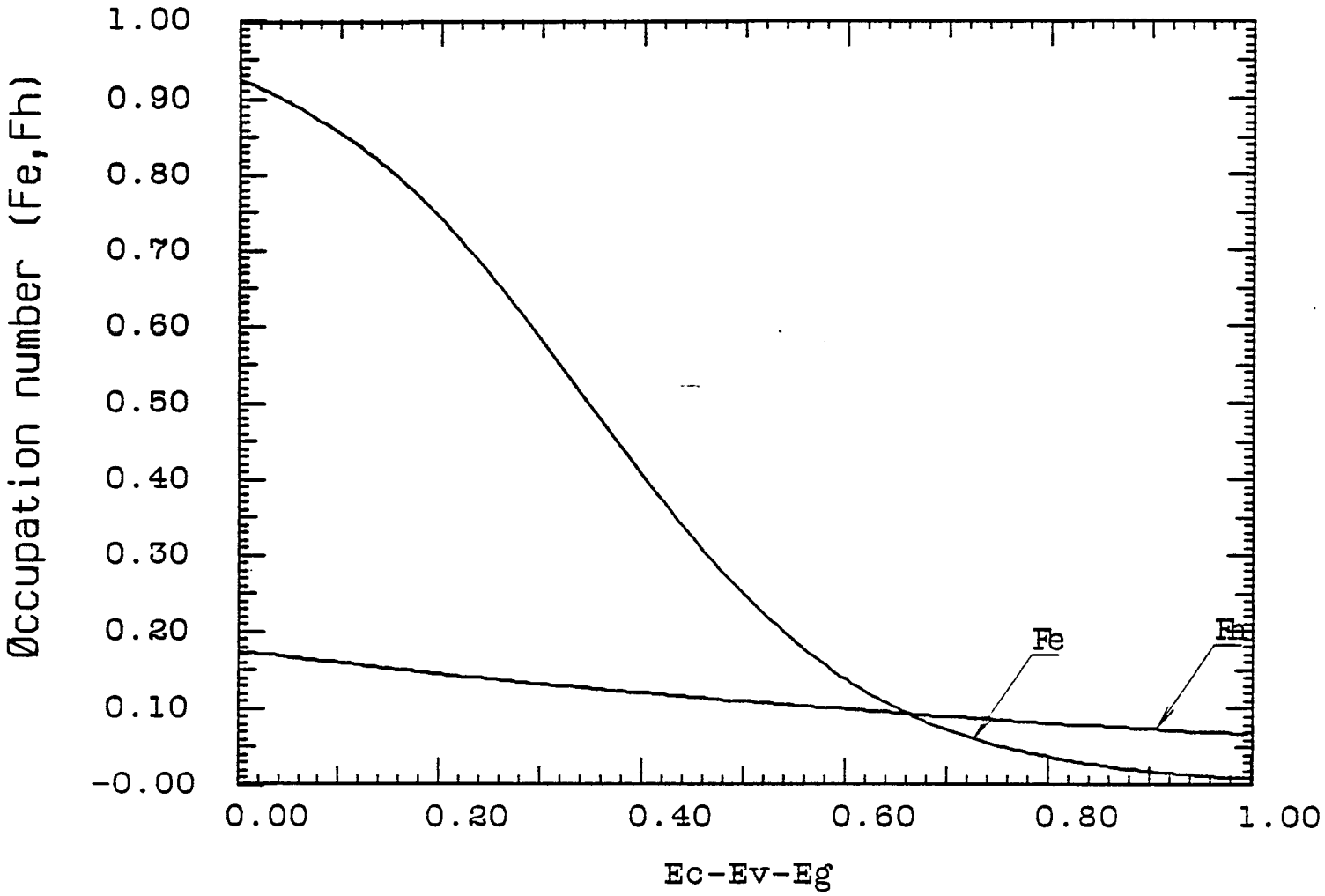

Figure 4.1.4a. The occupation probability for electrons and holes. The carrier density is $n_e = n_h = 2 \times 10^{19}$ cm^{-3} and carrier temperature = 1400 K.

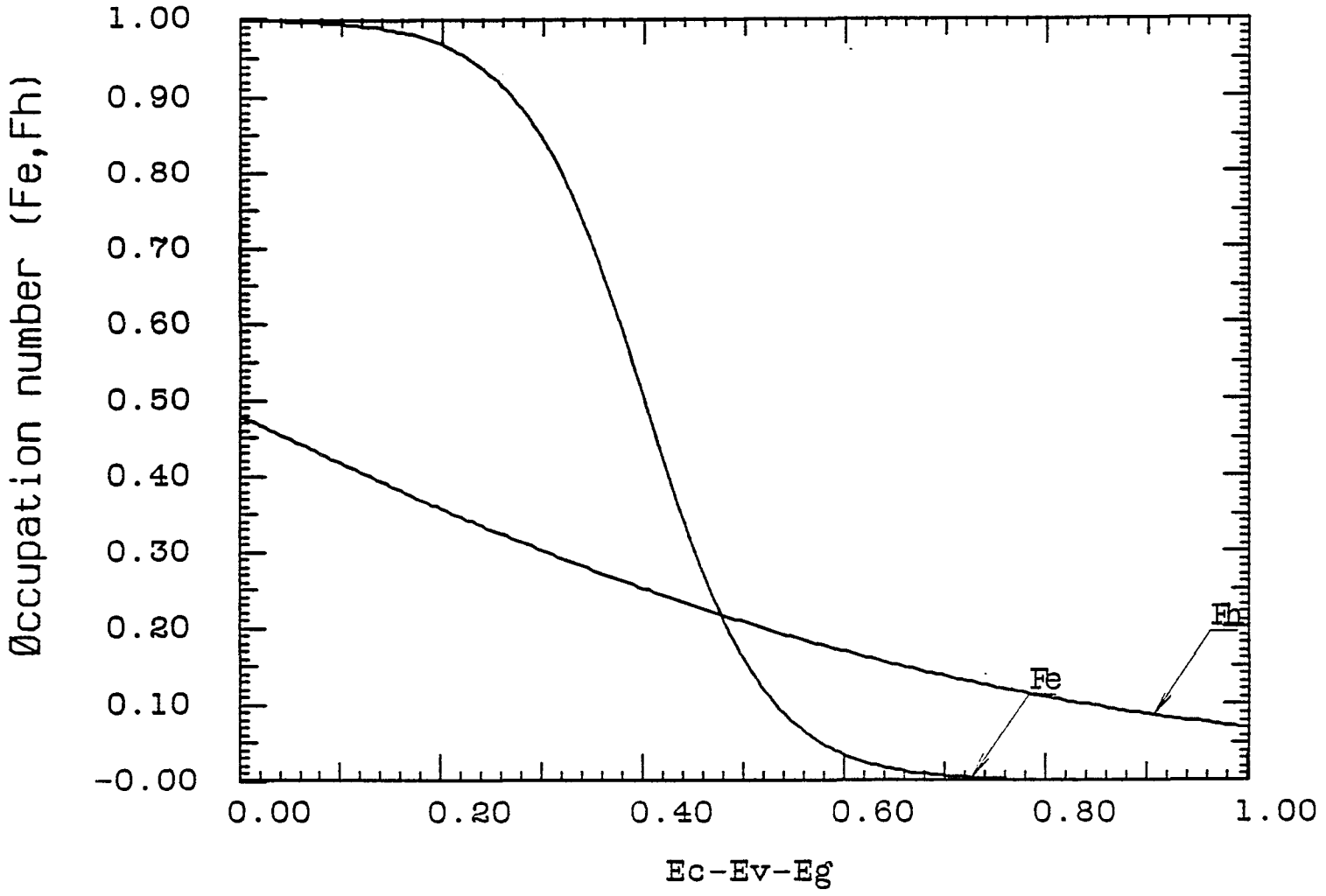

Figure 4.1.4b. The occupation probability for electrons and holes. The carrier density is $n_e = n_h = 2 \times 10^{19}$ cm^{-3} and carrier temperature = 600 K.

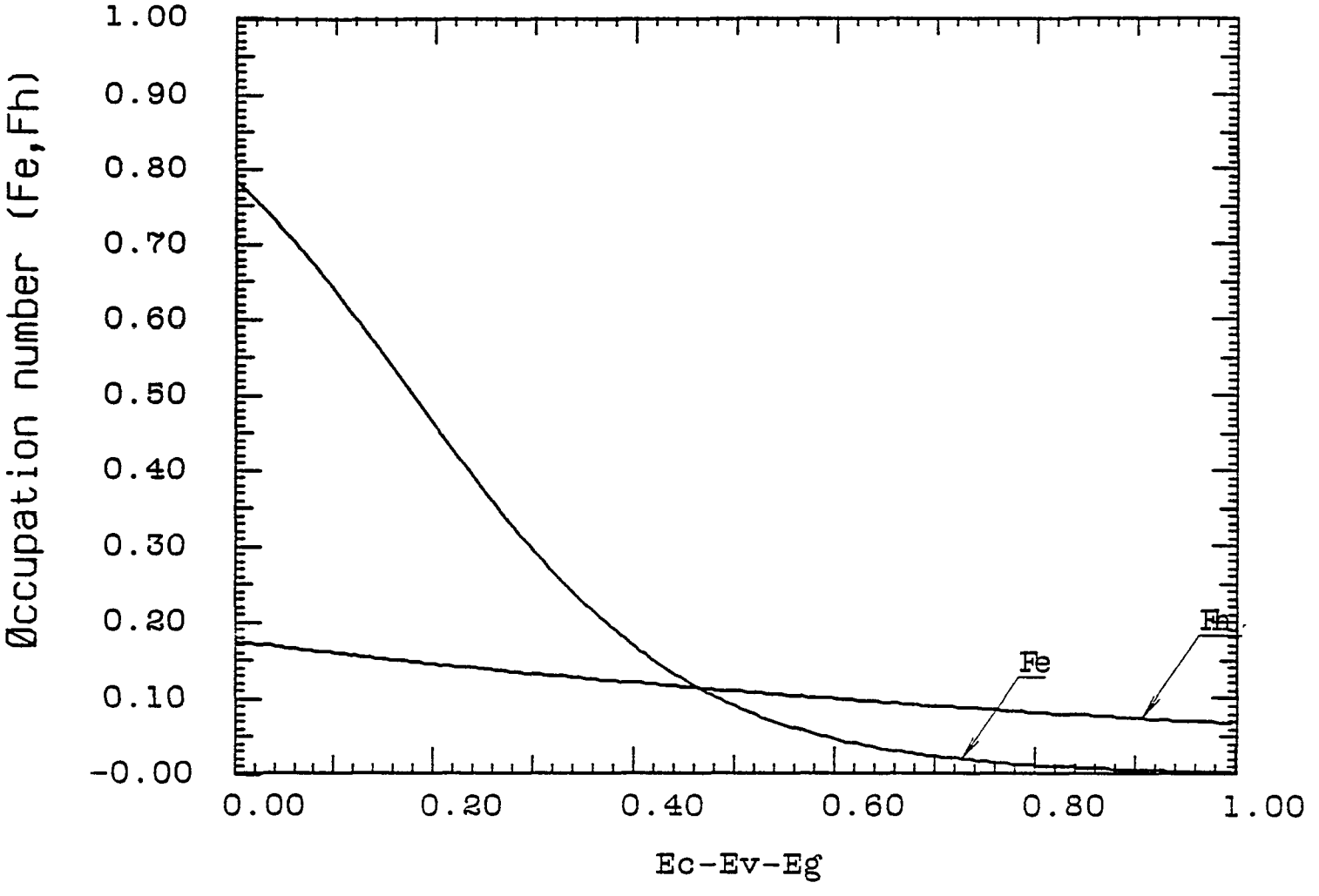

Figure 4.1.5a. The occupation probability for electrons and holes. The carrier density is n_e = 1 x 10^{19} cm^{-3}, n_h = 2 x 10^{19} cm^{-3} and the carrier temperature = 1400 K.

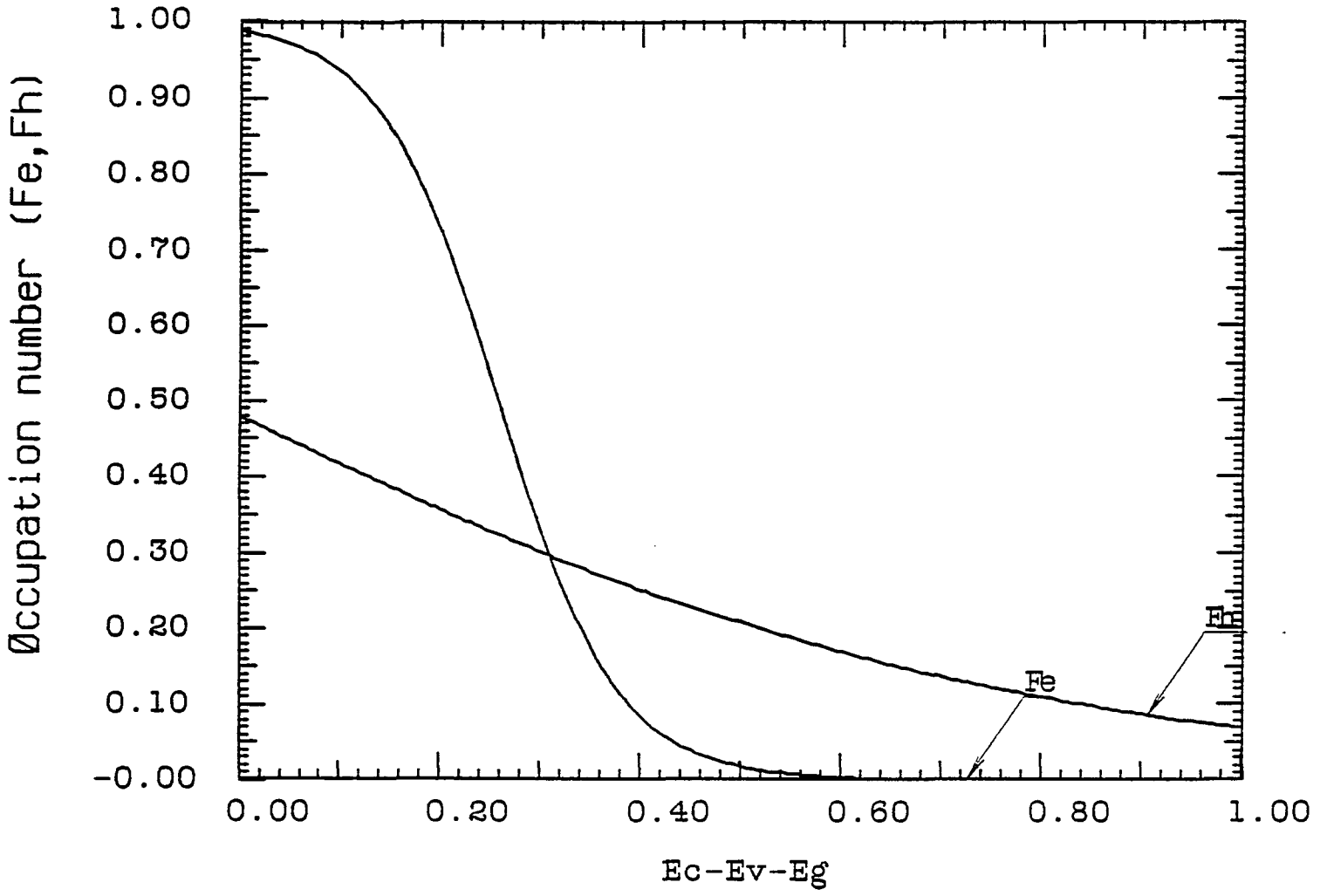

Figure 4.1.5b. The occupation probability for electrons and holes. The carrier density is $n_e = 1 \times 10^{19}$ cm^{-3}, $n_h = 2 \times 10^{19}$ cm^{-3} and the carrier temperature = 600 K.

as electrons scatter back from the side valleys. At higher energies, as the carrier temperature decreases, F_e decreases rapidly while F_h decreases less. At energies closer to the band edge, F_e and F_h both increase but F_e remains greater than F_h. The relative electron and hole contributions to the bleaching will also change with carrier density. The occupation probabilities, F_e and F_h at a carrier density of 1×10^{19} cm^{-3} is plotted in figures 4.1.6a and b at T_c = 1400 K and 600 K respectively.

4.1.4 Heavy-hole, light-hole and splitoff contributions to the absorption coefficient

In the experimental data of this thesis, absorption from the splitoff band to the conduction band is evident. The relative contributions of the heavy-hole, light-hole and splitoff bands will be approximated from the measured steady state absorption of the sample and the joint density of states of each of the three valence bands with the conduction band, assuming the bands are parabolic and isotropic. The light-hole band in the region of interest (1.65 to 2.0 eV) is approximately parallel to the heavy-hole band and displaced about 100 meV below the heavy-hole band. The effective masses used were: conduction band mass =0.063 m_o, the heavy-hole and light-hole masses =0.5 m_o and the splitoff mass =0.145 m_o. The corresponding reduced masses are 0.056 m_o (HH-cond. and LH-cond.) and 0.044 m_o (SO-cond.).

The absorption coefficient depends on the joint density of states (which has a $\mu_r^{3/2}\sqrt{(\hbar\omega - E_g)}$ dependence) and the optical matrix

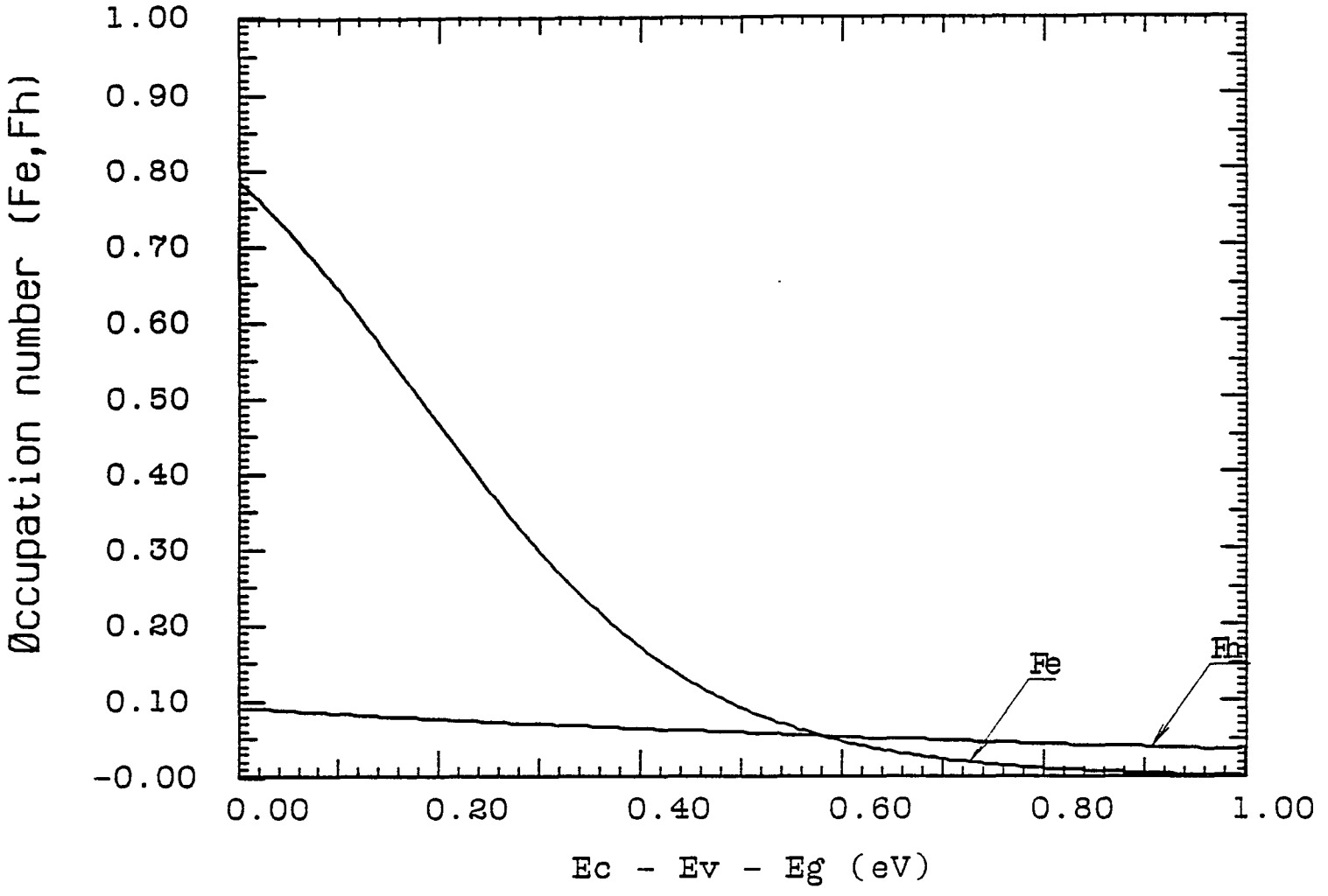

Figure 4.1.6a. The occupation probability for electrons and holes. The carrier density is $n_e = 1 \times 10^{19}$ cm^{-3}, $n_h = 1 \times 10^{19}$ cm^{-3} and the carrier temperature = 1400 K.

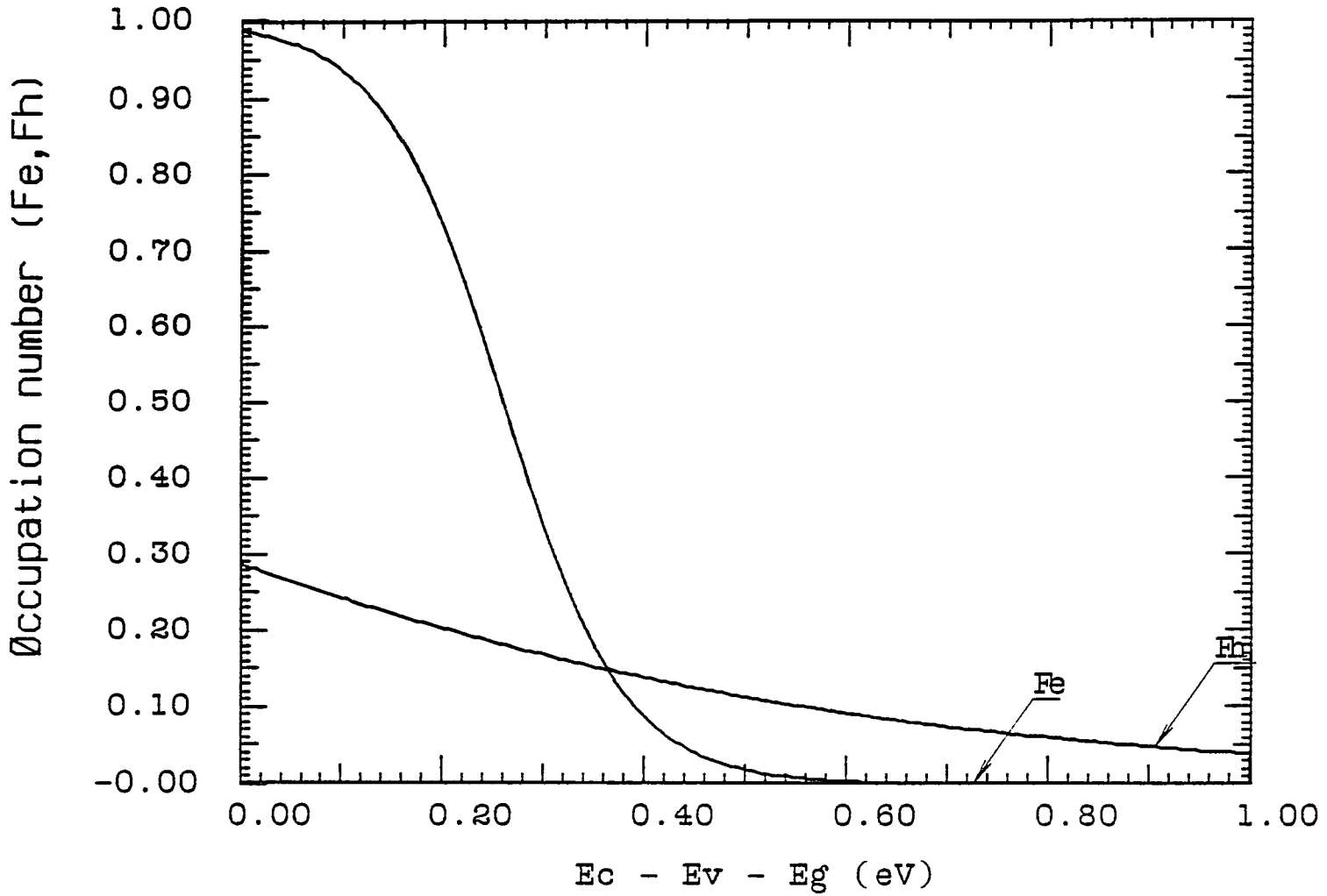

Figure 4.1.6b. The occupation probability for electrons and holes. The carrier density is $n_e = 1 \times 10^{19}$ cm^{-3}, $n_h = 1 \times 10^{19}$ cm^{-3} and the carrier temperature = 600 K.

element coupling the conduction and valence bands. In the Kane band model the conduction is S like and the valence band is P like. Near k=0, the conduction band wave function is $|c, \frac{1}{2}, \pm\frac{1}{2}>$ and the valence band wave functions are $|v, \frac{3}{2}, \pm\frac{3}{2}>$ (heavy-hole), $|v, \frac{3}{2}, \pm\frac{1}{2}>$ (light-hole) and $|v, \frac{1}{2}, \pm\frac{1}{2}>$ (splitoff). The corresponding square of the optical matrix elements are in the ratio of 3:1:2.[40] The absorption coefficients are then in the ratio

$$\begin{aligned} &\text{Heavy-hole:} && 3\,(0.056)^{3/2}\,(\hbar\omega-1.424)^{1/2} && \\ &\text{Light-hole:} && 1\,(0.056)^{3/2}\,(\hbar\omega-1.524)^{1/2} && (4.1.21) \\ &\text{Splitoff:} && 2\,(0.044)^{3/2}\,(\hbar\omega-1.765)^{1/2} && (\hbar\omega > 1.765\ \text{eV}) \\ & && 0 && (\hbar\omega < 1.765\ \text{eV})\ . \end{aligned}$$

Non-parabolicity of the conduction band will increase the relative contribution from the heavy-hole and light-hole bands since the conduction band density of states will increase faster than k^2. The non-parabolicity of the splitoff band will decrease the relative contribution from the splitoff band since the density of states increases slower than k^2 in the splitoff band. The precise contributions from each valence band transition would require detailed knowledge of the band curvature and electron wave functions at K away from the zone center ($\approx 10^7$ cm^{-1} for 2.01 eV excitation).

Since, in this thesis an exact fitting of the data to a distribution function can not be done except to show that within the

first 800 fs the distribution is neither a Fermi-Dirac nor Maxwellian distribution, the relative strengths of the three transitions will be approximated by considering the bands to be parabolic. A complete detailed analysis of the data would require fitting an electron density and temperature and a hole density and temperature (in each band) with an unknown distribution. The electron density (in the central valley) and the hole density are not equal since a significant fraction of the electrons scatter to the other valleys.

At the laser photon energy of 2.01 eV, using eq. 4.1.21, 62% of the electrons are excited from the heavy-hole band and 19% from each of the light-hole and splitoff bands. The inclusion of band non-parabolicity will reduce the splitoff band transitions to 5 - 10%. The experimental pump and probe absorption results of this thesis indicate the splitoff contribution is much less than calculated from a model of simple parabolic bands and that reducing the splitoff contribution in eq. 4.1.21c by a factor of about 4 is more consistent with the experimental results (see section 4.4).

Although the number of carriers excited from the splitoff band is small compared to the number excited from the heavy-hole and light-hole bands, Its relative contribution to the bleaching is not necessarily small. Transitions from the splitoff band probe states at lower energies in the conduction band, which have a much higher occupation number than the states probed by transitions from the heavy-hole and light-hole bands which are at higher energies. As an example, consider the change in absorption seen by a 2.01 eV probe.

Assume the hole density, $n_h = 2 \times 10^{19}\ cm^{-3}$ and the electron density, $n_e = 1 \times 10^{19} cm^{-3}$ (Γ-valley) with a carrier temperature of 1000 K. The calculated quasi-Fermi levels are $\mu_h = 0.087$ meV and $\mu_e = 0.200$ meV. (band gap renormalization is neglected). The energies of the optically coupled states of a 2.01 probe are given by

$$\mathcal{E}_c = \frac{0.50\ (2.01-1.424)}{0.5+0.063} = 0.520 \text{ eV}$$

$$\mathcal{E}_{HH} = -\frac{0.063\ (2.01-1.424)}{0.5+0.063} = -0.066 \text{ eV} \qquad \text{(HH - C)} \qquad (4.1.22a)$$

$$\mathcal{E}_c = \frac{0.50\ (2.01-1.524)}{0.5+0.063} = 0.432 \text{ eV}$$

$$\mathcal{E}_{LH} = -\frac{0.063\ (2.01-1.524)}{0.5+0.063} - 0.1 = -0.154 \text{ eV} \qquad \text{(LH - C)} \qquad (4.1.22b)$$

$$\mathcal{E}_c = \frac{0.145(2.01-1.765)}{0.145+0.063} = 0.171 \text{ eV}$$

$$\mathcal{E}_{HH} = -\frac{0.063\ (2.01-1.765)}{0.145+0.063} - 0.341 = -0.415 \text{ eV} \qquad \text{(SO - C)} \qquad (4.1.22c)$$

The occupation probabilities (assuming a Fermi-Dirac distribution) in the optically coupled region are

$$F_e + F_h = \left[1+\exp\left[\frac{.520-.200}{.08617}\right]\right]^{-1} + \left[1+\exp\left[\frac{.087+.066}{.08617}\right]\right]^{-1}$$
$$= 0.024 + 0.145 = 0.169 \qquad \text{(HH-C)} \qquad (4.1.23a)$$

$$F_e + F_h = \left[1+\exp\left[\frac{.432-.200}{.08617}\right]\right]^{-1} + \left[1+\exp\left[\frac{.087+.154}{.08617}\right]\right]^{-1}$$
$$= 0.063 + 0.057 = 0.120 \qquad \text{(LH-C)} \qquad (4.1.23b)$$

$$F_e + F_h = \left[1+\exp\left[\frac{.171-.200}{.08617}\right]\right]^{-1} + \left[1+\exp\left[\frac{.087+.415}{.08617}\right]\right]^{-1}$$
$$= 0.583 + 0.003 = 0.586 \qquad \text{(SO-C)} \qquad (4.1.23c)$$

and the change in absorption is

$$\delta\alpha = \delta\alpha_{HH-C} + \delta a_{LH-C} + \delta a_{SO-C} = -(4.21+0.91+4.39) \times 10^3 cm^{-1} . \quad (4.1.24)$$

For a 2.01 eV probe, transitions from the splitoff band account for 46% of the change in α although less than 20% of the carriers are excited from the splitoff band. The splitoff contribution to the bleaching is caused by excited electrons occupying states in the conduction band and will depend strongly on the fraction of electrons in the Γ-valley. On the other hand, at 2.01 eV, the heavy-hole contribution to the bleaching is primarily due to holes and will not be very sensitive to the electron distribution. Taking the splitoff contribution to be 5% of α at 2.01 eV, results in the splitoff transitions accounting for 17% of $\delta\alpha$.

Similar calculations for a 1.8 eV probe give

$$\delta\alpha = \delta\alpha_{HH-C} + \delta a_{LH-C} + \delta a_{SO-C} = -(7.76 + 2.78 + 2.68) \times 10^3 \ cm^{-1} \quad (4.1.25)$$

while for 2.2 eV probe, the absorption change is given by

$$\delta\alpha = \delta\alpha_{HH-C} + \delta a_{LH-C} + \delta a_{SO-C} = -(5.09 + 0.72 + 3.41) \times 10^3 \ cm^{-1}. \quad (4.1.26)$$

In these cases, the splitoff contribution to $\delta\alpha$ is 20% and 37% for 1.8

and 2.2 eV probes respectively.

Inclusion of band gap renormalization in the above calculations would require accurate knowledge of how the band structure changes with carrier temperature. Using the room temperature change in band gap (given by Eq. 4.1.14) and assuming a rigid shift in band structure, the change in absorption at 2.01 eV can be calculated.

The change in band gap as given by Eq. 4.1.14 for a carrier density of $n_h = 2 \times 10^{19}$ cm^{-3} and $n_e = 1 \times 10^{19}$ cm^{-3}, is 100 meV. Eqs. 4.1.22a,b and c must be adjusted to reflect the renormalized band gap. The change in α_{BR} from Eq. 4.1.13 is

$$\delta\alpha_{BR}=\left(\delta\alpha_{HH-C}+\delta a_{LH-C}+\delta a_{SO-C}\right)_{BR}=(.153+.056+0.105)\times 10^{4}\ \text{cm}^{-1} \quad (4.1.27)$$

The energy of the optically coupled states becomes:

$$\mathcal{E}_c = \frac{0.50\ (2.01-1.424+.1)}{0.5+0.063} = 0.609 \text{ eV}$$

$$\mathcal{E}_{HH} = -\frac{0.063\ (2.01-1.424+.1)}{0.5+0.063} = -0.066 \text{ eV} \qquad (HH - C) \quad (4.1.28a)$$

$$\mathcal{E}_c = \frac{0.50\ (2.01-1.524+.1)}{0.5+0.063} = 0.432 \text{ eV}$$

$$\mathcal{E}_{LH} = -\frac{0.063\ (2.01-1.524+.1)}{0.5+0.063} - 0.1 = -0.154 \text{ eV} \qquad (LH - C) \quad (4.1.28b)$$

$$\mathcal{E}_c = \frac{0.145(2.01-1.765+.1)}{0.145+0.063} = 0.171 \text{ eV} \qquad (SO - C) \quad (4.1.28c)$$

$$\mathcal{E}_{HH} = - \frac{0.063\ (2.01-1.765+.1)}{0.145+0.063} - 0.341 = - 0.415\ \text{eV}$$

and the occupation probabilities are given by

$$F_e + F_h = \left[1+\exp\left[\frac{.609-.200}{.08617}\right]\right]^{-1} + \left[1+\exp\left[\frac{.087+.077}{.08617}\right]\right]^{-1}$$
$$= 0.009 + 0.130 = 0.139 \qquad \text{(HH-C)} \qquad (4.1.29a)$$

$$F_e + F_h = \left[1+\exp\left[\frac{.520-.200}{.08617}\right]\right]^{-1} + \left[1+\exp\left[\frac{.087+.166}{.08617}\right]\right]^{-1}$$
$$= 0.024 + 0.050 = 0.074 \qquad \text{(LH-C)} \qquad (4.1.29b)$$

$$F_e + F_h = \left[1+\exp\left[\frac{.241-.200}{.08617}\right]\right]^{-1} + \left[1+\exp\left[\frac{.087+.445}{.08617}\right]\right]^{-1}$$
$$= 0.383 + 0.002 = 0.385 \qquad \text{(SO-C)} \ . \qquad (4.1.29c)$$

The change in absorption is calculated from Eq. 4.1.16 and is now given by

$$\delta\alpha = \delta\alpha_{HH-C} + \delta a_{LH-C} + \delta a_{SO-C} = (-.127 + .014 - .0151) \times 10^3\ \text{cm}^{-1}. \qquad (4.1.30)$$

In this case, $\delta\alpha$ is a factor of 4 less than $\delta\alpha$ given by Eq. 4.1.24 (without renormalization) and the splitoff band transitions account for 57% of $\delta\alpha$.

4.2 Experimental procedure for time resolved pump and probe absorption

4.2.1 Optical setup

The pump and probe absorption technique involves the use of two laser pulses, a high intensity pump pulse and a weak probe pulse. The high intensity pump should have a photon energy great enough to photoexcite the sample in the region of interest. The pump pulse should be intense enough to excite a population sufficient to produce a measurable change in absorption. The second (probe) pulse's intensity should be weak so as to not induce any changes in absorption. The photon energy (or energies) of the probe pulse should be such that it optically couples states in the regions of interest. The transmitted intensity of the probe pulse is measured as a function of the delay time between the pump and probe pulses. From the measured changes in transmission, one calculates the change in absorption as a function of delay time at the probe frequencies. These absorption changes then give information about the excited state population.

The experimental apparatus for pump and probe absorption measurements is shown in fig. 4.2.1. The laser is split into two equally intense pulses by a beam splitter. A variable optical delay line, consisting of a corner cube mounted on a stepping motor, is inserted in the pump pulse's path. The other pulse is focused into a cell of CCL_4 to produce a broadband continuum probe. The probe pulse is attenuated and its polarization is rotated 45 degrees with respect to the pump. Filters are used to select discrete probe energies and

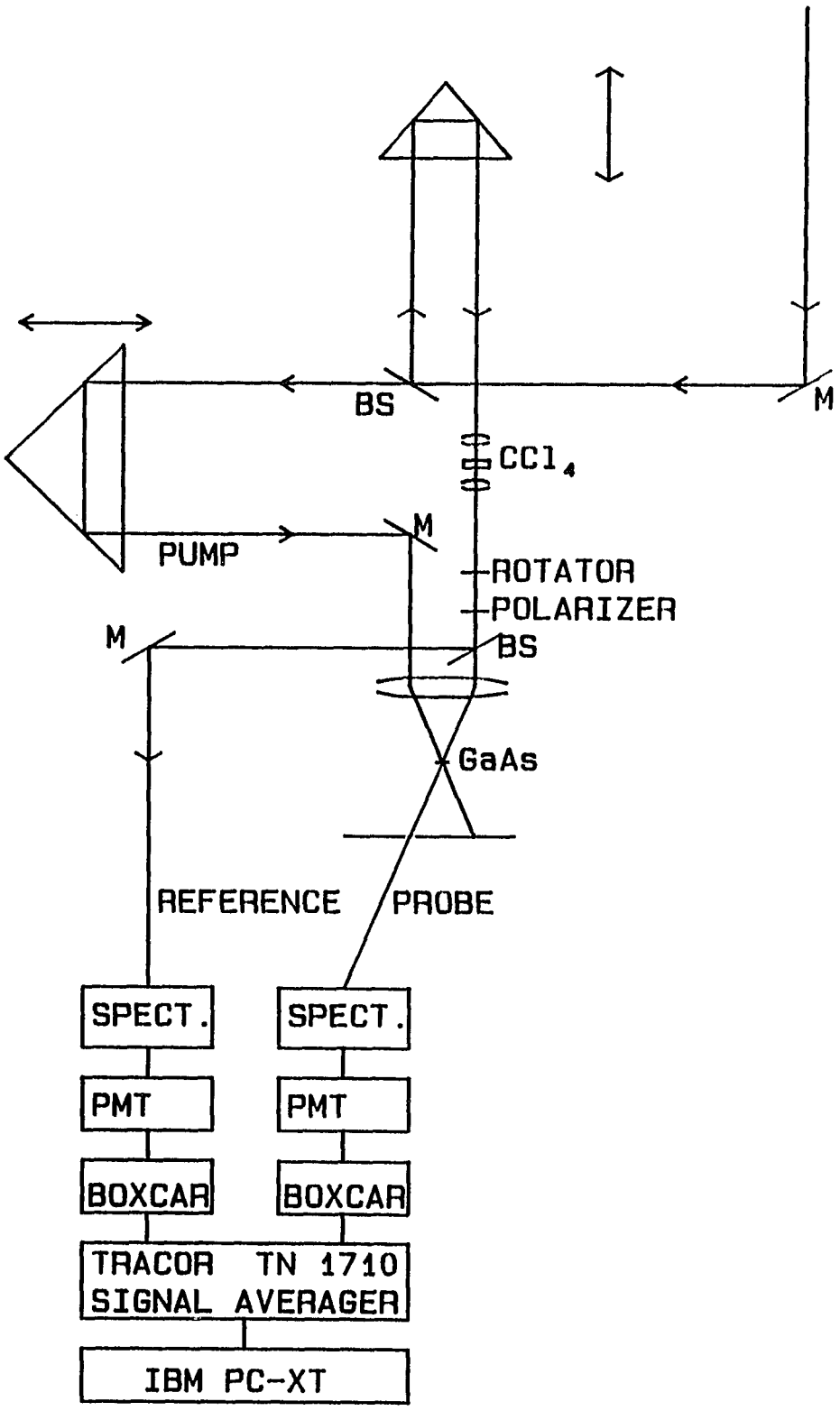

Figure 4.2.1. Experimental setup for the pump and probe absorption experiment. The Photomultiplier tubes can be replaced by an OMA.

reduce the probe intensity. A polarizer is inserted in the probe path which can be rotated to allow the probe polarization to be either parallel or perpendicular to the pump without changing the optical path length of the probe. A thin glass plate is inserted in the probe path to reflect a small portion of the probe pulse energy to serve as a reference for normalization of laser intensity fluctuations. The two pulses are aligned to be parallel but not collinear and then focused to overlap on the sample. Then the transmitted intensity of the probe and the reference pulses are detected. Initial alignment and data were taken without the continuum cell. Later, data was taken with the continuum probe pulse.

4.2.2 Spatial and temporal alignment of pump and probe pulses

Accurate measurements of the time dependence of the induced absorption requires precise spatial overlap of the two pulses as well as an accurate measurement of the optical delay between the pulses.

In order to accurately determine the temporal overlap of the pump and probe pulses, the sample was removed and replaced with a KDP crystal, mounted at the phase matching angle for second harmonic generation of the pump and probe pulses (see chapter 3). The delay between the pulses was adjusted to maximize the second harmonic produce by the mixing of the two pulses. The delay between pump and probe could be adjusted by translating the corner cube by a stepping motor. The resolution of the stepping motor is 2 μ (4 μ round trip) which corresponds to 13.33 fs.

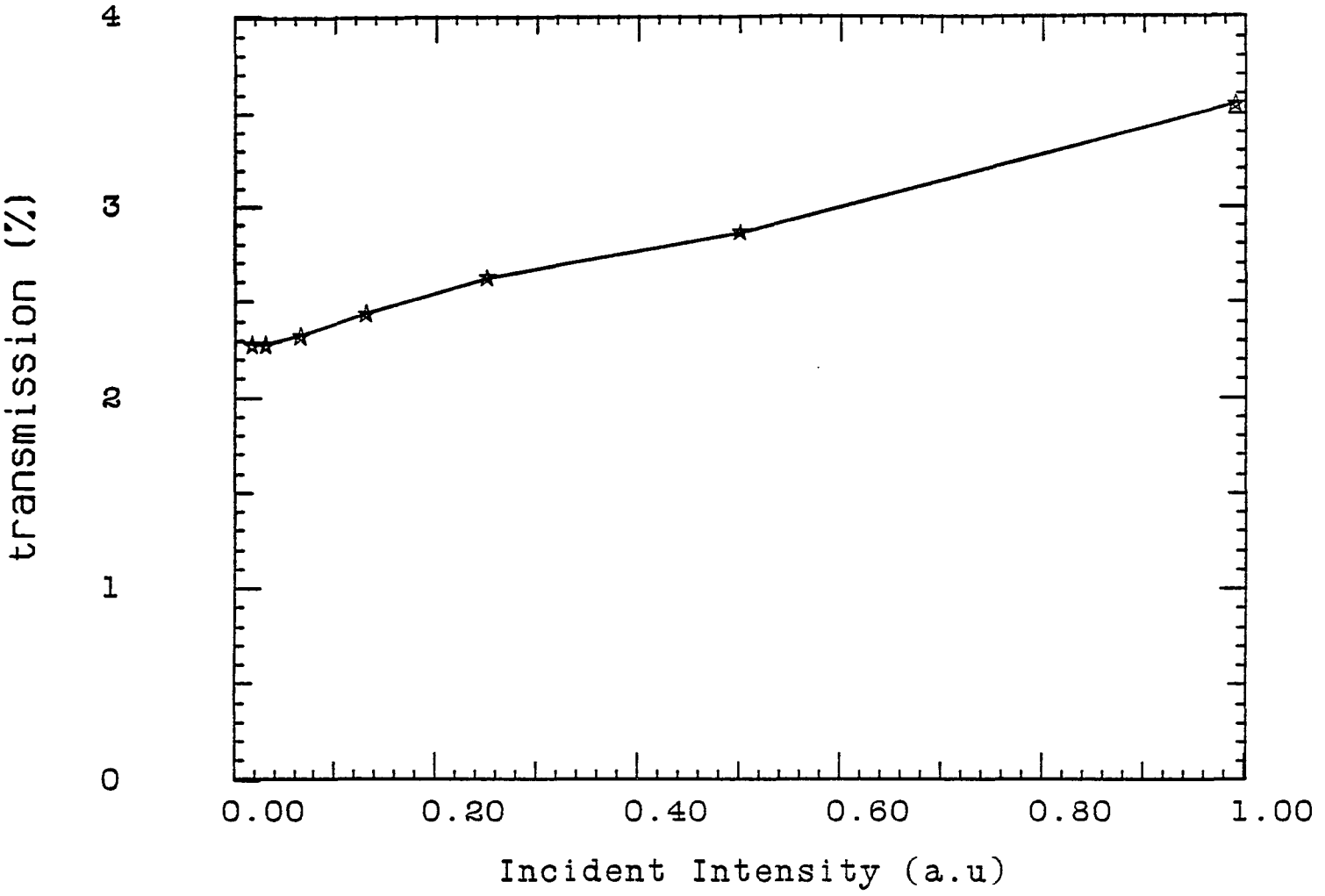

Figure 4.2.2. Transmitted intensity of pump pulse as a function of pump pulse intensity. The maximum pump fluence is 4×10^{-2} J cm^{-2} .

To ensure that the entire probe pulse was within the excited region, the probe pulse was focused to a smaller spot size than the pump spot size. An aperture, the size of the pump spot, was placed at the sample site and it was verified that the entire probe pulse was incident within the aperture. A more accurate test of the spatial overlap was then made. The transmitted intensity of the pump was measured as a function of incident pump intensity (fig. 4.2.2). The probe was blocked. The percentage increase in pump transmission, due to self bleaching, was equal to the change in transmission of the perpendicularly polarized probe (at the pump frequency) at zero time delay. The perpendicular polarization reduced the coherent artifact by a factor of $< 10^{-2}$. At zero time delay, the pump and probe pulses both see the same absorption coefficient and therefore the induced transmission changes [$\delta T/T$] for the probe and pump will be equal if the two are spatially overlapped.

4.2.3 Detection equipment - monochromatic probe

In pump and probe absorption with a broadband probe pulse, one has the option of monitoring the transmission at a fixed wavelength while varying the time delay. This can be repeated at different wavelengths. Alternately one can measure the entire transmitted spectrum at a fixed time delay and then repeat at other time delays.

Varying the time delay while fixing the probe wavelength gives more averaging and is better suited for studying the population at specific energies of interest; i.e. at the point were electrons would scatter back to the Γ-valley from the X or L-valleys. In this

technique it is much more difficult to determine the carrier distribution since fewer wavelengths are available. Additionally, data is taken over a longer period of time and long term laser fluctuations can distort the results. In this configuration the probe and reference pulses are focused into different spectrometers and detected by identical photomultipliers. The output voltages of the photomultiplier tubes were integrated by two identical gated boxcar integrator. The boxcars were manufactured by Stanford Research Systems Inc., model number SR280. The triggering of the boxcar gate was controlled by the circuitry that triggered the Nd:YAG laser. The jitter was less than 0.5 ns and if the laser did not fire, the boxcar would not be triggered. The gate width was set to 20 ns, which was wide enough to insure that the 10 ns wide output signal of the photomultiplier was entirely within the gate. The averaging time of the boxcars was selected by the number of triggering events rather than a fixed time constant so an equal number of laser pulses would be detected within each time constant. The averaging time was set in the range of 10 to 30 pulses. The temporal resolution of the detection apparatus is determined by the distance the stepping motor moves within the boxcar averaging time, in addition to the pulse width.

The analog output of the two boxcar integraters were directed to the input of a signal averager, Tracor Northern model number TN 1710. The signals were digitized and stored in memory. The signal averager had the capability to simultaneously digitize the two input signals and store them in separate memories. After each scan was completed, the data was transferred to a PC XT. The dwell time of the

signal averager was adjusted so that each scan took from 10 to 20 minutes. The number of scans averaged was between 4 (for 2.01 eV probe) and 16 (for the continuum probe).

The optical path delay was varied by a microprocessor controlled stepping motor, manufactured by Aerotech Inc. The stepping motor is model number ATS 302MM and the controller is a Unidex III. The Unidex III was programmed to trigger a signal averager scan at the start of each motor translation and to coordinate the motor speed with the signal averager dwell time and the number of motor sweeps with the number of scans. The Unidex was programmed to vary the motor translation speed during a scan. The motor was moved at a slower speed near zero delay to allow more averaging without broadening the temporal resolution beyond the pulse width within the first picoseconds. At greater delay times the motor speed was increased. This reduced temporal resolution but shortened averaging time and reduced the amount of data that had to be rejected due to long term fluctuations of the laser. The Unidex program also halted data acquisition and motor translation after each scan so data could be transferred to the PC XT.

The PC XT program to accept the data examined each individual data point of the reference signal. If it did not fall within predetermined limits that point was not included in the averaging. After the selected number of scans, the ratio of probe to reference was plotted on the monitor and the data could either be written to disk for further analysis or additional data could be collected. The

averaging program was weighted by the number of accepted data points so the rejected points did not influence the data.

4.2.4 Detection equipment - continuum probe

In the second technique the broadband probe and reference pulses are detected by an Optical Multichannel Analyzer with a flat field spectrometer. In this method one simultaneously measures $\delta\alpha$ over a broad energy range and then determines the excited carrier distribution. The measurements are repeated at different delay times between pump and probe.

In this technique, the probe and reference pulses were aligned parallel but at a different height, and focused into the slit of a flat field spectrometer and imaged onto two separate tracks of an Optical Multichannel Analyzer. A low resolution grating was selected to allow measurements to be taken in the range of 6000 Å to 7600 Å. The slit width was 250 μ; this sacrificed spectral resolution but insured that the entire probe and reference pulses were focused into the slit.

The OMA III is manufactured by Princeton Applied Research, model number 1460. The detector is a Silicon Intensified Target (SIT) camera with an S-20 response, model number 1254E. The controller for the SIT is model number 1216. The OMA detector has a 1 cm^2 target area. It can be divided into 500 channels vertically and 500 tracks horizontally. Each channel corresponds to different wavelengths. The spectral resolution of the OMA is determined by the spectrometer

grating and slit width, with the ultimate resolution of the OMA being 5 channels. The resolution of this system was 3 nm. The OMA detector was divided into 2 tracks, each 2 mm in height and separated by 3 mm. The Probe was imaged onto one track and the reference onto the other track. Care was taken to insure that the probe and reference did not overlap onto each other's track. A neon lamp was used to calibrate both tracks of the OMA. The collection optics, spectrometer and detector were aligned to insure that each channel corresponded to the same wavelength on both tracks. This was done to within an accuracy of less than 3 channels (1 nm). The number, size and positions of the active tracks is programmed using the OMA III operating system software.

Spectrum was taken at different delay times. At each delay, about 1200 laser pulses were averaged. The probe and reference were written to separate files on disk. At regular intervals, a background (dark current and ambient room light) curve and an unexcited transmission curve were taken.

Later, the data was transferred to a PC XT for processing. Software was used to correct for the small misalignment of the probe and reference tracks. The background signal was subtracted out and the probe signal was normalized to the reference signal. The data was then divided by the unexcited transmission data to give $(T+\delta T)/T$.

4.2.5 Measurement of pump pulse energy

For direct band to band photoexcitation, if free carrier and

two photon absorption is small, the number of electron-hole pairs produced is equal to the number of photons absorbed. Determining the number of absorbed photons involves measuring the pulse energy and spot size at the sample. The number absorbed is equal to the total number of photons less the number reflected and transmitted. Therefore, the laser pulse energy and spot sized were measured.

An accurate measurement of the femtosecond laser pulse energy is not easy. Most commercially available energy meters can not measure the combination of very high peak power (gigawatts) and very low average power (< 5 milliwatts) of femtosecond lasers operating at a few hertz. Pyroelectric detectors, which have a sensitivity of less than a microjoule damage at intensities greater than 10^6 watts cm^{-2}. They also pick up a large amount of noise (both optical and electronic) generated during the firing of the amplifier system and are therefore not suitable for measuring the pulse energy. Attempts to measure the pulse energy with a pyroelectric detector failed to give reasonable and consistent results. Volume calorimeters, which can handle large peak intensities as well as large average power, have a noise level of a few milliwatts. The average laser power is estimated to be on the order of 5 milliwatts (0.25 millijoules per pulse at 20 Hz). Measurements of pulse energy using a Scientech volume calorimeter gave an average pulse energy of 300 microjoules with an error or ± 300 microjoules and was therefore unacceptable for consistent or accurate measurements of pulse energy.

For consistent and accurate measurements of the pulse energy, a

photodiode was calibrated and used to measure pulse energy. The diode was a Hamamatsu vacuum photodiode, model R1328-03, with an S-20 spectral response. The photodiode is linear in incident pulse energy below its saturation level of 10 volts output. The diode was calibrated with the second harmonic output of a high powered modelocked ND:YAG laser. The infrared output of the Nd:YAG was blocked by filters and the output was adjusted to give a second harmonic of 5 millijoules per pulse (50 milliwatts average power). The output energy was measured by a Scientech volume calorimeter. A glass slide inserted in the laser, at close to normal incidence reflected 0.4 millijoules (4% from each surface) into the photodiode. Neutral density filters were placed in front of the photodiode to attenuate the light until the output voltage was 1 volt. A large number of ND filters (ND 50's and ND 70's) were used to slowly attenuate the laser rather then ND 3's which were more likely to be bleached. It was verified that the output voltage increased linearly when an ND filter was removed. This confirmed that the filters were not being bleached and that the output voltage was linear up to about 15 volts. The measured sensitivity of the photodiode at 5300 Å was 50 volts/microjoule. The calibration of the diode was uncorrected for its spectral response. At 6200 Å, the sensitivity of an S-20 detector falls by a factor of two from 5300 Å. The photodiode sensitivity was consistent with the calibration using the signal from the 114 MHz train. The cw power of the train was measured with a Newport power meter to be 9 milliwatts (80 picojoules per pulse) and the oscillator signal on the photodiode was 3-4 millivolts.

The pump pulse spot size at the sample site was accurately measured by replacing the sample with a razor blade mounted on a stepping motor. The pump intensity was measured as the razor blade was translated, first horizontally then vertically, in the plane of the sample. The horizontal and vertical spot sizes (from the 10% to the 90% transmission points) were 0.7 and 0.5 mm respectively. The total excitation area was 0.27 mm^2.

The maximum pump energy was 100 microjoules as measured by the calibrated photodiode. The number of photons in the pump pulse is 3 x 10^{14} photons. The reflected intensity was measured to be about 35% of the incident beam and the transmission is about 3% (under high excitation). The sample thickness is 0.75 μ (this is the thickness reported by the source of the samples. This is the same thickness as determined by steady state absorption using the absorption data reported by Sell and Casey.[41] Assuming uniform concentration through the sample, the density of photons absorbed is 10^{21} cm^{-3}. This carrier density is totally inconsistent with the experimentally determined carrier density of 2 x 10^{19} cm^{-3}. The discrepancy (a factor of 50) is far greater than can be accounted for by experimental error and I can offer no explanation. The thin (0.75 μ) sample and large (0.5 mm) spot size rule out diffusion as a mechanism for reducing carrier density.

4.2.6 GaAs sample description

The GaAs (sample #2) used in this experiment was 0.75 μ thick. The sample is p-type, doped 5 x 10^{17} cm^{-3}. The sample was grown by

molecular beam epitaxy with a 2 μ $Al_{.5}Ga_{.5}As$ cover layer on the front face and 1 μ layer on the back face. The sample was mounted onto a glass cover slip of approximately 100 μ thickness. The steady state absorption spectra is shown in chapter 2. The AlGaAs eliminated the surface states reducing surface recombination.

4.3 Time resolved absorption measurements with a monochromatic probe

4.3.1 Introduction

Time resolved absorption measurements were made on GaAs with 2.01 eV excitation. The excitation pulse excited carriers from the heavy-hole, light-hole and splitoff bands. The room temperature band gap is 1.424 eV. For the electrons excited from the heavy-hole band, the excess energy given to the electrons is 520 meV, and 66 meV is given to the holes; for excitation from the light-hole band, 432 meV is given to the electrons and 154 meV to the holes and for excitation from the splitoff band, 171 meV is given to the electrons and 74 meV to the holes. Electrons excited from the heavy-hole band have sufficient energy to scatter to the X-valleys (486 meV) by emission or absorption of a phonon. Electrons excited from the heavy-hole and light-hole bands have enough energy to scatter to the L-valleys (286 meV). About 80% of the total excess energy is given to the electrons and 20% to the holes. Data was taken with probe energies in the range of 1.75 eV to 2.01 eV.

4.3.2 Discussion of experimental data

The 2.01 eV time resolved transmission data at three different pump fluences (4×10^{-2} J cm^{-2}, 2×10^{-2} J cm^{-2} and 8×10^{-3} J cm^{-2}) is shown in figures 4.3.1 and 4.3.2 for parallel and orthogonally polarized pump and probe beams. The transmission data at probe energies of 1.75 eV and 1.82 eV are plotted in figures 4.3.3a, and b. Intervalley scattering, LO - phonon emission, e-e, h-h and e-h interactions all occur with in the pulse width. The rapid relaxation

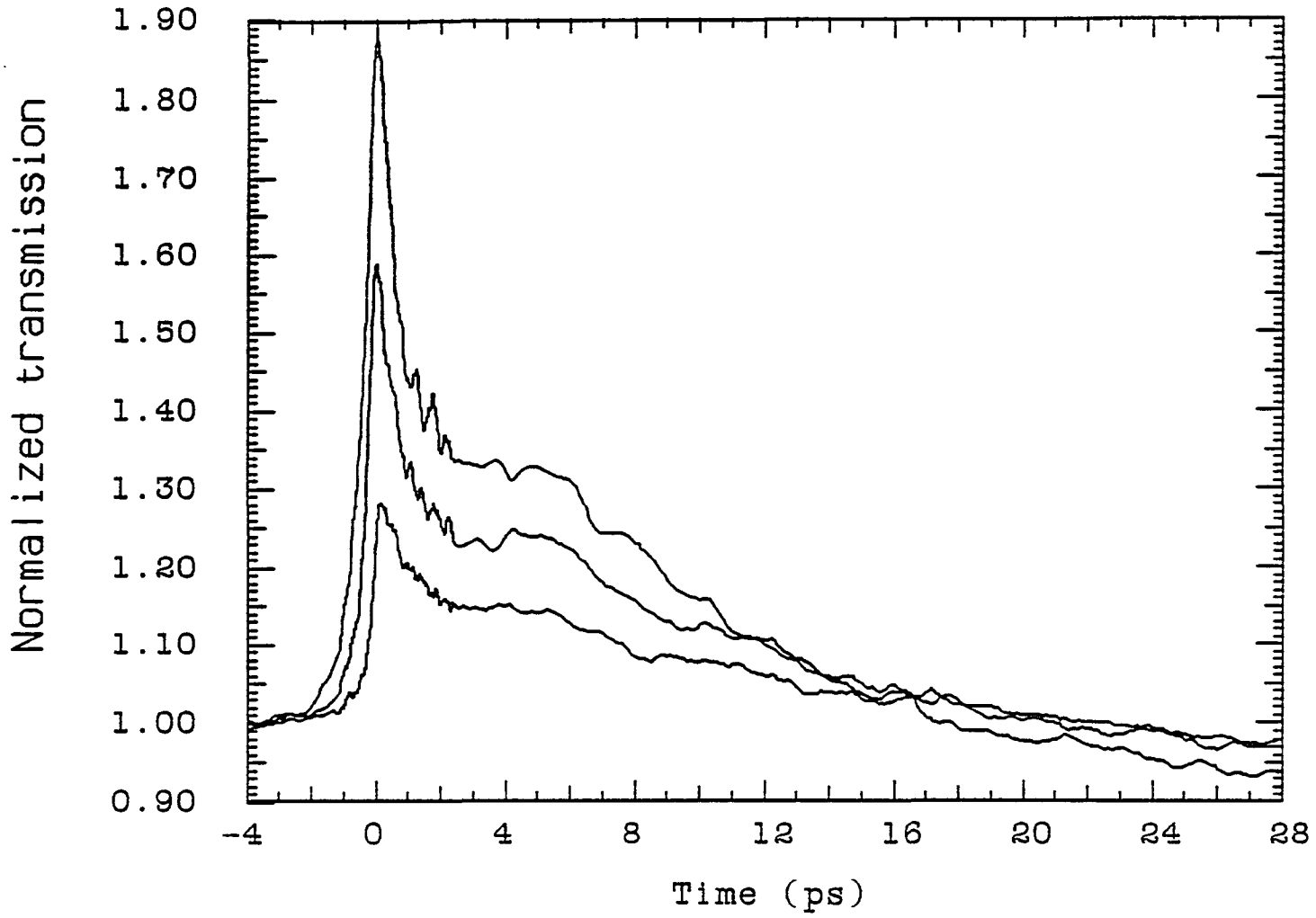

Figure 4.3.1. Time resolved transmission data at 2.01 eV for pump fluences of 4 x 10^{-2} J cm^{-2}, 2 x 10^{-2} J cm^{-2} and 8 x 10^{-3} J cm^{-2} at 2.01 eV. The pump and probe are parallel polarized.

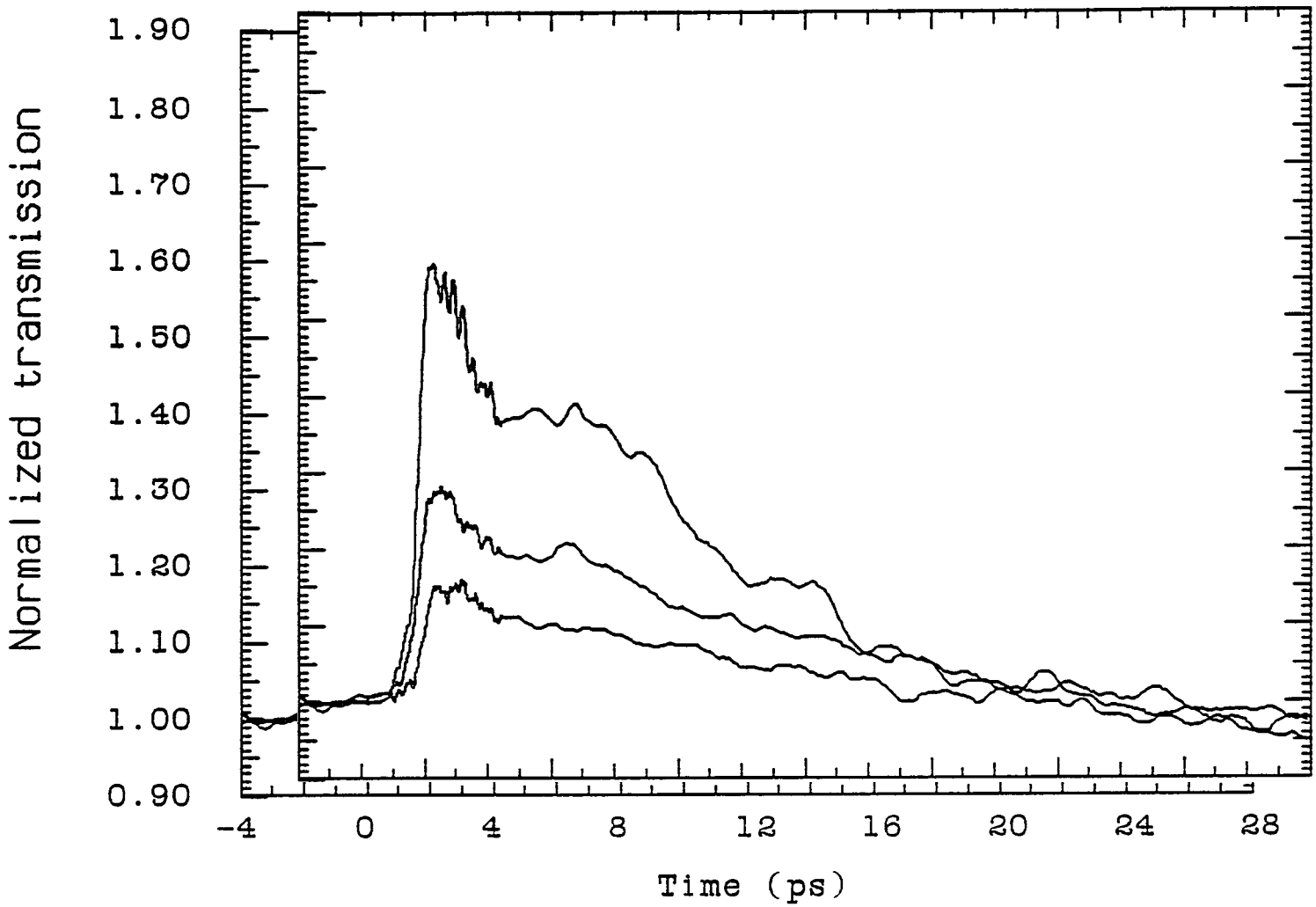

Figure 4.3.2. Time resolved transmission data at 2.01 eV for pump fluences of 4 x 10^{-2} J cm^{-2}, 2 x 10^{-2} J cm^{-2} and 8 x 10^{-3} J cm^{-2} at 2.01 eV. The pump and probe are orthogonally polarized.

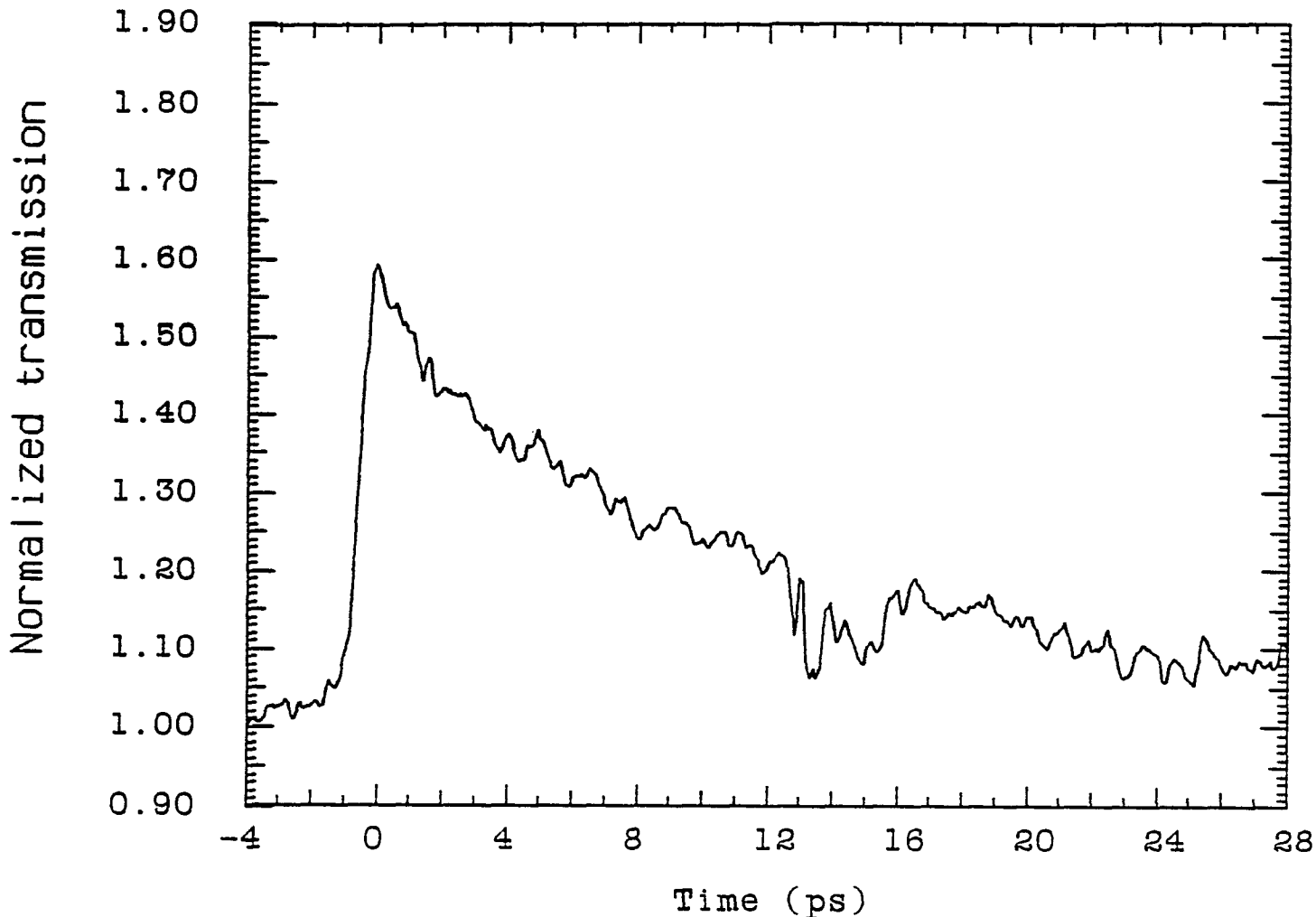

Figure 4.3.3a. Time resolved transmission data at 1.82 eV for a pump fluence of 4×10^{-2} J cm^{-2} at 2.01 eV.

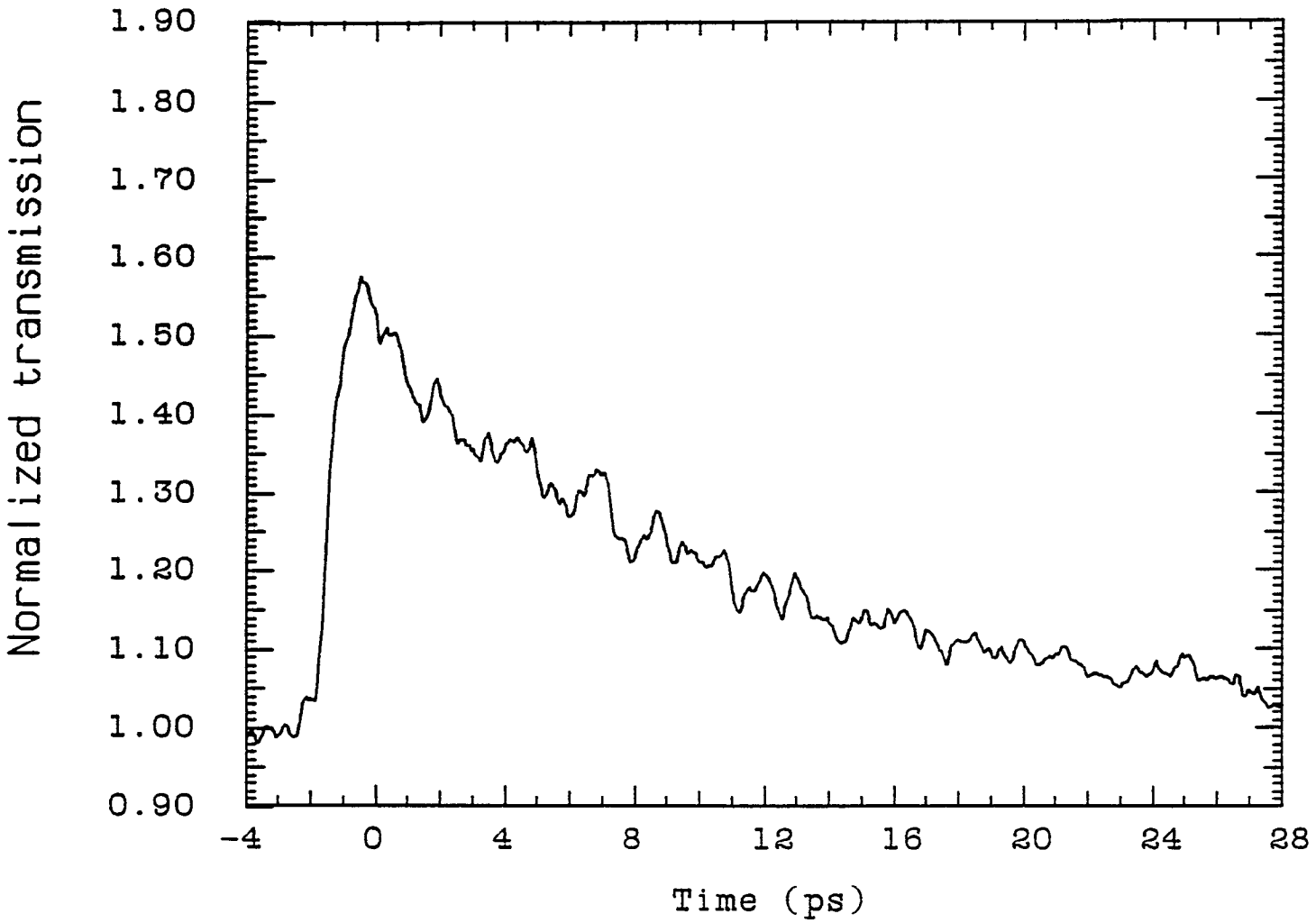

Figure 4.3.3b. Time resolved transmission data at 1.75 eV for a pump fluence of 4 x 10^{-2} J cm^{-2} at 2.01 eV.

in the initial 2 ps is a combination of e-h and h-e interactions cooling the electrons and heating the holes as well as energy loss to the lattice and intervalence band scattering of holes from the splitoff to the heavy-hole band. The longer relaxation is the result of carrier cooling, recombination and increased absorption resulting from increased band gap renormalization as the carriers cool.

Within the first 0.5 psec, the coherence spike is clearly evident in the parallel polarization data but not in the orthogonally polarized data. At $t = 0$, δT is approximately linear with pump intensity, the coherence spike does not have the expected quadratic dependence on I_{pump} of four-wave mixing. This departure from quadratic dependence is the result of large changes in both the real and imaginary parts of the index of refraction and is discussed in detail in chapter 5 of this thesis.

The increase in transmission after 4 ps is clearly evident in all data taken with a degenerate pump and probe and is not evident at the other probe energies. Since this increase in transmission occurs only at this probe energy it can not be explained by changes in the temperature or density of the distribution. This transmission increase has not be reported in other absorption work on GaAs.

At delay times greater than about 20 ps, the normalized transmission falls below unity ($\delta\alpha > 0$) This increase in absorption is the consequence of band gap renormalization. The data taken with a higher intensity pump exhibits a greater absorption increase due to

band gap renormalization.

The temperature dependence of the induced change in transmission at 2.01 eV has been calculated in GaAs over a range of densities consistent with the experimental results and shown in figures 4.3.4a,b through 4.3.6a,b. The calculations are done with the splitoff band transitions taken to be 18%, 9% and 0% of the absorption coefficient at 2.01 eV. In figures 4.3.4a, 4.3.5a and 4.3.6a, band gap renormalization has been neglected. In figures 4.3.4b, 4.3.5b and 4.3.6b, the transmission change is calculated from Eq. 4.1.19 with the change in band gap due to renormalization assumed to be independent of carrier temperature. The electron and hole densities are taken to be equal. These results are not very dependent on carrier temperature and inconsistent with the experimental data (see figures 4.3.1 and 4.3.2 although the calculated transmission changes are on the same order as those observed. A better model would require including a temperature dependent δE_g, as well as allowing the electron and/or hole concentrations to change on a ps time scale. The greater inconsistency is between the carrier density inferred from the measured δt ($\approx 10^{19}$ cm^{-3}) compared to the carrier density determined by the number of photons absorbed ($>5 \times 10^{20}$ cm^{-3}).

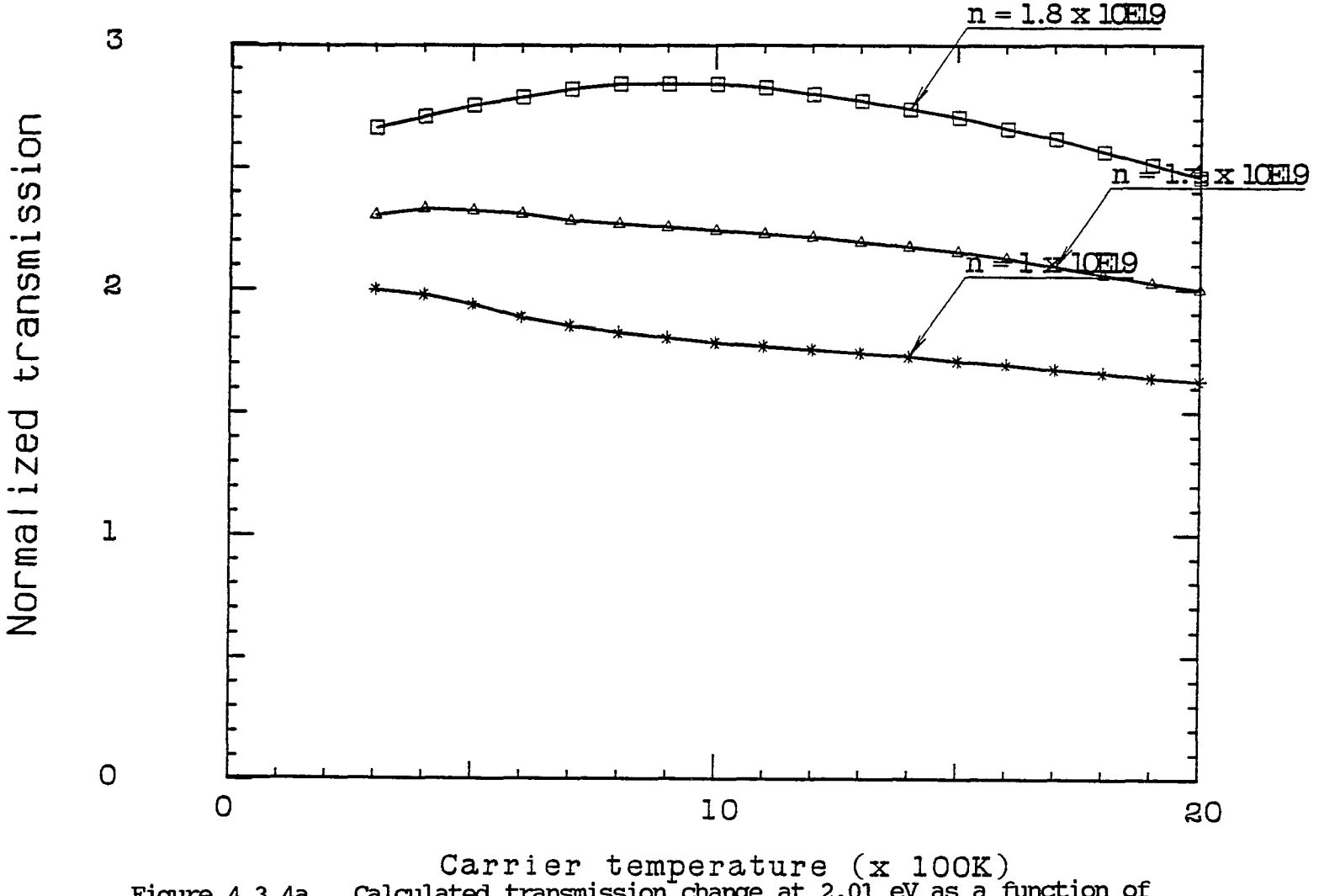

Figure 4.3.4a. Calculated transmission change at 2.01 eV as a function of T_c. Split-off band transitions are assumed to account for 18% of the unexcited absorption coefficient. Band gap renormalization is not included.

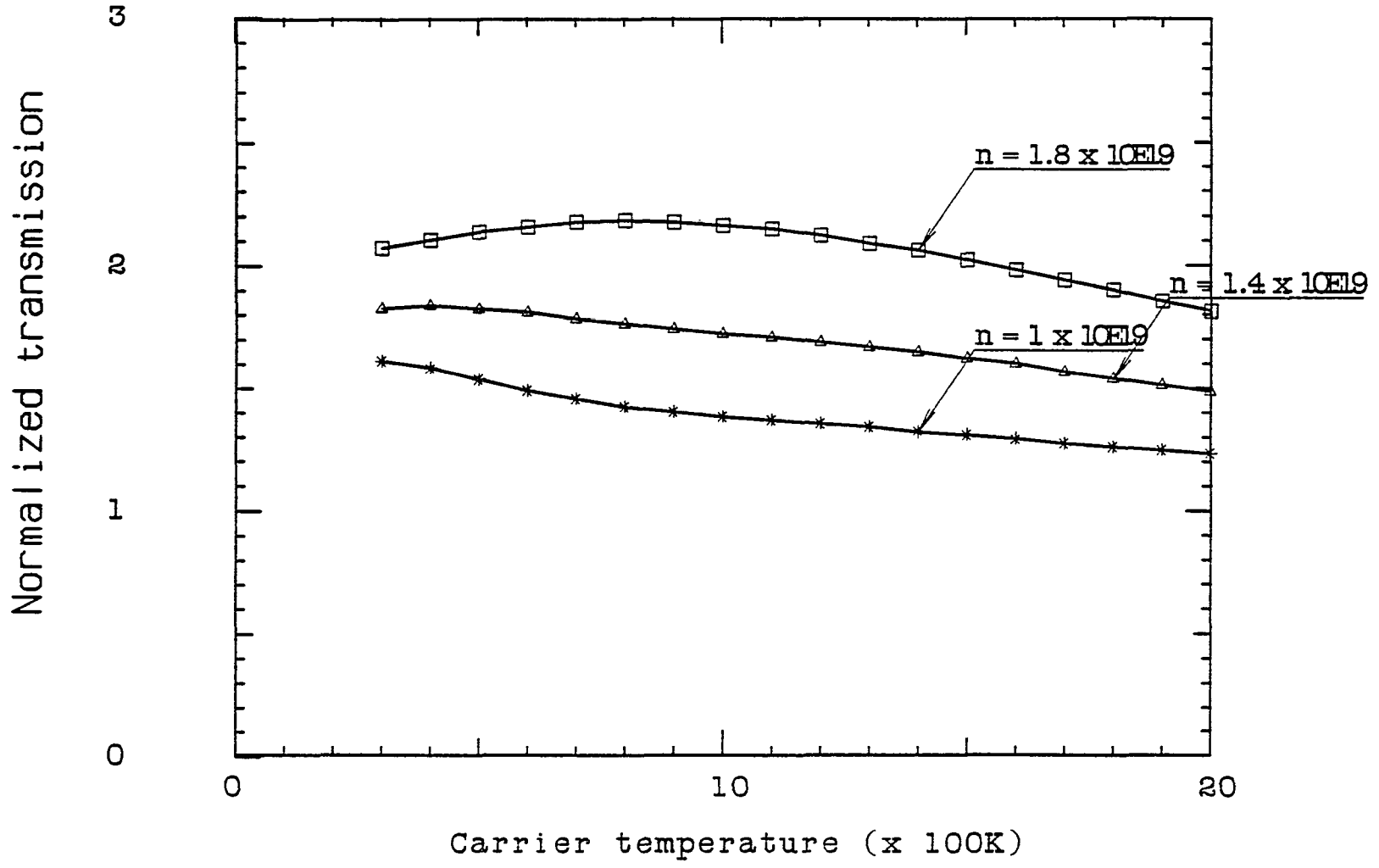

Figure 4.3.4b. Calculated transmission change at 2.01 eV as a function of T_c. Split-off band transitions are assumed to account for 18% of the unexcited absorption coefficient. Band gap renormalization is included.

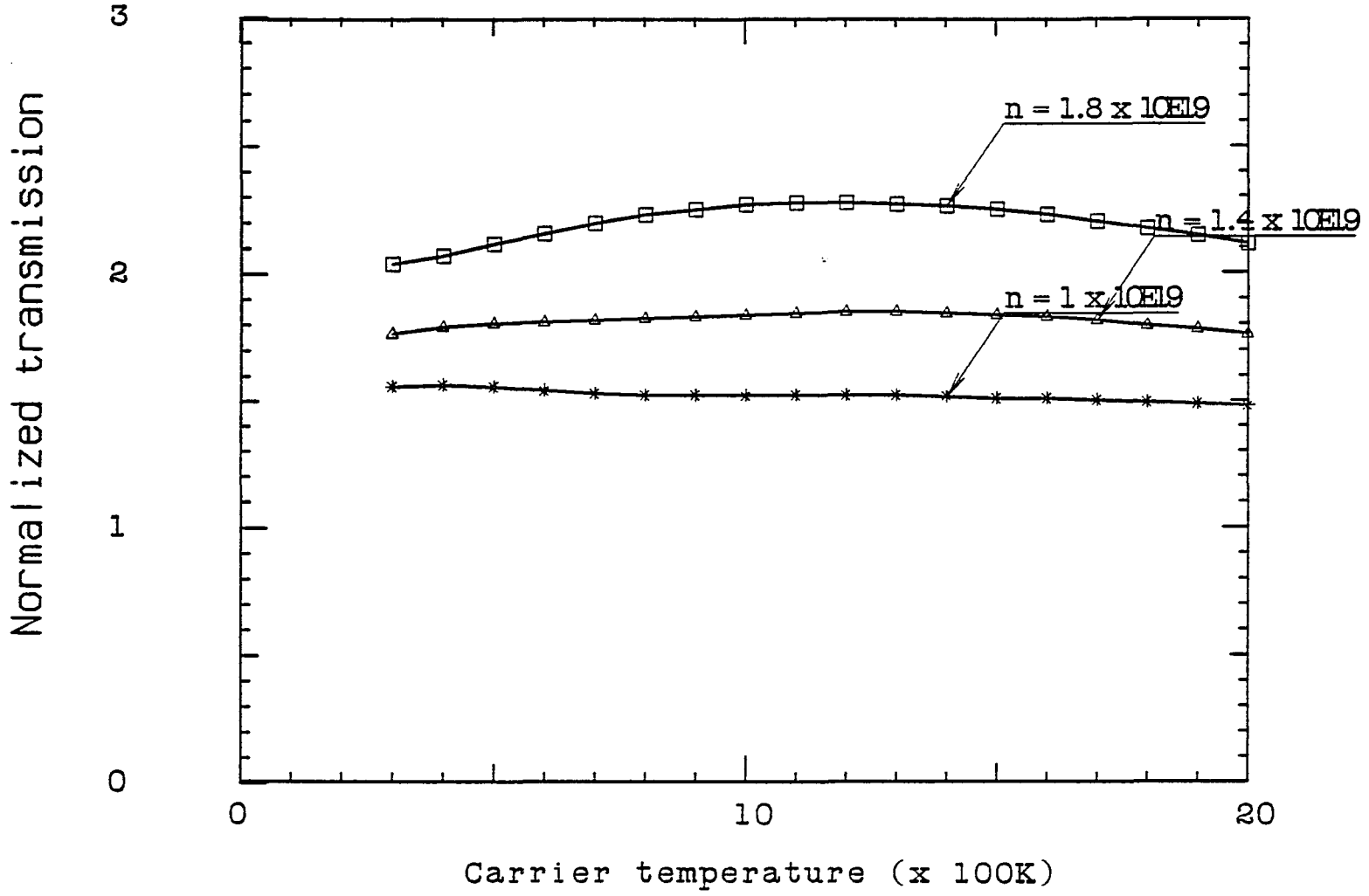

Figure 4.3.5a. Calculated transmission change at 2.01 eV as a function of T_c. Split-off band transitions are assumed to account for 9% of the unexcited absorption coefficient. Band gap renormalization is not included.

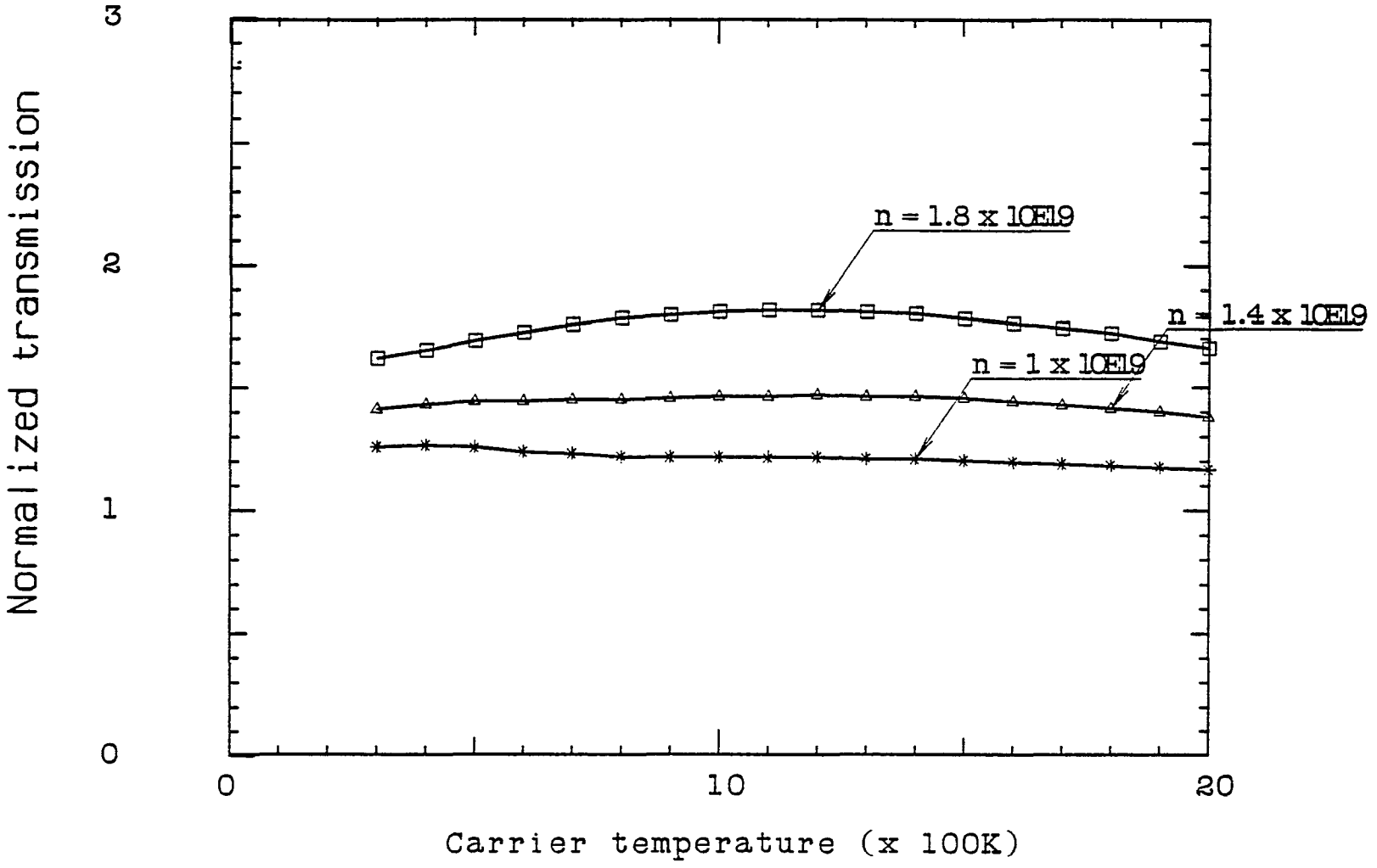

Figure 4.3.5b. Calculated transmission change at 2.01 eV as a function of T_c. Split-off band transitions are assumed to account for 9% of the unexcited absorption coefficient. Band gap renormalization is included.

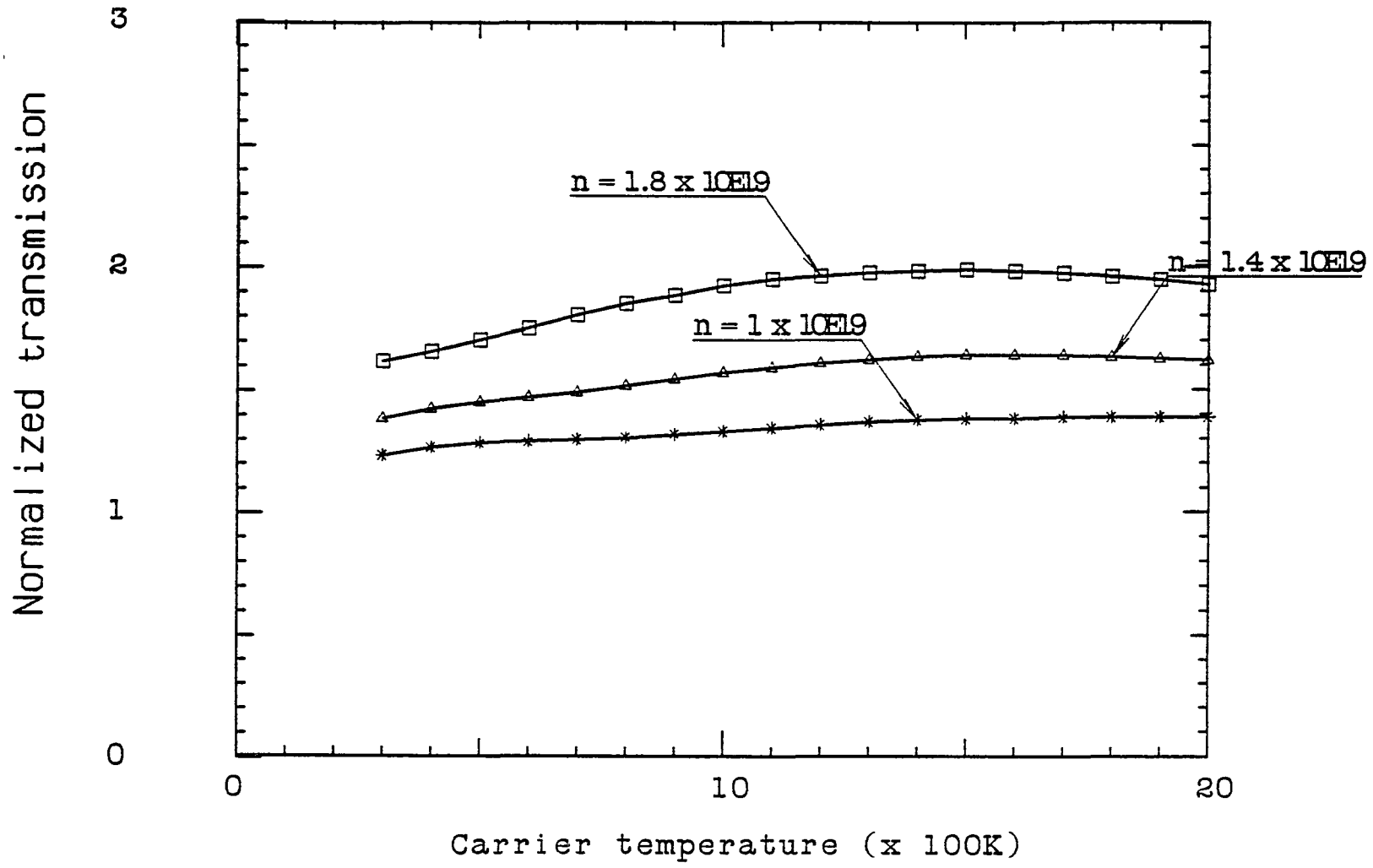

Figure 4.3.6a. Calculated transmission change at 2.01 eV as a function of T_c. Split-off band transitions are neglected. Band gap renormalization is not included.

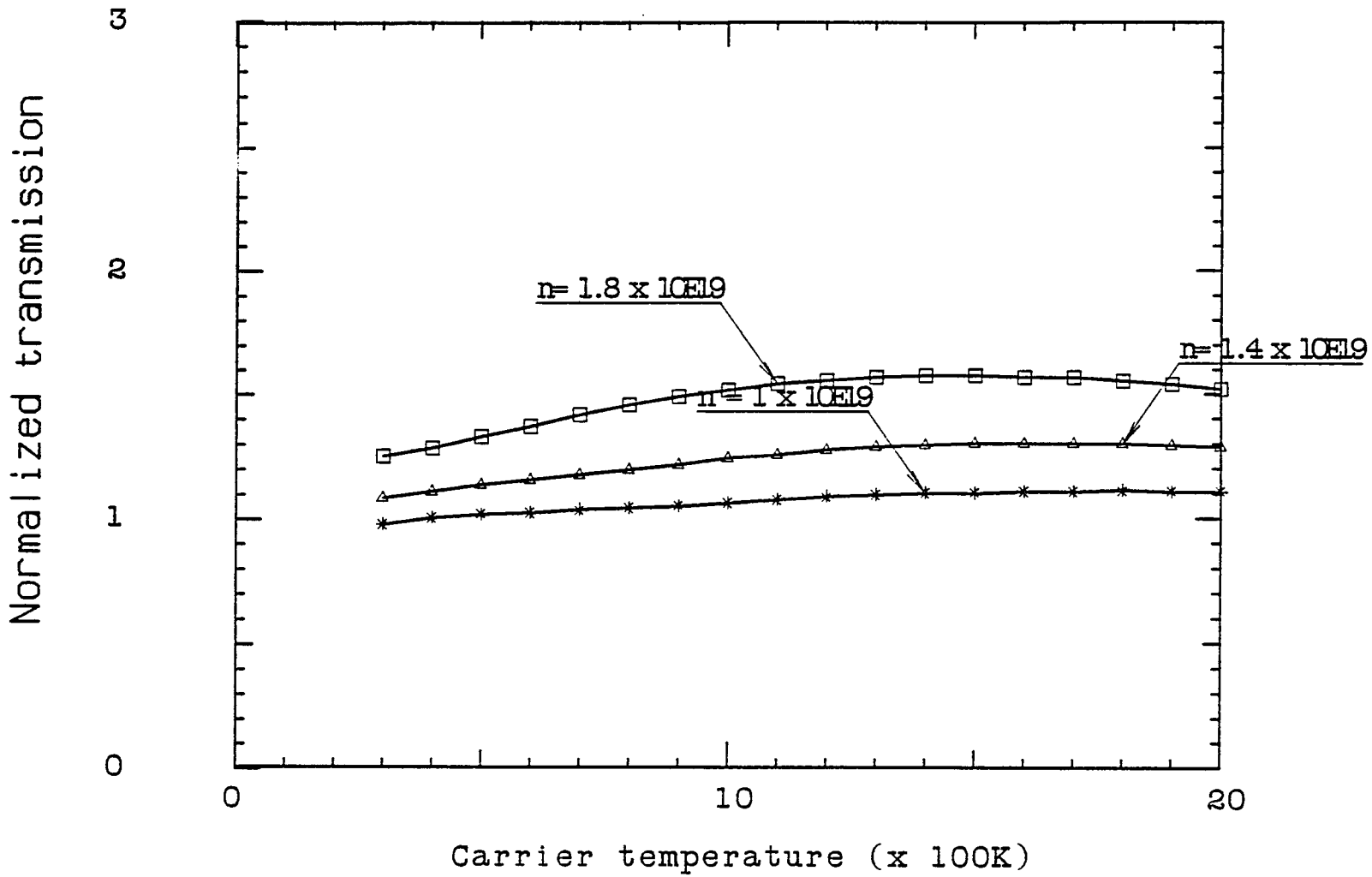

Figure 4.3.6b. Calculated transmission change at 2.01 eV as a function of T_c. Split-off band transitions are neglected. Band gap renormalization is included.

4.4 Time resolved measurements of the carrier distribution function

4.4.1 Direct experimental evidence of a non-thermal carrier distribution function

As discussed in section 4.1.2, the induced absorption changes allow a determination of the carrier distribution function. In this section, the results of time resolved absorption measurements, taken at room temperature in GaAs over the energy range of 1.6 to 2.0 eV, are presented and discussed. The excited transmission at probe delays of -117, +117, +500, and +833 femtoseconds are shown in figures 4.4.1a through 4.4.1d in the energy range of 1.63 to 2.00 eV. The respective carrier populations ($F_e + F_h$) as calculated from eq 4.1.20 for a parabolic conduction band and a single parabolic valence band are shown in figures 4.4.2a through 4.4.2d. The value of α_o was that measured in chapter 2.4. At the high carrier temperatures encountered in the first picosecond, the change in band gap because of renormalization is small and therefore, are not included in these calculations.

The most evident fact in the distribution function at earlier delay times, is that it is neither Maxwellian nor Fermi-Dirac like. In fact the occupation number is greater at higher energy states than at lower energy states. Although the distribution function has evolved from a δ-function like distribution on a faster time scale than the resolution of the experiment, at this density ($>10^{19}$) the distribution does not obtain a Fermi-Dirac like distribution until 800 fs after excitation. The distribution evolves by e-e, h-h, h-e and

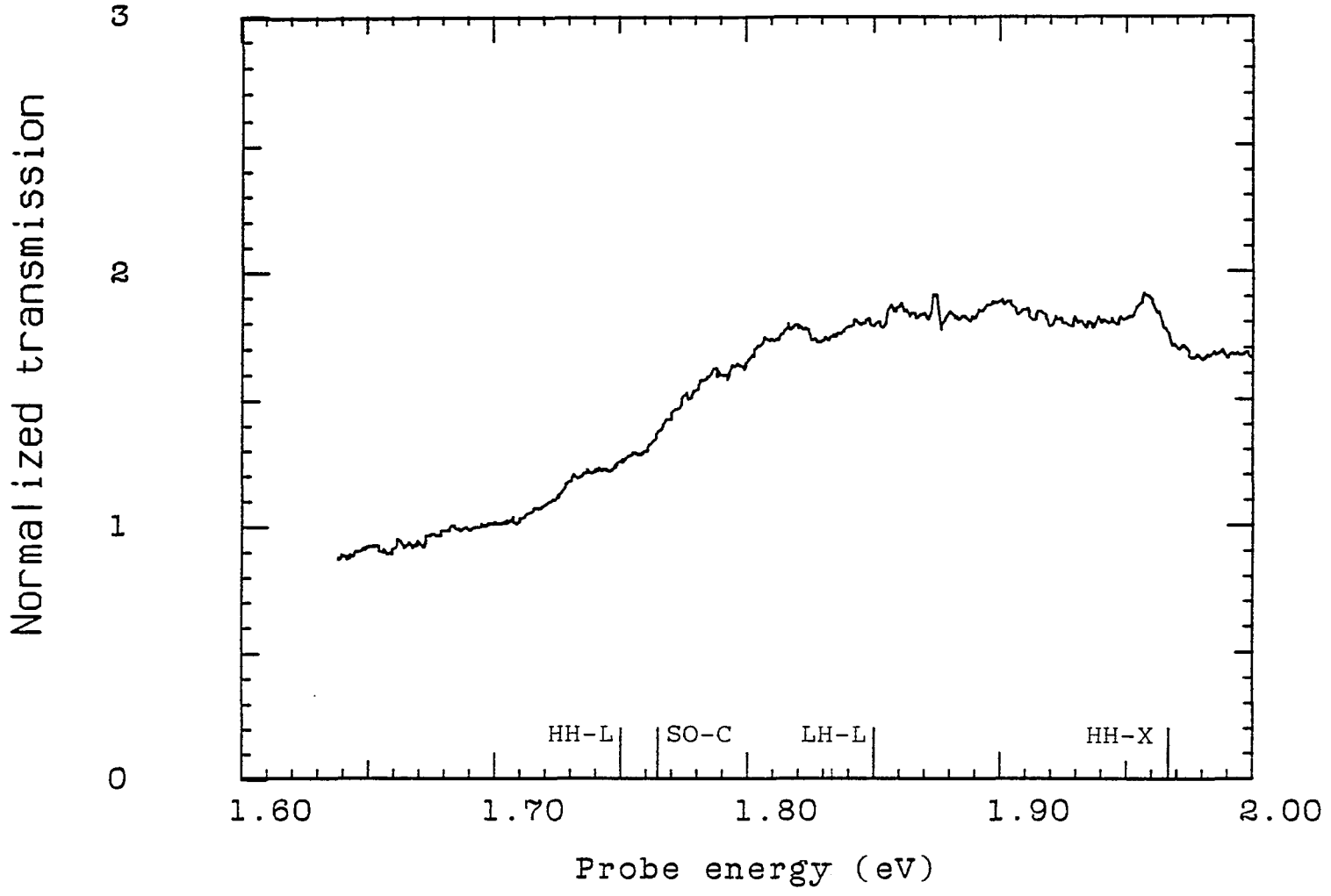

Figure 4.4.1a. Normalized transmission at a delay time of -117 fs.

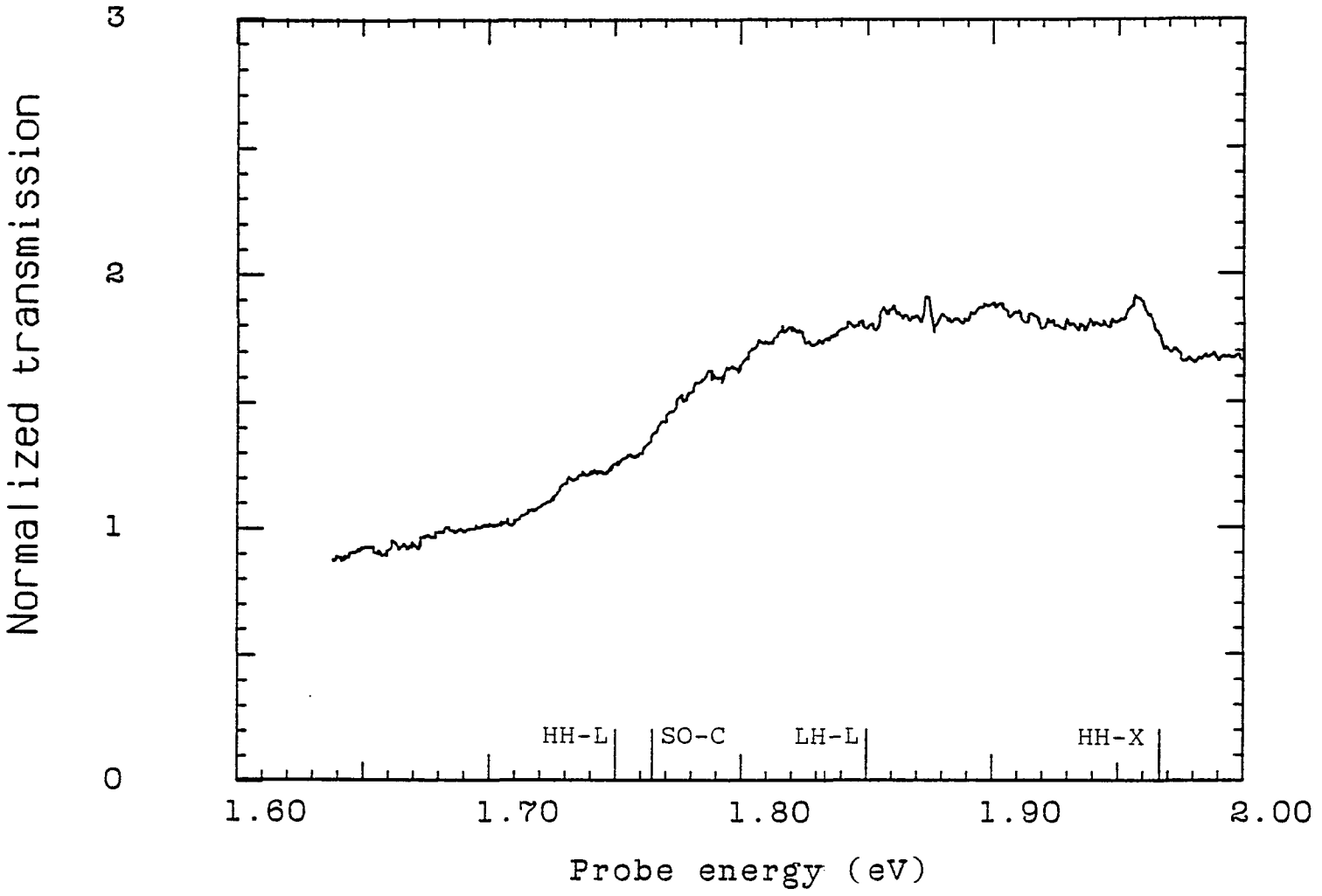

Figure 4.4.1b. Normalized transmission at a delay time of +117 fs.

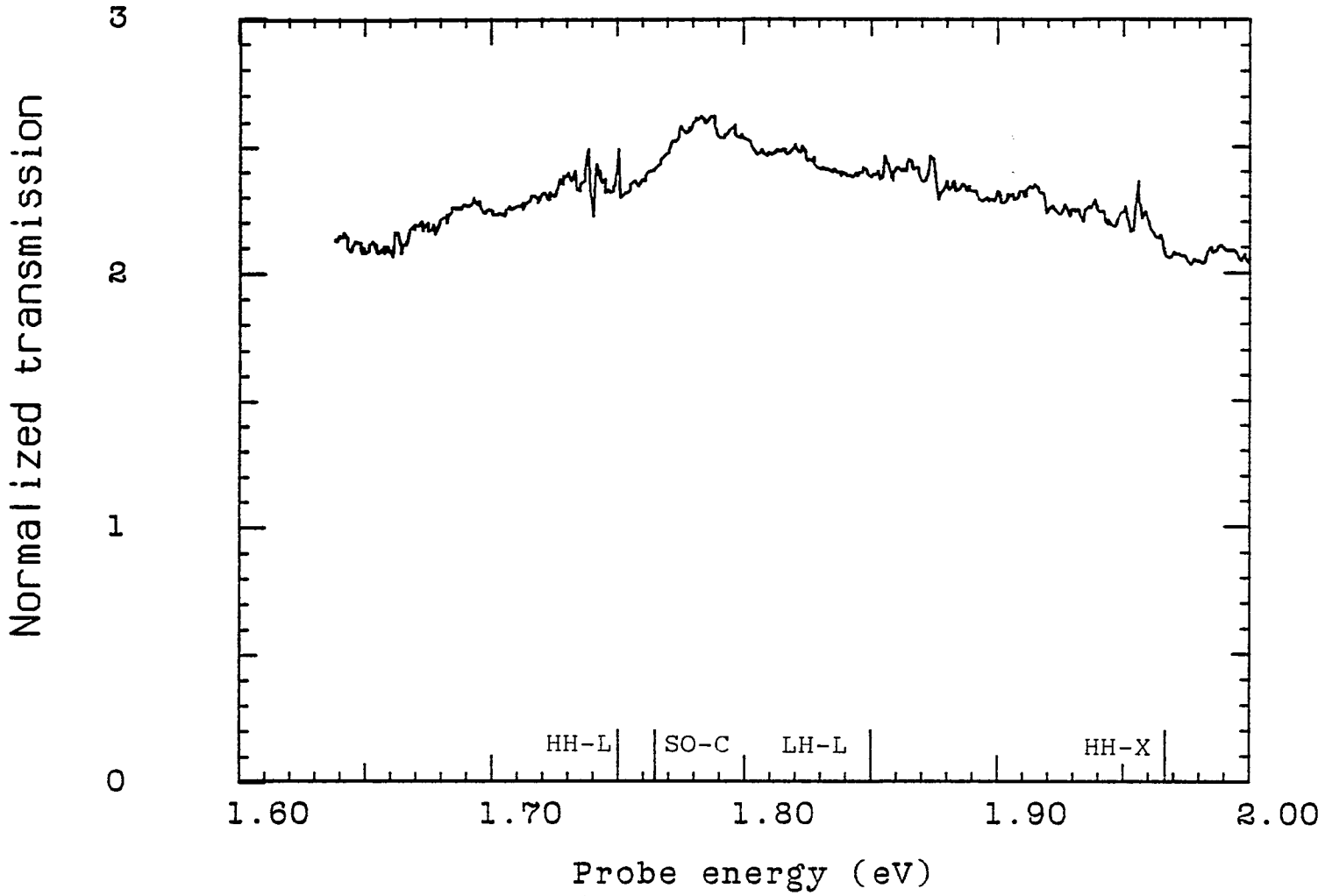

Figure 4.4.1c. Normalized transmission at a delay time of +500 fs.

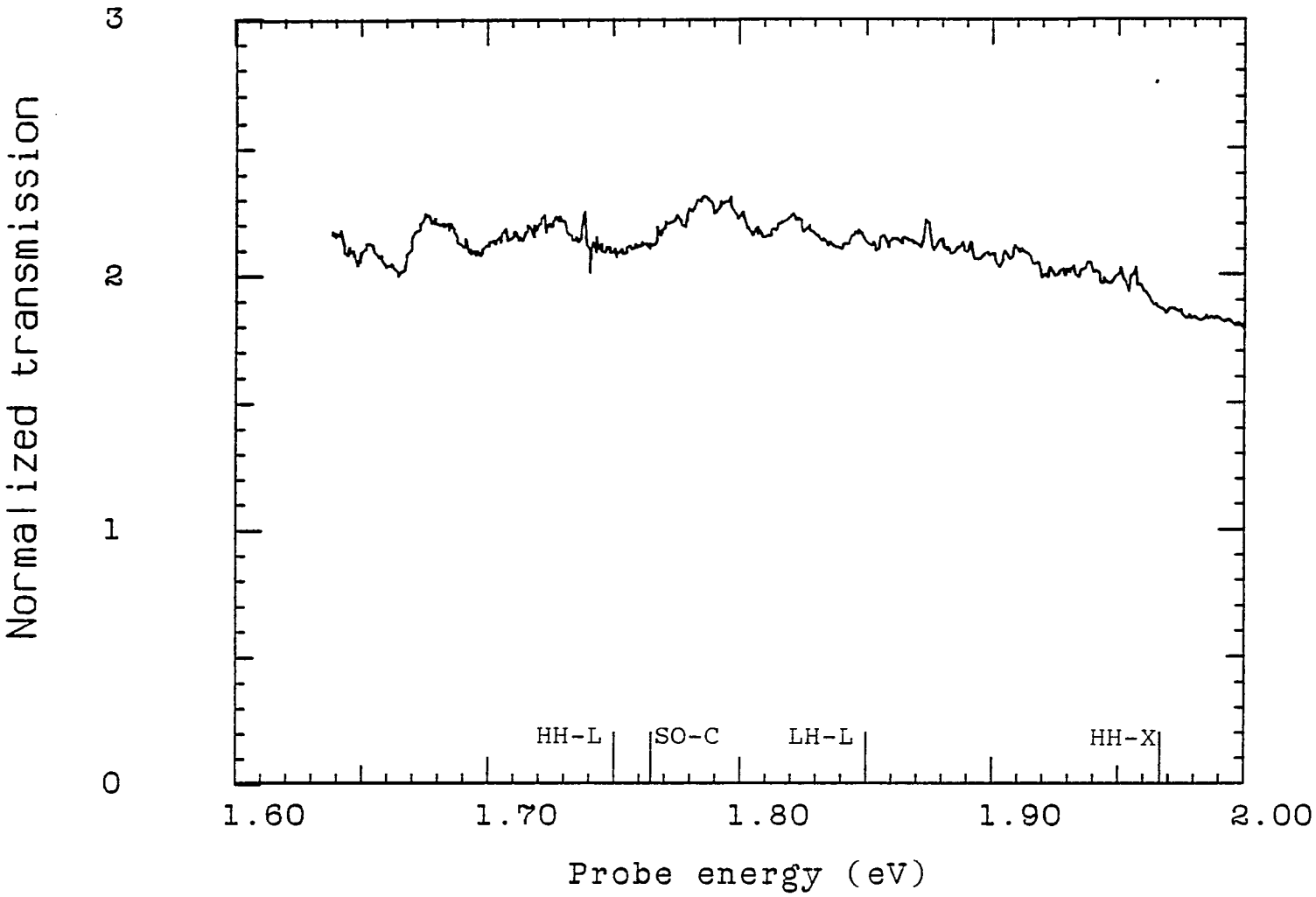

Figure 4.4.1d. Normalized transmission at a delay time of +833 fs.

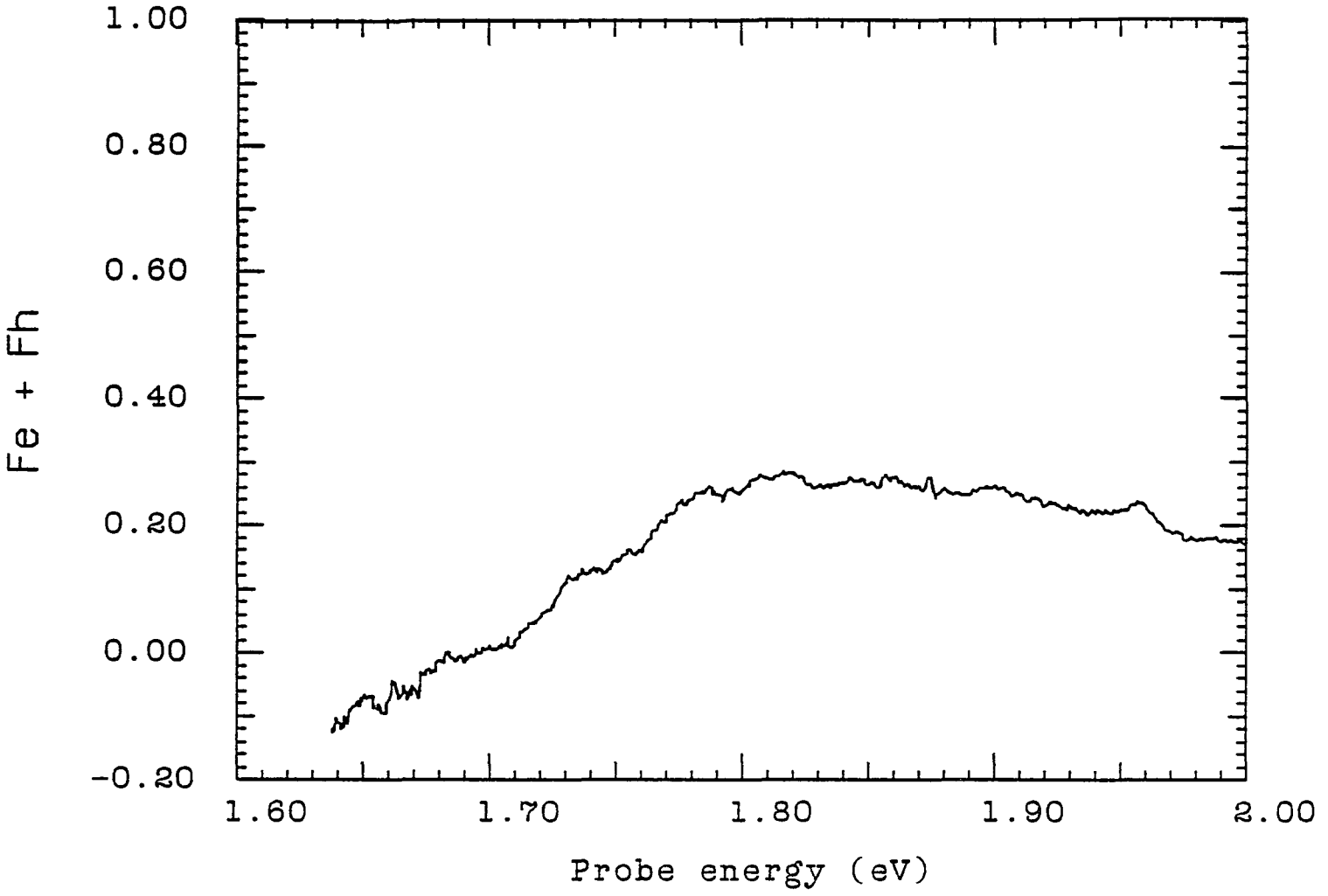

Figure 4.4.2a. Fermi factors ($f_e + f_h$) at -117 fs delay, assuming single parabolic conduction and valence bands. Band gap renormalization is not included in calculations.

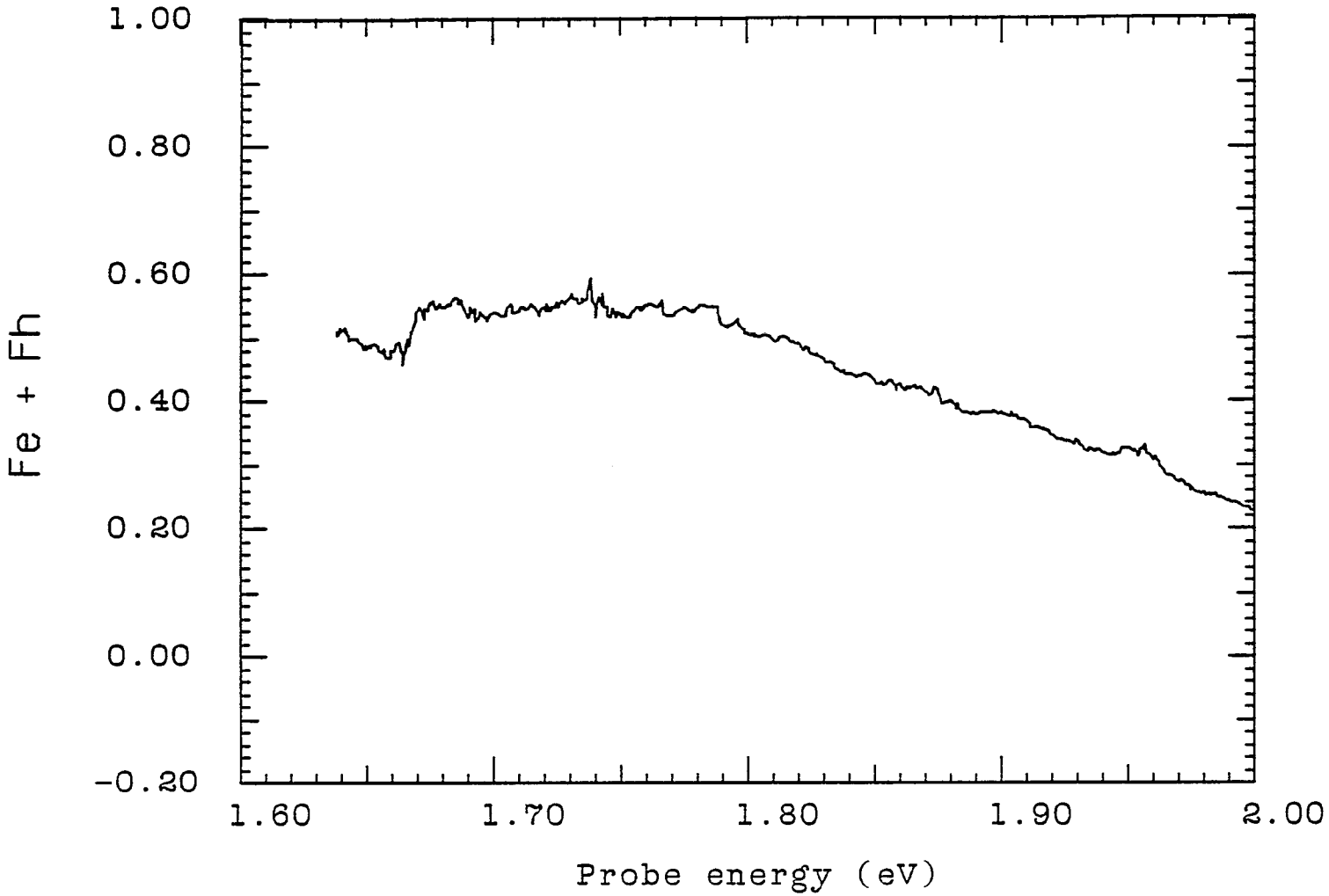

Figure 4.4.2b. Fermi factors ($f_e + f_h$) at +117 fs delay, assuming single parabolic conduction and valence bands. Band gap renormalization is not included in calculations.

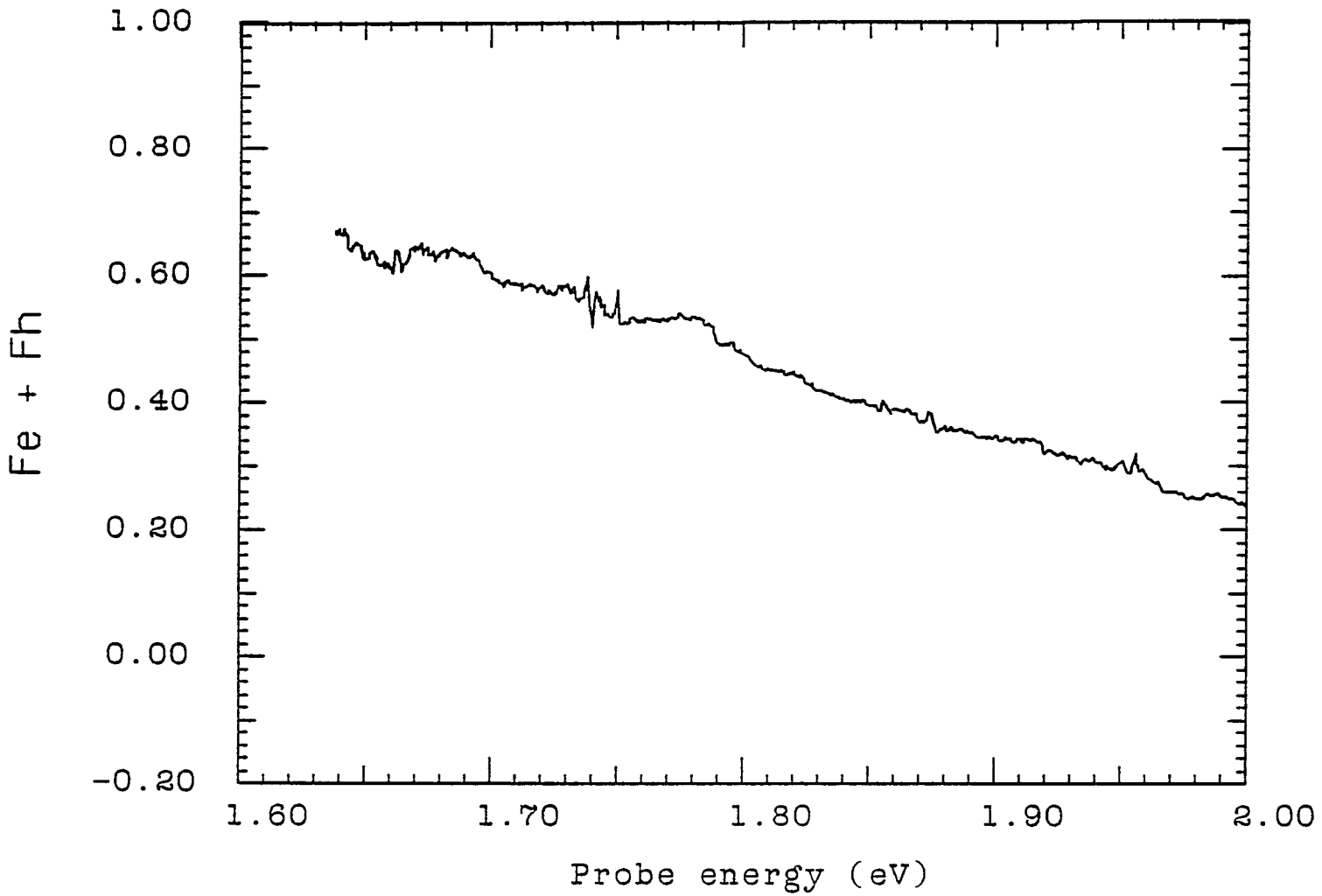

Figure 4.4.2c. Fermi factors ($f_e + f_h$) at +500 fs delay, assuming single parabolic conduction and valence bands. Band gap renormalization is not included in calculations.

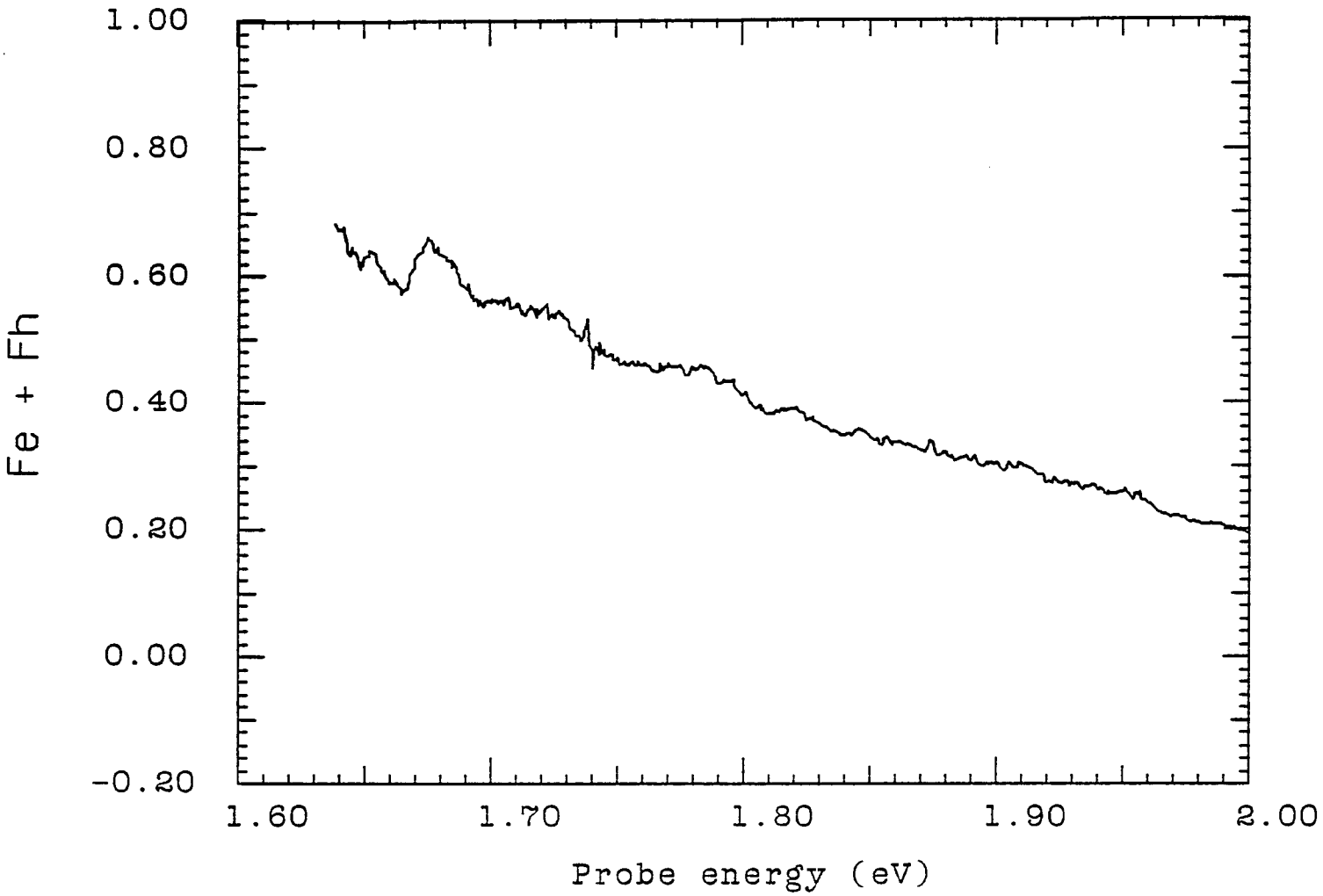

Figure 4.4.2d. Fermi factors ($f_e + f_h$) at +833 fs delay, assuming single parabolic conduction and valence bands. Band gap renormalization is not included in calculations.

e-h scattering. These scattering times were not resolved in this experiment but other experimental work[29-36] have measured these times to be on the order of tens of femtoseconds.

My results show that a thermalized distribution forms on a slower time scale then the e-e or h-h scattering times because it takes many carrier scattering events to form a thermalized distribution. The data taken at 1.17 ps delay can be fitted by a Fermi-Dirac distribution with an electron quasi-Fermi level of 230 meV, a hole quasi-Fermi level of 200 meV and a carrier temperature of 1400 ± 100 K (see figure 4.4.3). The corresponding carrier densities are $n_e = 1.25 \pm .1 \times 10^{19}$ cm^{-1} and $n_h = 1.9 \pm .2 \times 10^{19}$ cm^{-3}. In order to fit the data at any carrier reasonable temperature, the contribution to $\delta\alpha$ from splitoff band transitions had to be reduced by a factor of 2 for all probe energies.

A more accurate fitting routine would require including band non-parabolicity into calculations of density of states and higher order corrections to the Kane band model in determining the optical matrix elements and band gap renormalization. The effect of these corrections would probably be less than the errors introduced by the poor signal to noise of the data and would not change the central thesis of this work showing the non-thermal distribution in the first 800 fs of excitation.

Other significant features include an increase in the bleaching at probe energies greater than 1.765 eV; a bump in the transmission at

1.96 eV and a decrease in transmission above 1.97 eV. An accurate understanding of this data requires inclusion of the light-hole, splitoff and heavy-hole valence bands as well as the L and X-valleys of the conduction band.

The range of probe energies was such that conduction band states, in the Γ-valley, above and below transitions from the splitoff band (1.765 eV) were interrogated as well as those states in the Γ-valley degenerate with the X and L-valleys. The probe energy corresponding to splitoff band edge transitions is marked on figs. 4.4.1a-d as SO-C. The probe energies for transitions from the heavy-hole and light-hole bands to the conduction band degenerate with the X and L-valley minima are also shown as HH-L (1.75 eV), HH-X (1.97 eV), and LH-L (1.85 eV). LH-X is greater than 2.0 eV and therefore not shown on these figures.

The increase in the transmission at probe energies greater than 1.76 ev is evident in figs. 4.4.1a-d. This increase is explained by a contribution from the splitoff band. The splitoff contribution is greater at earlier time delays when there is still a significant hole population in the splitoff band. The initial kinetic energy given to the holes in the splitoff band is about the same as the heavy-hole band (75 mev). The initial density of holes in the splitoff band is determined by the optical matrix element coupling the splitoff and conduction bands and the joint density of states which depends on $\mu_r^{3/2}$ (μ_r = 0.056 m_o for heavy-hole-conduction band and 0.044 m_o for splitoff-conduction band). However, the density of states in the

valence bands depend on $m_h^{3/2}$ (m_h 0.5 m_o for the heavy-hole and 0.145 m_o for the splitoff band). Therefore, initially splitoff band states have a higher probability of being occupied than the heavy-hole and light-hole and the splitoff transitions are more strongly bleached. This is why for small time delays (fig. 4.4.1a and 4.4.1b at -117 and +117 fs) the splitoff contribution is greater than at longer time delays. As the holes scatter to the other valence bands the relative hole contribution of the splitoff band to the bleaching decreases to almost zero as the holes in the three valence bands reach equilibrium. The bleaching of the splitoff-conduction band transition at longer time delays is due only to electrons.

The bump in the transmission at 1.96 eV indicates an increase in the electron population at 0.470 eV above the bottom of the conduction band. This is the approximate energy of electrons scattering back from the X-valleys to the Γ-valley. It is also one phonon energy below the pump energy. At small time delays, this increase in the population at this energy is the result of excited electrons emitting an LO-phonon. At longer delays the increase is from electrons scattering back from the X-valleys. The decrease in transmission above 1.97 eV is also an effect of intervalley scattering. This decrease in transmission indicates that the high energy electrons scatter to the side valleys at a faster rate than the rate at which they maintain a Fermi-Dirac distribution.

A more accurate interpretation of the data would require increased time resolution and an extension of the range of probe

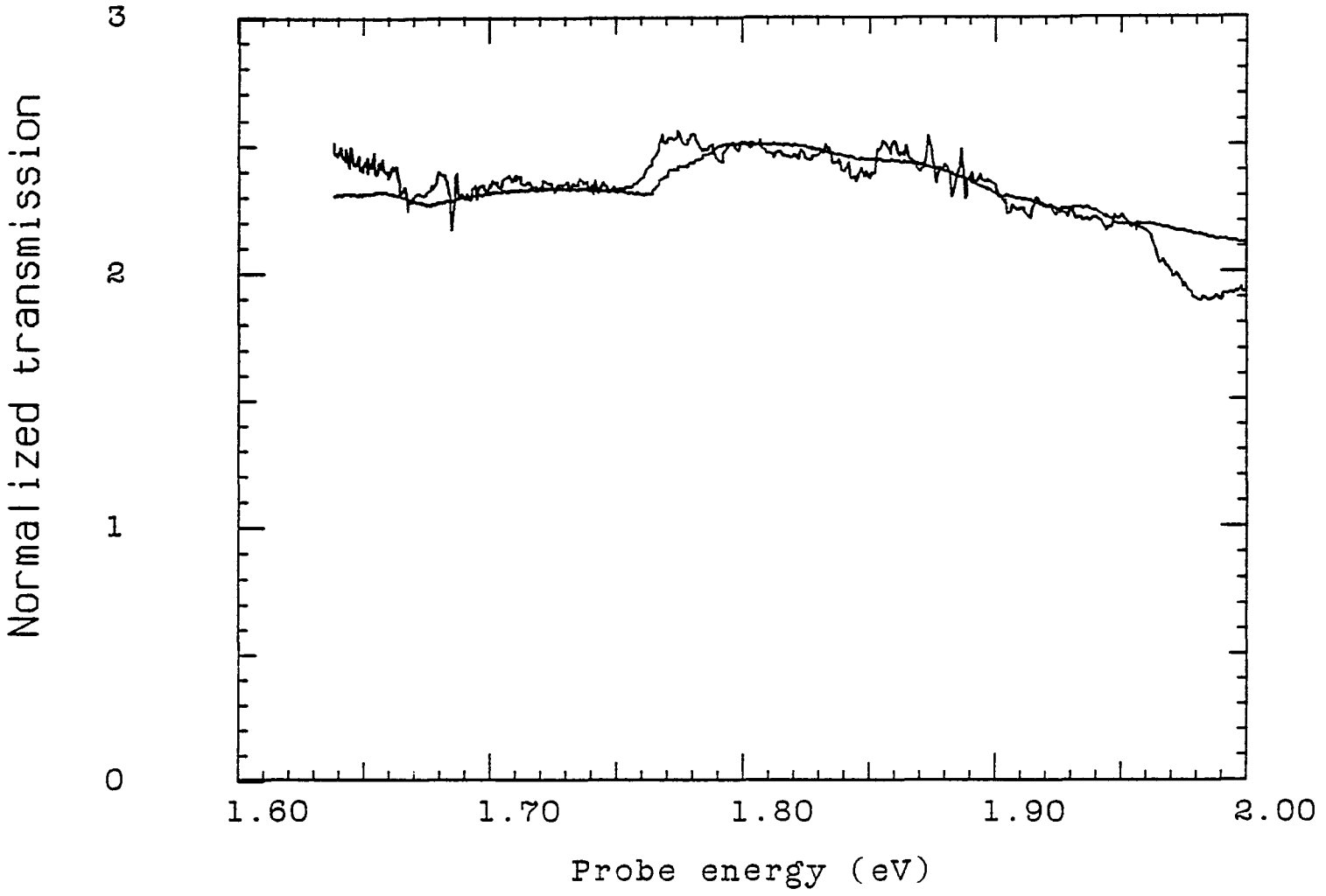

Figure 4.4.3. Normalized transmission at 1.17 ps and the transmission calculated for a Fermi-Dirac distribution at 1400 K and quasi-Fermi levels, μ_e = 230 meV (n_e = 1.25 x 10^{19} cm^{-3}) and μ_h = 200 meV (n_h = 1.9 x 10^{19} cm^{-3}). Band gap renormalization is not included in calculations.

energies to both higher and lower energies. The data could then be compared to Ensemble Monte Carlo results to better understand carrier-carrier and intervalley scattering. By studying other III-V semiconductors such as $Al_xGa_{1-x}As$, splitoff band transitions and/or intervalley scattering can be eliminated at the pump energy, simplifying the analysis of the data and allowing for a more accurate determination of the different carrier scattering mechanisms.

4.5 Notes

[1]E. M. Conwell, **Solid State Physics Supplement 9**, (Academic, 1967).

[2]W. Fawcett, A. D. Boardman and S. Swain, J. Phys. Chem. Sol. **31**, 1963 (1970).

[3]B. R. Nag, **Electron Transport in Compound Semiconductors**, Springer-Verlag, Berlin (1980).

[4]J. Shah, Solid State Electron, **21**, 43 (1978).

[5]J. Shah and R. F. Leheny, in **Semiconductors Probed by Ultrafast Laser Spectroscopy, Vol I**, ed. by R. R. Alfano, Academic Press, New York, NY (1984).

[6]P. Lugli and D. K. Ferry, Physica **117**B, 251 (1983).

[7]C. Jacoboni and L. Reggiani, Rev. Mod. Phys. **55**, 645 (1983).

[8]P. Lugli and D. K. Ferry, IEEE Transactions on Electron Devices, ED-**32**, 2431 (1985).

[9]J. Zimmermann, P. Lugli,and D. K. Ferry, Solid State Electron, **26**, 233 (1986).

[10]M. A. Osman, H. L. Grubin, J. P. Kreskovsky and D. L. Ferry, SPIE PROC. **793**, 94 (1987).

[11]P. Lugli, C. Jacoboni and L. Reggiani, SPIE Proc. **793**, 102 (1987).

[12]M. A. Osman and D. K. Ferry, J. Appl. Phys. **61**, 5330 (1987).

[13]M. A. Osman and D. K. Ferry, Phys. Rev. B **36**, 6018 (1987).

[14]D. K. Ferry, M. A. Osman, R. Joshi and M.-J. Kann, Solid State Electron, **31**, 401 (1988).

[15]M. A. Osman and H. L. Grubin, Solid State Electron, **31**, 471 (1988).

[16]D. W. Bailey, C. J. Stanton, M. A. Artaki, K. Hess, F. W. Wise and C. L. Tang, Solid State Electron, **31**, 467 (1988).

[17]J. L. Pankove, **Optical Processes in Semiconductors**, Dover, New York (1971).

[18]C. V. Shank, R. L. Fork, R. F. Leheny, and J. Shah, Phys. Rev. Lett. **42**, 112 (1979).

[19]R. F. Leheny, J. Shah, R. L. Fork, C. V. Shank, and A. Migus. Solid State Comm. **31**, 809 (1979).

[20]W. Potz and P. Kocevar, Phys Rev B 28, 7040 (1980).

[21]R. J. Seymour, M. Junnarkar and R. R. Alfano, Solid State Comm. **41**, 657 (1982).

[22]J. A. Kash, J. C. Tsang and J. M. Hvam, Phys. Rev. Lett. **54**, 2151 (1985).

[23]A. C. S. Algarte, Phys. Rev. B **32**, 2388 (1985).

[24]T. Amand and J. Collet, J. Phys. Chem Solids **46**, 1053 (1985).

[25]A. J. Taylor and J. M. Wiesenfeld, Phys. Rev. B, **35**, 2321 (1987).

[26]E. M. Conwell and M. O. Vassell, J. Phys. Soc. Japan **21**, 527 (1966).

[27]J. L. Birman, M. Lax and R. Loudon, Phys. Rev. **145**, 620 (1966).

[28]E. Yoffa, Phys. rev. B **23**, 1909 (1981).

[29]J.L. Oudar, A. Migus, D. Hulin, G. Grillon, J. Etchepare and A. Antonelli, Phys. Rev. lett. **53**, 384 (1984).

[30]W. Z. Lin, L. G. Fujimoto, E. P. Ippen and R. A Logan, Appl. Phys. Lett. **50**, 124 (1987).

[31]R. W. Schoenlein, W. Z. Lin, E. P. Ippen and F. G. Fujimoto, Appl. Phys. Lett. **51**, 1442 (1987).

[32]W. Z. Lin, L. G. Fujimoto, E. P. Ippen and R. A. Logan, Appl. Phys. Lett. **51**, 161 (1987).

[33]A. J. Taylor, D. J. Erskine and C. L. Tang, Appl. Phys. Lett. **43**, 989 (1983).

[34]D. J. Erskine, J. Taylor and C. L. Tang, Appl. Phys. lett. **45**, 54 (1984).

[35]M. J. Rosker, F. W. Wise and C. L. Tang, Appl. Phys. Lett. **49**, 1726 (1986).

[36]F. W. Wise, I. A. Walmsley and C. L. Tang, Appl. Phys. Lett. **51**, 605 (1987).

[37]W. F. Brinkman and T. M. Rice, Phys. Rev. B **7**, 1508 (1973).

[38]J. Shah. R. F. Leheny and C. Lin, Solid State Commun. **18**, 1035 (1978).

[39]S. Tanaka, H. Yosida, H. Saito and S. Shionoya, in reference 5.

[40]E. J. Johnson, R. J. Seymour and R. R. Alfano, in **Semiconductors Probed by Ultrafast Laser Spectroscopy, Vol II**, ed. by R. R. Alfano, Academic Press, New York, NY (1984).

[41]D. D. Sell and H. C. Casey, J. Appl. Phys. **45**, 800 (1974).

Chapter 5 Intervalley scattering times in GaAs measured by time resolved four-wave mixing

5.1 Transient gratings and four-wave mixing

5.1.1 Introduction

When two or more laser beams interact in a medium, an interference grating is formed. The grating depends on the light frequency and the angle between the directions of propagation (see figure 5.1.1). The interference pattern gives rise to a spatial variation in the intensity or polarization. The electric fields for two beams of the same frequency and polarization propagating in the directions $\mathbf{k}_1$ and $\mathbf{k}_2$ are given by

$$E_1 = E_{1o}(t)\ \hat{z}\ \exp{-i\left(\omega t-\left[\frac{k}{n}\cos(\frac{\Theta}{2})x + \frac{k}{n}\sin(\frac{\Theta}{2})y\right]\right)}$$

$$E_2 = E_{2o}(t)\ \hat{z}\ \exp{-i\left(\omega t-\left[\frac{k}{n}\cos(\frac{\Theta}{2})x - \frac{k}{n}\sin(\frac{\Theta}{2})y\right]\right)} \qquad (5.1.1)$$

where the x axis is the bisector of the angle formed by $\mathbf{k}_1$ and $\mathbf{k}_2$, the x-y plane is the plane containing $\mathbf{k}_1$ and $\mathbf{k}_2$ and Θ is angle between the two beams in the material. The intensity, for S polarized fields, is given by

$$I(t) = I_1 + I_2 + 2\sqrt{I_1 I_2}\cos\left[2\sin(\frac{\Theta}{2})\ \frac{k}{n}\ y\right] . \qquad (5.1.2)$$

For $I_1 = I_2$, the intensity modulation varies between a maximum of $4I_1$ and a minimum of 0. For P polarization the intensity is given by

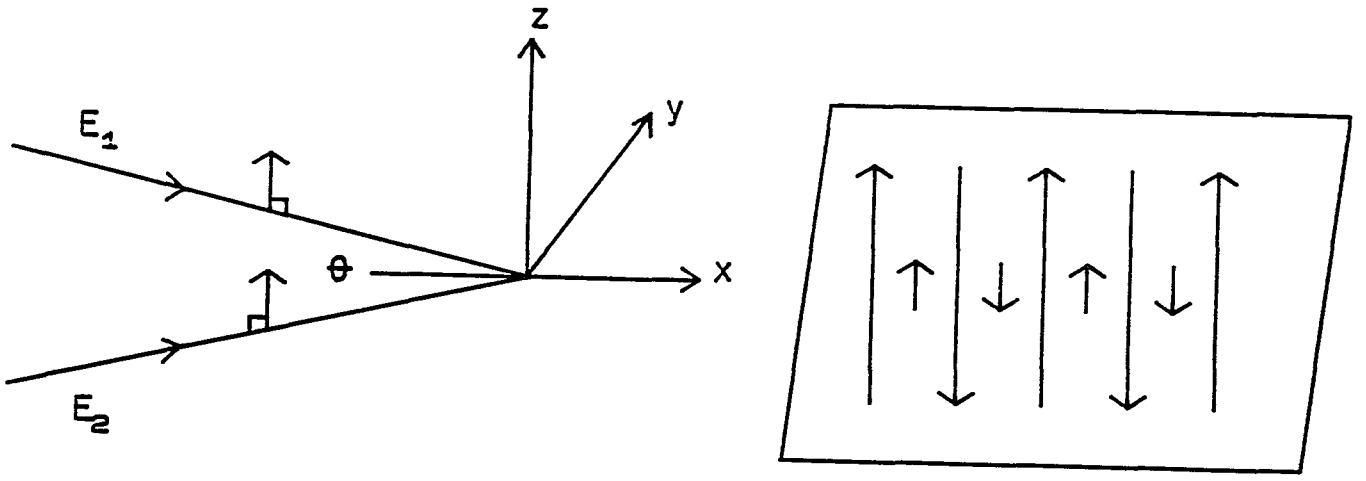

Figure 5.1.1. Interference pattern formed by two electric fields with parallel polarization. This geometry gives rise to a concentration (population) grating.

$$I(t) = I_1 + I_2 + 2\sqrt{I_1 I_2}\left[\cos^2(\tfrac{\Theta}{2}) - \sin^2(\tfrac{\Theta}{2})\right]\cos\left[2\sin(\tfrac{\Theta}{2})\,\frac{k}{n}\,y\right]. \quad (5.1.3)$$

For $I_1 = I_2$, the intensity modulation varies between a maximum of $2I_1(1 + \cos^2(\frac{\Theta}{2}) - \sin^2(\frac{\Theta}{2}))$ and a minimum of $2I_1(1-\cos^2(\frac{\Theta}{2})+\sin^2(\frac{\Theta}{2}))$. The grating separation, d, between points of maximum intensity is independent of the laser polarization. Using Snell's law to express d in terms of the incident angle in air, the grating separation is given by

$$d = \frac{\lambda_e}{2\sin(\frac{\theta}{2})} \quad (5.1.4)$$

where λ_e is the excitation wavelength and θ is the incident angle in air. The grating period is maximum when $\theta = 0^\circ$ or 180° and minimum when $\theta = 90^\circ$.

If the index of refraction of the material is nonlinear with intensity, the resulting interference pattern gives rise to a spatial modulation of the index across the sample. This spatial modulation of the index acts as a grating which will self-diffract the excitation beams as well as diffract a third laser beam that spatially and temporally overlaps the grating. When the modulation is due to real part of the index, the grating is called a **phase grating.** When the modulation is in the imaginary part of the index (change in absorption), the grating is called an **amplitude grating.**[1-5]

In the experimental conditions of this thesis work, both an

amplitude and phase grating exist. The scattered angle is given by the grating equation. If Φ is the angle the probe beam makes with the normal to the grating plane and λ_p is the probe wavelength then the scattered angle, Ω, is given by

$$\sin \Omega - \sin \Phi = m \frac{2 \lambda_p \sin(\frac{\theta}{2})}{\lambda_e} \quad (m = 0, \pm 1, \pm 2 \ldots . \quad (5.1.5)$$

For self-diffraction, $\Phi = \pm\frac{\theta}{2}$, $\lambda_e = \lambda_p$ and for small angles, the first order scattering is in the $\frac{3}{2}\theta$ and $-\frac{3}{2}\theta$ directions relative to the angle bisector of the beams (relative to the beam direction the angles are 2θ and $-\theta$). Note, that the zeroth order self-diffraction is in the forward direction and gives rise to the coherence artifact that has been observed in pump and probe absorption measurements.[6-10] The scattering directions for self-diffraction are shown in figure 5.1.2. For the case of $\lambda_p \neq \lambda_e$, the scattering angles for different orders of λ_p are shown in figure 5.1.3. More details are given in sections 5.3.1 and 5.3.2 and figure 5.3.2.

5.1.2 Concentration and orientation gratings

When the change in the index of refraction is caused by a spatial variation in the excited population density, the grating is referred to as a population or **concentration grating.**[11,12] A concentration grating is formed by the interference pattern of 2 parallel polarized laser beams as discussed in the previous section. For a pulsed excitation, the grating has a lifetime that depends on the pulse width and the relaxation processes in the material. The

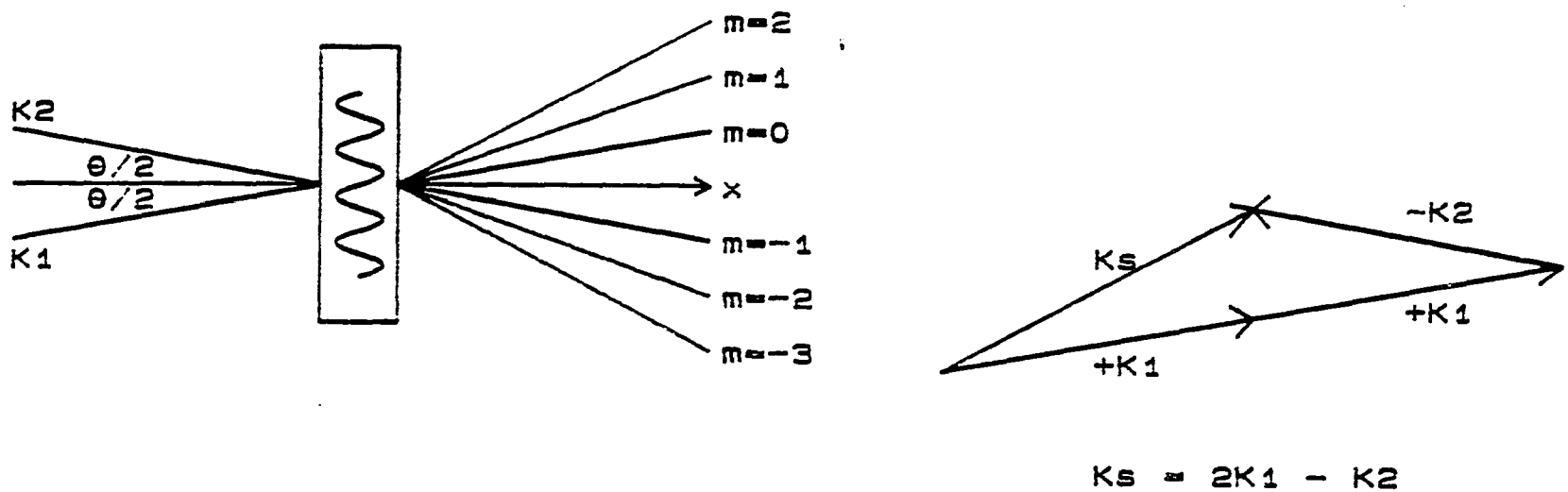

Figure 5.1.2. Scattering directions for self-diffraction in a two pulse grating experiment. The angle between the two beams is θ and the first order diffraction in in the +2θ and -θ directions.

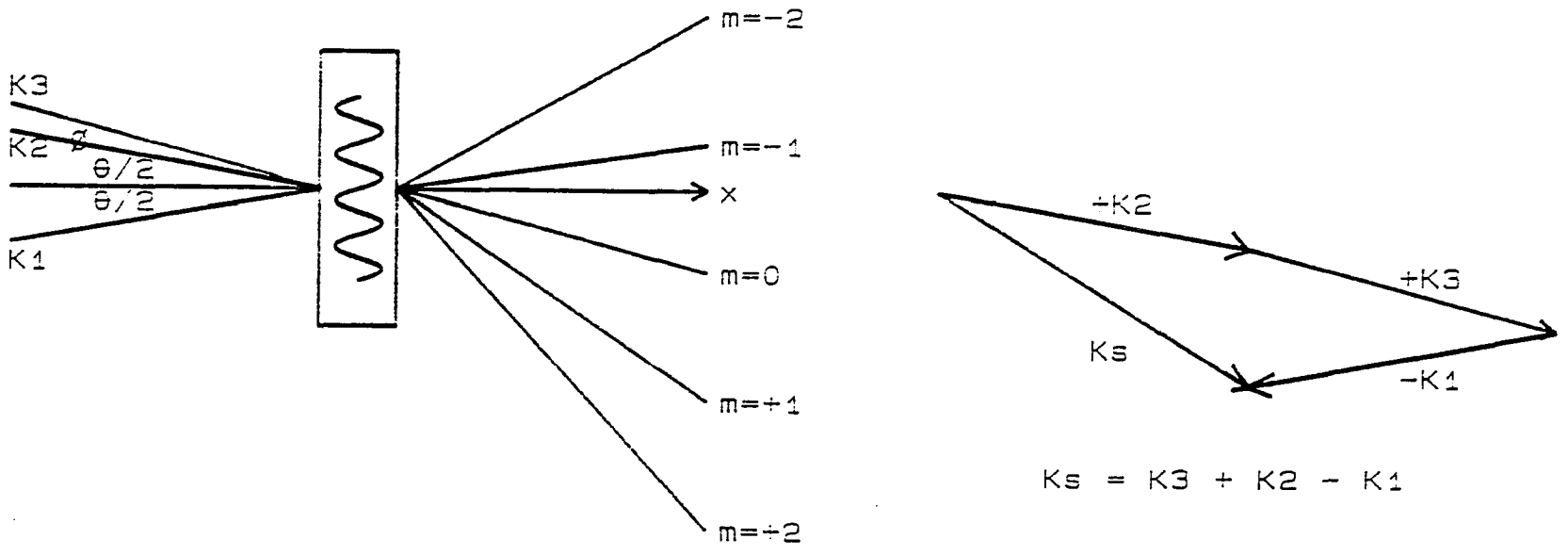

Figure 5.1.3. Scattering directions for a non-degenerate probe in a three pulse grating experiment. The angle between the pump beams is θ and the angle the probe makes with the bisector of the pump beams is ø.

concentration grating can decay by recombination of the excited carriers or by diffusion of carriers from the peaks to the nodes of the grating. Time resolved transient grating measurements have studied relaxation processes in dyes,[9,10,13] organic crystals,[14,15] as well as free carrier recombination and diffusion in Ge,[16-18] Si,[19,20] CdS,[21,22] and GaAs.[23-25]

If the two equal intensity pump beams are orthogonally polarized, the resulting electric field (figure 5.1.4) is given by

$$E(t) = E_o(t)\exp -i\left[\omega t - \frac{k}{n}\left[\cos(\frac{\theta}{2})x - \sin(\frac{\theta}{2})y\right]\right]\left[\hat{y} + \exp i\left[\frac{2k}{n}\sin(\frac{\theta}{2})y\right]\hat{z}\right]. \quad (5.1.6)$$

The intensity is constant but the electric field varies in direction across the plane of the sample. If the selection rules favor excitation with one polarization over another then one still gets a modulation in refractive index. In this geometry, the grating strength depends on the orientation of the excitation and decays as the orientation of the excitation randomizes i.e. by momentum relaxation[18,27] or dephasing[25,28]. This type of grating is referred to as an **orientation grating**.[1,12]

While the grating picture give a good understanding of the experimental setup and the different scattering angles, it does not necessarily give insight into the physics involved in the formation of the transient grating. The interpretation of transient grating signals in semiconductors have been varied and subject to controversy.[6,29] An alternate approach to the grating picture is to

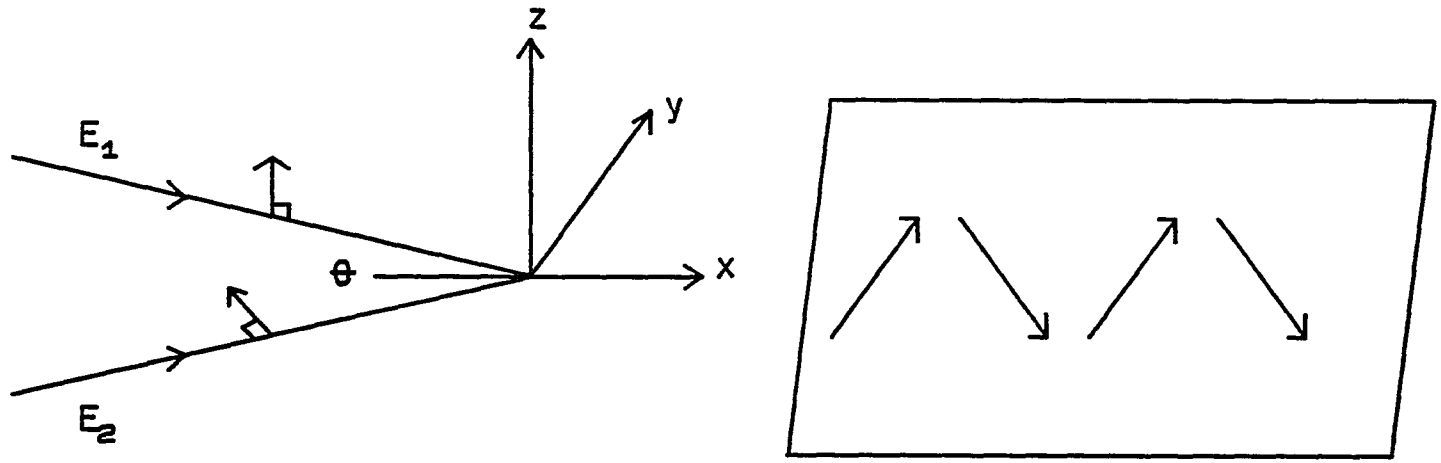

Figure 5.1.4. Interference pattern formed by two electric fields with orthogonal polarization. This geometry gives rise to an orientation grating.

consider the problem as one of four-wave mixing.

When an intense electric field is incident on a non-linear material, the resulting polarization can be expanded in powers of the electric field.[30,31]

$$P_i = \chi^{(1)}_{ij} E_j + \chi^{(2)}_{ijk} E_j E_k + \chi^{(3)}_{ijkl} E_j E_k E_l + \ldots . \qquad (5.1.7)$$

The second order term, $\chi^{(2)}$, is responsible for second harmonic generation (see section 3.2) and parametric mixing. $\chi^{(2)}$ produces a polarization at either the sum or difference frequency, not at the source frequency and $\chi^{(2)}$ vanishes if the sample has inversion symmetry (such as GaAs). The phase matching conditions were discussed in section 2.2. The third order term is non-zero in both centrosymmetric and non-centrosymmetric materials. When the $\chi^{(3)}$ term involves 3 source waves forming a fourth wave, the process is referred to as four-wave mixing. The phase matching conditions are given by

$$\mathbf{K}_s = \mathbf{K}_1 + \mathbf{K}_2 - \mathbf{K}_3 \qquad (5.1.8)$$

$$\omega_s = \omega_1 + \omega_2 - \omega_3 \qquad (5.1.9)$$

where i, j, k = 1, 2, 3. The phase matching conditions for four-wave mixing in a thin sample can always be satisfied.[3,7]

In the four-wave mixing interpretation of an experiment, the intensity of the scattered signal is related to the changes in the

dielectric function due to excitation by the source fields. In section 5.2, the free carrier contribution to the dielectric function in GaAs will be considered including the intraband term (Drude or free carrier population) and the interband term (contribution due to absorption saturation).[32]

5.2 Free carrier contribution to the dielectric function in GaAs

5.2.1 Introduction

Time resolved four-wave mixing has been used to study free carrier recombination and diffusion in semiconductors.[16-24] Steady state measurements (and non-time resolved measurements using nanosecond pulses) of the electronic third order non-linearities have been used to study relaxation of free carrier energy and momentum and intervalley scattering in GaAs and other III-V semiconductors.[33-36] Most of this work was at frequencies below band gap. One common technique is to measure $\chi^{(3)}$ as a function of the difference frequency, $\delta\omega$, between two laser beams as $\delta\omega \rightarrow 0$. Under these conditions, carriers at lattice temperature and relatively low density, the non-linearities are due to band non-parabolicity and electron-phonon scattering. In this situation there is no bleaching of absorption and most of the electrons remain in the Γ-valley although Kash and Wolff[35] used this technique to study the contributions to $\chi^{(3)}$ due to intervalley scattering in n-GaAs and n-GaSb. They observed that the dependence on $\delta\omega$ of the strength of the four-wave mixing signal changed as the sample temperature was elevated, allowing conduction band electrons to scatter from the Γ to the L-valleys.

Theoretical discussions of the optical non-linearities in III-V semiconductors have considered the effects of band non-parabolicity and carrier energy and momentum relaxation.[37-45] Most of these works have only considered frequencies below or just at the band edge. Kahen

and Leburton[45] calculate the different contributions to the real part of the dielectric constant (ε_1) from the different valleys of GaAs and other III-V semiconductors assuming the valence band is filled and the conduction band empty. They find that the Γ-valley contributes only about 5 - 10% to $\varepsilon_1(0)$ and the L and X-valleys contribute 90 - 95%. They do not consider the changes to ε_1 due to optical excitation. Wherrett and Higgins[42] first consider the effects of absorption saturation as well as changes in refraction for a two level system and then extend their model to a two band system. They find that absorption saturation reduces the refractive index at frequencies below the band gap but at frequencies above the Fermi level the refractive change turns positive.

In this section, using the standard[32] expressions for the free carrier contribution to the dielectric function, $\delta\varepsilon_1$ will be calculated in GaAs under the experimental conditions. The dependence of $\delta\varepsilon_1$ on carrier density, carrier temperature and the intervalley distribution of excited electrons will be examined. It will be shown that under the experimental conditions (subpicosecond time scale, probe photon energy high above band gap and high carrier density and temperature), the strength of the **transient concentration grating** signal is determined by the distribution of electrons between the Γ and L-valleys.

5.2.2 Intraband and interband contributions to $\delta\varepsilon_1$

The electronic contribution to the dielectric constant is given by[32,46-47]

$$\varepsilon_1(\omega) = 1 - \frac{4\pi e^2}{3\hbar^2\omega^2}\int \frac{d^3k}{4\pi^3}\sum_n F(E_n)\nabla_k{}^2 E_n(k) \qquad \text{(intraband)} \tag{5.2.1a}$$

$$+ \frac{\hbar^2 e^2}{\pi^2 m^2}\sum_{nn'}{}'\int \frac{d^3k\ \{F(E_n) - F(E_{n'})\}\,|p_{nn'}|^2}{(E_n - E_{n'})[(\hbar\omega)^2 - (E_n - E_{n'})^2]} \qquad \text{(interband)}$$

$$\varepsilon_2(\omega) = \frac{2\pi e^2}{m^2\omega^2}\sum_{nn'}{}'\int \frac{d^3k}{4\pi^3}\{F(E_n) - F(E_{n'})\}\,|p_{nn'}|^2\,\delta(\hbar\omega - E_n - E_{n'}) \tag{5.2.1b}$$

where m is the free electron mass, $|p_{nn'}|^2$ is the momentum matrix element between bands n and n', $E_n(k)$ is the energy of the n^{th} band and F(E) is the carrier distribution function in the n^{th} band. The intraband term is a free electron like term which in the case of parabolic bands reduces to the Drude expression for the polarizability of a free electron gas. The interband term results from transitions between bands. Changes in the absorption coefficient caused by bleaching under conditions of high excitation results in changes in the interband term in the electronic contribution to the dielectric function.

In order to calculate the effects of the intervalley distribution of electrons, as well as carrier temperature to changes in the dielectric function under intense optical excitation, I initially assume a single parabolic valence band and a parabolic central valley for the conduction band.

The change in ε due to optical pumping is given by

$$\delta\varepsilon_1(\omega) = -\frac{4\pi e^2}{3\hbar^2\omega^2}\int\frac{d^3k}{4\pi^3}\left[F_e(E_e)\nabla_k^2 E_e(k) - F_h(E_h)\nabla_k^2 E_h(k)\right] \quad \text{(intraband)}$$

(5.2.2a)

$$+\frac{\hbar^2e^2}{\pi^2m^2}\int\frac{d^3k\,\{F_e(E_e) + F_h(E_h)\}\,|p_{nn'}|^2}{(E_e-E_h)\,[(\hbar\omega)^2-(E_e-E_h)^2]} \quad \text{(interband)}$$

$$\delta\varepsilon_2(\omega) = +\frac{2\pi e^2}{m^2\omega^2}\int\frac{d^3k}{4\pi^3}\{F_e(E_e) + F_h(E_h)\}\,|p_{nn'}|^2\,\delta(\hbar\omega-E_e-E_h)\ . \quad (5.2.2b)$$

For parabolic bands $\nabla_k^2 E_n(K) = 3\hbar^2/m_n^*$; F_e and E_e (F_h, E_h) are the carrier distribution function and energy in the conduction (valence) band. The hole distribution function, $F_h = 1-F_e$. The matrix element is taken from k·p perturbation theory[48,49] $|p_{nn'}|^2 = \hbar\omega_g\frac{m^2}{4m^*}$; where m^* is the reduced effective mass and m is the free electron mass.

The intraband term is negative in sign and proportional to the total excited population and is independent of the carrier temperature or distribution for parabolic bands. It is given by

$$\delta\varepsilon_1(\omega) = -\frac{4\pi e^2}{\omega^2}\left(\frac{n}{m_e^*}+\frac{p}{m_h^*}\right) = -\frac{4\pi e^2 n}{m_r^*\omega^2} \quad \text{(intraband)} \quad (5.2.3)$$

where n (p) is the number of electrons (holes) and m_r^* is the reduced effective mass. For photoexcitation, the total number of excited electrons and holes are equal.

Changing the interband part of Eq. 5.2.2 from an integral in k space to an integral in energy, where the joint density of states is

used in the interband term, gives

$$\delta\varepsilon_1(\omega) = \frac{e^2 E_g (2m_r)^{1/2}}{\pi\hbar} \int_{E_g}^{\infty} \frac{(E-E_g)^{1/2} dE\{F_e(E)+F_h(E)\}}{(E_e-E_h)[(\hbar\omega)^2-(E_e-E_h)^2]} \quad \text{(interband)}. \quad (5.2.4)$$

The integral in Eq. 5.2.4 depends on the distribution of electrons among the different valleys of the conduction band through the distribution function of the electrons (F_e) and the energy of the electrons (E_e). The side valleys of GaAs have a much larger density of states than the Γ-valley, therefore the occupation probability, F_e, for the L and X valleys will be less than for the Γ-valley. The electrons in the L and X valleys will also be at greater energy, E_e, than electrons in the Γ-valley ($\Delta_{L-\Gamma}$ = 0.286 eV and $\Delta_{X-\Gamma}$ = 0.486 eV at 300 K). The evaluation of the interband integral in Eq. 5.2.4 will be discussed in the next section. The evaluation of $\delta\varepsilon_2$ will be discussed in section 5.2.5.

5.2.3 Interband contribution to $\delta\varepsilon_1$ of the valence band and the Γ- valley of the conduction band

Before evaluating the interband term in Eq. 5.2.4, I separate the integral into three regions: an integral from E_g to $\omega-\Delta$; an integral from $\omega-\Delta$ to $\omega+\Delta$; and an integral from $\omega+\Delta$ to ∞ . The three integrals for the interband term are

$$\delta\varepsilon_1(\omega) = \frac{e^2 E_g (2m_r)^{1/2}}{\pi\hbar} \int_{E_g}^{\hbar\omega-\Delta} \frac{(E-E_g)^{1/2} dE\{F_e(E)+F_h(E)\}}{(E)\,[(\hbar\omega)^2-(E)^2]} \quad (5.2.5a)$$

$$+ \frac{e^2 E_g (2m_r)^{1/2}}{\pi\hbar} \int_{\hbar\omega-\Delta}^{\hbar\omega+\Delta} \frac{(E-E_g)^{1/2} dE\{F_e(E)+F_h(E)\}}{(E)\,[(\hbar\omega)^2-(E)^2]} \qquad (5.2.5b)$$

$$+ \frac{e^2 E_g (2m_r)^{1/2}}{\pi\hbar} \int_{\hbar\omega+\Delta}^{\infty} \frac{(E-E_g)^{1/2} dE\{F_e(E)+F_h(E)\}}{(E)\,[(\hbar\omega)^2-(E)^2]} \quad . \qquad (5.2.5c)$$

In the first integral (5.2.5a) the integrand is always positive and hence 5.2.5a is positive. The integrand in the third integral (5.2.5c) is always negative and hence 5.2.5c is negative. When $\hbar\omega$ is greater than the energy separation of most of the electrons and holes (i.e. high above band gap) the interband term is positive and therefore will tend to cancel the negative intraband term, if all the electrons are in the Γ-valley. When $\hbar\omega$ is just above gap the interband term is negative and less than the intraband term. For $\hbar\omega$ below band gap, the only contribution to $\delta\varepsilon_{1inter}$ is from Eq. 5.2.5c (< 0); and for $\hbar\omega << E_g$, the denominator in 5.2.5c is large and thus $|\delta\varepsilon_{1inter}| << |\delta\varepsilon_{1intra}|$.

In order to evaluate the interband contribution to $\delta\varepsilon_1$ at $\hbar\omega$, first consider Eq. 5.2.5b. If Δ is taken $<< k_B T_c$, then F_e and F_h are constant over the range of integration. It is assumed that on the time scale of the experiment (≈ 1-10 ps) the electrons and holes have reached a common temperature. E and $\hbar\omega$ + E are replaced by $\hbar\omega$ and $2\hbar\omega$ respectively, then Eq.5.2.5b becomes

$$\delta\varepsilon_1(\omega) = + \frac{e^2 E_g (2m_r)^{1/2} [F_e+F_h]}{2\pi\hbar(\hbar\omega)^2} \int_{\hbar\omega-\Delta}^{\hbar\omega+\Delta} \frac{(E-E_g)^{1/2} dE}{(\hbar\omega)-(E)} \qquad (5.2.6)$$

and defining $\xi = E - E_g$ and $\vartheta = \hbar\omega - E_g$; Eq. 5.2.6 reduces to

$$\delta\varepsilon_1(\omega) = + \frac{e^2 E_g (2m_r)^{1/2} [F_e+F_h]}{2\pi\hbar(\hbar\omega)^2} \int_{\vartheta-\Delta}^{\vartheta+\Delta} \frac{\xi^{1/2}\, d\xi}{\vartheta - \xi} \quad . \qquad (5.2.7)$$

The resonant part of $\delta\varepsilon_1$ becomes[50]

$$\delta\varepsilon_1(\omega) = \frac{e^2 E_g (2m_r)^{1/2} [F_e+F_h]}{2\pi\hbar(\hbar\omega)^2} \left[2\sqrt{\xi} - \sqrt{\vartheta}\, \ln\left| \frac{\sqrt{\vartheta} + \sqrt{\xi}}{\sqrt{\xi} - \sqrt{\vartheta}} \right| \right]_{\vartheta-\Delta}^{\vartheta+\Delta} \qquad (5.2.8)$$

which simplifies to

$$\delta\varepsilon_1(\omega) = + \frac{e^2 E_g (2m_r)^{1/2} [F_e+F_h]}{2\pi\hbar(\hbar\omega)^2} \Delta \sqrt{\hbar\omega - E_g} \quad . \qquad (5.2.9)$$

The contribution to $\delta\varepsilon_1$ from carriers resonant with the probe energy depends on the population in the coupled region (F_e+F_h) and the probe energy. Closer to band gap, F_e and F_h are larger, but $\sqrt{\hbar\omega-E_g}$ is smaller, high above gap, $\sqrt{\hbar\omega-E_g}$ is larger but F_e and F_h are smaller. The computer program used to calculate $\delta\varepsilon_1$ evaluates Eq. 5.2.3, 5.2.5a,c and Eq. 5.2.9 (in place of 5.2.5b) separately. The resonant part of $\delta\varepsilon_1$ (Eq. 5.2.9) is a smaller contribution then the rest of the conduction and valence bands.

5.2.4 L-valley contribution to $\delta\epsilon_1$

As discussed in chapter 4, when GaAs is photoexcited by photons of energy more than 0.325 eV above the band gap, the energy given to

the electrons is greater than 0.286 eV, which is the energy separation between the conduction band minimum (located at k=0 in GaAs) and the L-valley minima. Electrons scatter from the Γ-valley to the L-valley in under 80 fs.[51,52] Theoretical calculations[53] show at high density greater than 75% of the excited electrons scatter to the L valley for 2.0 eV excitation. The electrons that scatter into the L-valley do not contribute to the absorption changes at the probe energies (1.5eV ≤ $\hbar\omega$ ≤ 2.0eV). The bleaching of the absorption at 3.1 eV (direct transitions from the heavy-hole valence band to the L-valley minima at the zone edge) is small due to large density of states of the four L-valley minima[54] and the absence of holes at the zone edge.

I assume that all electrons in L-valley are at the band minima, with is reasonable since electrons lose 0.286 eV of kinetic energy when scattering into the L-valley. Additionally, the carriers in the L-valley are less screened due to the higher effective mass and therefore rapidly lose energy by polar optical phonon emission[55] (the carriers density is on the order of 10^{19} cm^{-3}).

The L-valley contribution to $\delta\varepsilon_1(\omega)$ from Eq. 5.2.2 is then given by

$$\delta\varepsilon_1(\omega) = + \frac{4\hbar^2 e^2 n_L}{m^* [(\hbar\omega)^2 - (E_L)^2]} \qquad \text{(L-interband)} \qquad (5.2.10)$$

where n_L is the electron density in the L-valleys. The reduced mass was taken to be the electron effective mass, m_L^*; $f_h = 0$; E_L (valence band to L minima) = 3.1 eV and the factor of 4 was added to account for the 4 equivalent L-valleys. For $\hbar\omega$ < 3.1 eV, $(\hbar\omega)^2-(E_L)^2$ < 0 and

the L-valley contribution to the interband term is negative and much smaller than the Γ-valley contribution. The L-valley contribution is included in the computer calculations of $\delta\varepsilon_1$.

The large anisotropy and non-parabolicity of the L-valleys also changes the contribution of electrons in the L-valley to the intraband component of $\delta\varepsilon_1$ through $\nabla_k^2 E(k)$ in equation 5.2.2a. The non-parabolicity will increase the magnitude of the intraband term while the larger effective mass of the L-valley will reduce the magnitude of the intraband term. In the calculations of $\delta\varepsilon_1$, the differences in the intraband contribution between electrons in the L or Γ-valleys was not considered.

5.2.5 Calculation of $\delta\varepsilon_2$

For a simple parabolic valence and conduction band, Eq. 5.2.2b for $\delta\varepsilon_2$ simplifies to

$$\delta\varepsilon_2(\omega) = + \left[\frac{\pi e^2 E_g}{2\omega^2 m^*}\right]\left[\frac{(2m_r)^{3/2}}{2\pi^2\hbar^3}\right] X$$

$$\int_{E_g}^{\infty} dE(E-E_g)^{1/2}\{F_e(E_e)+F_h(E_h)\}\delta(\hbar\omega-E_e-E_h) \quad . \qquad (5.2.11)$$

$\delta\varepsilon_2$ depends only on the probability of occupation of states in the probe's optically coupled region and not on the entire excited population. For probe energies less than 3.1 eV, electrons in the L-valleys do not contribute to $\delta\varepsilon_2$. In the case of a nearly

monochromatic probe, F_e and F_h in the optically couple region can be taken as constant and Eq 5.2.11 becomes

$$\delta\varepsilon_2(\omega) = + \left[\frac{\pi e^2 E_g}{2\omega^2 m_r^*}\right]\left[\frac{(2m_r)^{3/2}}{2\pi^2\hbar^3}\right](\hbar\omega - E_g)^{1/2}\{F_e(E_e)+F_h(E_h)\} \qquad (5.2.12)$$

where E_e and E_h are given by

$$E_e = \frac{m_v}{m_v+m_c}(\hbar\omega - E_g) \qquad (5.2.13a)$$

$$E_h = \frac{m_c}{m_v+m_c}(\hbar\omega - E_g) \qquad (5.2.13b)$$

Eq. 5.2.12 for $\delta\varepsilon_2$ is evaluated by computer for a range of carrier densities and temperatures. The results are discussed in section 5.2.7, as well as the changes in the real part of the dielectric function.

5.2.6 Effects of band non-parabolicity

Both the conduction band and the light-hole valence band of GaAs deviate strongly from being parabolic.[54-56] The much larger density of states of the heavy-hole band compared to the light-hole band reduces the effects of band non-parabolicity in the valence band but for the conduction band, the non-parabolicity can not be neglected at densities greater than 10^{18} cm^{-3}. Blakemore[54] derives the non-parabolicity parameters, α for the conduction band and β for the light-hole band, for GaAs, by expanding the Kane band model[57] to include the additional perturbations caused by the other bands (see reference 54 for details). Expanding E(k) to terms in k^4, the

dispersion relationship for the conduction band is

$$E - E_g \simeq \frac{\hbar^2 k^2}{2m_c^*} + \frac{\alpha}{E_g}\left(\frac{\hbar^2 k^2}{2m_c^*}\right)^2 \qquad (5.2.14)$$

and for the light-hole band is

$$E \simeq -\left(\frac{\hbar^2 k^2}{2m_l^*}\right) - \frac{\beta}{E_g}\left(\frac{\hbar^2 k^2}{2m_l^*}\right)^2 \quad . \qquad (5.2.15)$$

The values of α and β at 300 K are -0.83, -3.57 respectively. Since $\alpha < 0$ and $\beta < 0$, the effective mass (and density of states) increases with greater energy. The relationship between electron density, temperature and quasi-Fermi level in the conduction band is given by

$$n_e = 2\left(\frac{m_c^* k_B T}{2\pi\hbar^2}\right)^{\frac{3}{2}}\left[\mathcal{F}_{1/2}\left(\frac{u_e}{k_B T}\right) - \left(\frac{15\alpha k_B T}{4E_g}\right)\mathcal{F}_{3/2}\left(\frac{u_e}{k_B T}\right)\right] \quad . \qquad (5.2.16)$$

Where $\mathcal{F}_{1/2}$ and $\mathcal{F}_{3/2}$ are the Fermi functions of order 1/2 and 3/2.

The non-parabolicity of the conduction band effects both the interband and intraband part of $\delta\epsilon_1$. The non-parabolicity appears in the intraband term (Eq. 5.2.4) through the $\nabla_k^2 E_c(k)$ term which now depends on k. The intraband term will have both a carrier temperature and a density dependence that is not linear in density since electrons at larger k (larger energy) will contribute more to the intraband term. The effects of higher carrier density will be mitigated somewhat by the fact that the non-parabolicity of the conduction band

keeps the quasi-Fermi level less than in a parabolic band. The non-parabolic corrections to $\nabla_k^2 E_c(k)$ require detailed knowledge of the band structure and will not be included in the thesis calculations.

The effect of band non-parabolicity on the interband term depends on the probe frequency. Band non-parabolicity enters into the interband term through its effect on the quasi-Fermi level. Because of the non-parabolicity of the conduction band, the density of states increases faster than $(E-E_g)^{1/2}$ and this results in a significantly lower quasi-Fermi level than in a parabolic band, this is most significant at high densities and at high carrier temperatures. Using Eq. 5.2.16, the quasi-Fermi levels for a parabolic and a non-parabolic bands were calculated, for a range of electron densities and temperatures. The effect of band non-parabolicity is most noticeable at probe energies near the quasi-Fermi level. If one examines the integrand in the interband term (in Eqs. 5.2.5a,b,c), one sees that electrons (holes) at energies less (greater) than the optically coupled states of the probe energy (i.e. $\hbar\omega > E_e - E_h$), give a positive contribution to $\delta\varepsilon_1$ while higher (lower) energy electrons (holes) (i.e. $\hbar\omega < E_e - E_h$) give a negative contribution to $\delta\varepsilon_1$. The simplest correction for band non-parabolicity would be to use a density dependent effective mass.[56] The computer program used to calculate $\delta\varepsilon_1$ from Eq. 5.2.3 and 5.2.5a,b,c is adjusted to include the density dependent effective mass and the non-parabolic quasi-Fermi levels in both the interband and intraband terms . This procedure corrects for the non-parabolic effects on the distribution function of the excited carriers; it does not correct for the effects of band non-parabolicity

on the response of excited carriers to the probe field through the $\nabla_k^2 E_n(k)$ term. For the conduction band, I accomplish this by calculating the quasi-Fermi level for a given density and temperature from Eq. 5.2.16 and then adjusting the effective mass such that this value of u_e gives the correct electron density for a parabolic band.

The equation that determines the electron density dependent effective mass, μ_c^*, is

$$(\mu_c^*)^{\frac{3}{2}} = \frac{(m_c^*)^{\frac{3}{2}}\left[\mathcal{F}_{1/2}\left(\frac{u_e}{k_B T}\right) - \left(\frac{15\alpha k_B T}{4E_g}\right)\mathcal{F}_{3/2}\left(\frac{u_e}{k_B T}\right)\right]}{\mathcal{F}_{1/2}\left(\frac{u_e}{k_B T}\right)} \qquad (5.2.17)$$

A similar calculation for the valence band is made where the heavy-hole band is considered to be parabolic but the light-hole band is non-parabolic. The relationship between hole density, temperature and hole quasi-Fermi level is given by

$$n_h = 2\left(\frac{k_B T}{2\pi\hbar^2}\right)^{\frac{3}{2}}\left[\left[m_h^{*\frac{3}{2}} + m_l^{*\frac{3}{2}}\right]\left[\mathcal{F}_{1/2}\left(\frac{u_h}{k_B T}\right)\right] - m_l^{*\frac{3}{2}}\left(\frac{15\beta k_B T}{4E_g}\right)\mathcal{F}_{3/2}\left(\frac{u_h}{k_B T}\right)\right] \quad . \quad (5.2.18)$$

The valence band density dependent effective mass, μ_v^* is given by

$$(\mu_v^*)^{\frac{3}{2}} = \frac{\left[\left[m_h^{*\frac{3}{2}} + m_l^{*\frac{3}{2}}\right]\left[\mathcal{F}_{1/2}\left(\frac{u_h}{k_B T}\right)\right] - m_l^{*\frac{3}{2}}\left(\frac{15\beta k_B T}{4E_g}\right)\mathcal{F}_{3/2}\left(\frac{u_h}{k_B T}\right)\right]}{\left[\mathcal{F}_{1/2}\left(\frac{u_h}{k_B T}\right)\right]} \quad . \quad (5.2.19)$$

The computer program used to calculate $\delta\varepsilon_1$ was adjusted to use the density dependent effective masses, μ_e^* and μ_h^*, in both the intraband and interband terms (Eqs 5.2.3, 5.2.5a, and 5.2.5c). This procedure corrects for the non-parabolic effects on the distribution function of the excited carriers by allowing the use of the electron and hole quasi-Fermi levels as calculated for non-parabolic bands; it does not correct for the effects of non-parabolicity on the response of excited carriers to the probe field through the $\nabla_k^2 E_n(k)$ term.

5.2.7 Calculations of the dependence of $\delta\epsilon_1$ and $\delta\varepsilon_2$ on the carrier distribution function

As seen from Eq. 5.2.4, the interband contribution to the dielectric function depends on the carrier distribution function. In this section, I calculate $\delta\varepsilon_1$ and $\delta\varepsilon_2$ due to optical excitation for different distributions of electron density between the Γ and L-valleys at a range of carrier temperatures . The total number of electrons is constant (and equal to the number of holes). The calculations are made for different probe frequencies above the band gap.

For the sake of comparison, I also calculate $\delta\varepsilon_1$ for $\hbar\omega$ = 0.8 eV (well below band gap) although no data was taken at energies below band gap. All calculations assume a Fermi-Dirac distribution with the electrons and holes at a common temperature greater than the lattice temperature. This is a valid assumption on a 1 to 10 ps time scale although, it is not valid within the 500 fs width of the excitation pulses.[58] The carrier densities and temperatures are consistent with

the results of absorption measurements discussed in chapter 4.

The intraband and interband contributions to $\delta\varepsilon_1$ for probe energies of 0.8, 1.65, 1.71, 1.77, 1.84 and 2.0 eV are plotted in figures 5.2.1a-f (note the different ordinate scale for 0.8 eV). The hole density is 1.2×10^{19} cm^{-3} and the carrier temperature is 900 K. The total number of electrons in the Γ and L valleys is equal to the number of holes. As seen in figures 5.2.1a-f, the intraband term is negative and independent of the electron distribution between valleys. The interband term is positive for $\hbar\omega > E_g$ and increases as electrons scatter back from the L to the Γ-valley. For a 0.8 eV probe, we see that the interband contribution to $\delta\varepsilon_1$ is negative and small. The frequency dependence of the interband and intraband terms of $\delta\varepsilon_1$ have been plotted in figure 5.2.2 in the energy range of 0.5 to 2.4 eV. The carrier temperature is 600 K, $n_e = n_h = 1.2 \times 10^{19}$ cm^{-3} with 83% of the electrons in the Γ-valley. The intraband term is always negative and decreases as $(\hbar\omega)^{-2}$ as expected from equation 5.2.2. The interband term is negative for $\hbar\omega < E_g$ and becomes positive when $\hbar\omega$ is about 100 meV above E_g. The interband term increases as $\hbar\omega$ increases until it reaches a maximum around 1.7 eV. The energy at which $\delta\varepsilon_{1inter}$ is a maximum will change with carrier temperature.

$\delta\varepsilon_2$ has been calculated for the same conditions as $\delta\varepsilon_1$ and plotted in figures 5.2.3a-e corresponding to probe energies of 1.65, 1.71, 1.77, 1.84 and 2.01 eV. Note that $\delta\varepsilon_2 = 0$ for $\hbar\omega < E_g$.

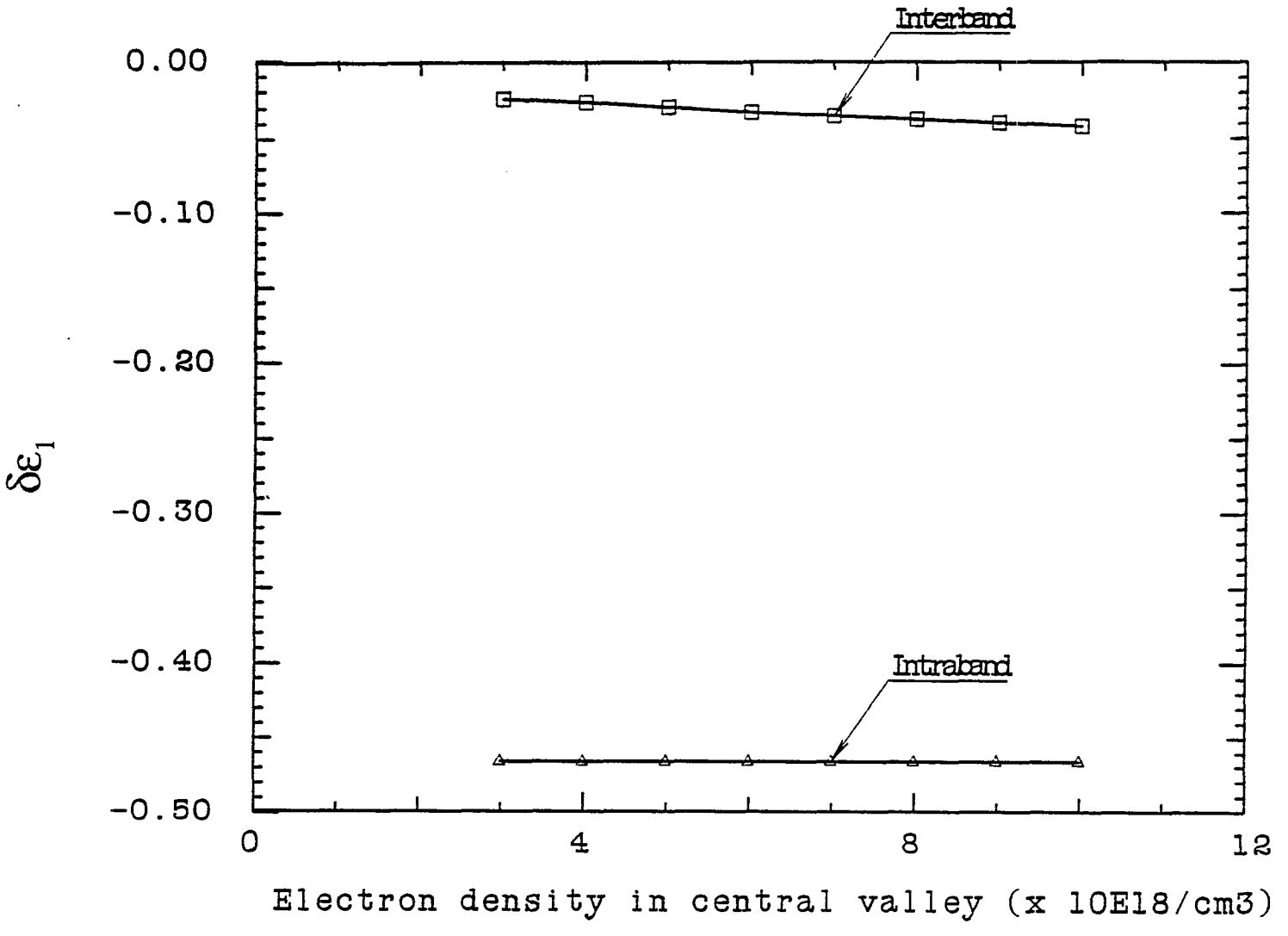

Figure 5.2.1a. Intraband and interband contributions to $\delta\epsilon_1$ for a 0.80 eV probe calculated as a function of electron density in the Γ-valley. The total density, $n_e=n_h$ = 1.2 x 10^{19} cm^{-3} and the carrier temperature = 900 K.

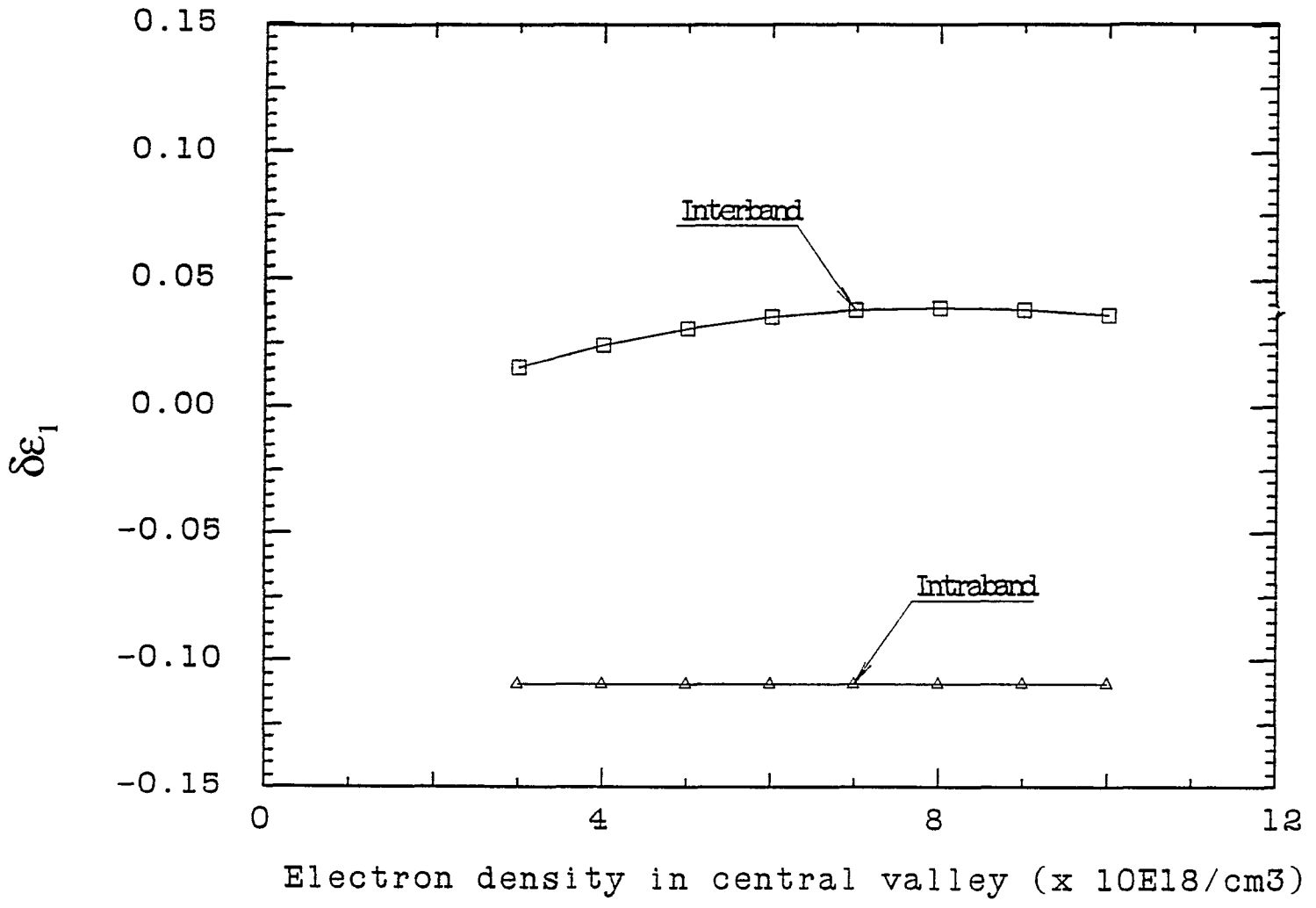

Figure 5.2.1b. Intraband and interband contributions to $\delta\epsilon_1$ for a 1.65 eV probe calculated as a function of electron density in the Γ-valley. The total density, $n_e=n_h$ = 1.2 x 10^{19} cm^{-3} and the carrier temperature = 900 K.

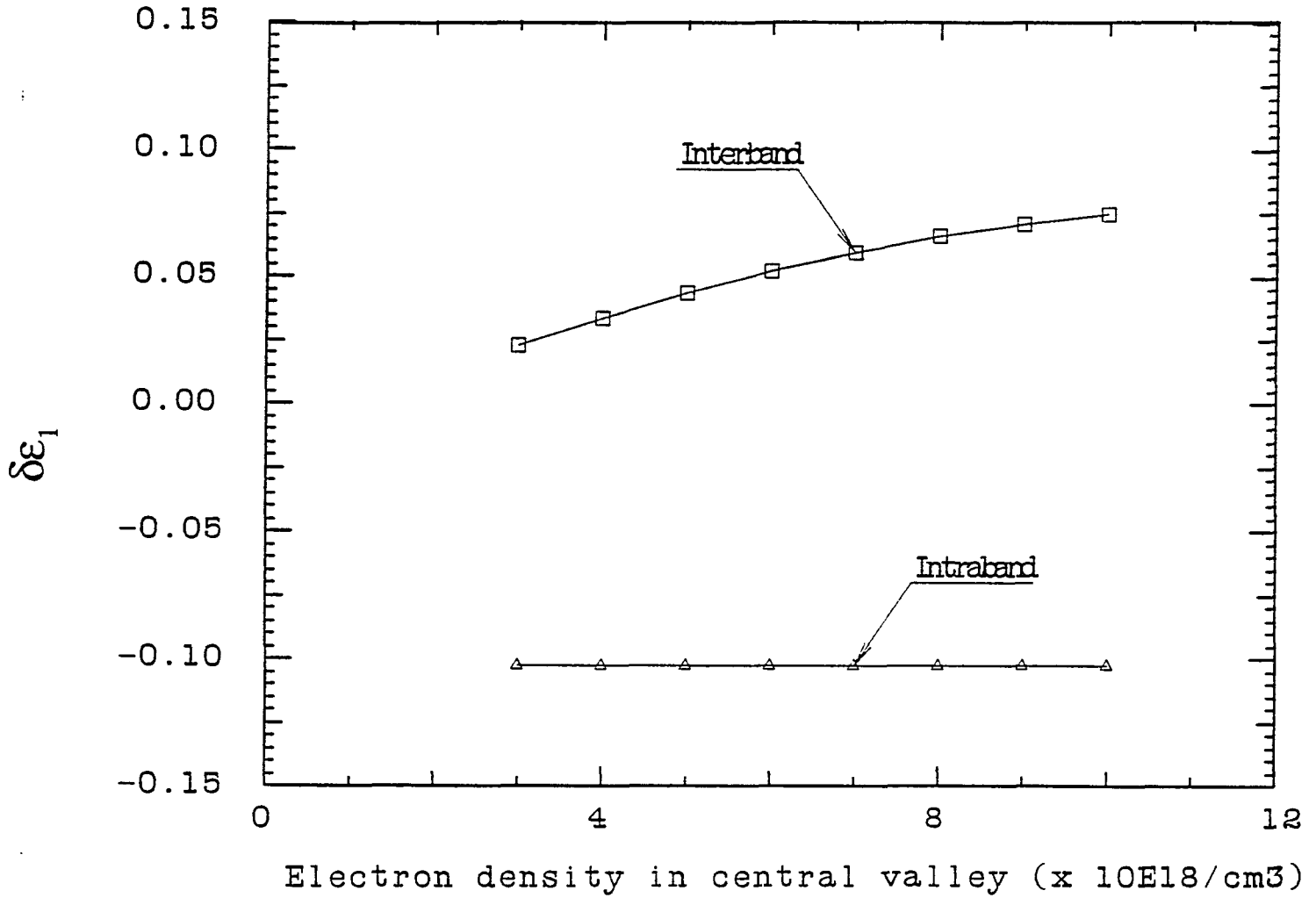

Figure 5.2.1c. Intraband and interband contributions to $\delta\epsilon_1$ for a 1.71 eV probe calculated as a function of electron density in the Γ-valley. The total density, $n_e=n_h$ = 1.2 x 10^{19} cm^{-3} and the carrier temperature = 900 K.

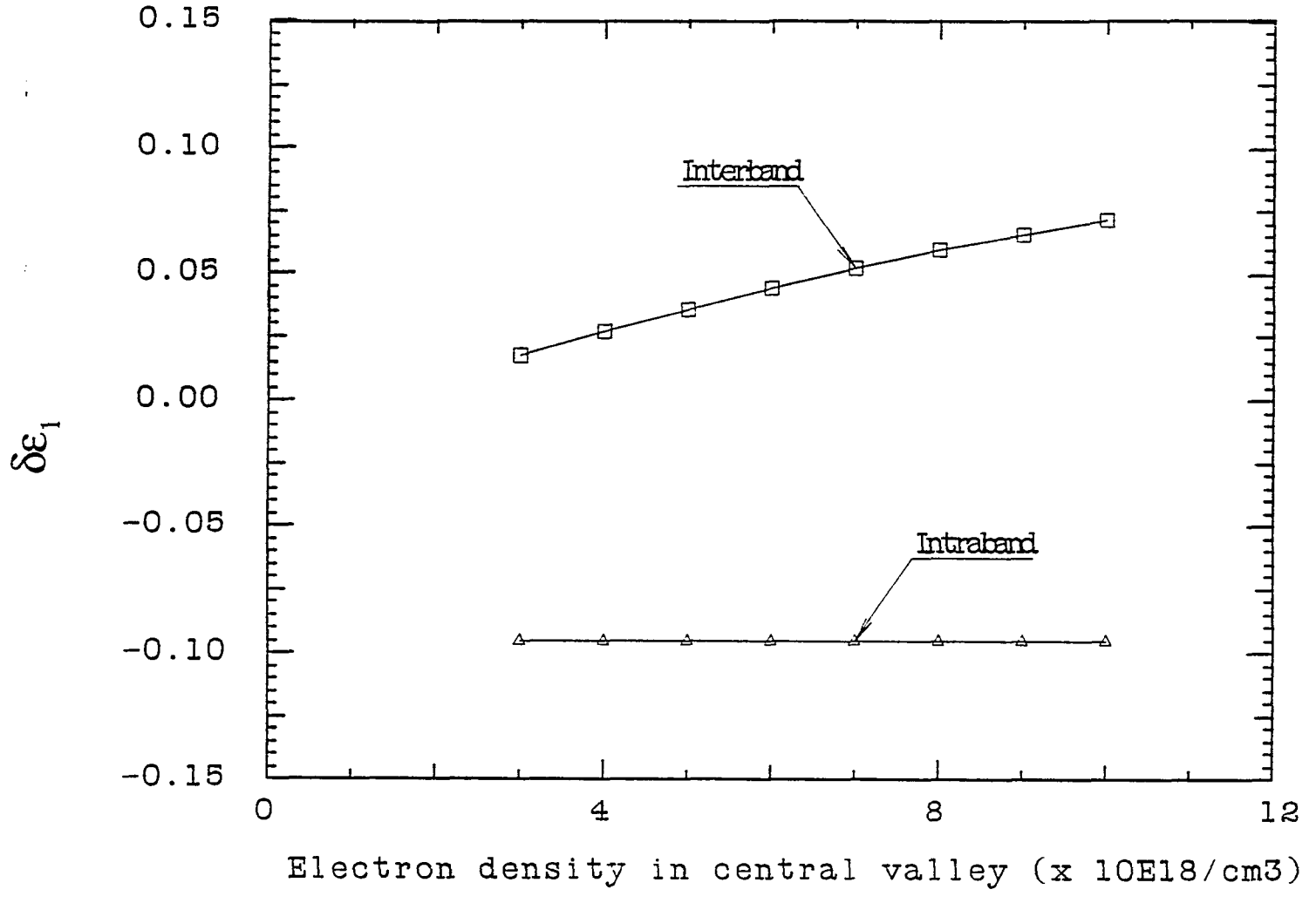

Figure 5.2.1d. Intraband and interband contributions to $\delta\epsilon_1$ for a 1.77 eV probe calculated as a function of electron density in the Γ-valley. The total density, $n_e = n_h = 1.2 \times 10^{19}$ cm^{-3} and the carrier temperature = 900 K.

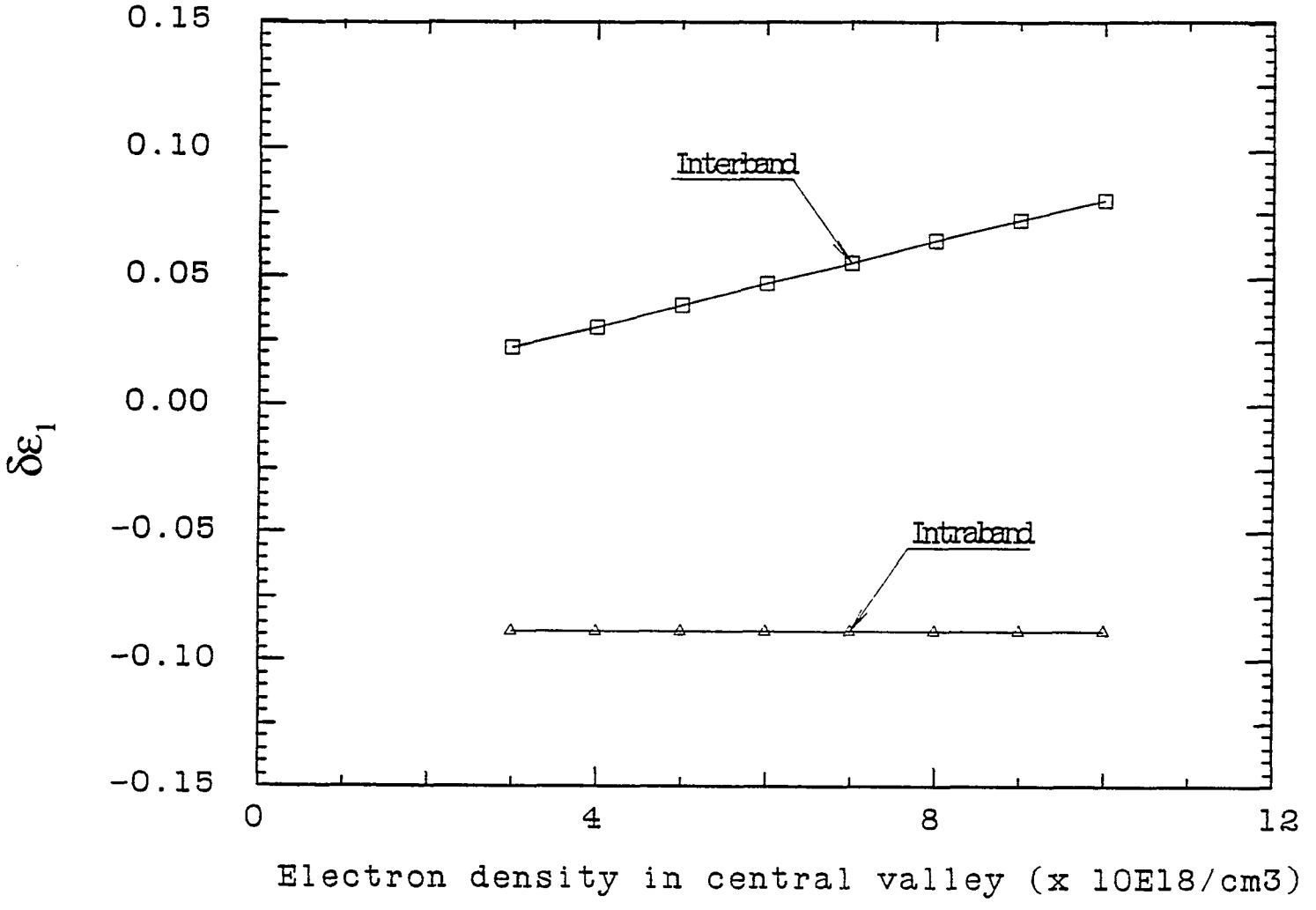

Figure 5.2.1e. Intraband and interband contributions to $\delta\epsilon_1$ for a 1.84 eV probe calculated as a function of electron density in the Γ-valley. The total density, $n_e = n_h = 1.2 \times 10^{19}$ cm^{-3} and the carrier temperature = 900 K.

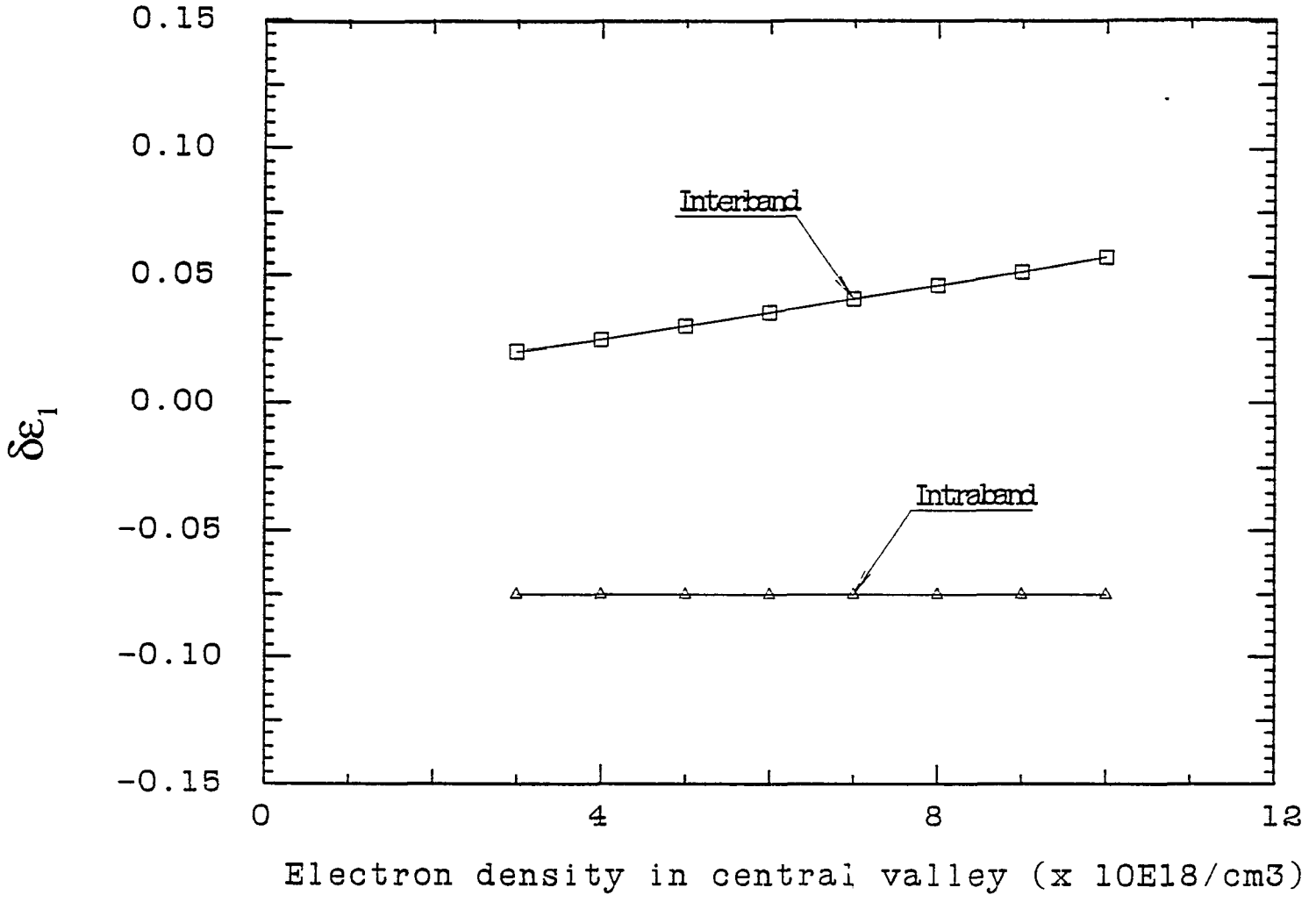

Figure 5.2.1f. Intraband and interband contributions to $\delta\epsilon_1$ for a 2.01 eV probe calculated as a function of electron density in the Γ-valley. The total density, $n_e=n_h$ = 1.2 x 10^{19} cm^{-3} and the carrier temperature = 900 K.

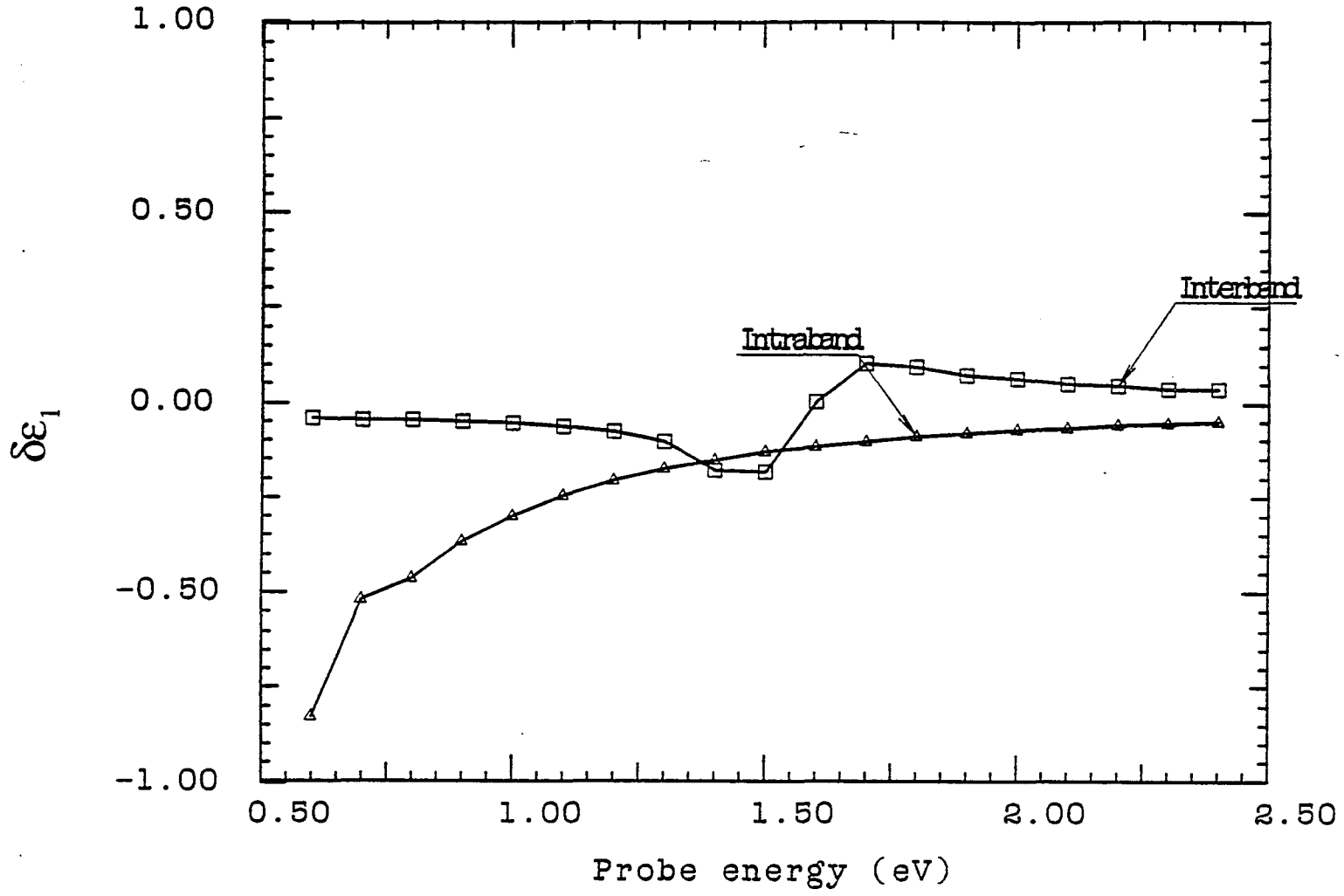

Figure 5.2.2. Interband and Intraband contributions to $\delta\epsilon_1$ as a function of probe energy. Total carrier density is 1.2 x 10^{19} and carrier temperature = 600 K. The density of electrons in the Γ-valley is 1 x10^{19} cm^{-3}.

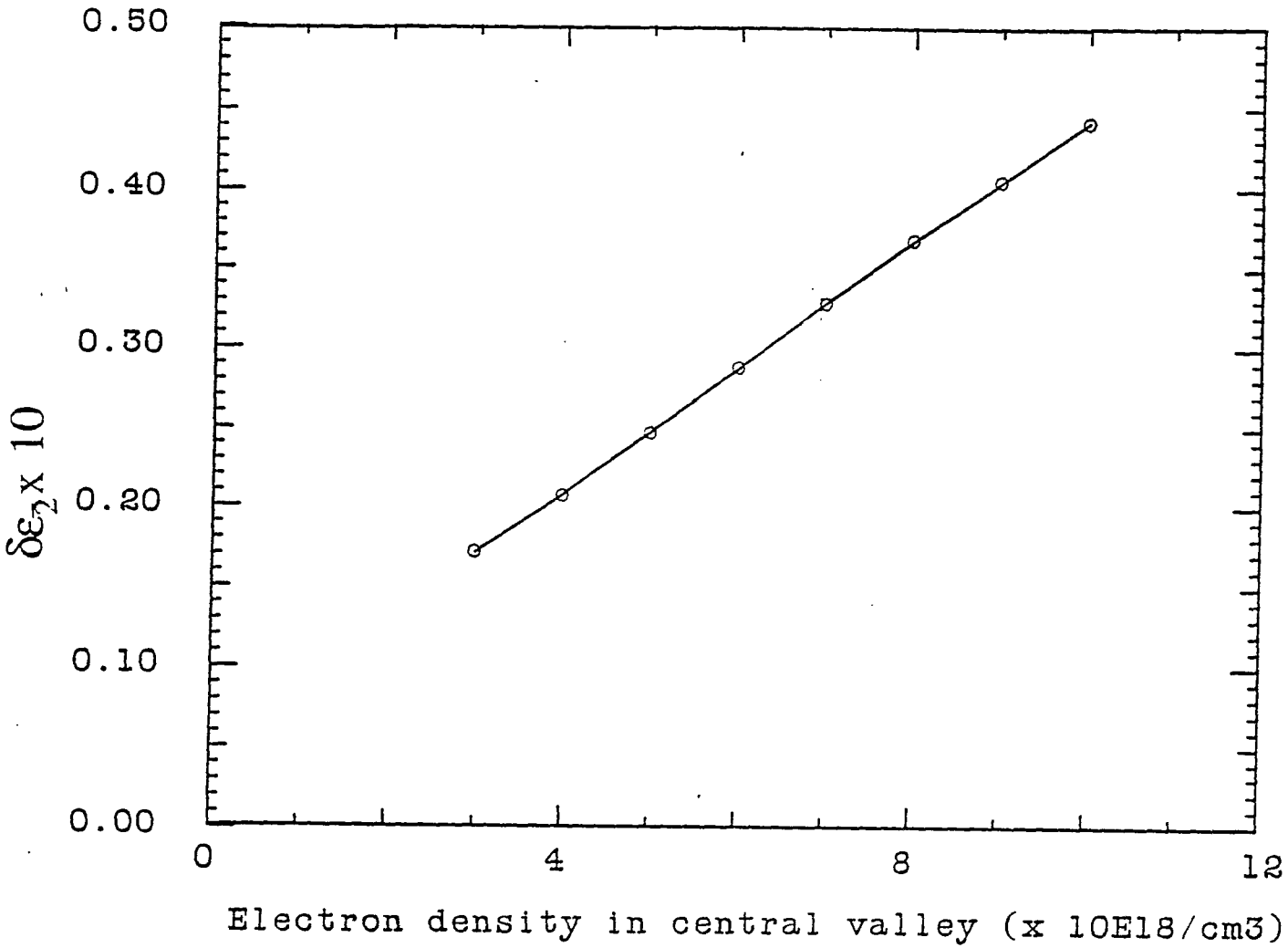

Figure 5.2.3a. $\delta\epsilon_2$ for a 1.65 eV probe calculated as a function of electron density in the Γ-valley. The total density, $n_e=n_h$ = 1.2 x 10^{19} cm^{-3} and the carrier temperature = 900 K.

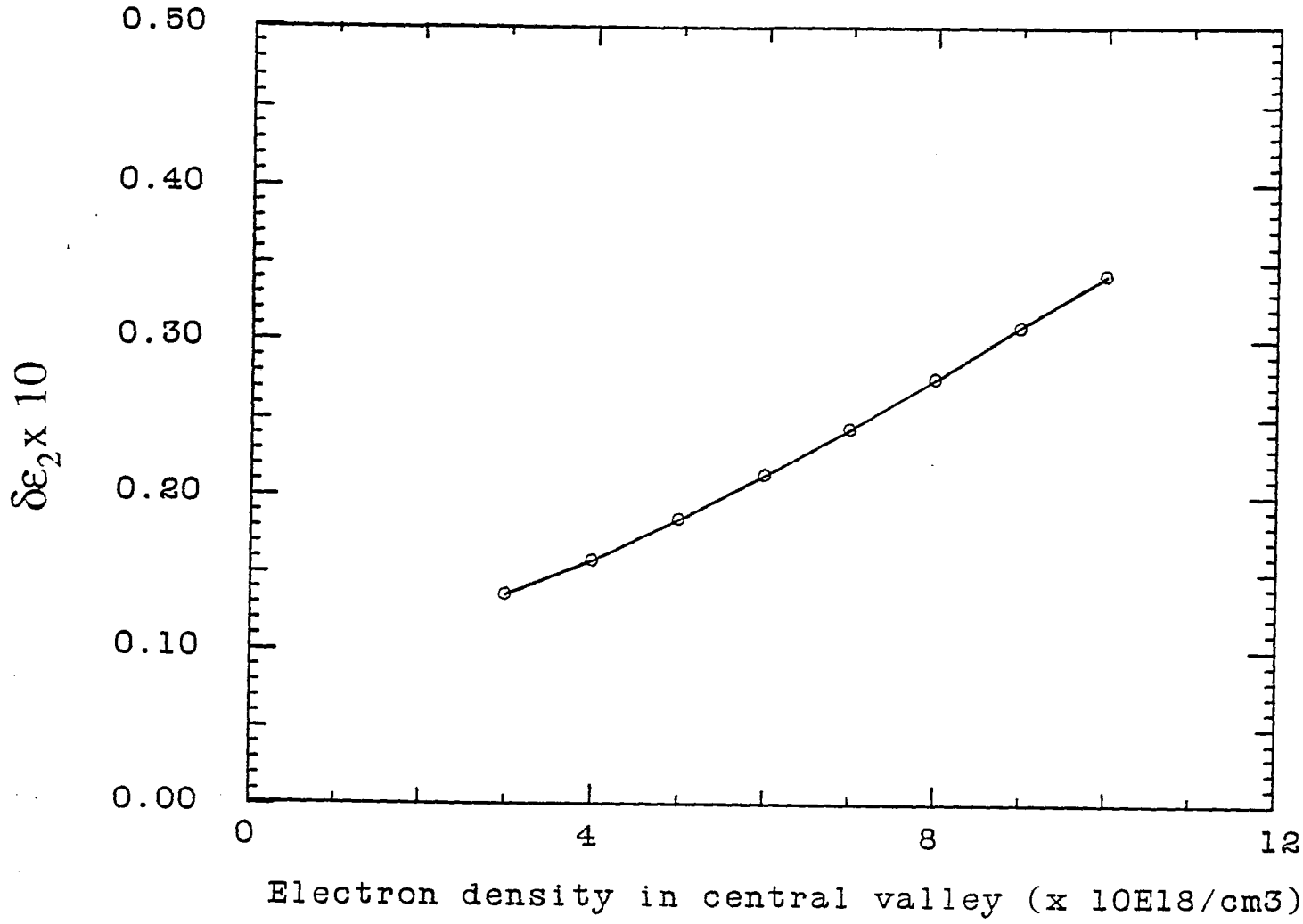

Figure 5.2.3b. $\delta\epsilon_2$ for a 1.71 eV probe calculated as a function of electron density in the Γ-valley. The total density, $n_e=n_h$ = 1.2 x 10^{19} cm^{-3} and the carrier temperature = 900 K.

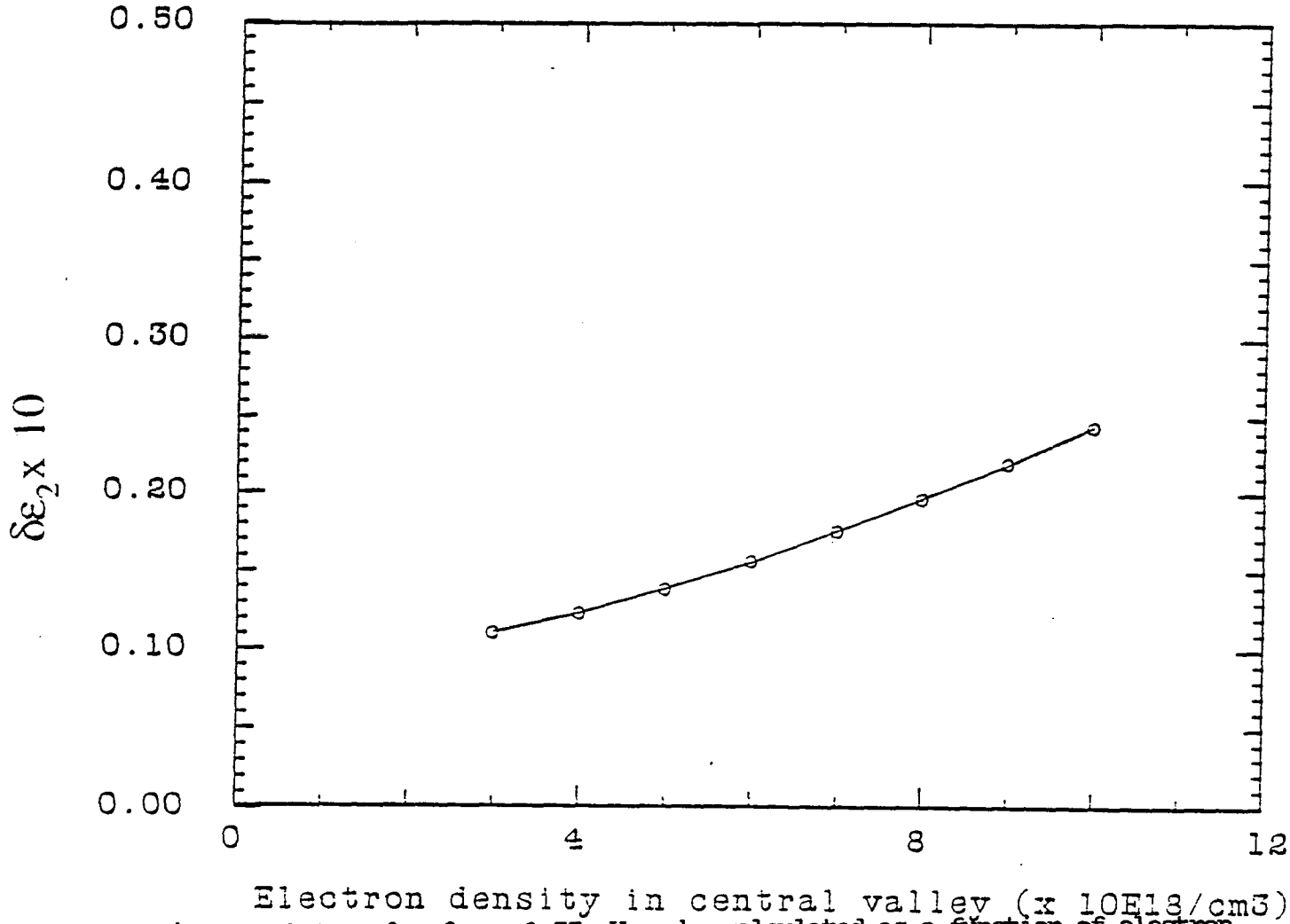

Figure 5.2.3c. $\delta\epsilon_2$ for a 1.77 eV probe calculated as a function of electron density in the Γ-valley. The total density, $n_e=n_h$ = 1.2 x 10^{19} cm^{-3} and the carrier temperature = 900 K.

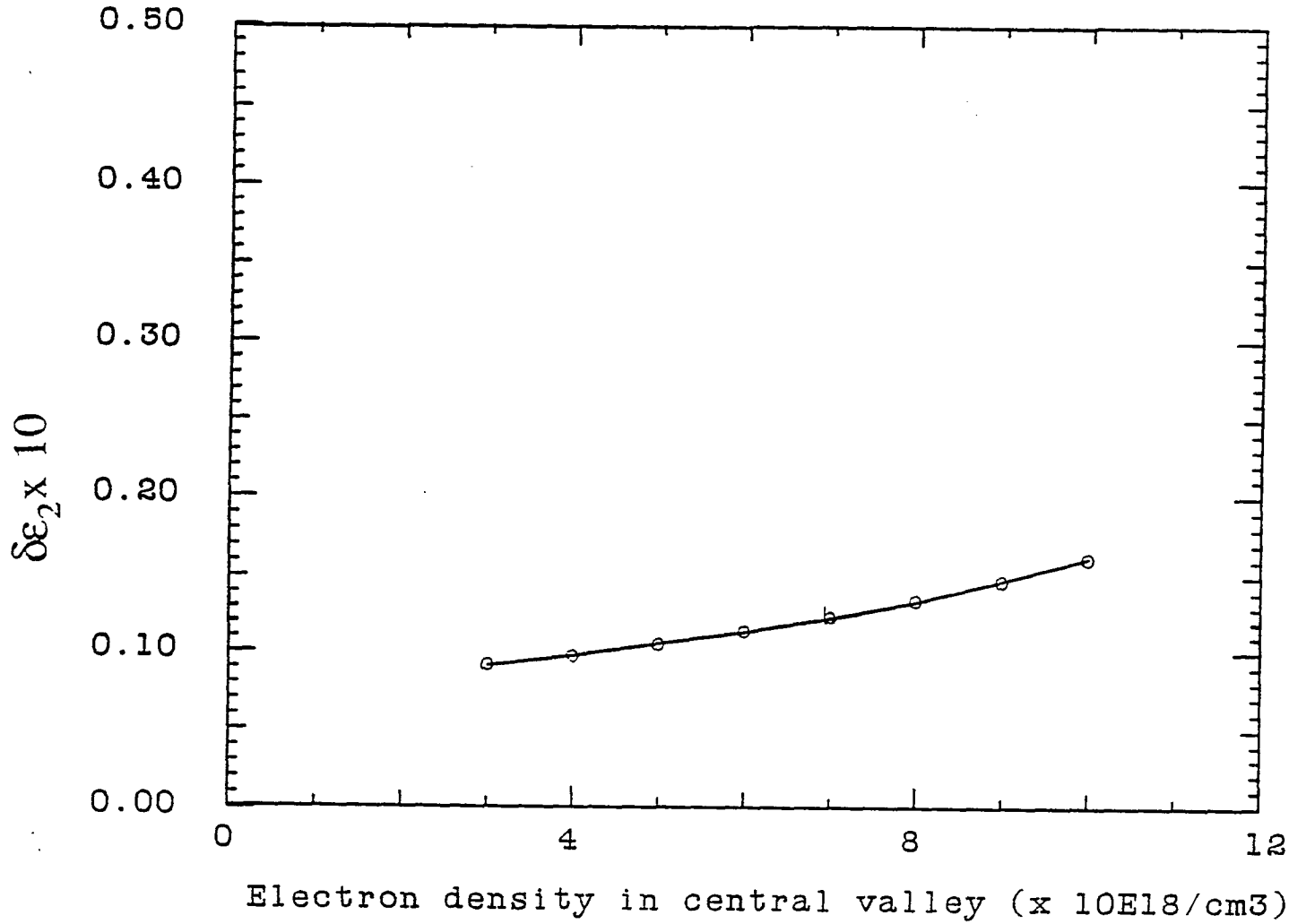

Figure 5.2.3d. $\delta\epsilon_2$ for a 1.84 eV probe calculated as a function of electron density in the Γ-valley. The total density, $n_e=n_h$ = 1.2 x 10^{19} cm^{-3} and the carrier temperature = 900 K.

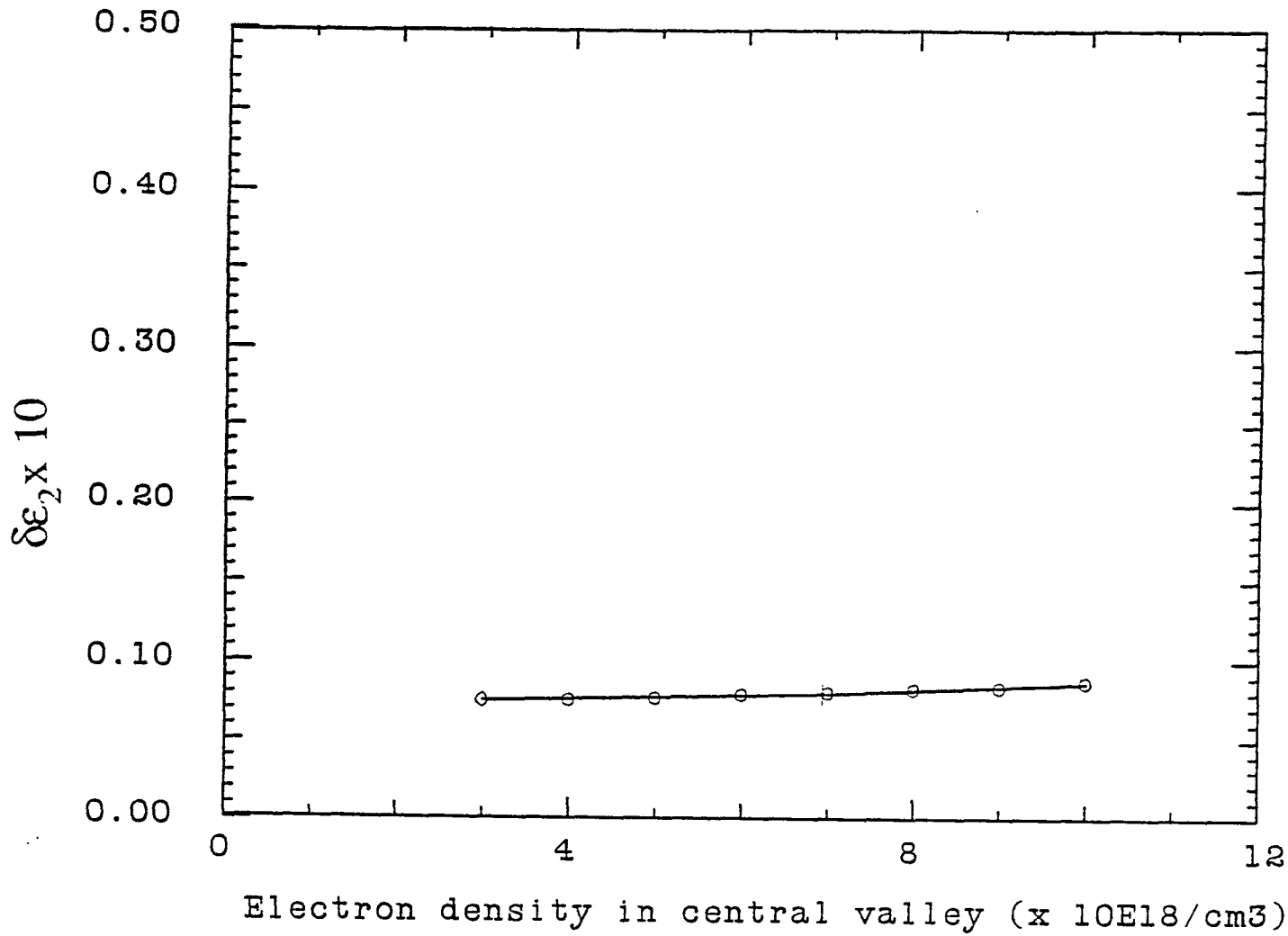

Figure 5.2.3e. $\delta\epsilon_2$ for a 2.01 eV probe calculated as a function of electron density in the Γ-valley. The total density, $n_e=n_h$ = 1.2 x 10^{19} cm^{-3} and the carrier temperature = 900 K.

Since the diffracted intensity depends on $|\delta\epsilon|^2 = |\delta\epsilon_1|^2 + |\delta\epsilon_2|^2$, figures 5.2.4a-f show $|\delta\epsilon|^2$ for the same frequencies as figures 5.2.1a-f. At frequencies well above the electron quasi-Fermi level (i.e. 1.77 eV, 1.84 eV and 2.0 eV), $|\delta\epsilon|^2$ decreases to zero as electrons scatter back from the L-valley to the Γ valley. At frequencies closer to the band edge (i.e. 1.65 eV), the decrease in $|\delta\epsilon|^2$ is much less and $|\delta\epsilon|^2$ falls by only a factor of <2 as the number of the carriers in the L valley decreases from 75% to 25%. Below band gap (0.80 eV), $|\delta\epsilon|^2$ is almost independent of electron distribution between valleys.

The dependence of $\delta\epsilon$ on carrier temperature is also examined. When the probe optically couples states that are high above the electron quasi-Fermi energy, the interband term is not very sensitive to the small changes in the Fermi energy, and $|\delta\epsilon|^2$ decrease slightly as carriers cool. When the optically coupled states are close to the Fermi energy, the interband contribution is more sensitive to changes in the Fermi level. In this case, carrier cooling reduces $|\delta\epsilon|^2$ much more significantly. Since the holes are not degenerate at these densities, the coupled valence band states are always far below the hole quasi-Fermi level.

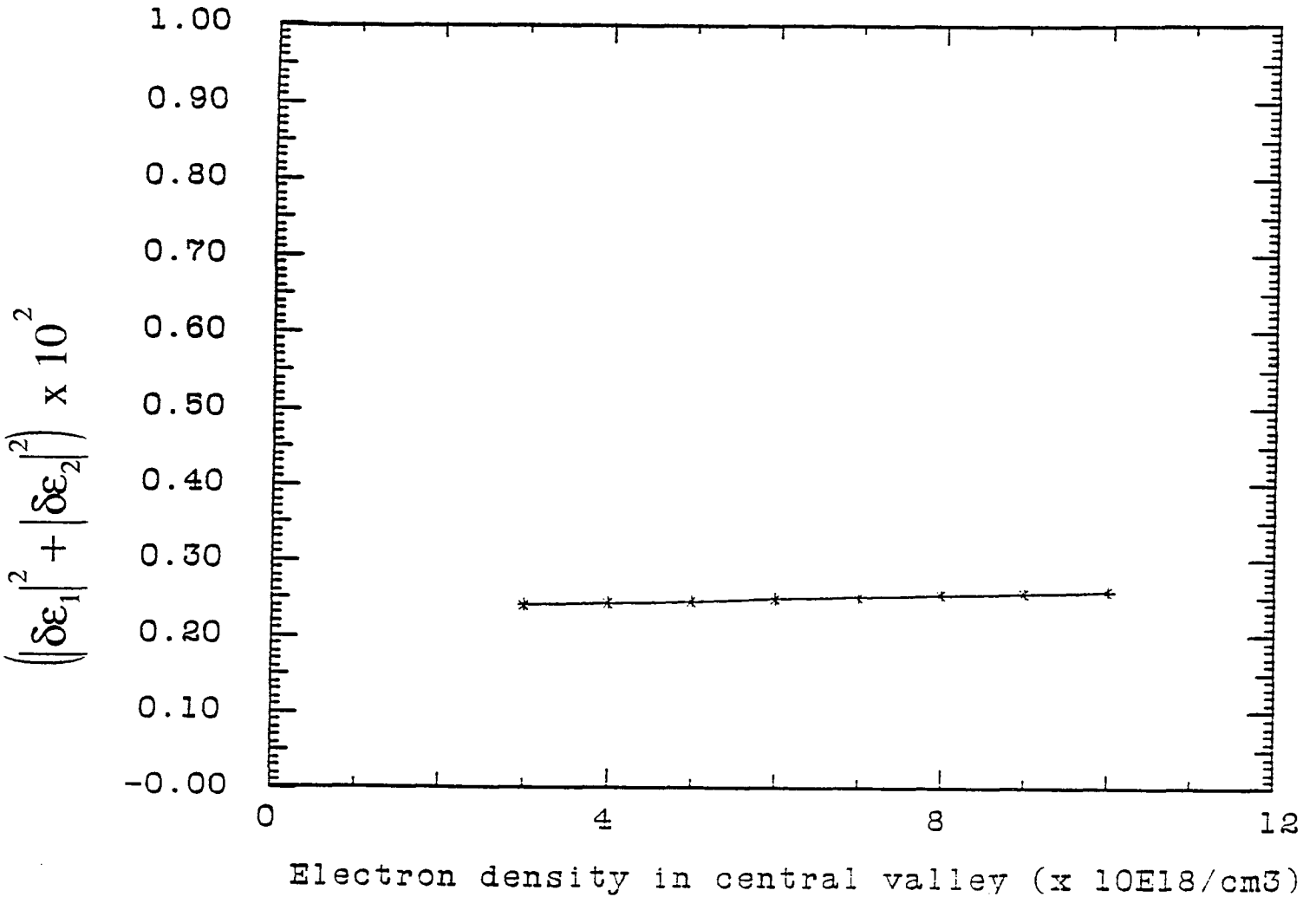

Figure 5.2.4a. $|\delta\epsilon|^2$ for a 0.80 eV probe calculated as a function of electron density in the Γ-valley. The total density, $n_e = n_h = 1.2 \times 10^{19}$ cm^{-3} and the carrier temperature = 900 K.

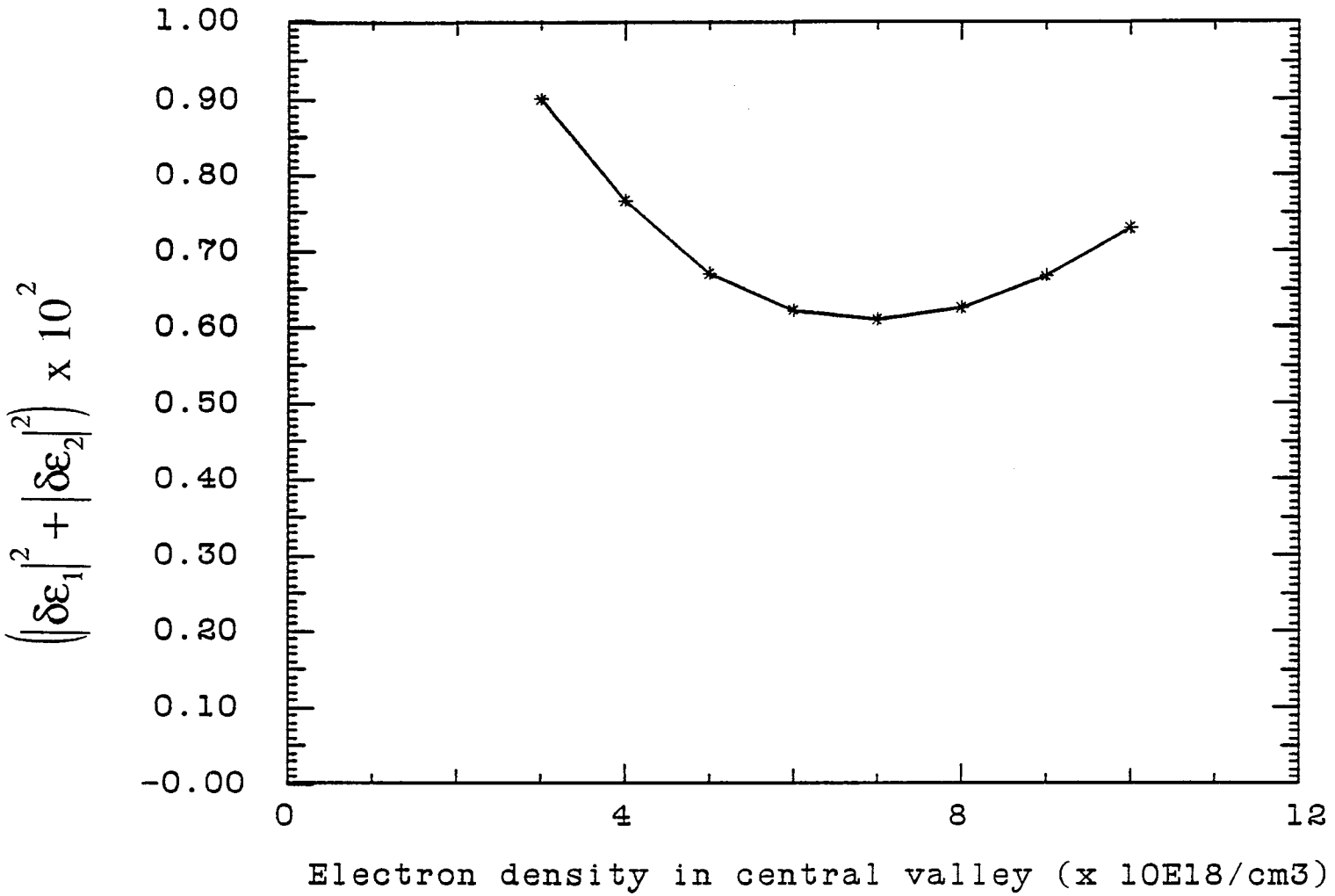

Figure 5.2.4b. $|\delta\epsilon|^2$ for a 1.65 eV probe calculated as a function of electron density in the Γ-valley. The total density, $n_e = n_h = 1.2 \times 10^{19}$ cm^{-3} and the carrier temperature = 900 K.

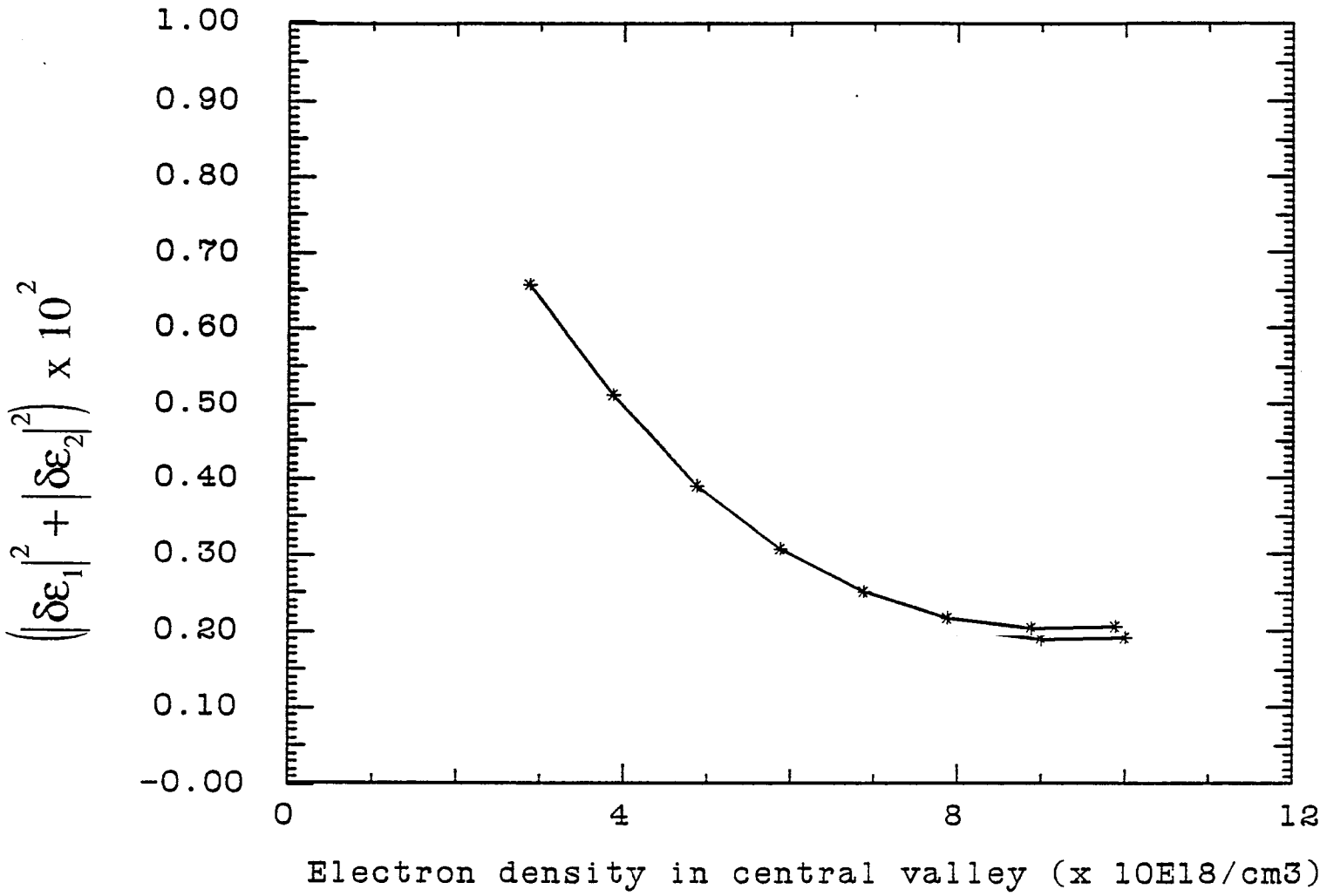

Figure 5.2.4c. $|\delta\epsilon|^2$ for a 1.71 eV probe calculated as a function of electron density in the Γ-valley. The total density, $n_e = n_h = 1.2 \times 10^{19}$ cm^{-3} and the carrier temperature = 900 K.

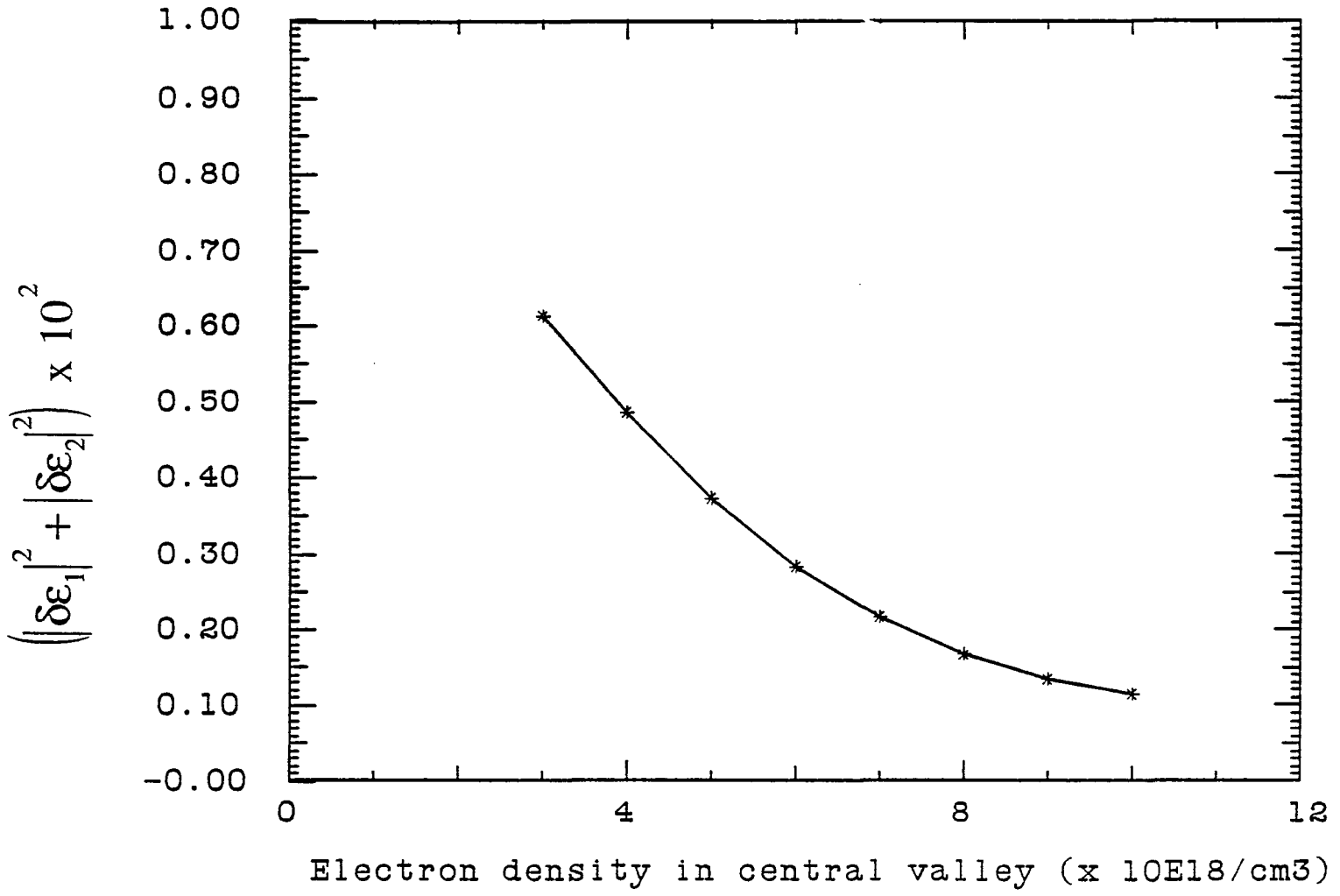

Figure 5.2.4d. $|\delta\epsilon|^2$ for a 1.77 eV probe calculated as a function of electron density in the Γ-valley. The total density, $n_e = n_h = 1.2 \times 10^{19}$ cm^{-3} and the carrier temperature = 900 K.

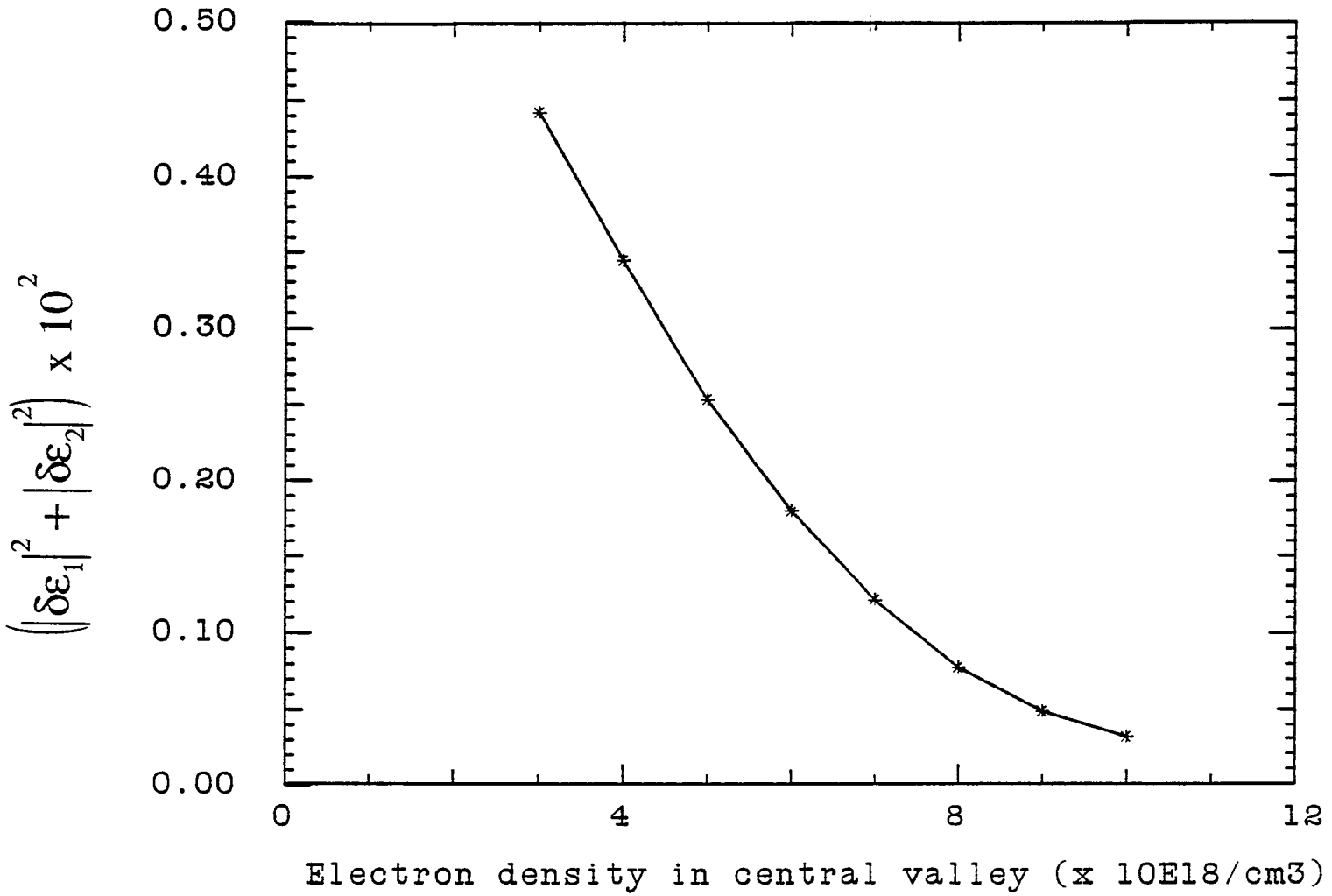

Figure 5.2.4e. $|\delta\epsilon|^2$ for a 1.84 eV probe calculated as a function of electron density in the Γ-valley. The total density, $n_e = n_h = 1.2 \times 10^{19}$ cm^{-3} and the carrier temperature = 900 K.

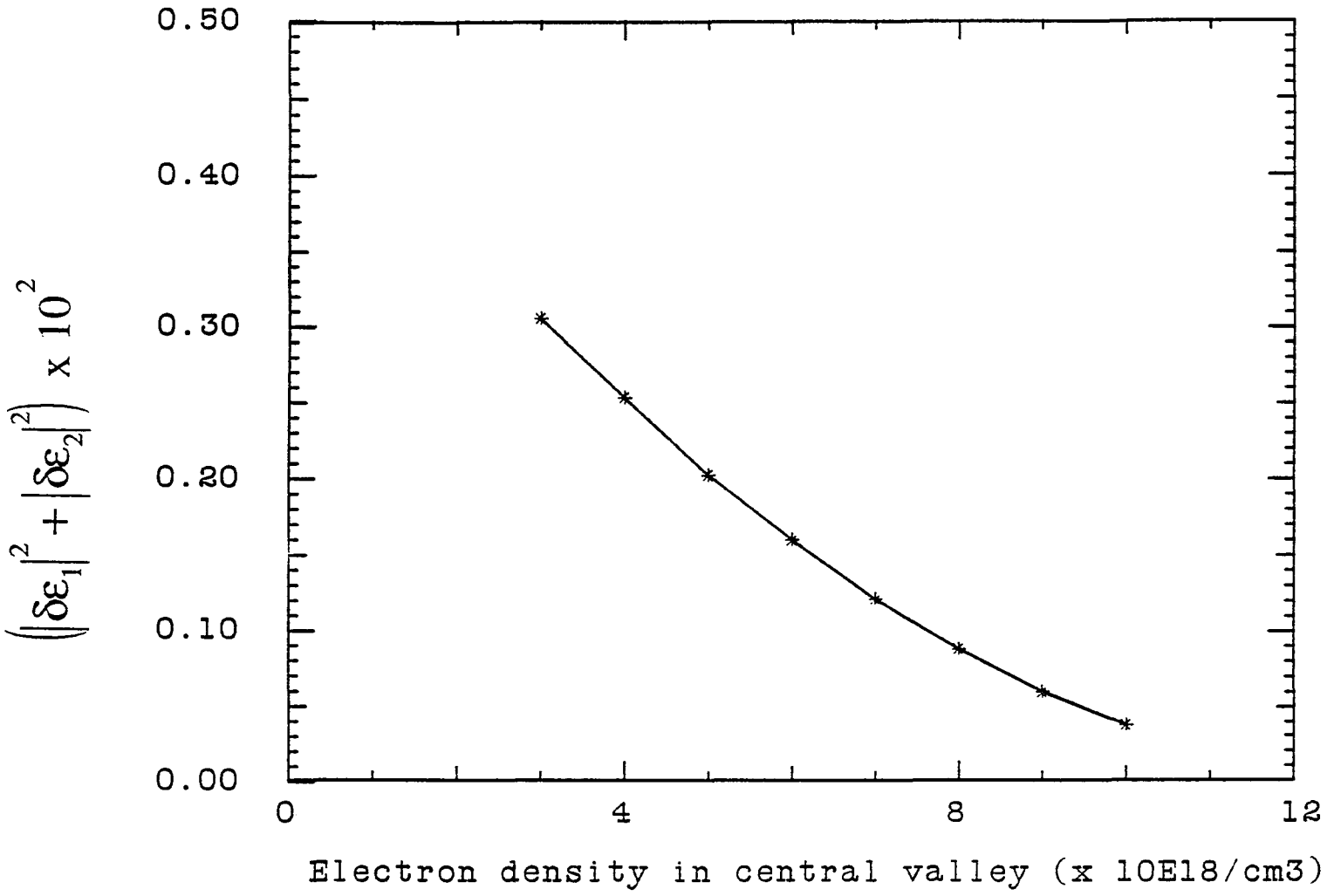

Figure 5.2.4f. $|\delta\epsilon|^2$ for a 2.01 eV probe calculated as a function of electron density in the Γ-valley. The total density, $n_e = n_h = 1.2 \times 10^{19}$ cm^{-3} and the carrier temperature = 900 K.

5.3 Experimental procedure

5.3.1 Experimental optics

The experimental apparatus used for time resolved four-wave mixing is shown in figure 5.3.1. The output of the amplified femtosecond laser system is split into three pulses. A variable delay line is placed in the optical path of each pulse. The direction of propagation of the pulses are aligned to be parallel and coplanar and then focused onto the sample. The angles that the pulses make with each other determine the direction of the scattered signal. In fig 5.3.1, the angle between pulses 2 and 3 is θ, while pulse 1 makes an angle Φ with the bisector of pulses 2 and 3, $\Phi > \theta/2$. Pulse 1 was chosen as the probe pulse and pulses 2 and 3 are the pump pulses. In each optical path a polarizer and a rotator, if necessary, was inserted to allow independent selection of each pulse's polarization.

The grating spacing was adjusted by changing the separation of the two pump pulses before focusing. This was accomplished by moving mirror M2 in fig. 5.3.1 and appropriately adjusting the delay in pulse 2. Most of the data was taken with $\theta = 4^{\circ}$ and $\Phi = 3^{\circ}$. This gives a grating spacing of 9 microns for an excitation wavelength of 620 nm. Apertures were placed after the sample to block all the scattered light except for the signal. Table 5.3.1 lists the angles for all possible first order scattering directions.

Initially data was taken with the two pump and the probe pulses at the same frequency (degenerate four-wave mixing). The beam

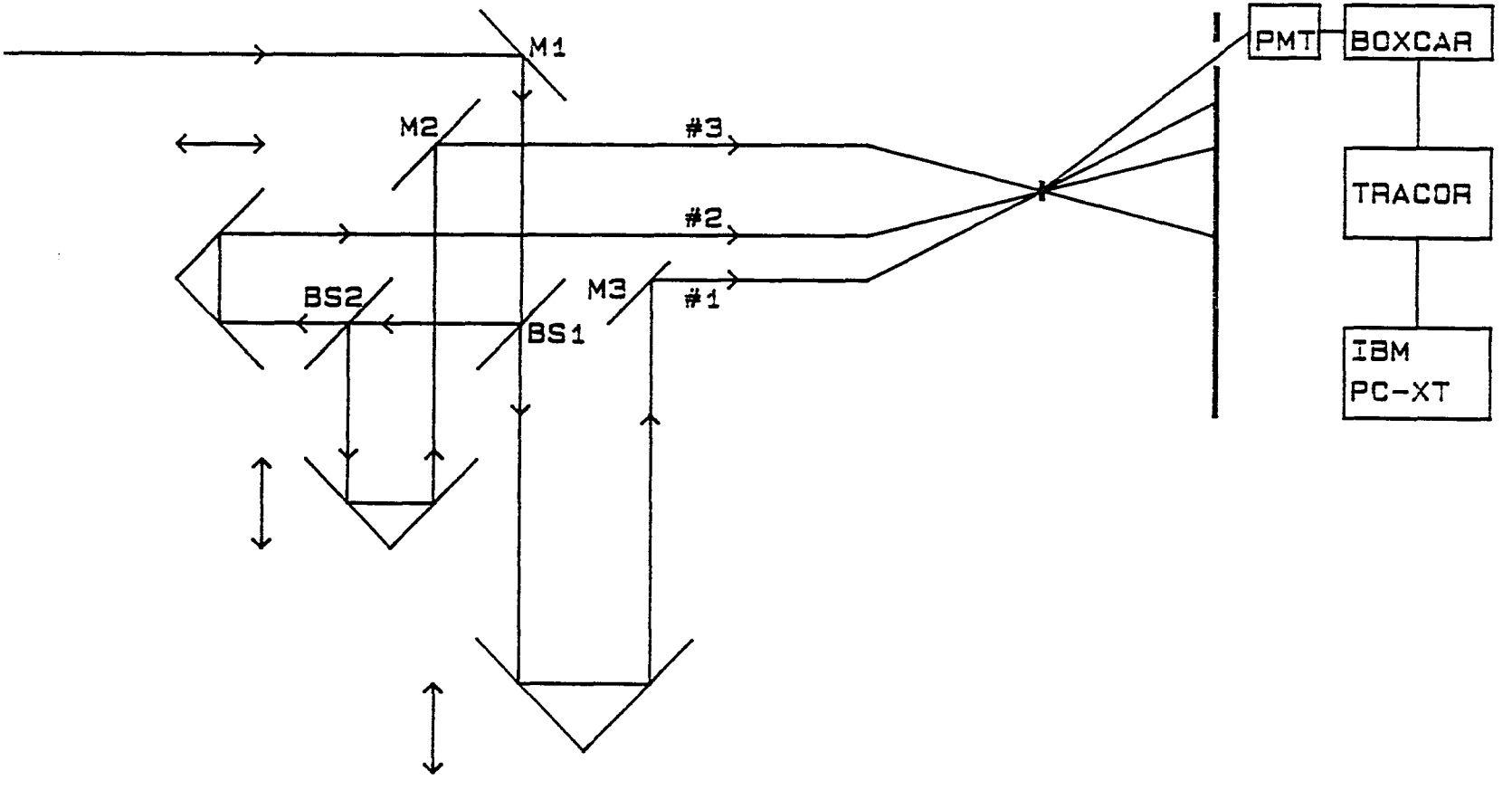

Figure 5.3.1. Experimental setup for the three pulse transient grating experiments. Pulses 2 and 3 are the pump pulses and pulse 1 is the probe. Signal is detected in the $K_1 + K_2 - K_3$ direction.

splitters were selected to give 47% of the energy to each pump pulse and 6% to the probe pulse. Later, the split in laser energy was adjusted to give 33% to each pulse. A cell of CCl_4 was inserted in the probe path and the probe pulse was focused into the cell to produce a broadband continuum probe. Filters were used to select different probe wavelengths. The total laser pulse energy was approximately 0.4 millijoules. The laser was loosely focused to a 1 mm spot size on the sample.

5.3.2 Spatial and temporal alignment of the three pulses

To insure proper spatial and temporal overlap of the 3 pulses, the sample was replaced with a KDP crystal. The alignment and optical delay of the two pump pulses was adjusted to maximize the second harmonic produced by the two pulses. Next the alignment and optical delay of the probe pulse was adjusted to maximize the second harmonic produced by the probe pulse and one of the pump pulses. It was then verified that this also maximized the second harmonic produced by the probe and the other pump pulse. When properly aligned, six second harmonic pulses, were observed on a UV card in back of the KDP crystal. This determined the temporal overlap with a resolution of under 200 fs.

In order to improve the temporal overlap of the pump pulses, a more precise alignment technique was utilized. It consists of simultaneously monitoring the self-diffraction of the pump pulses, with two identical photodiodes in the 2θ and $-\theta$ directions, as one of the pump pulses was delayed with respect to the other. The two curves

are time reversed images of each other with a separation of 50 fs between peaks. The zero delay is the midpoint of the two peaks.

5.3.3 Detection apparatus

The degenerate four-wave mixing signal was detected by a Hamamatsu vacuum photodiode and a gated boxcar integrator. The boxcar integrator was manufactured by Stanford Research Systems Inc., model SR280. The triggering of the boxcar's gate was controlled by the circuitry that triggered the Nd:YAG laser. The jitter was less than 0.5 ns and if the laser did not fire, the boxcar would not be triggered. The gate width was set to 5 ns, which was wide enough to insure that the 1 ns output of the photodiode was entirely within the gate. The averaging time of the boxcar is selected by the number of triggering events rather than a fixed time constant so an equal number of laser pulses would be detected within each time constant. The averaging time was set in the range of 10 to 30 pulses.

The analog output of the boxcar integrator was directed to the input of a signal averager, Tracor Northern model TN 1710. The signal was digitized and stored in memory. The signal averager had the capability to simultaneously digitize four different input signals and store in separate memories. The signal averager could add a preselected number of scans in memory and then output the data to an x-y plotter or to the serial port of a computer. The dwell time of the signal averager was adjusted so that each scan took from 5 to 15 minutes. The number of scans averaged was between 4 and 12.

The optical path delay was varied by a microprocessor controlled stepping motor, manufactured by Aerotech Inc. The stepping motor is a model ATS 302MM and the controller is a Unidex III. The resolution of the stepping motor is 2 microns (4 microns round trip) corresponding to 13.3 fs. The Unidex III was programmed to trigger a signal averager scan at the start of each motor translation cycle and to coordinate the motor speed and number of cycles with the signal averager dwell time and number of scans respectively. The Unidex program also halted data acquisition and motor translation during data transfer to the PC-XT.

Because of the much weaker signal with the continuum probe, the photodiode was replaced by a photomultiplier tube. A spectrometer was installed in front of the PMT for wavelength selection of the signal. Both the time constant of the boxcar and the number of individual scans had to be increased considerably to improve the signal to noise due to the very large fluctuations in the intensity of the continuum.

5.3.4 Selection of the correct scattered pulse for measuring the transient grating relaxation time

When the KDP was removed and the GaAs sample inserted, pulses in 12 different directions were observed exiting from the sample. These twelve pulses correspond to the 27 different possible phase matching combinations, given by

$$\mathbf{K}_s = \mathbf{K}_i + \mathbf{K}_j - \mathbf{K}_k \qquad (i,j,k = 1,2,3) \qquad (5.3.1a)$$

$$\omega_s = \omega_i + \omega_j - \omega_k \qquad (5.3.1b)$$

Fifteen terms are in the direction of the three transmitted pulses (the 15 terms for either i=k or j=k; and shown by directions E, F and I in fig. 5.3.2). Six of these terms (the terms where i=j≠k, directions A, C, D, G, K and L in fig. 5.3.2) are from two pulse gratings and there would be no signal if either of the two source pulses were blocked but not if the third pulse was blocked. In each of this six terms, a laser pulse is self-scattered from itself and one of the other pulses so there is only signal when the two pulses temporally overlap. This two-pulse signal has a width that depends primarily on the pulse shape and coherence length. Information about the material relaxation time can only be obtained by deconvolution of the detected signal.

The other three diffracted pulses (the six terms for which i≠j≠k, directions B, H and J in fig 5.3.2) are the **pulses of interest.** They correspond to one pulse scattering from the interference pattern of the other two pulses. This is the geometry that allows the measurement of the relaxation time of the grating by measuring the scattered intensity as a function of the probe pulse delay. For most of the three pulse transient grating curves, pulse 1 is used as the probe and the signal was detected in the B direction (given by $\mathbf{K}_s = \mathbf{K}_1 + \mathbf{K}_2 - \mathbf{K}_3$). These six terms are repeated in Eqs. 5.3.2a-f and 5.3.3a-c.

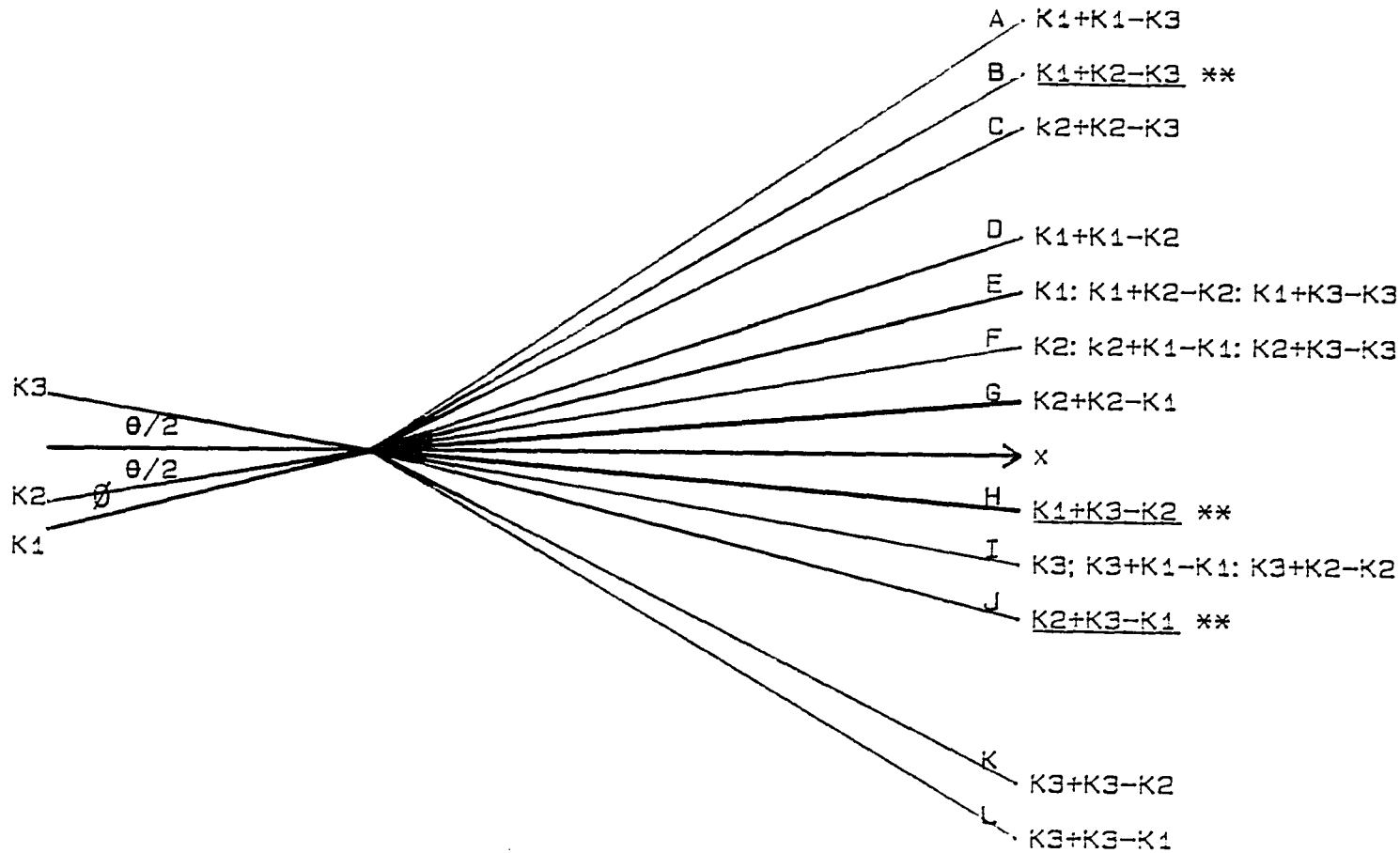

Figure 5.3.2. The twelve different first order scattering directions in a 3 pulse grating experiment. Ecah direction corresponds to combinations listed in table 5.3.1. Directions B, H, and J, involve all three pulses. Most of the data was taken in direction B. The angle between pulses 2 and 3 is θ while the angle between pulse1 and the bisector of 2 and 3 is Ø.

The source of the pulse scattering in direction B is

$$\mathbf{K}_s = \mathbf{K}_1 + \mathbf{K}_2 - \mathbf{K}_3 \qquad (5.3.2a)$$

$$\mathbf{K}_s = \mathbf{K}_2 + \mathbf{K}_1 - \mathbf{K}_3 \qquad (5.3.2b)$$

$$\omega_s = \omega_2 + \omega_1 - \omega_3 \qquad (5.3.3a)$$

and the sources for direction H and J are, respectively

$$\mathbf{K}_s = \mathbf{K}_1 + \mathbf{K}_3 - \mathbf{K}_2 \qquad (5.3.2c)$$

$$\mathbf{K}_s = \mathbf{K}_3 + \mathbf{K}_1 - \mathbf{K}_2 \qquad (5.3.2d)$$

$$\omega_s = \omega_3 + \omega_1 - \omega_2 \qquad (5.3.3b)$$

$$\mathbf{K}_s = \mathbf{K}_2 + \mathbf{K}_3 - \mathbf{K}_1 \qquad (5.3.2e)$$

$$\mathbf{K}_s = \mathbf{K}_3 + \mathbf{K}_2 - \mathbf{K}_1 \qquad (5.3.2f)$$

$$\omega_s = \omega_2 + \omega_3 - \omega_1 \quad . \qquad (5.3.3c)$$

In each case the last pulse in Eqs. 5.3.2a-f (the term with the - sign) acts as only a pump pulse while the other two pulses act as both pump and probe. Experimentally, if all pulses are at the same frequency, delaying pulse 3 (2, 1) while measuring the signal in direction B (H, J) gives only the coherence length of the pulse. The

Source terms	Scattered angle (first order)	θ_{sx} (x-axis)	θ_{sp} (probe)
$K_s = K_1 + K_1 - K_1$	$\Phi + \Phi - \Phi$	+3.00	0.00
$K_s = K_1 + K_1 - K_2$	$\Phi + \Phi - \theta/2$	+4.00	+1.00
$K_s = K_1 + K_1 - K_3$	$\Phi + \Phi + \theta/2$	+7.96	+4.96
$K_s = K_1 + K_2 - K_1$	$\Phi + \theta/2 - \Phi$	+2.00	-1.00
$K_s = K_1 + K_2 - K_2$	$\Phi + \theta/2 - \theta/2$	+3.00	0.00
$K_s = K_1 + K_2 - K_3$	$\Phi + \theta/2 + \theta/2$	+6.97	+3.97
$K_s = K_1 + K_3 - K_1$	$\Phi - \theta/2 - \Phi$	-2.00	-5.00
$K_s = K_1 + K_3 - K_2$	$\Phi + \theta/2 - \theta/2$	-1.00	-4.00
$K_s = K_1 + K_3 - K_3$	$\Phi - \theta/2 + \theta/2$	+3.00	0.00
$K_s = K_2 + K_1 - K_1$	$\theta/2 + \Phi - \Phi$	+2.00	0.00
$K_s = K_2 + K_1 - K_2$	$\theta/2 + \Phi - \theta/2$	+3.00	1.00
$K_s = K_2 + K_1 - K_3$	$\theta/2 + \Phi + \theta/2$	+6.97	+4.97
$K_s = K_2 + K_2 - K_1$	$\theta/2 + \theta/2 - \Phi$	+1.00	-1.00
$K_s = K_2 + K_2 - K_2$	$\theta/2 + \theta/2 - \theta/2$	+2.00	0.00
$K_s = K_2 + K_2 - K_3$	$\theta/2 + \theta/2 + \theta/2$	+5.98	+3.98
$K_s = K_2 + K_3 - K_1$	$\theta/2 - \theta/2 - \Phi$	-2.99	-4.99
$K_s = K_2 + K_3 - K_2$	$\theta/2 - \theta/2 - \theta/2$	-2.00	-4.00
$K_s = K_2 + K_3 - K_3$	$\theta/2 - \theta/2 + \theta/2$	+2.00	0.00
$K_s = K_3 + K_1 - K_1$	$-\theta/2 + \Phi - \Phi$	-2.00	0.00
$K_s = K_3 + K_1 - K_2$	$-\theta/2 + \Phi - \theta/2$	-1.00	+1.00
$K_s = K_3 + K_1 - K_3$	$-\theta/2 + \Phi + \theta/2$	+3.00	+5.00
$K_s = K_3 + K_2 - K_1$	$-\theta/2 + \theta/2 - \Phi$	-2.99	-0.99
$K_s = K_3 + K_2 - K_2$	$-\theta/2 + \theta/2 - \theta/2$	-2.00	0.00
$K_s = K_3 + K_2 - K_3$	$-\theta/2 + \theta/2 + \theta/2$	+2.00	+4.00
$K_s = K_3 + K_3 - K_1$	$-\theta/2 - \theta/2 - \Phi$	-6.96	-4.96
$K_s = K_3 + K_3 - K_2$	$-\theta/2 - \theta/2 - \theta/2$	-5.98	-3.98
$K_s = K_3 + K_3 - K_3$	$-\theta/2 - \theta/2 + \theta/2$	-2.00	0.00

Table 5.3.1. The 27 combinations for four-wave mixing. The third column gives the first order scattering angles with respect to the x-axis. The last column gives the first order scattering with respect to the probe (the first pulse listed after the equal sign in column one) calculated for $\Phi=3^\circ$ and $\theta=4^\circ$. The combinations involving all three pulses are in bold.

delay of either of the other two pulses gives the grating relaxation time as well as the coherence spike.

The different scattering directions are summarized in table 5.3.1. The usual terminology is to give the angle relative to the probe beam's incident direction (θ_{sp} in table 5.3.1) but in order to clarify the scattering directions, the angles (θ_{sx} in table 5.3.1) are given with respect to the bisector of pulses 2 and 3 (the x-axis in fig. 5.3.2) as well as the probe pulse. For example, the sixth term, $K_s = K_1 + K_2 - K_3$, in table 5.3.1 corresponds to pulse 1 scattering from the grating formed by pulses 2 and 3. The signal is diffracted by an angle of 3.97° with respect to the propagation direction of pulse 1 and 6.97° with respect to the x-axis. But the twelfth term in table 5.3.1, $K_s = K_2 + K_1 - K_3$, corresponds to pulse 2 scattering from the grating formed by pulses 1 and 3. The scattering angle is different, $\theta_{sp} = 4.97^\circ$, then for the sixth term because the pulses 1 and 3 intersect at a different angle then pulses 2 and 3 (i.e. different grating spacing). However since the incident direction of pulse 2 was different than pulse 1, the scattered signal emerges in the same direction as for the sixth term ($\theta_{sx} = 6.97^\circ$).

The expression for the transient four-wave mixing signal for a three level system (excited state, ground state and reservoir) with the electric dipole approximation, in the direction $\mathbf{K}_s = \mathbf{K}_1 + \mathbf{K}_2 - \mathbf{K}_3$, is given by[28,31]

$$G(\tau) = \int_{-\infty}^{+\infty} |E_1(t+\tau)|^2 \left| \int_{-\infty}^{t} E_2(\Theta)E_3^*(\Theta)\ A(t-\Theta)d\Theta \right|^2 dt \qquad (5.3.4a)$$

$$+ \int_{-\infty}^{+\infty} |E_2(t)|^2 \left| \int_{-\infty}^{t} E_1(\Theta+\tau)E_3^*(\Theta)\ A(t-\Theta)d\Theta \right|^2 dt \qquad (5.3.4b)$$

where $A(t-\Theta)$ is the response of the medium. The variable delay is in pulse 1. The term 5.3.4a, is the source term for the signal with E_1 as the probe field and E_2 and E_3 as the source (pump) fields. E_1 will vanish if E_2 and E_3 are not coherent. The term 5.3.4b, when E_1 is delayed, gives the coherence spike if E_1 and E_3 are coherent. In this case, E_1 is also a source field while E_2 is a probe field. In this direction, E_3 is always a source field. If A(t) is long compared to the pulse width, then by delaying E_1 (E_2), one measures the grating relaxation from term 5.3.4a (5.3.4b) and the coherence spike from 5.3.4b (5.3.4a). The delay of E_3 only gives the coherence spike. If A(t) is short compared to the laser pulse both 5.3.4a and 5.3.4b essentially gives the laser pulse width. Any information about A(t) must be learned from deconvoluting the curves.

The decision to select the pulse scattered in the direction given by $\mathbf{K}_1 + \mathbf{K}_2 - \mathbf{K}_3$ was based on the ease of isolating the light in this direction by apertures. Based on this, pulse 1 was selected as the probe pulse and the pulse intensities were adjusted to give the 6%, 47%, and 47% energy distribution to pulses 1, 2 and 3, respectively, as stated previously. When the probe pulse's polarization is parallel to the pump pulses' polarization, one detects

the grating signal (Eq. 5.3.4a) and the coherence spike (Eq. 5.3.4b) but if the probe polarization is perpendicular to the pump pulses' polarization, the signal has the polarization of the probe while the coherence spike has the polarization of pump pulse 2. A polarizer in front of the detector can eliminate detection of the coherence spike. Initially, data was taken with all three pulses parallel and they clearly exhibit the coherence spike. Curves taken at a later date, had the probe perpendicularly polarized to the pumps and no coherence spike is evident in the data. In non-degenerate four-wave mixing, ($\omega_1 \neq \omega_2 = \omega_3$) there is no coherence spike at the probe frequency.

5.4 Discussion of experimental results

5.4.1 Three pulse concentration grating data with degenerate pump and probe pulses

In this section, the data was collected with all three pulses at the same wavelength (6200 Å). The pump pulses were parallel polarized (P). Initial data was taken with the probe polarization parallel to the pumps, later the probe polarization was rotated to S. In this case, the coherence spike intensity was greatly reduced and its polarization (P) was orthogonal to the signal (S). The source of the coherence spike, in the signal direction, is pulse 2 scattering from the grating formed by pulses 1 and 3 and has the polarization of pulse 2. Also, if pulses 1 and 3 are orthogonally polarized, they form an orientation grating which, for GaAs, is much less efficient then the concentration grating formed by pulses 2 and 3. Most of the data was taken with a 4° angle between the pump pulses and a 3° angle between the probe and the bisector of the pump pulses.

Experimental data was collected over a range of pump intensities, grating spacing and sample temperatures (from 4 K to 295 K). The signal decays in 5 ± 1 ps which corresponds to a grating relaxation time of 10 ± 2 ps and is independent of pump intensity and grating spacing. The diffraction efficiency is proportional to the square of the index modulation. Using the model of only carrier recombination and diffusion (neglecting changes in absorption), the grating lifetime is given by[12]

$$\frac{1}{T_g} = \frac{4\pi^2 D}{d^2} + \frac{1}{T_r} \qquad (5.4.1)$$

where d is the grating spacing, D is the diffusion coefficient, and t_r is the carrier lifetime.

The experimental results are inconsistent with either recombination or diffusion as the relaxation mechanism of the grating. The radiative lifetime of GaAs is nanoseconds[59] although at these carrier densities auger recombination dominates. At a carrier density of 1×10^{19} cm^{-3}, with Auger and two-body recombination coefficients[60] of $\approx 7 \times 10^{-31}$ cm^6 sec^{-1} and 3.4×10^{-11} cm^3 sec^{-1}, the effective recombination time is several hundred picoseconds. Auger recombination can be further ruled out by the lack of intensity dependence to the grating relaxation. Typical curves are displayed in figures 5.4.1a-d; the laser intensities are changed by a factor of 16 between the high intensity (fig. 5.4.1a) and the low intensity (fig. 5.4.1d). The existence of a long (greater than 20 ps) component to the grating signal in the non-degenerate case is further evidence that the recombination time is longer than twice the 5 ps decay of the grating.

For similar reasons, diffusion can be eliminated as the mechanism for the grating decay. The long component for near band edge measurements shows that the spatial modulation of the carriers exists for a time much longer than 10 ps. Data was taken with the angle between the pump beams equal to 2, 4 and 8 degrees corresponding to a grating spacing of 18, 9 and 4 microns.

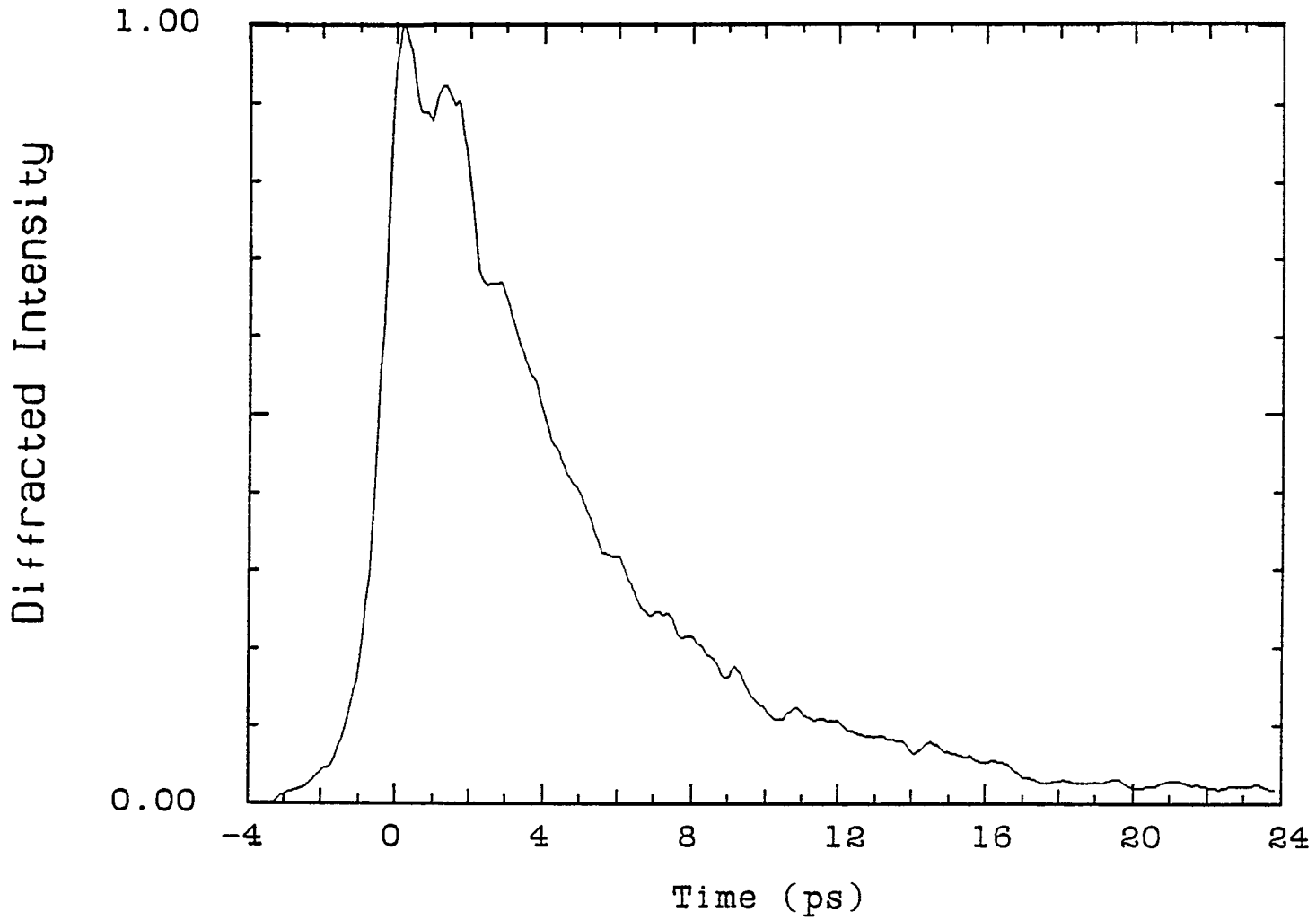

Figure 5.4.1a. Diffracted intensity from a three pulse concentration grating. The pump pulses are at maximum intensity. The grating spacing is 9 microns and the probe photon energy is 2 eV.

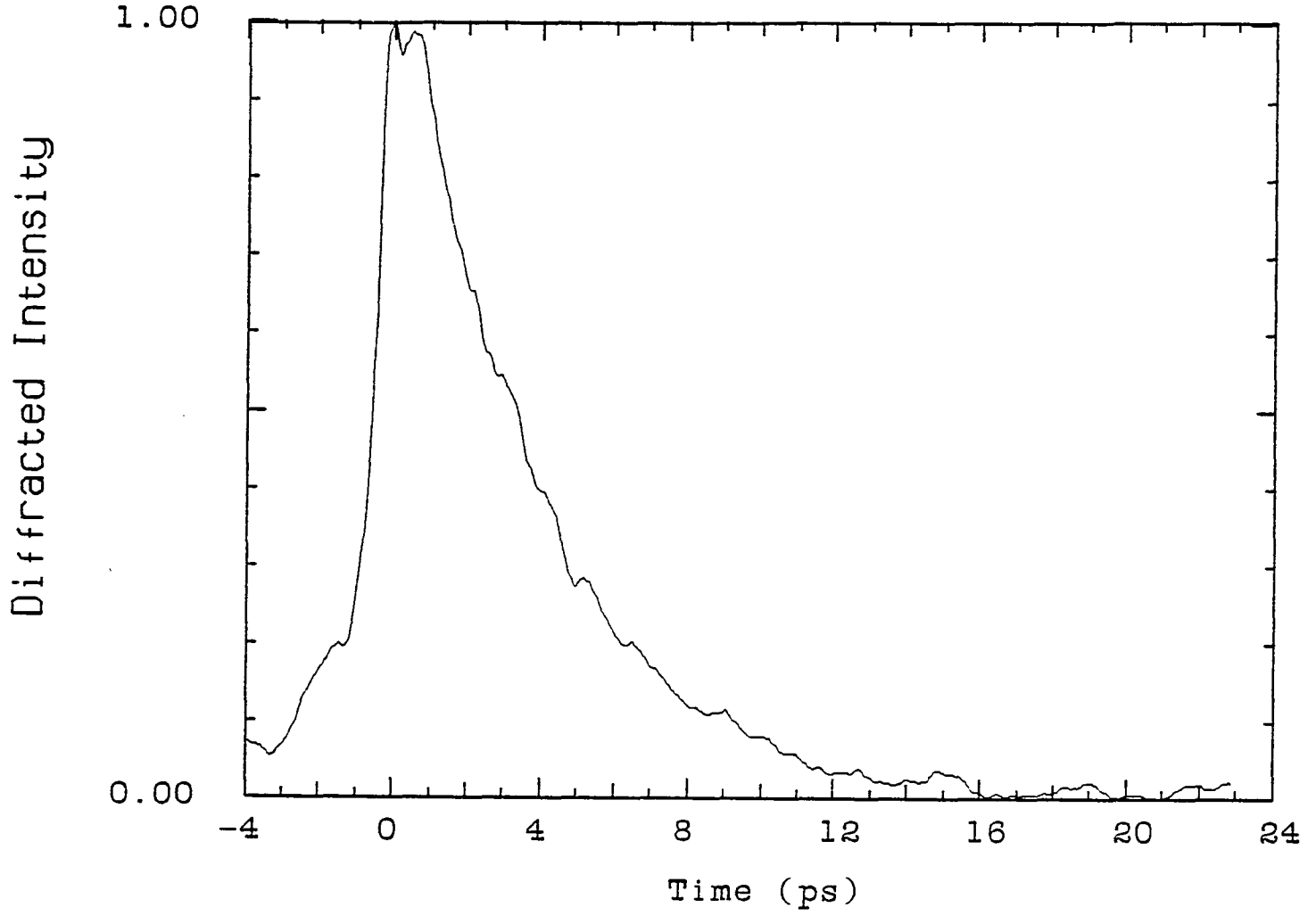

Figure 5.4.1b. Diffracted intensity from a three pulse concentration grating. The pump pulses are attenuated by a factor of three. The grating spacing is 9 microns and the probe energy is 2 eV.

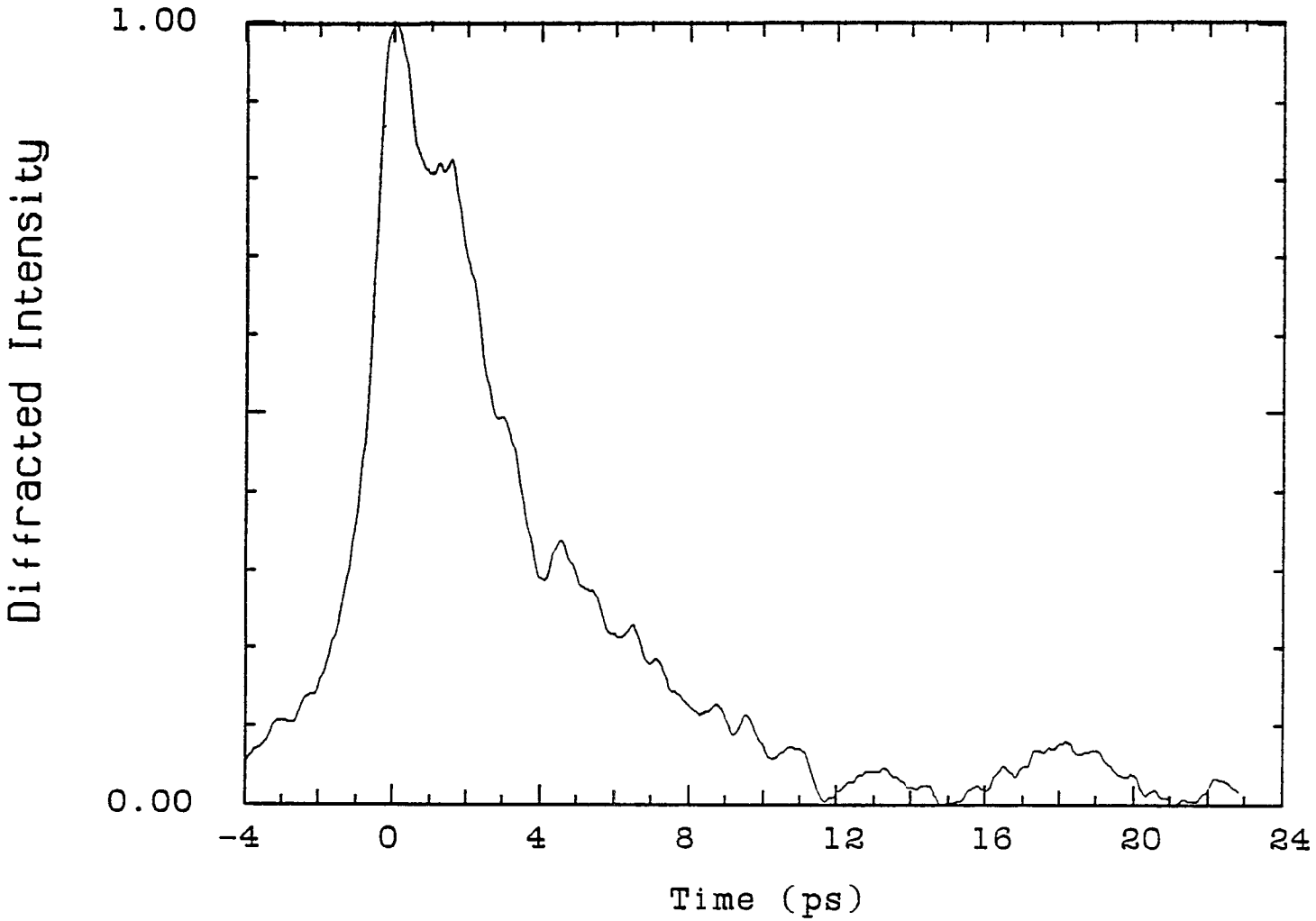

Figure 5.4.1c. Diffracted intensity from a three pulse concentration grating. The pump pulses are attenuated by a factor of five. The grating spacing is 9 microns and the probe energy is 2 eV.

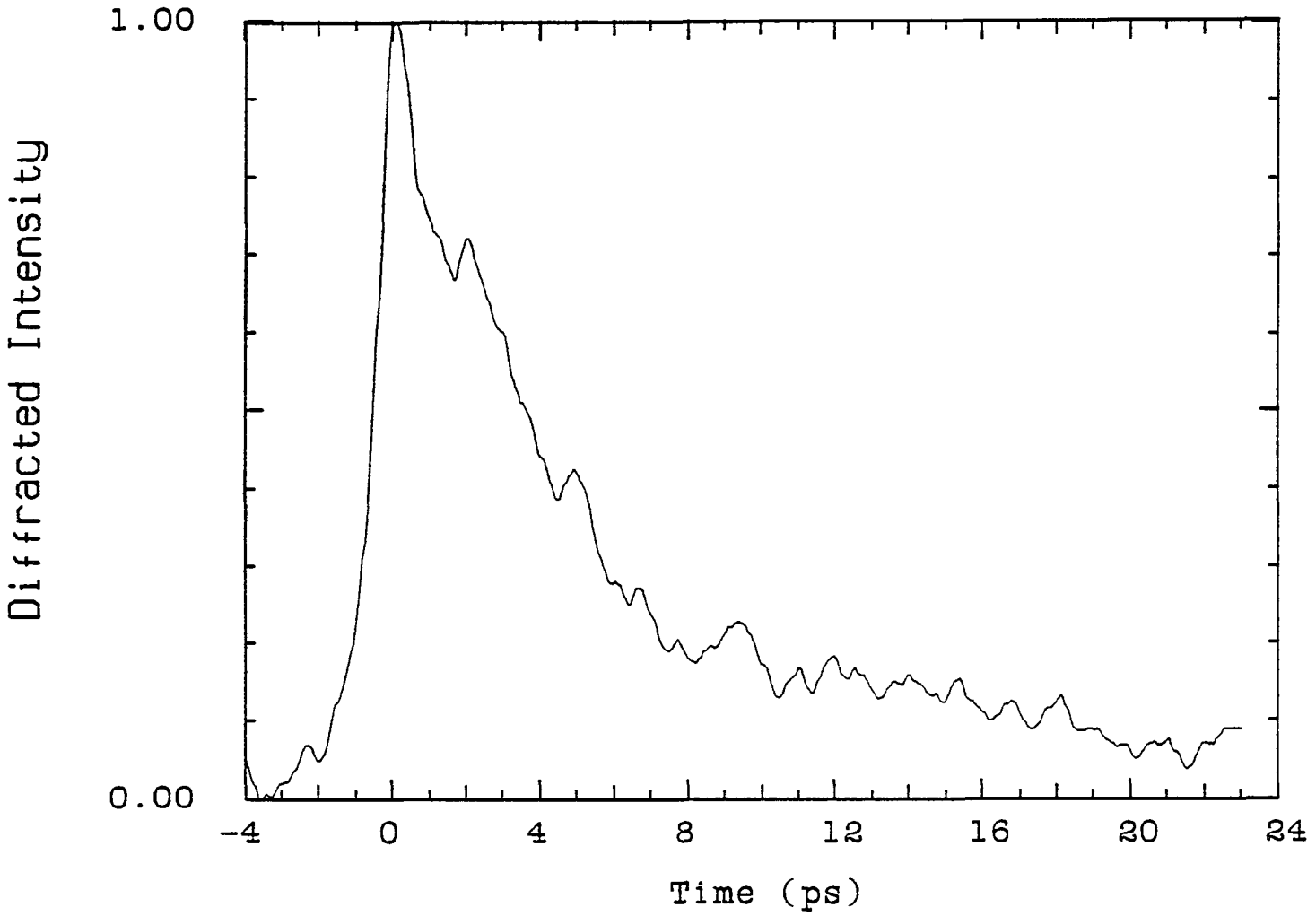

Figure 5.4.1d. Diffracted intensity from a three pulse concentration grating. The pump pulses are attenuated by a factor of sixteen. The grating spacing is 9 microns and the probe energy is 2 eV.

Figures 5.4.2a and b show the diffracted signal taken at grating spacings of 4 and 18 microns; the data in figures 5.4.1a-d were taken with a 9 micron grating spacing. The probe polarization was rotated 90° with respect to the pump pulses and a polarizer was used to block the coherence spike. For all three angles, the signal decayed in 5 ps, giving a different value for the diffusion coefficient at each grating spacing. The values of D given by Eq.5.4.1 would be 1.6×10^4, 4×10^3 and 8×10^2 cm^2 sec^{-1} for the 18, 9 and 4 micron spacings, respectively, if the grating decay mechanism was diffusion. There is no physical reason for different gratings spacings to have different diffusion coefficients. These values of D are also much larger than those in the literature.[33] Ballistic diffusion as the grating decay mechanism is contradicted by the lack of dependence of the grating decay time on the grating spacing or pump intensity.

5.4.2 Three pulse concentration grating data with non-degenerate pump and probe

Since the degenerate four-wave mixing data made it apparent that the source of the GaAs non-linearity was not a simple population grating but also depended on the carrier temperature and distribution function, additional transient grating data was taken over a range of probe energies.

The energy distribution of the three pulses was adjusted (by changing BS1 in figure 5.3.1) to be approximately equal. Neither the direction nor polarization of pump pulses 2 and 3 at 6200 Å were

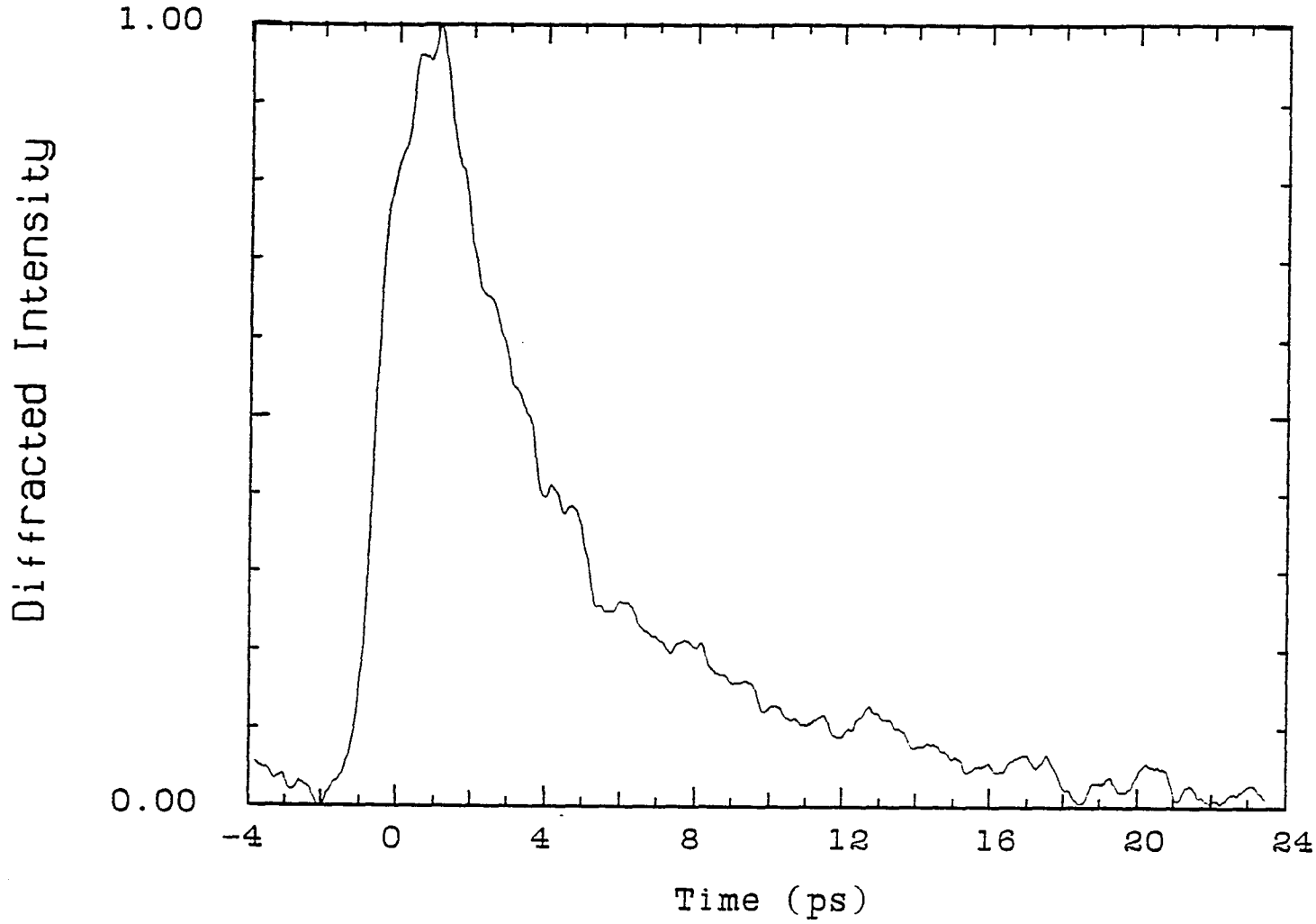

Figure 5.4.2a. Diffracted intensity at a grating spacing of 4 microns.

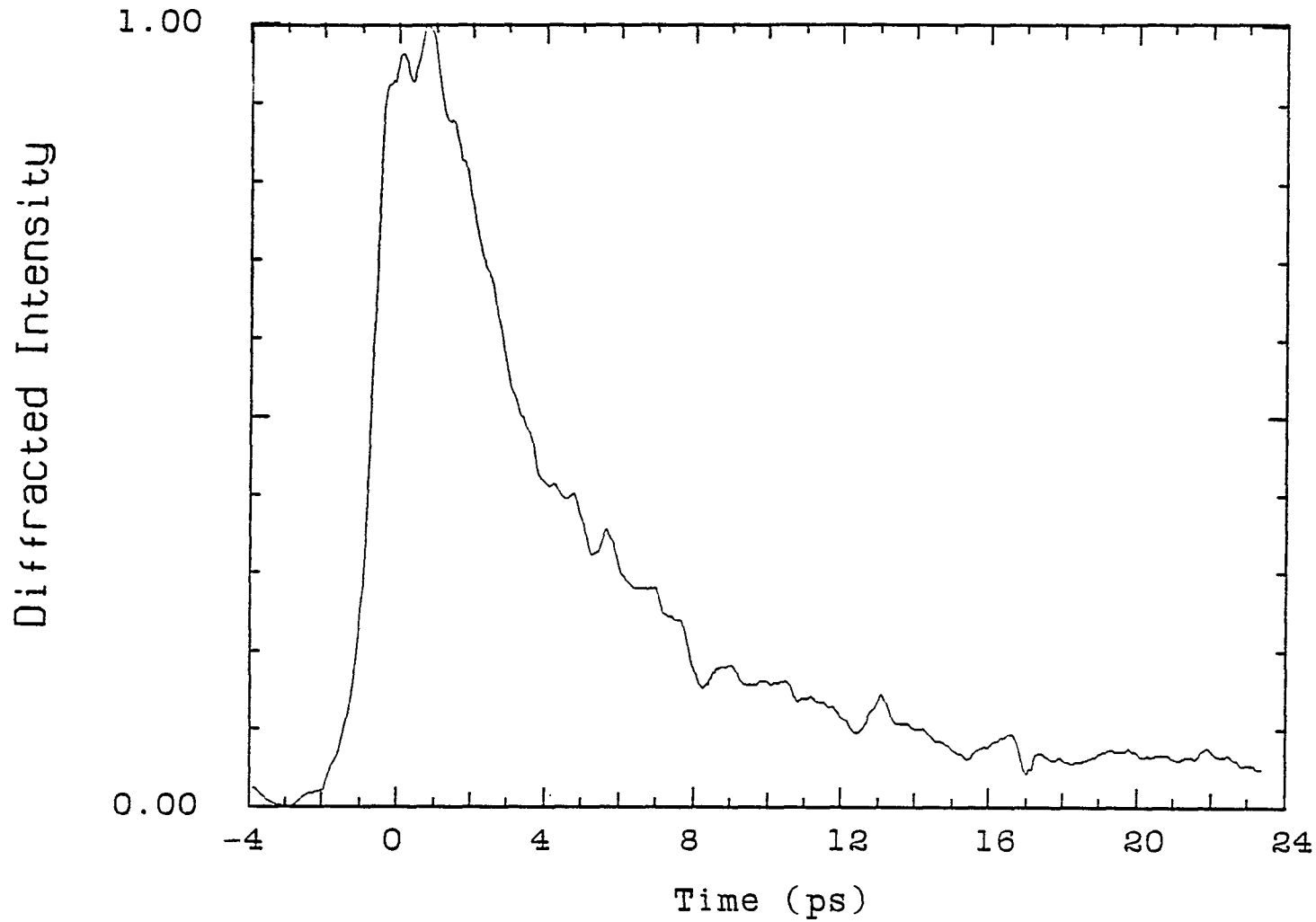

Figure 5.4.2b. Diffracted intensity at a grating spacing of 18 microns.

changed. However a 1 cm cell of CCl_4 was inserted in the path of probe (pulse 1). Pulse 1 was tightly focused into the cell by a convex lens of 5 cm focal length and then recollimated by a 2.5 cm focal lens. The direction of propagation of the probe was not changed. A 2-59 corning filter was inserted in the probe path to reduce the intensity of the probe at 6200 Å but not at longer wavelengths. The delay line was adjusted to compensate for the longer travel time of the probe. The photodiode detector was replaced by a spectrometer and an R943 photomultiplier tube with a GaAs response.

The transient grating curves taken at probe energies of 1.84 eV (6750 Å), 1.77 eV (7000 Å), 1.71 eV (7250 Å), 1.653 eV (7500 Å), 1.60 eV (7750 Å),, and 1.55 eV (8000 Å) are shown in figures 5.4.3a-f. The pump photon energy of 2.0 eV was not changed. The curves exhibit a two component relaxation, a short component of 4-6 picoseconds and a long component, longer than the experimental delay line. The amplitude of the long component relative to the short component increases as the probe energy is tuned closer to the band gap. This is consistent with the model in section 5.2, where, at energies high above band gap, the four-wave mixing signal in GaAs depends on the distribution of electrons between the different valleys (the fast component) but near (or below) band gap, the intraband term dominates and the grating decays by recombination and diffusion.

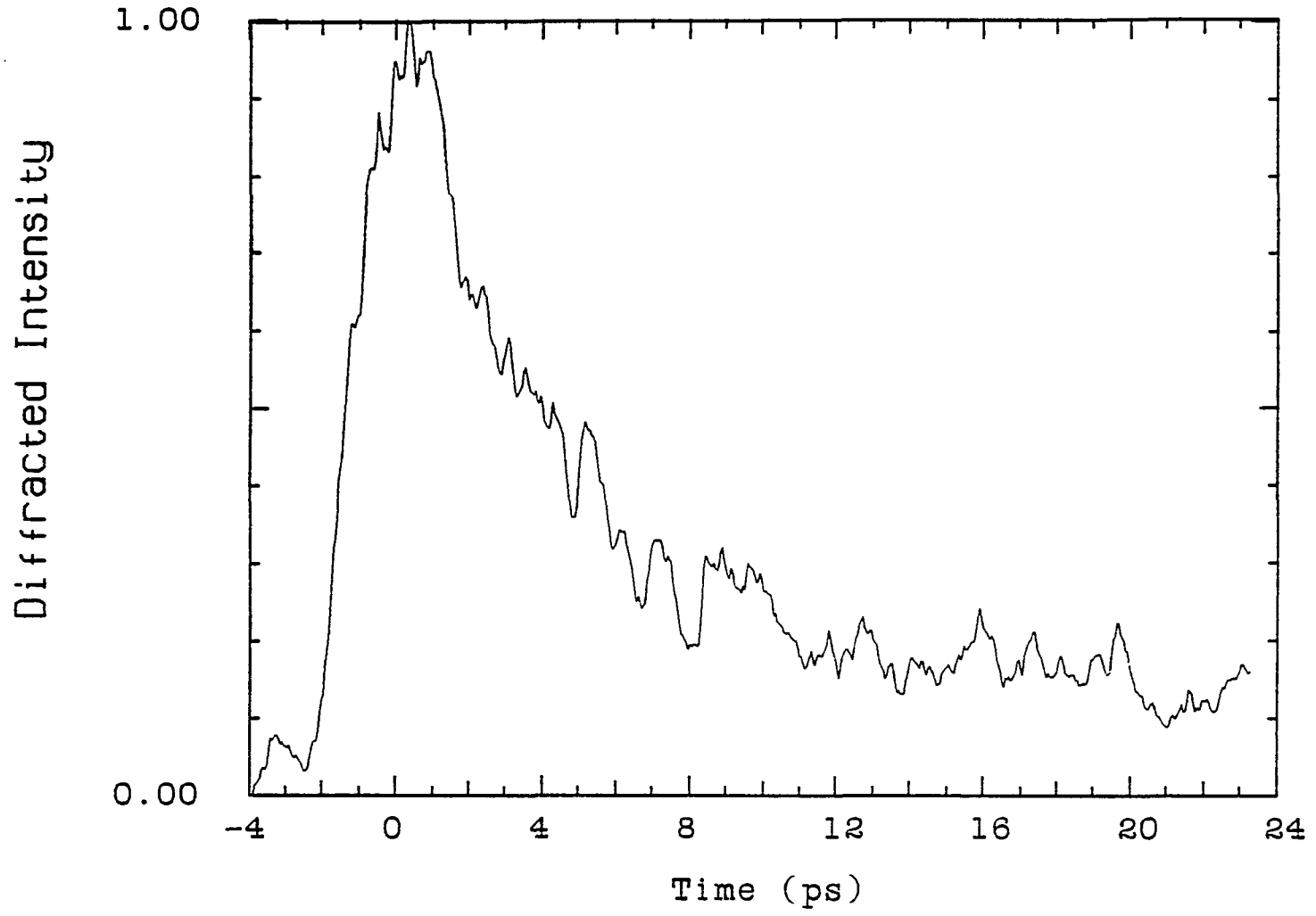

Figure 5.4.3a. Diffracted intensity for a probe energy of 1.84 eV. The pump energy is 2.0 eV. The grating spacing is 9 microns.

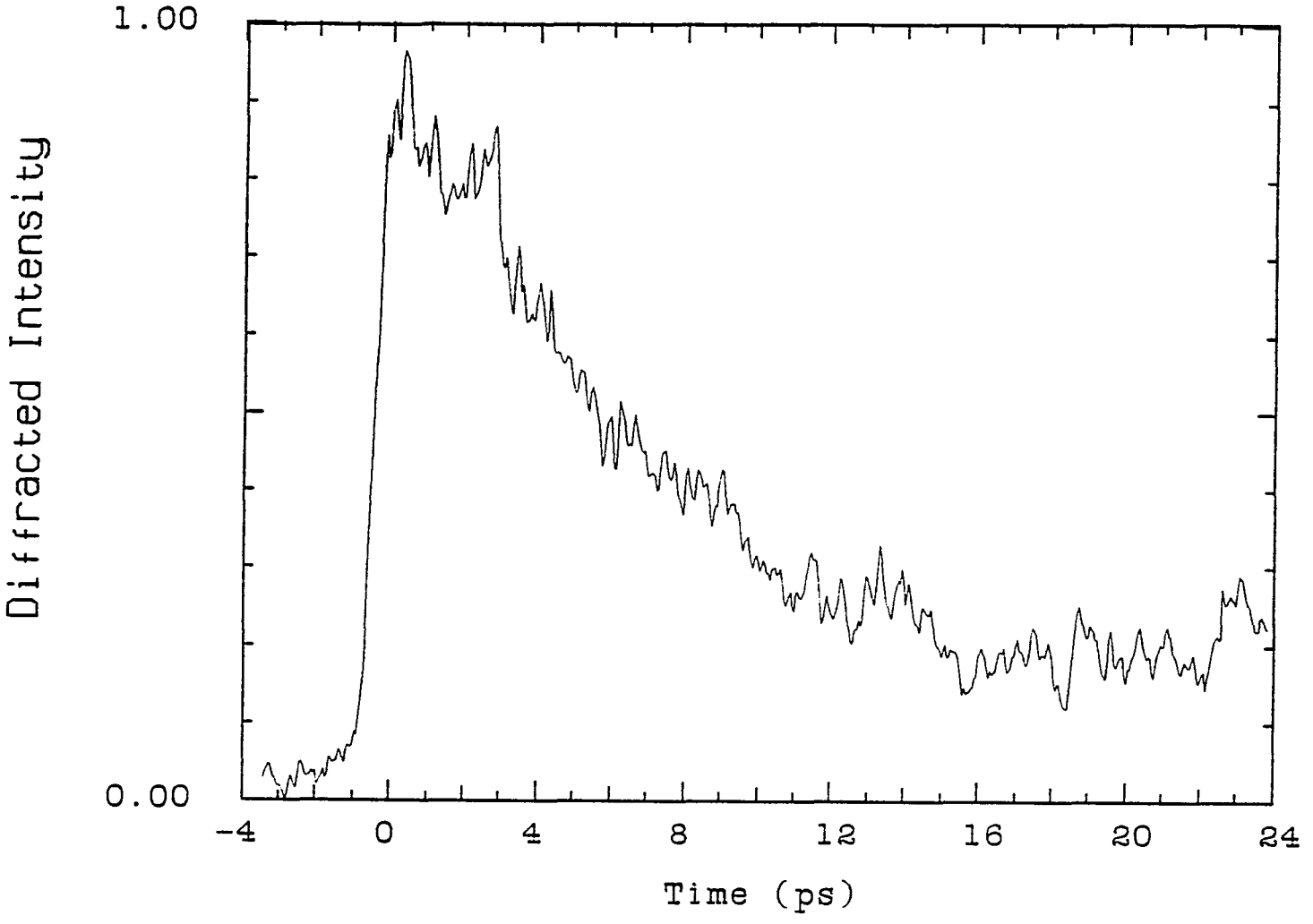

Figure 5.4.3b. Diffracted intensity for a probe energy of 1.77 eV. The pump energy is 2.0 eV. The grating spacing is 9 microns.

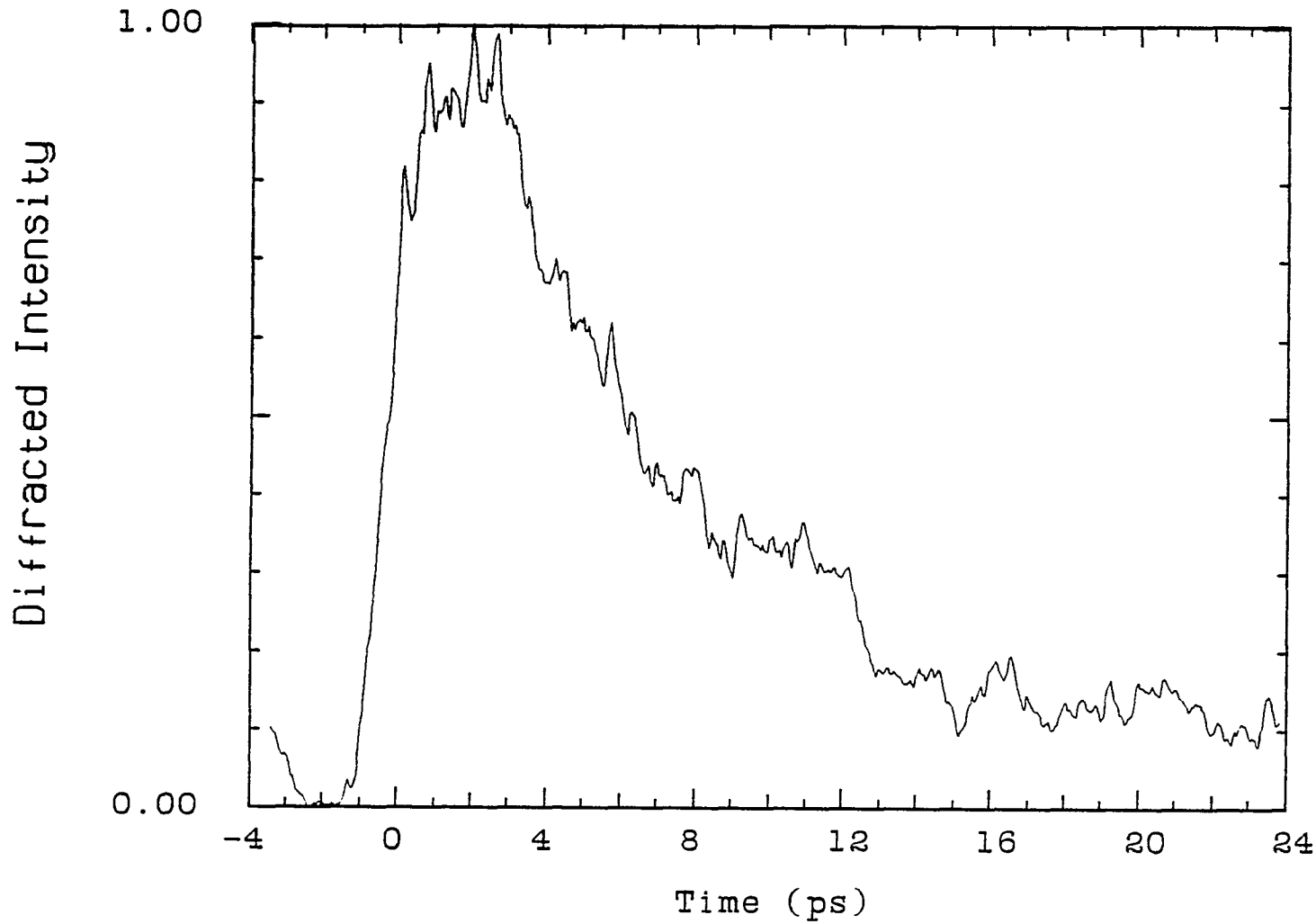

Figure 5.4.3c. Diffracted intensity for a probe energy of 1.71 eV. The pump energy is 2.0 eV. The grating spacing is 9 microns.

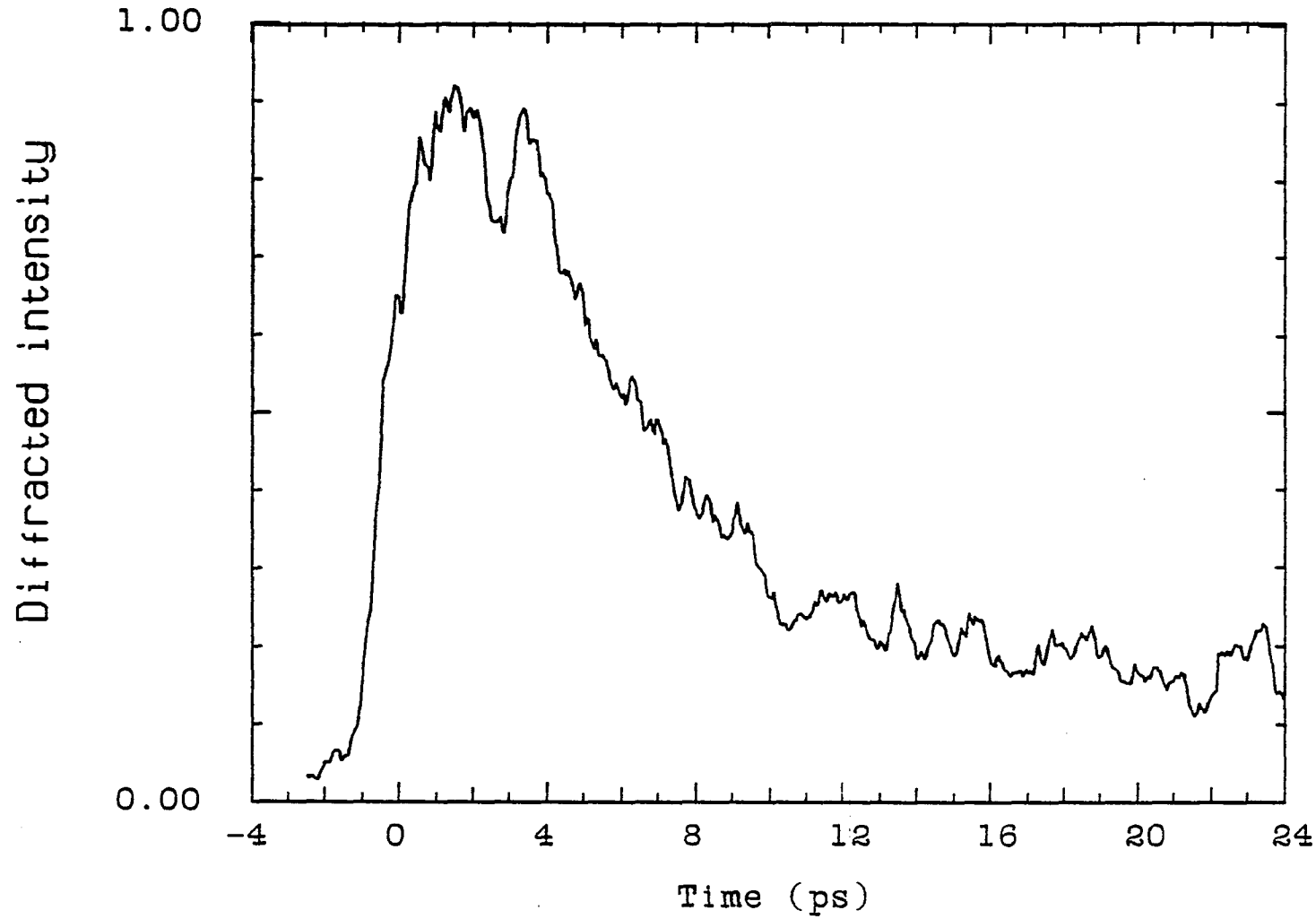

Figure 5.4.3d. Diffracted intensity for a probe energy of 1.65 eV. The pump energy is 2.0 eV. The grating spacing is 9 microns.

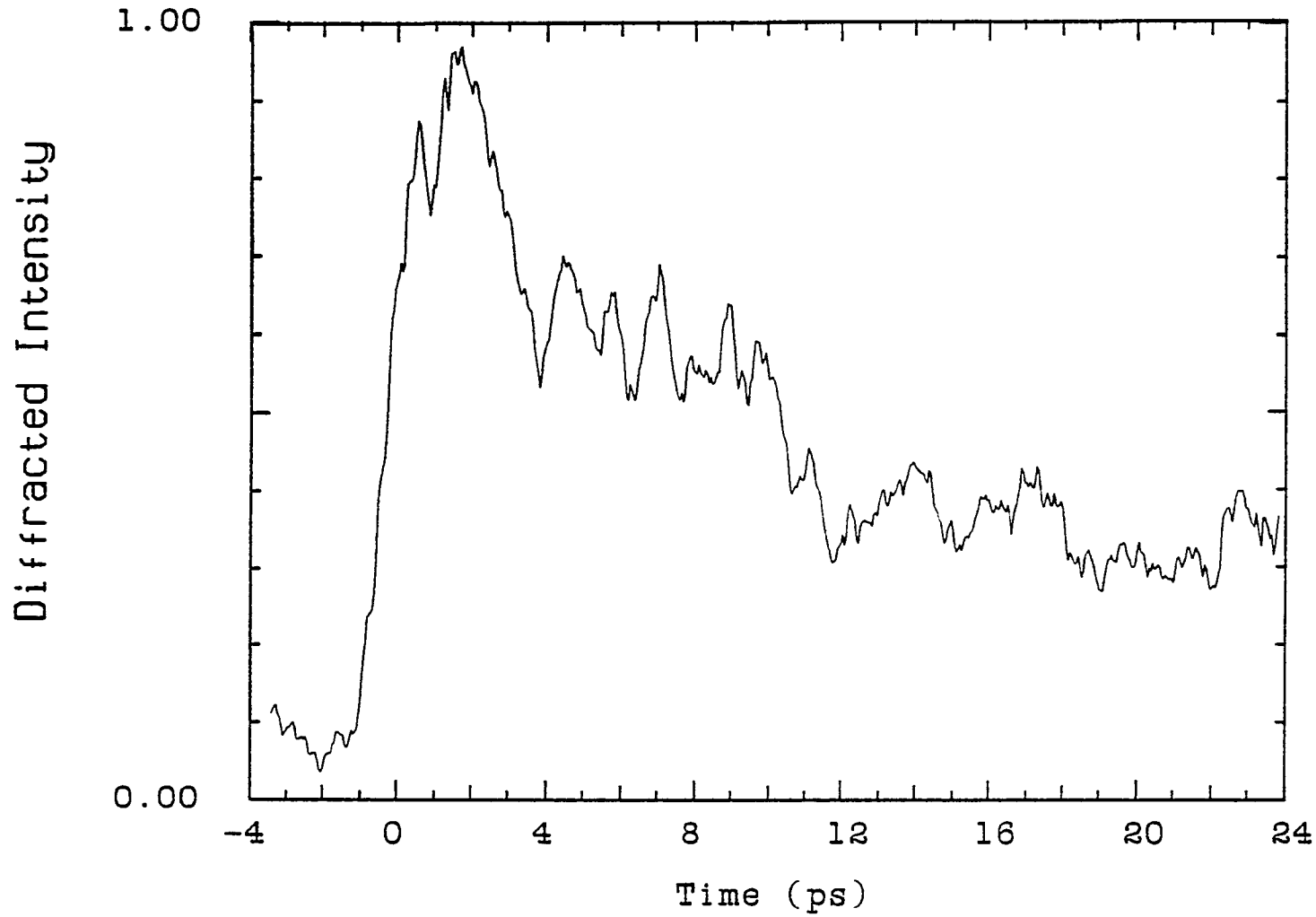

Figure 5.4.3e. Diffracted intensity for a probe energy of 1.60 eV. The pump energy is 2.0 eV. The grating spacing is 9 microns.

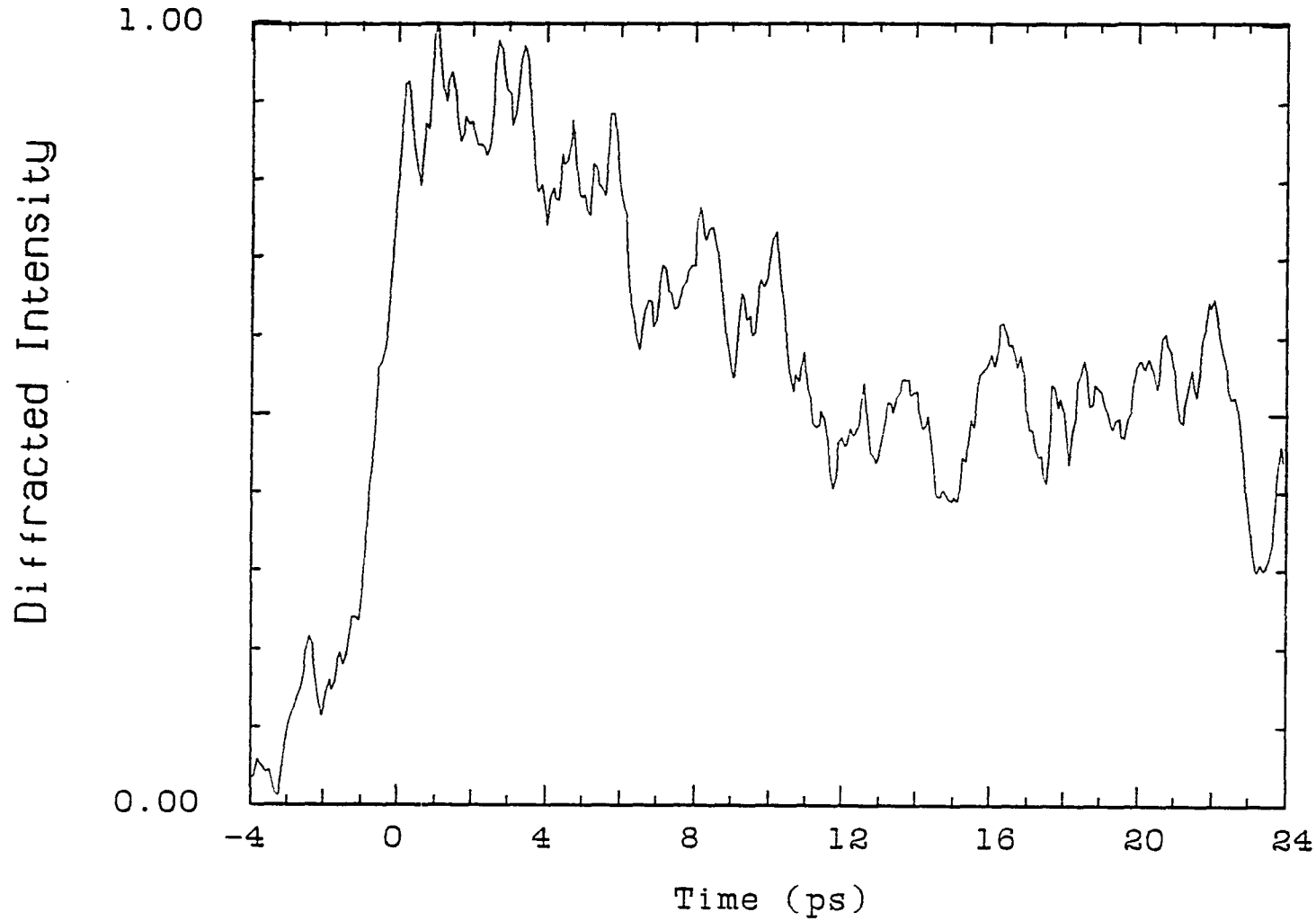

Figure 5.4.3f. Diffracted intensity for a probe energy of 1.55 eV. The pump energy is 2.0 eV. The grating spacing is 9 microns.

5.4.3 Determination of the effective L → Γ intervalley scattering time in GaAs from transient grating data

In order to understand the grating decay under these experimental conditions, one must examine the change in the dielectric function under intense optical excitation. As discussed in section 5.2, the change in the dielectric function is caused by both changes to the refractive index (real part of n) and to the absorption (imaginary part of n). Using the model presented in section 5.2, the grating decay is caused by the increase in the interband contribution to $\delta\varepsilon_1$ and to $\delta\varepsilon_2$ as electrons scatter back to the Γ-valley from the L-valleys.

The scattering time for electrons to scatter from the Γ to the L-valleys has been measured to be under 80 fs.[51,52] The return time, due to the smaller density of states in the Γ-valley is about 25 times slower. Under the conditions of high carrier density and temperature, a thermalized distribution will have a significant fraction of electrons in the Γ-valley with enough energy to transfer to the L-valley (0.286 eV). Therefore electrons can undergo multiple scattering back and forth between the Γ and L-valleys before relaxing to the bottom of the Γ-valley. Shah et al[61] using measurements of the photoluminescence risetime and the Ensemble Monte Carlo method have determined the intervalley return rate. Their results give an L to Γ intervalley scattering time of 2.7 ps.

The effective L → Γ scattering time is determined by fitting the four-wave mixing signal with the calculation of $|\delta\varepsilon|^2$ in section

5.2.7. Theoretical calculations of $|\delta\varepsilon|^2$, assuming cooling rates of 0, 50, 100, and 150 K/ps, were compared to the degenerate four-wave mixing curves. The carrier temperature at 1 ps is taken to be 1400 K and the final temperature is 500 K (this is consistent with the pump and probe absorption data of chapter 4). The excited population $n_e = n_h = 1.2 \times 10^{19}$ cm^{-3}. This is 60% of the estimated carrier density determined in the pump and probe absorption of chapter 4; the smaller density was used since the grating spot size was 60% larger than the pump spot size in the absorption data. It is assumed that only 20% of the electrons are in the Γ-valley at 1 ps.[53]

The proceedure used to fit the curves, consisted of first plotting $|\delta\varepsilon|^2$ at 2.0 eV, as function of the electron distribution (as in figure 5.2.4f) for temperatures in the range of 500 to 1400 K at 50 K intervals. The curves were normalized such that $|\delta\varepsilon|^2 = 0.9$ for the carrier conditions of: T= 1400 K, $n_h = 1.2 \times 10^{19}$ cm^{-3}, $n_{e\Gamma} = 2.5 \times 10^{19}$ cm^{-3} and $n_{eL} = 9.5 \times 10^{19}$ cm^{-3}, as described in the previous paragraph; 0.9 is the measured diffracted intensity relative to the intensity at t=0 (see the curve in figure 5.4.1a). Next, the carrier temperatures were calculated at 1 ps intervals for cooling rates of 0, 50, 100 and 150 K/ps. For each assumed cooling rate, at 1 ps intervals, it was determined which Γ and L valley populations would give a relative value of $|\varepsilon|^2$ consistent with the measured decrease in the diffracted intensity. This gave $n_L(t)$. An exponential decay, for the L-valley population, was assumed, of the form

$$n_L(t) = n_L(0) \exp\left(\frac{-t}{\tau eff}\right) \qquad (5.4.2)$$

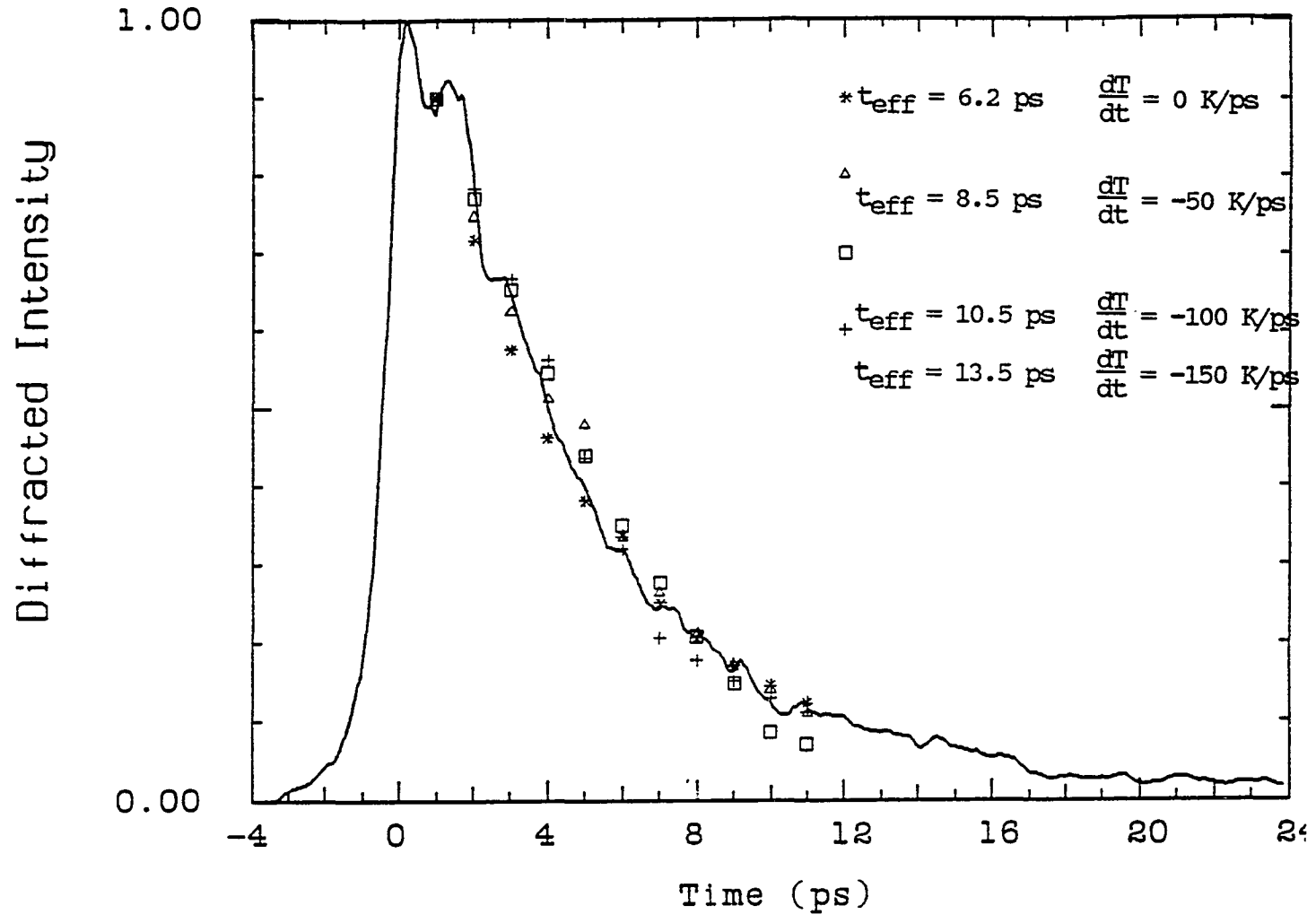

Figure 5.4.4. Typical transient grating curve and the calculated grating signal for different cooling rates and effective L to Γ scattering times.

where τ_{eff} is the effective L → Γ scattering time. A linear least squares fit was made for $Ln[n_L(t)]$ to give τ_{eff}. This was repeated for cooling rates of 0, 50, 100 and 150 K/ps. The L → Γ times as determined by this method were 6.2, 8.2, 10.5, and 13.5 ps respectively. A typical grating signal curve is shown in fig 5.4.4 as well as the grating signal calculated for: τ_{eff} = 6.2 ps, $\frac{dT}{dt}$ = 0 K/ps; τ_{eff} = 8.2 ps, $\frac{dT}{dt}$ = -50 K/ps; τ_{eff} = 10.5 ps, $\frac{dT}{dt}$ = -100 K/ps; and τ_{eff} = 13.5 ps, $\frac{dT}{dt}$ = -150 K/ps.

The distribution and temperature dependence of $\delta\varepsilon$ differs with probe frequency, hence the non-degenerate transient grating data can, in principle, be analyzed to separate the component of the grating relaxation due to carrier cooling from the component due to L → Γ scattering. A combination of the poor signal to noise of the non-degenerate grating signal and other corrections omitted from the theoretical calculations (i.e. band gap renormalization, band non-parabolicity, etc) make it impossible to do a more precise separation of the L → Γ grating component from the component due to carrier cooling. However, from the results of pump and probe absorption measurements, the carrier cooling rate is estimated to be between 50 and 100 K/ps. From this, the L → Γ effective scattering rate is determined to be 9 ± 2 ps.

5.4.4 Orientation grating in GaAs

GaAs has cubic symmetry and therefore the 21 non-zero elements of $\chi^{(3)}_{ijkl}$ are those for which i=j=k=l, i=j and k=l, i=k and j=l, and i=l and j=k. The other 60 terms are zero.[31]

In a three pulse orientation grating experiment, with the two pump pulses polarized in the $\hat{y}$ and $\hat{z}$ direction, and the probe pulse polarized in the $\hat{z}$ direction, $\chi^{(3)}_{zzyz}$ and $\chi^{(3)}_{yzyz}$ are the source terms for the nonlinear polarization. The $\chi^{(3)}_{yzyz}$ term is the $\hat{y}$ polarized pump pulse scattering from the grating formed by the other pump pulse and the probe pulse. The signal is $\hat{y}$ polarized and is the population grating signal discussed previously. $\chi^{(3)}_{zzyz}$ is the source term for the $\hat{z}$ polarized probe scattering from the orientation grating formed by the pump pulses. From symmetry, for a cubic material this term should be zero.

In GaAs, the conduction band is S-like and the valence bands are P-like. Most (>60%) of the electrons photoexcited by a 2.0 eV laser are excited from the heavy-hole band. These electrons are excited with their momentum oriented perpendicular to the electric field. The orientation of these planes change as the direction of the electric field polarization rotates across the sample. This lowers the symmetry of the GaAs by creating a preferred direction (perpendicular to the momentum planes) and $\chi^{(3)}_{zzyz}$ is no longer equal to zero. This orientation grating decays as the electrons and holes randomize direction in k-space by carrier-carrier, polar phonon emission and intervalley (for electrons) scattering. Oudar[27] studied the polarization dependence of pump and probe absorption results to measure the momentum relaxation time in GaAs. It was found to be 190 fs. This work was done close to band edge, where there was no phonon emission and at moderate carrier concentrations ($\approx 10^{17}$).

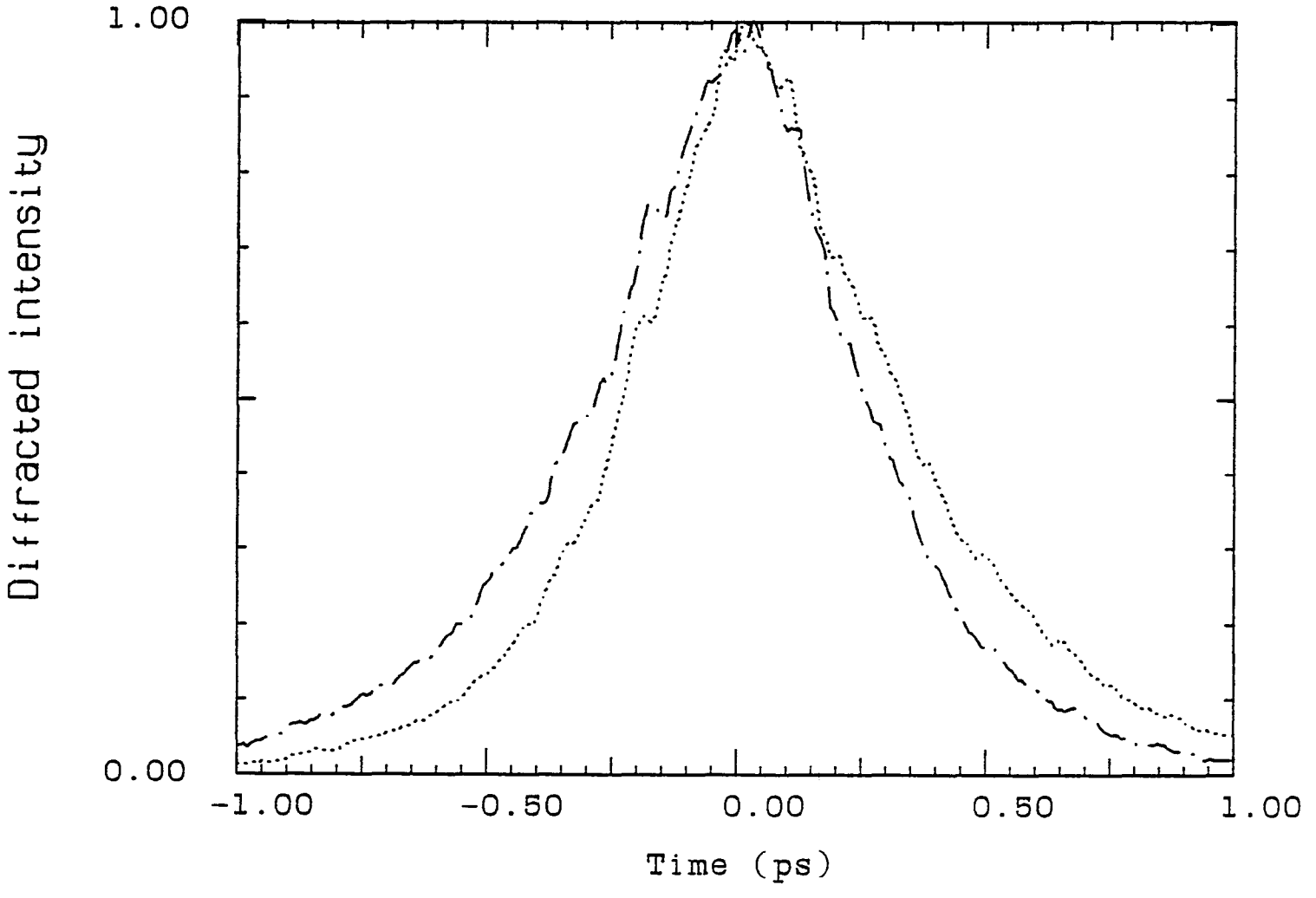

Figure 5.4.5. Two pulse orientation grating signal in $K_2 + K_2 - K_3$ and $K_3 + K_3 - K_2$ directions. The two diffracted signals are monitored simultaneously. T_{shift} = 65 fs.

The three pulse orientation grating experiment did not resolve the momentum relaxation time. Shorter pulses of less than 100 fs should be used to determine t_M. The detected signal was approximately equal to the pulse autocorrelation and depended principally on the pulse width, and the exactness of the temporal overlap of the pump pulses. Deconvolution of the signal is impossible due to the poor signal to noise and the lack of information about the exact pulse shape (which was highly chirped).

Even though the temporal resolution was poor, an alternate attempt was made to estimate the momentum relaxation time from the orientation grating signal. The probe pulse was blocked and the signal in the 2θ and $-\theta$ directions were detected simultaneously by two photodiodes. The signal was in directions "C" ($\mathbf{K}_2 + \mathbf{K}_2 - \mathbf{K}_3$) and "K" ($\mathbf{K}_3 + \mathbf{K}_3 - \mathbf{K}_2$) in figure 5.3.2. Using only two pulses simplified the temporal alignment. Since the two signals were detected simultaneously, fluctuations in the laser bandwidth or pulse width would not distort the data. A typical set of curves are shown in figure 5.4.5. Pulse #2 was delayed from -1.7 to + 1.7 ps. In the $\mathbf{K}_2 + \mathbf{K}_2 - \mathbf{K}_3$ direction, pulse #2 is both a pump as well as the probe pulse and therefore this diffracted signal is temporally delayed slightly due to the response of the material. In the $\mathbf{K}_3 + \mathbf{K}_3 - \mathbf{K}_2$ direction, pulse #3 is both a pump and the probe pulse. The diffracted signal is slightly shifted to earlier times (a negative delay for pulse #2 is a positive time delay for pulse #3).

The shift in time between signals in the 2θ and $-\theta$ directions

gives a measure of the momentum relaxation times. The temporal shift in the two curves in figure 5.4.5 at the intensity half maximum point is 65 fs. From this data and the analysis to be discussed in the next section, the momentum relaxation time is estimated to be 120 fs.

An expression for the diffracted signal in the $\mathbf{K}_2 + \mathbf{K}_2 - \mathbf{K}_3$ direction is given by[28,31]

$$G_2(\tau) = \int_{-\infty}^{+\infty} |E_2(t+\tau)|^2 \left| \int_{-\infty}^{t} E_2(\Theta+\tau)E_3^*(\Theta)\, A(t-\Theta)d\Theta \right|^2 dt \qquad (5.4.3)$$

and in the $\mathbf{K}_3 + \mathbf{K}_3 - \mathbf{K}_2$ direction, the diffracted signal is given by

$$G_3(\tau) = \int_{-\infty}^{+\infty} |E_3(t-\tau)|^2 \left| \int_{-\infty}^{t} E_3(\Theta-\tau)E_2^*(\Theta)\, A(t-\Theta)d\Theta \right|^2 dt \qquad (5.4.4)$$

where A(t), for an orientation grating, is the response of the GaAs to the anisotropic momentum distribution. It is clear that $G_2(\tau) = G_3(-\tau)$. Any asymmetry in $G(\tau)$ is due to the finite response of the material. If A(t) were a δ-function, $G(\tau)$ would be symmetric about τ

Consider a gaussian pulse, $I = I_o \exp(^{-t^2}/_{\tau_p 2})$, and an exponential response, $A(t) = A_o \exp(^{-t}/_{\tau_M})$, where τ_M is the momentum relaxation time. The inner integral in Eq 5.4.3 can be expressed in terms of an error function. Eq. 5.4.3 becomes

$$G(\tau) = \int_{-\infty}^{\infty} \exp\left[-\frac{t^2}{\tau_p^2} - \frac{\tau^2}{2\tau_p^2} - \frac{\tau}{\tau_M} - \frac{2t}{\tau_M} + \frac{\tau_p^2}{2\tau_M^2}\right] \mathrm{erfc}^2\left[-\frac{t}{\tau_p} - \frac{\tau}{2\tau_p} + \frac{\tau_p}{2\tau_M}\right] dt \ . \qquad (5.4.5)$$

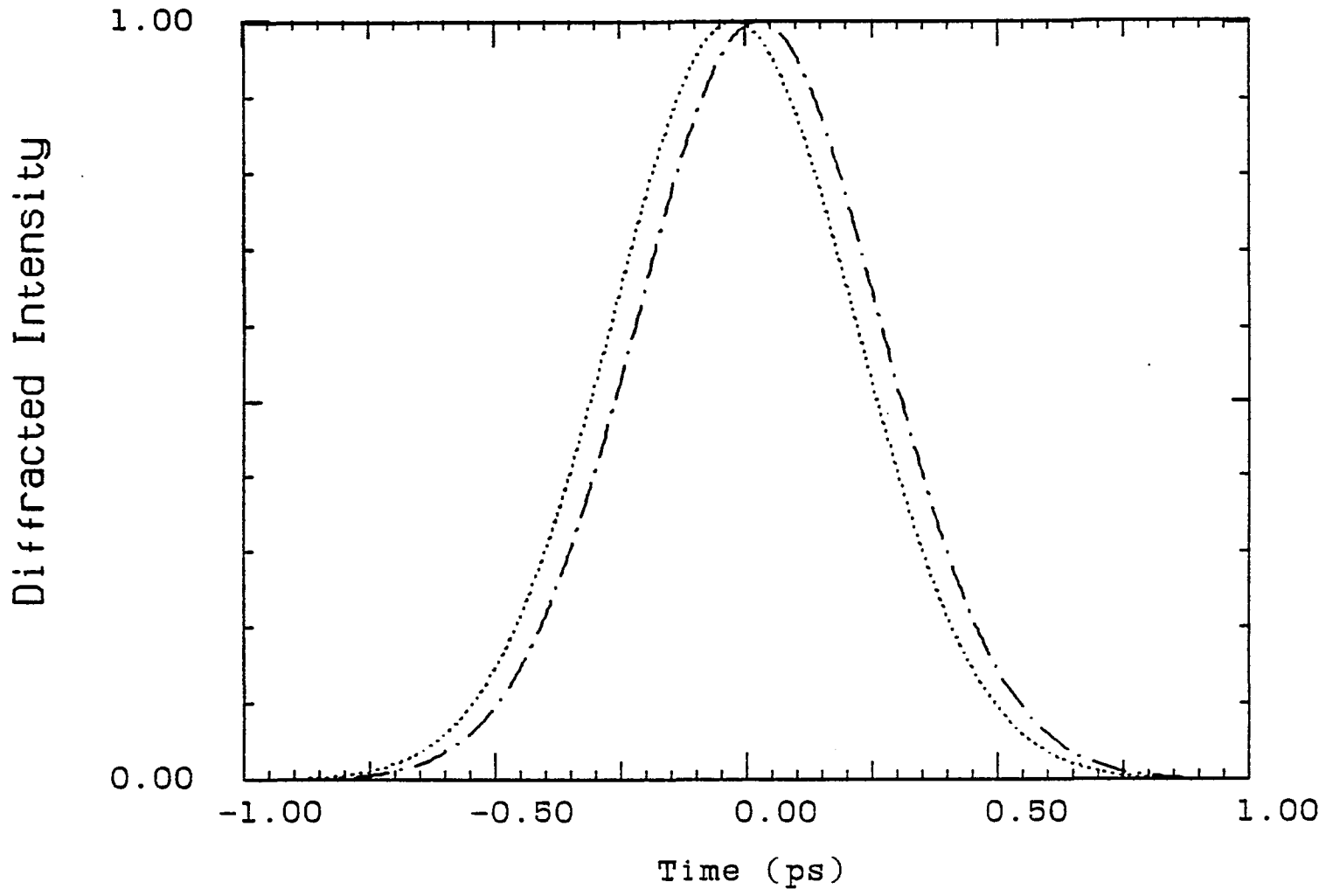

Figure 5.4.6a. Calculated grating signal in the $K_2 + K_2 - K_3$ and $K_3 + K_3 - K_2$ directions for a 450 fs gaussian pulse (FWHM) and a momentum relaxation time of 100 fs.

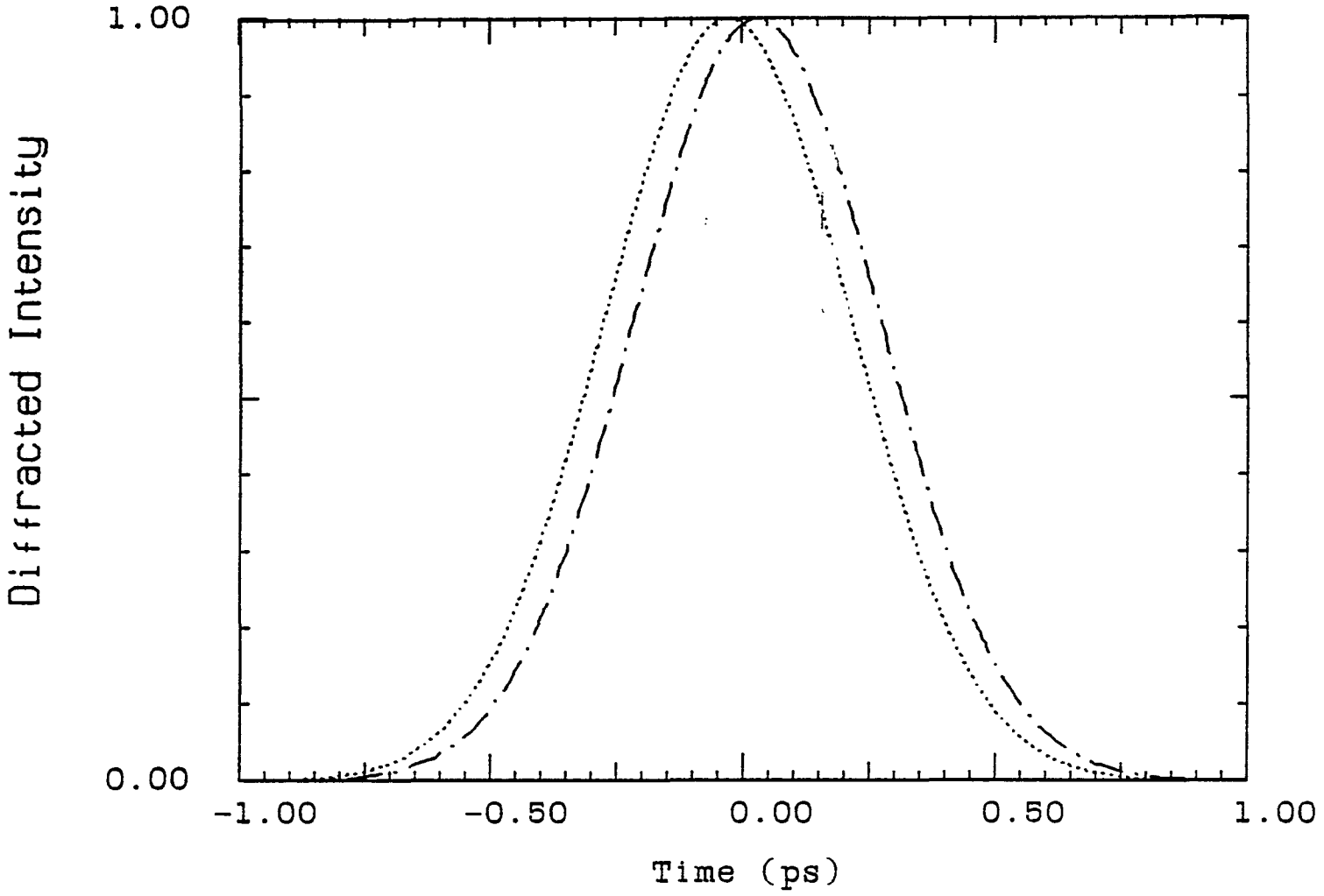

Figure 5.4.6b. Calculated grating signal in the $K_2 + K_2 - K_3$ and $K_3 + K_3 - K_2$ directions for a 450 fs gaussian pulse (FWHM) and a momentum relaxation time of 125 fs.

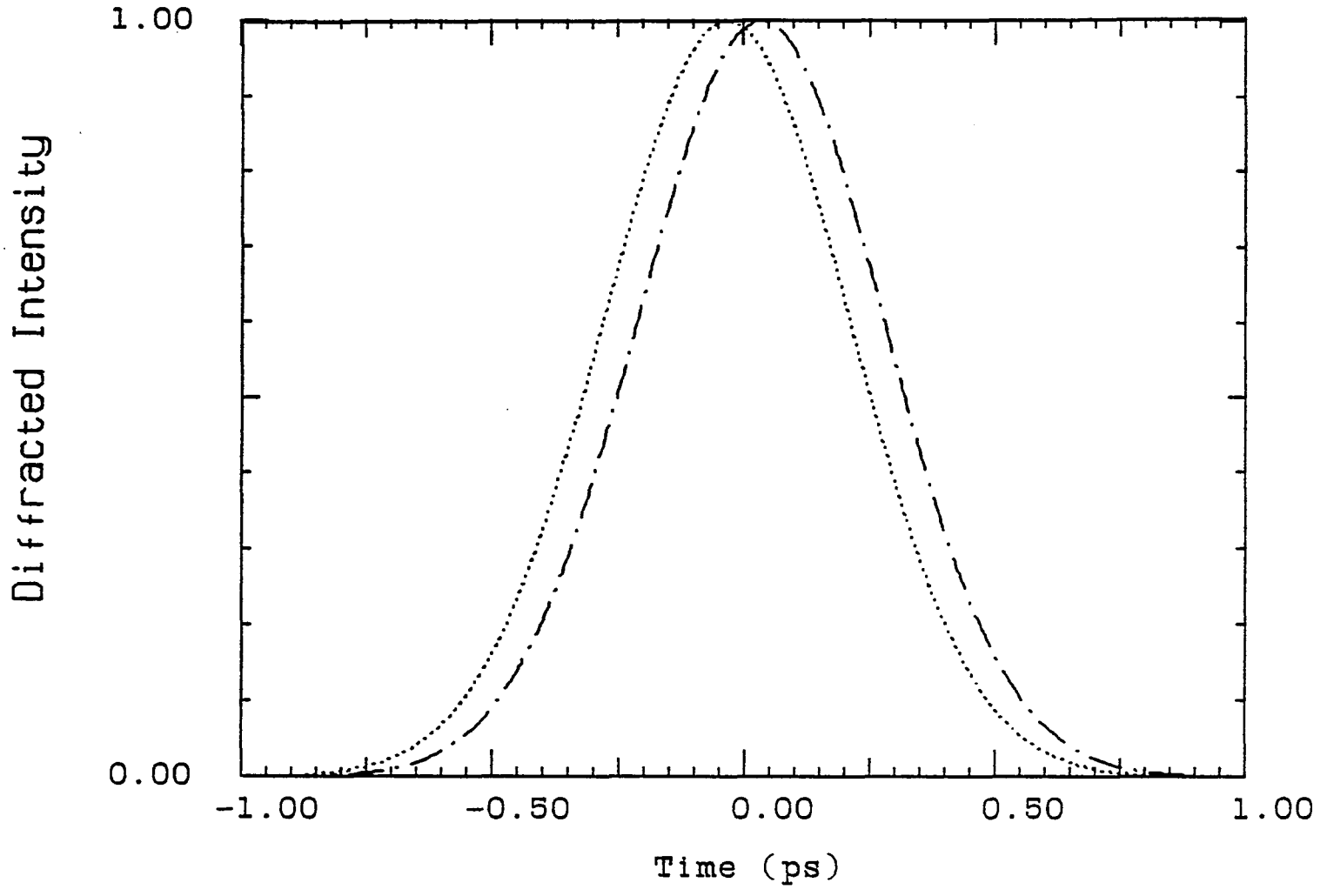

Figure 5.4.6c. Calculated grating signal in the $K_2 + K_2 - K_3$ and $K_3 + K_3 - K_2$ directions for a 450 fs (FWHM) gaussian pulse and a momentum relaxation time of 150 fs.

This integral was evaluated for a 450 fs pulse (FWHM) and momentum relaxation times, τ_M, in the range of 50 to 500 fs, by approximating the error function[63] and numerically integrating. The results ($G(\tau)$ and $G(-\tau)$ are plotted in figure 5.4.6a-c for τ_M = 100, 125, 150 fs respectively. In figure 5.4.7, the peak shift, τ_{shift}, is plotted as a function of τ_M. The shift in the curves is defined as the difference in the points of half maximum intensity between $G(\tau)$ and $G(-\tau)$. The half maximum points were chosen rather than the peak position because noise fluctuation in the data made a precise determination of the peak intensity very difficult. The intensity FWHM of $G(\tau)$ is plotted in figure 5.4.8 as a function of τ_M. As can be seen by figure 5.4.8, the FWHM of $G(\tau)$ is not sensitive to τ_M for $\tau_M < \tau_p$ and therefore measuring the signal FWHM in not as accurate a method as measuring the time shift of the peak position of the scattered signal.

A comparison of these calculations with the data in figure 5.4.5 show that the carrier momentum randomizes by carrier-carrier scattering in about 120 fs. A more accurate fit would require a detailed knowledge of the pulse shape, chirp and shorter pulses.

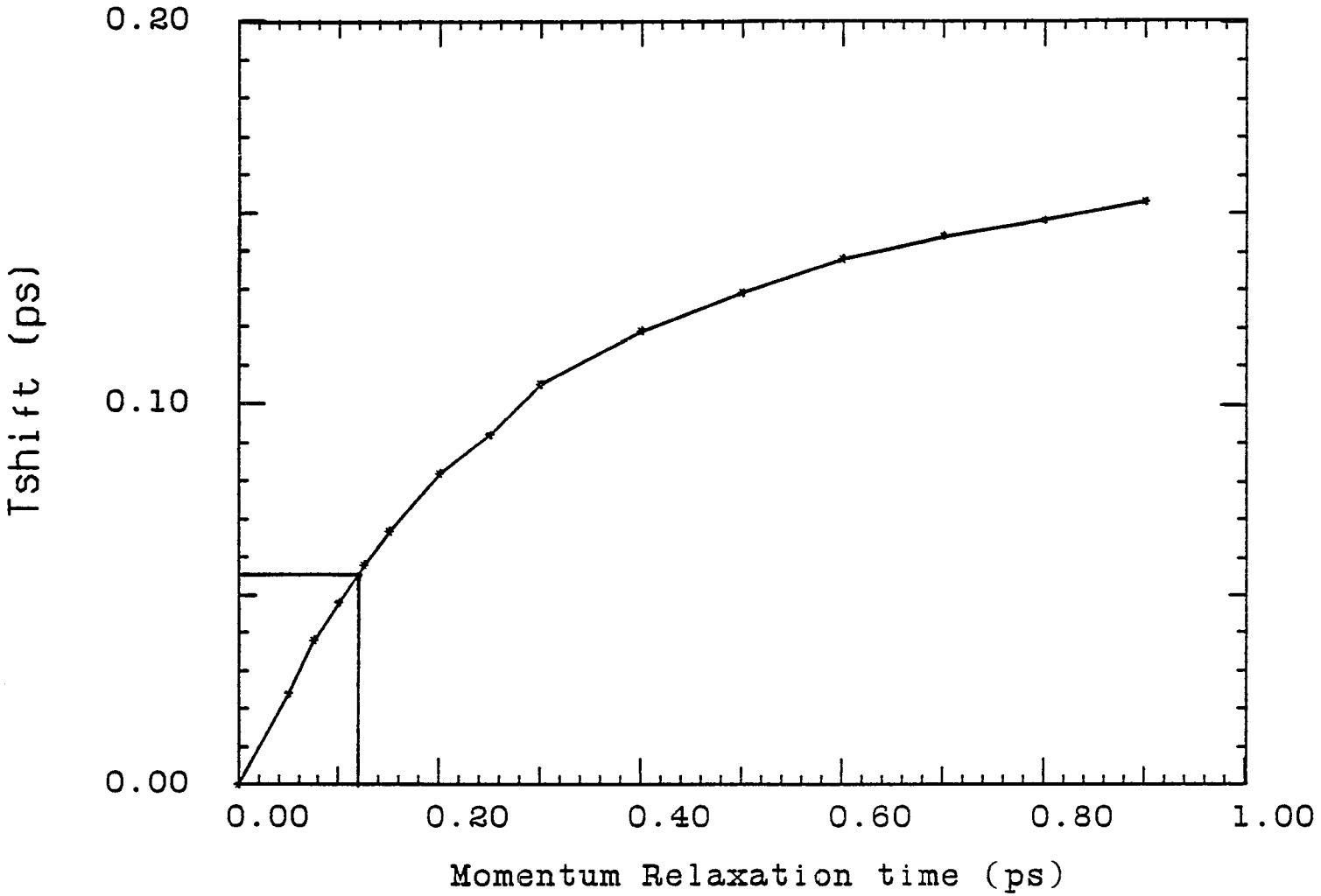

Figure 5.4.7. Calculated shift (at FWHM) between 2θ and -θ directions plotted as a function of momentum relaxation time for a 450 fs gaussian pulse.

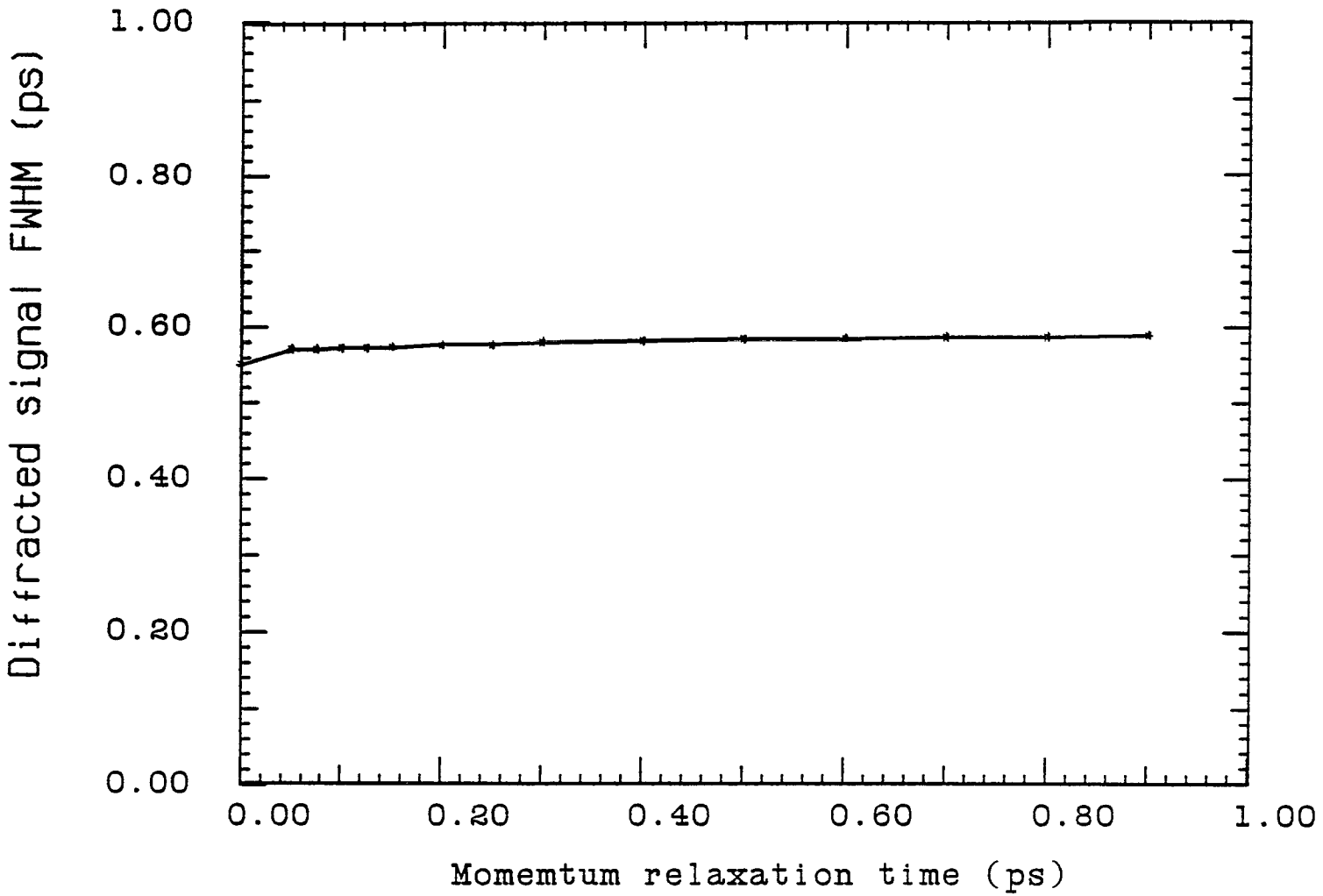

Figure 5.4.8. Calculated FWHM of 2 pulse grating signal as a function of momentum relaxation time for a 450 fs gaussian pulse.

5.5 Notes

[1]J. P. Woerdman, Phys. Lett. **32A**, 305 (1970).

[2]J. P. Woerdman. PhD Thesis (1971).

[3]H. J. Eichler, P. Günter, D. W. Pohl, **Laser-Induced Dynamic Gratings**, (Springer-Verlag, Berlin 1985) P 26.

[4]K. A. Nelson, R. Casalegno, R. J. D. Miller and M. D. Fayer, J. Chem. Phys. **77**, 1144 (1982).

[5]H.J. Eichler, F. Massmann, E. Biselli, K. Richter, M. Glotz,L. Konetzke and X. Yang, Phys. Rev. B 36, 3247 (1987).

[6]C. V. Shank and D. H. Auston, Phys. rev. Lett. **34**, 479 (1975).

[7]H. J. Eichler, Optica Acta **24**, 631 (1977).

[8]Z. Vardeny and J. Tauc, Optics Commun. 39, 396 (1981).

[9]H. J. Eichler, D. Langhans and F. Massman, Optics Commun. **50**, 117 (1984).

[10]S. L. Palfrey and T. F. Heinz, J.Opt. Soc. B **2**, 674 (1985).

[11]A. L. Smirl, T. F. Boggess, B. S. Wherrett, G. P. Perryman and A. Miller, IEEE J. Quant. Electon. QE-19, 690 (1983).

[12]A. L. Smirl, in **Semiconductors Probed by Ultrafast Laser Spectroscopy Vol 1**, ed. by R. R. Alfano (Academic Press, New York 1986).

[13]D. W. Phillion, D. J. Kuizenga and A. E. Siegman, Appl. Phys. Lett. **27**, 85 (1975).

[14]J. R. Salcedo and A. E. Siegman, IEEE J. Quant. Electron.**QE-15**, 250 (1979).

[15]D. N. Rao, R. Burzynski, X. Mi and P. N. Prasad, Appl. Phys. Lett. **48**, 387 (1986).

[16]S. C. Moss, J. R. Lindle, H. J. Mackey and A. L. Smirl, Appl. Phys. Lett. **39**, 227 (1981).

[17]A. L. Smirl, S. C. Moss and J. R. Lindle, Phys. Rev. B **25**, 2645 (1982).

[18]A. L. Smirl, T. F. Boggess, B. S. Wherrett, G. P. Perryman and A. Miller, Phys. Rev. lett. **49**, 933 (1982).

[19]V. J. Newell, T. S. Rose and M. D. Fayer, Phys. Rev. B **32**, 8035 (1985).

[20]H. Bergner, V. Brückner and M. Supianek, IEEE J. Quant. Electron. **QE-22**, 1306 (1986).

[21]H. Saito and E. O. Göbel, Phys. Rev. B **31**, 2360 (1985).

[22]Y. Aoyagi, Y. Segawa and S. Namba, IEEE J. Quant. Electron. **QE-22**, 1320 (1986).

[23]H. Saito and E. O. Göbel, Opt. Lett. **11**, 354 (1986).

[24]C. A. Hoffman, K. Jarasiunas, H. J. Gerritsen and A. V. Nurmikko, Appl. Phys. Lett. **33**, 536 (1978).

[25]L. Schultheis, J. Kuhl, and A. Honold, Phys. Rev. Lett. **57**, 1797 (1986).

[26]L. Schultheis, A. Honold, J. Kuhl, and K. Köhler, Phys. Rev. B **34**, 9027 (1986).

[27]J. L Oudar, A. Migus, D. Hulin, G. Grillon, J. Etchepare and A. Antonetti, Phys. Rev. Lett. **53**, 384 (1984).

[28]A. M. Weiner, S. De Silvestri, and E. P. Ippen, J. Opt. Soc. Am. B **2**, 654 (1985).

[29]C. J. Kennedy, J. C. Matter, A. L. Smirl, H. Weiche, F.Hopf, S. Pappu and M. Scully, Phys. Rev. Lett. **32**, 419 (1974).

[30]A. Yariv, **Quantum Electronics**, (John Wiley & Sons, New York 1975).

[31]Y. R. Shen, **The Principles of Nonlinear Optics**, (John Wiley & Sons, New York 1984) Pp 242-264.

[32]D. H. Auston, S. McAfee, C. V. Shank, E. P. Ippen and O. Teschke, Solid State Electronics **21**, 147 (1978).

[33]J. J. Wynne, Phys. Rev. **178**, 1295 (1969).

[34]S. Y. Yuen and P. A. Wolff, Appl. Phys. Lett. **40**, 457 (1982).

[35]K. Kash, P. A. Wolff and W. A. Bonner, Appl. Phys. Lett.**42**, 173 (1983).

[36]S. Y. Yuen, P. A. Wolff, L. R. Ram-Mohan and R. A. Logan, Solid State Commun. **56**, 489 (1985).

[37]S. S. Jha and N. Bloembergen, IEEE J. Quantum Electron. **QE-4**, 670 (1968).

[38]C. C. Wang and N. W. Ressler, Phys. Rev. **188**, 1291 (1969).

[39]T. Yajima and H. Souma, Phys. Rev. A **17**, 309 (1978).

[40]R. K. Jain and M. B. Klein, Appl. Phys. Lett. **35**, 454 (1979).

[41]B. Jensen, IEEE J. Quant. Electron. QE-18, 1361 (1982).

[42]B. S. Wherrett and N. A. Higgins, Proc. R. Soc. Lond. A **379**, 67 (1982).

[43]B. S. Wherrett, A. L. Smirl and T. F. Boggess, IEEE J. Quantum Electron. **QE-19**, 680-689 (1983).

[44]K. C. Rustagi, Appl. Phys. Lett. **44**, 1121 (1984).

[45]K. B. Kahen and J. P. Leburton, Phys. Rev. B **32**, 5177 (1985).

[46]H. Ehrenreich, in **Optical Properties of Solids**, ed. by J. Tauc, (Academic Press New York 1966).

[47]D. Pines, **Elementary Excitations in Solids**, (W.A.Benjamin, Inc. New York 1964).

[48]L. M. Narducci, S. S. Mitra, R. A. Shatas, P. A. Pfeiffer and A. Vaidyanathan, Phys. Rev. B **14**, 2508 (1975).

[49]J. Callaway, **Quantum Theory of the Solid State**, Part A, Chapt. 4 (Academic Press, New York 1974).

[50]The principle part of the integral in equation 5.2.7 can be found in tables of integrals. Such as I. S. Gradsteyn and I. M. Ridzak, **Tables of Integrals, Series, and Products**, (Academic Press, New York, 1980) Pg.71 #2.2131 and #2.211.

[51]A. J. Taylor, D. J. Erskine, and C. L. Tang, J.Opt. Soc Am. B **2**, 663 (1985).

[52]W. Z. Lin, L. G. Fujimoto, and E. P. Ippen, Appl. Phys.Lett. **50**, 124 (1987).

[53]M. A. Osman and H. L. Grubin, Solid State Elect. **31**, 471 (1988).

[54]J. S. Blakemore, J. Appl. Phys. 53, R123 (1982).

[55]E. Yoffa, Phys. rev. B **23**, 1909 (1981).

[56]H. R. Chandrasekhar and A. K. Ramdas, Phys. Rev. B **21**, 1511 (1980).

[57]E. O. Kane, J. Phys. Chem. Solids 1, 249 (1957).

[58]M. A. Osman and D. K. Ferry, Phys. Rev. B **36**, 6018 (1987).

[59]Unpublished synchroscan streak camera measurements of the photoluminescence lifetime show the recombination time on these samples to be several nanoseconds under low excitation. (The samples were excited by the unamplified pulse train. The carrier density based on pulse energy, spot size and absorption coefficient is 10^{14} cm^{-3}.

[60]D. G. McLean, M. G. Roe, A. I. Souza and P. E. Wigen, Appl. Phys. Lett. **48**, 992 (1986).

[61]J. Shah, B. Deveaud, T. C. Damen, W. T. Tsang, A. C. Gossard and P. Lugli, Phys. Rev. Lett. **59**, 2222 (1987).

[62]Zimmerman, P. Lugli,and D. K. Ferry, Solid State Elect. **26**, 233 (1986).

[63]M. Abramowitz and I. A. Stegun, Handbook of Mathematical Functions, (National Bureau of Standards, Washington D. C. 1964). Pg 299 Eq. # 7.1.25.

Chapter 6 Conclusions and future research

The conclusions of this thesis work as well as areas for future related research are summerized below.

The femtosecond laser system constructed for this thesis work is currently operational with a pulse width of 50 femtoseconds duration. The femtosecond laser amplifier gain is 5×10^6. Optimization of the DODCI concentration and the use of the appropriate mirrors can reduce the oscillator pulse width to $\approx$ 30 fs. The amplified pulse can be compressed by the use of either a grating pair or four prisms to give output pulses of under 100 fs in duration and greater than 100 microjoules per pulse (peak power > 10^9 watts cm^{-2}).

The results of the pump and probe absorption experiment show that the excited carriers achieve a thermalized distribution after 800 fs. This time is much longer than the carrier-carrier scattering time indicating that it takes 30 to 40 carrier-carrier collisions to achieve a Fermi-Dirac distribution. Pump and probe absorption, as a direct measurement of the excited carrier distribution function is an excellent experimental technique for studying hot carriers in GaAs.

Future research requires a shorter pulse width (< 50 fs) to increase the temporal resolution and thereby clarify much of this work. These future efforts can be used study electron-hole energy transfer by probing at energies much greater than the pump photon energy. Studying the time resolved transmission changes at the onset

of splitoff band transistions can yield information about intervalence band scattering (SO → HH and SO → LH).

In this thesis, the first measurements of both the dispersion and bleaching components of the free carrier contribution to $\delta\varepsilon$ were studied by the time-resolved transient grating technique. These results were used to determine the L → Γ intervalley scattering time in GaAs. This effective time was measured to be 9 ps indicating a L → Γ time of 3 ps. The results of the orientation grating experiment, by comparing the four-wave mixing signal in the 2θ and $-\theta$, were used to measure the momentum relaxation time. This time was determined to be 140 fs.

Future efforts with a shorter pulse width (<50 fs) can contunue this work with increased temporal resolution and attempted to separate the electron and hole components of the momentum relaxation. Transient orientational grating experiments can also be used to study momentum relaxation of excited carriers in AlGaAs-GaAs superlattices.

Appendix

Fdcond.for

```
c       This program calculates the quasi-Fermi levels for the
c       conduction band of GaAs correcting for band non-parabolicity.
        dimension eln(30), xqfl(900)
        write(*,813)
813     format(1x,'use for non-para. cond. band ')
        write(*,815)
815     format(1x,'destination file for fermi-level'/)
        open(3,file='eflnp.dat',status='new')
        write(*,96)
96      format(1x,'enter how many different densities to compute')
        read(*,*) inumb
        write(*,98)
98      format(1x,'enter density of excited carriers')
        do 97 l=1,inumb
        read(*,*) eln(l)
97      continue
        write(*,21)
21      format(1x,'Enter Max. & Min. Temp. & Temp. Interval')
        read(*,*) itmx
        read(*,*) itmn
        read(*,*) itv
        ittn=(itmx-itmn)/itv+1
        write(3,109) inumb
        write(3,109) ittn
109     format(1x,I4)
        icqfl=0
        xm=.063*sqrt(.063)
        eg=1.424
        a=15.*.830/(4.*1.424)
102     do 95 l=1,inumb
        do 1 i=itmn,itmx,itv
        WRITE(*,*) eln(l),I
        t=float(i)
        tk=(8.617e-5)*t
        ala=4.83E15*t*sqrt(t)/eln(l)
        do 701 j=1,150
        efg=float(j-1)*.2/tk-3./tk
        if(efg.le.-80.) efg = -80.
        if(efg.ge.1.) goto 703
        fg=exp(efg)/(1.+.27*exp(efg))
        fge=(alog(1.+.27*exp(efg)))/.27
        goto 704
703     fg=.752*((efg**2+1.7)**.75)
        fge=.3*efg**2*sqrt(efg)+1.73*sqrt(efg)
704     continue
        if(fg.le.1e-35) fg=0.0
        at=ala*xm*(fg+a*tk*fge)-1.
        if(at.ge.0) goto 709
701     continue
```

```
709     do 2 j=1,500
        efg1=efg-float(j-1)*.0005/tk
        if(efg1.ge.1.) goto 3
        fg=exp(efg1)/(1.+.27*exp(efg1))
        fge=(alog(1.+.27*exp(efg1)))/.27
        goto 4
3       fg=.752*((efg1**2+1.7)**.75)
        fge=.3*efg1**2*sqrt(efg1)+1.73*sqrt(efg1)
4       continue
        at=ala*xm*(fg+a*tk*fge)-1.
        ab=at*at
        if(ab.le.0.0001) goto 9
2       continue
        write(*,718) t
718     format(1x,'fermi level not found',f5.0)
        efg1=-10000.
9       ef=efg1*tk
        icqfl=icqfl+1
        xqfl(icqfl)=ef
1       continue
95      continue
        do 732 i=1,inumb
        write(3,*) eln(i)
        do 734 j=1,ittn
        ix=ittn*(i-1)+j
        temp=float(itmn+itv*(j-1))
        write(3,733) temp,xqfl(ix)
733     format(1x,f5.0,2x,f7.4)
734     continue
732     continue
        end
```

Fdcondp.for

```
c       This program calculates the quasi-Fermi level for the
c       conduction band of GaAs assuming a parabolic band.
        dimension eln(30), xqfl(900)
        write(*,813)
813     format(1x,'use for parabolic conduction band')
        open(3,file='eflp.dat',status='new')
        write(*,96)
96      format(1x,'enter how many different densities to compute')
        read(*,*) inumb
        write(*,98)
98      format(1x,'enter density of excited carriers')
        do 97 l=1,inumb
        read(*,*) eln(l)
97      continue
        write(*,21)
21      format(1x,'Enter Max. & Min. Temp. & Temp. Interval')
        read(*,*) itmx
        read(*,*) itmn
        read(*,*) itv
        ittn=(itmx-itmn)/itv+1
        write(3,109) inumb
        write(3,109) ittn
109     format(1x,I4)
        icqfl=0
        xg=.063*sqrt(.063)
        eg=1.424
102     do 95 l=1,inumb
        do 1 i=itmn,itmx,itv
        WRITE(*,*) eln(l),I
        t=float(i)
        tk=(8.617e-5)*t
        ala=4.83E15*t*sqrt(t)/eln(l)
        do 701 j=1,150
        efg=float(j-1)*.2/tk-3./tk
        if(efg.le.-80.) efg=-80.
        if(efg.ge.1.) goto 703
        fg=exp(efg)/(1.+.27*exp(efg))
        goto 704
703     fg=.752*((efg**2+1.7)**.75)
704     continue
        at=ala*xg*fg-1.
        if(at.ge.0) goto 709
701     continue
709     do 2 j=1,500
        efg1=efg-float(j-1)*.0005/tk
        if(efg1.ge.1.) goto 3
        fg=exp(efg1)/(1.+.27*exp(efg1))
        goto 4
3       fg=.752*((efg1**2+1.7)**.75)
4       continue
        at=ala*xg*fg-1.
        ab=at*at
```

```
      if(ab.le.0.0001) goto 9
2     continue
      write(*,718) t
718   format(1x,'fermi level not found',f5.0)
      efg1=-10000.
9     ef=efg1*tk
      icqfl=icqfl+1
      xqfl(icqfl)=ef
1     continue
95    continue
      do 732 i=1,inumb
      write(3,*) eln(i)
      do 734 j=1,ittn
      ix=ittn*(i-1)+j
      temp=float(itmn+itv*(j-1))
      write(3,733) temp,xqfl(ix)
733   format(1x,f5.0,2x,f7.4)
734   continue
732   continue
      end
```

Fdhh.for

```
c       This program calculates the quasi-Fermi level for the  valance
c       band of GaAs considering only the heavy-hole band.
        dimension eln(30), xqfl(900)
        write(*,813)
813     format(1x,'use for heavy hole valence band')
        open(3,file='vflhh.dat',status='new')
        write(*,96)
96      format(1x,'enter how many different densities to compute')
        read(*,*) inumb
        write(*,98)
98      format(1x,'enter density of excited carriers')
        do 97 l=1,inumb
        read(*,*) eln(l)
97      continue
        write(*,21)
21      format(1x,'Enter Max. & Min. Temp. & Temp. Interval')
        read(*,*) itmx
        read(*,*) itmn
        read(*,*) itv
        ittn=(itmx-itmn)/itv+1
        write(3,109) inumb
        write(3,109) ittn
109     format(1x,I4)
        icqfl=0
        xm=.5*sqrt(.5)
        eg=0.0
102     do 95 l=1,inumb
        do 1 i=itmn,itmx,itv
        WRITE(*,*) eln(l),I
        t=float(i)
        tk=(8.617e-5)*t
        ala=4.83E15*t*sqrt(t)/eln(l)
        do 701 j=1,150
        efg=float(j-1)*.2/tk-3./tk
        if(efg.ge.1.) goto 703
        if(efg.le.-80.) efg=-80.
        fg=exp(efg)/(1.+.27*exp(efg))
        goto 704
703     fg=.752*((efg**2+1.7)**.75)
704     continue
        at=ala*xm*fg-1.
        if(at.ge.0) goto 709
701     continue
709     do 2 j=1,500
        efg1=efg-float(j-1)*.0005/tk
        if(efg1.ge.1.) goto 3
        fg=exp(efg1)/(1.+.27*exp(efg1))
        goto 4
3       fg=.752*((efg1**2+1.7)**.75)
4       continue
        at=ala*xm*fg-1.
        ab=at*at
```

```
        if(ab.le.0.0001) goto 9
2       continue
        write(*,718) t
718     format(1x,'fermi level not found',f5.0)
        efg1=-10000.
9       ef=-efg1*tk
        icqfl=icqfl+1
        xqfl(icqfl)=ef
1       continue
95      continue
        do 732 i=1,inumb
        write(3,*) eln(i)
        do 734 j=1,ittn
        ix=ittn*(i-1)+j
        temp=float(itmn+itv*(j-1))
        write(3,733) temp,xqfl(ix)
733     format(1x,f5.0,2x,f7.4)
734     continue
732     continue
        end
```

Fdval.for

```
c       This program calculates the quasi-Fermi level for the  valance
c       band of GaAs considering the heavy-hole as parabolic and the
c       light-hole as non-parabolic.
        dimension eln(30), xqfl(900)
        write(*,813)
813     format(1x,'use for para. HH & non-para. LH val. band')
        write(*,815)
815     format(1x,'destination file for fermi-level'/)
        open(3,file='hflval.dat',status='new')
        write(*,96)
96      format(1x,'enter how many different densities to compute')
        read(*,*) inumb
        write(*,98)
98      format(1x,'enter density of excited carriers')
        do 97 l=1,inumb
        read(*,*) eln(l)
97      continue
        write(*,21)
21      format(1x,'Enter Max. & Min. Temp. & Temp. Interval')
        read(*,*) itmx
        read(*,*) itmn
        read(*,*) itv
        ittn=(itmx-itmn)/itv+1
        write(3,109) inumb
        write(3,109) ittn
109     format(1x,I4)
        icqfl=0
        xmhh=.5*sqrt(.5)
        xmlh=.076*sqrt(.076)
        eg=0.0
        a=3.8*15./(4.*1.424)
102     do 95 l=1,inumb
        do 1 i=itmn,itmx,itv
        WRITE(*,*) eln(l),I
        t=float(i)
        tk=(8.617e-5)*t
        ala=4.83E15*t*sqrt(t)/eln(l)
        do 701 j=1,150
        efg=float(j-1)*.2/tk-3./tk
        if(efg.ge.1.) goto 703
        fg=exp(efg)/(1.+.27*exp(efg))
        fge=(alog(1.+.27*exp(efg)))/.27
        goto 704
703     fg=.752*((efg**2+1.7)**.75)
        fge=.3*efg*efg*sqrt(efg)+1.73*sqrt(efg)
704     continue
        if(fg.le.1e-35) fg=0.0
        at=ala*((xmhh+xmlh)*fg+xmlh*a*tk*fge)-1.
        if(at.ge.0) goto 709
701     continue
709     do 2 j=1,500
        efg1=efg-float(j-1)*.0005/tk
```

```
        if(efg1.ge.1.) goto 3
        fg=exp(efg1)/(1.+.27*exp(efg1))
        fge=(alog(1.+.27*exp(efg1)))/.27
        goto 4
3       fg=.752*((efg1**2+1.7)**.75)
        fge=.3*efg1*efg1*sqrt(efg1)+1.73*sqrt(efg1)
4       continue
        at=ala*((xmhh+xmlh)*fg+xmlh*a*tk*fge)-1.
        ab=at*at
        if(ab.le.0.0001) goto 9
2       continue
        write(*,718) t
718     format(1x,'fermi level not found',f5.0)
        efg1=-10000.
9       ef=-efg1*tk
        icqfl=icqfl+1
        xqfl(icqfl)=ef
1       continue
95      continue
        do 732 i=1,inumb
        write(3,*) eln(i)
        do 734 j=1,ittn
        ix=ittn*(i-1)+j
        temp=float(itmn+itv*(j-1))
        write(3,733) temp,xqfl(ix)
733     format(1x,f5.0,2x,f7.4)
734     continue
732     continue
        end
```

Fdglx.for

```
c       This program calculates the quasi-Fermi level and density of
c       carriers in each valley of the conduction band of GaAs when
c       the valleys are in equilibrium (common temperature and
c       quasi-Fermi level). It considers the non-parabolicity of the
c       Γ valley but treats the L and X valleys as non-parabolic.
        dimension eln(30)
        write(*,813)
813     format(1x,'For non-para. cond. band considering all valleys')
        open(1,file='eflglx.dat',status='new')
        write(*,96)
96      format(1x,'enter how many different densities to compute')
        read(*,*) inumb
        write(*,98)
98      format(1x,'enter density of excited carriers')
        do 97 l=1,inumb
        read(*,*) eln(l)
97      continue
        write(*,21)
21      format(1x,'Enter Max. & Min. Temp. & Temp. Interval')
        read(*,*) itmx
        read(*,*) itmn
        read(*,*) itv
        ittn=(itmx-itmn)/itv+1
        icqfl=0
        xm=.063*sqrt(.063)
        xml=.56*sqrt(.56)
        xmx=.85*sqrt(.85)
        el=.285
        ex=.476
        a=15.*.830/(4.*1.424)
102     do 95 l=1,inumb
        do 1 i=itmn,itmx,itv
        t=float(i)
        tk=(8.617e-5)*t
        ala=4.83E15*t*sqrt(t)/eln(l)
        do 701 j=1,150
        efg=float(j-1)*.2/tk-3./tk
        if(efg.le.-80.) efg = -80.
        efl=efg-.286/tk
        efx=efg-.476/tk
        if(efl.le.-80.) efl=-80.
        if(efx.le.-80.) efx=-80.
        if(efg.ge.1.) goto 702
        fg=exp(efg)/(1.+.27*exp(efg))
        fge=(alog(1.+.27*exp(efg)))/.27
        goto 703
702     fg=.752*((efg**2+1.7)**.75)
        fge=.3*efg**2*sqrt(efg)+1.73*sqrt(efg)
703     if(efl.ge.1.) goto 704
        fl=exp(efl)/(1.+.27*exp(efl))
        goto 705
704     fl=.752*((efl**2+1.7)**.75)
```

```
705     if(efx.ge.1.) goto 706
        fx=exp(efx)/(1.+.27*exp(efx))
        goto 707
706     fx=.752*((efx**2+1.7)**.75)
707     continue
        at=ala*(xm*(fg+a*tk*fge)+xml*fl+xmx*fx)-1.
        if(at.ge.0) goto 709
701     continue
709     do 710 j=1,500
        efg1=efg-float(j-1)*.0005/tk
        efl1=efg1-.286/tk
        efx1=efg1-.476/tk
        if(efg1.ge.1.) goto 711
        fg=exp(efg1)/(1.+.27*exp(efg1))
        fge=(alog(1.+.27*exp(efg1)))/.27
        goto 712
711     fg=.752*((efg1**2+1.7)**.75)
        fge=.3*efg1**2*sqrt(efg1)+1.73*sqrt(efg1)
712     if(efl1.ge.1.) goto 713
        fl=exp(efl1)/(1.+.27*exp(efl1))
        goto 714
713     fl=.752*((efl1**2+1.7)**.75)
714     if(efx1.ge.1.) goto 715
        fx=exp(efx1)/(1.+.27*exp(efx1))
        goto 716
715     fx=.752*((efx1**2+1.7)**.75)
716     at=ala*(xm*(fg+a*tk*fge)+xml*fl+xmx*fx)-1.
        ab=at*at
        if(ab.le.0.0001) goto 9
710     continue
        write(*,718) t
718     format(1x,'fermi level not found',f5.0)
9       ef=efg1*tk
        zng=ala*xm*(fg+a*tk*fge)*1e-18*eln(1)
        znl=ala*xml*fl*1e-18*eln(1)
        znx=ala*xmx*fx*1e-18*eln(1)
        write(*,99) t,zng,znl,znx
        write(1,99) t,zng,znl,znx
99      format(1x,f5.0,2x,f5.3,2x,f5.3,2x,f5.3)
1       continue
95      continue
        end
```

Diele1.for

```
c       This program calculates the intraband and interband
c       contributions to δε1 for probe frequencies above band gap.
c       It uses Simpsons rule to integrate eq. 5.2.5a and 5.2.5c.
        dimension x1(6)
        integer hw,hw1,hw2
        real*8 x(1502),xnr
        open(4,file='c:\for\data\probener.dat',status='old')
        read(4,*) nprobe
        do 500 i=1,nprobe
        read(4,*) x1(i)
500     continue
        open(1,file='c:\for\data\efl.dat',status='old')
        open(2,file='c:\for\data\hfl.dat',status='old')
        open(3,file='diel.dat',status='new')
        read(2,*) numbhd,numbt
        read(1,*) numbed,numbt
        numb=numbhd*numbt
        do 899 ih= 1,numb
        read(2,*) tk,uh,xhm
        xfh=-uh/tk
        if(xfh.le.1.) goto 303
        f12h=.752*(xfh*xfh+1.65)**(.75)
        goto 304
303     f12h=exp(xfh)/(1.+.27*exp(xfh))
304     xhd=6.04e21*xhm*sqrt(xhm)*tk*sqrt(tk)*f12h
        xintr=-2.466e-20*xhd
201     do 203 in=1,numbed
        read(1,*) ue, xem
        xmr1=1./(1./xem+1./xhm)
        xmr=xmr1*sqrt(xmr1)
        do 15 k=1,nprobe
        xhw=x1(k)
        xh=xhw*xhw
        xintra=xintr/xh
        xx=1000.*(xhw-1.424)
        hw=int(xx)
        hw1=hw-6
        hw2=hw+6
        do 501 i=1,1502
        x(i)=0.0
501     continue
        do 10 i=1,hw1
        e=.001*float(i)
        fe=1./(1.+exp((.87*e-ue)/tk))
        fh=1./(1.+exp((uh+.13*e)/tk))
        x(i)=sqrt(e)*(fe+fh)/((e+1.424)*(xh-(e+1.424)**2))
10      continue
        do 20 i=hw2,1200
        e=.001*float(i)
        fe=1./(1.+exp((.87*e-ue)/tk))
        fh=1./(1.+exp((uh+.13*e)/tk))
        x(i)=sqrt(e)*(fe+fh)/((e+1.424)*(xh-(e+1.424)**2))
```

```
20      continue
        abc=(.87*(xhw-1.424)-ue)/tk
        fe=1./(1.+exp(abc))
        fh=1./(1.+exp((.13*(xhw-1.424)+uh)/tk))
        xr=float(iw)*7.9e-4*(fe+fh)/(2.*xh*sqrt(xhw-1.424))
        xnr=-x(1)-x(hw1)-x(hw2)-x(1200)
        do 100 i=1,hw1,2
        xnr=xnr+2.*x(i)+4.*x(i+1)
100     continue
        do 101 i=hw2,1499,2
        xnr=xnr+2.*x(i)+4.*x(i+1)
101     continue
        xnr=1.988e-2*xmr*xnr
        xinter=xnr+xr
        xfg=ue/tk
        if(xfg.le.1.0) goto 301
        f12g=.752*(xfg*xfg+1.65)**(.75)
        goto 302
301     f12g=exp(xfg)/(1.+.27*exp(xfg))
302     xed=6.04e21*xem*sqrt(xem)*tk*sqrt(tk)*f12g
        xld=xhd-xed
        xhd1=xhd*1.0E-18
        xed1=xed*1.0E-18
        xld1=xld*1.0E-18
        write(*,40) tk,xhw, xhd1, xed1,xld1
        write(3,40) tk,xhw,xhd1,xed1,xld1
40      format(1x,f5.4,2x,f5.2,2x,f5.2,2x,f5.2,2x,f5.2)
        xlinter=1.56e-21*xld/(xh-9.61)
        diel=xintra+xinter+xlinter
        diel2=diel*diel
        write(*,999) xintra,xinter,xlinter,diel,diel2
        write(3,999) xintra,xinter,xlinter,diel,diel2
999     format(1x,4(f6.4,3x),2x,f8.6)
15      continue
203     continue
899     continue
        stop
        end
```

Diele1bg.for

```
c       This program calculates δε1 for probe frequencies  below  band
c       gap.  It uses Simpsons rule to integrate Eq. 5.2.5c.
        dimension xhw1(20)
        real*8 x(1502),xnr
        open(1,file='c:\for\data\efl.dat',status='old')
        open(2,file='c:\for\data\hfl.dat',status='old')
        open(3,file='diel.dat',status='new')
        open(4,file='c:\for\data\probener.dat',status='old')
        read(4,*) nprobe
        do 151 i=1,nprobe
        read(4,*) xhw1(i)
151     continue
        read(2,*) numbhd,numbt
        read(1,*) numbed,numbt
        numb=numbhd*numbt
        do 899 ih= 1,numb
        read(2,*) tk,uh,xhm
        xfh=-uh/tk
        if(xfh.le.1.) goto 303
        f12h=.752*(xfh*xfh+1.65)**(.75)
        goto 304
303     f12h=exp(xfh)/(1.+.27*exp(xfh))
304     xhd=6.04e21*xhm*sqrt(xhm)*tk*sqrt(tk)*f12h
        xintr=-2.466e-20*xhd
201     do 203 in=1,numbed
        read(1,*) ue, xem
        xmr1=1./(1./xem+1./xhm)
        xmr=xmr1*sqrt(xmr1)
        do 15 ihw=1,nprobe
        xhw=xhw1(ihw)
        xh=xhw*xhw
        xintra=xintr/xh
        xx=1000.*(xhw-1.424)
        do 501 i=1,1502
        x(i)=0.0
501     continue
        do 10 i=1,1501
        e=.001*float(i)
        fe=1./(1.+exp((.87*e-ue)/tk))
        fh=1./(1.+exp((uh+.13*e)/tk))
        x(i)=sqrt(e)*(fe+fh)/((e+1.424)*(xh-(e+1.424)**2))
10      continue
        xnr=-x(1)-x(1500)
        do 100 i=1,1499,2
        xnr=xnr+2.*x(i)+4.*x(i+1)
100     continue
        xinter=1.988e-2*xmr*xnr
        xfg=ue/tk
        if(xfg.le.1.0) goto 301
        f12g=.752*(xfg*xfg+1.65)**(.75)
        goto 302
301     f12g=exp(xfg)/(1.+.27*exp(xfg))
```

```
302     xed=6.04e21*xem*sqrt(xem)*tk*sqrt(tk)*f12g
        xld=xhd-xed
        xhd1=xhd*1.0E-18
        xed1=xed*1.0E-18
        xld1=xld*1.0E-18
        write(*,40) tk,xhw, xhd1, xed1,xld1
        write(3,40) tk,xhw,xhd1,xed1,xld1
40      format(1x,f5.4,2x,f5.2,2x,f5.2,2x,f5.2,2x,f5.2)
        xlinter=1.56e-21*xld/(xh-9.61)
        diel=xintra+xinter+xlinter
        diel2=diel*diel
        write(*,999) xintra,xinter,xlinter,diel,diel2
        write(3,999) xintra,xinter,xlinter,diel,diel2
999     format(1x,4(f6.4,3x),2x,f8.6)
15      continue
203     continue
899     continue
        stop
        end
```

Diele2.for

```
c       This program is used to calculate δε2 from Eq. 5.2.12.
        DIMENSION FE(8,10,5), FH(10,5), XHW(5), DIELE2(8,10,5)
        OPEN(1,FILE='EFLNP.DAT',STATUS='OLD')
        OPEN(2,FILE='HFLVAL.DAT',STATUS='OLD')
        OPEN(3,FILE='DIELE2.DAT',STATUS='NEW')
        XHW(1)=1.653
        XHW(2)=1.71
        XHW(3)=1.77
        XHW(4)=1.84
        XHW(5)=2.01
        READ(2,*) ND,NT,DEN
        DO 100 J=1,10
        READ(2,*) T,UH
        TK=T*8.617E-5
        DO 100, I=1,5
        EH=-.063*(XHW(I)-1.424)/.563
        FH(J,I)=1./(1.+EXP((UH-EH)/TK))
100     CONTINUE
        READ(1,*) ND,NT
        DO 101 K=1,8
        READ(1,*) DEN
        DO 101 J=1,10
        READ(1,*) T,UE
        TK=T*8.617E-5
        DO 101 I=1,5
        EE=.5*(XHW(I)-1.424)/.563
        TEMP=(EE-UE)/TK
        FE(K,J,I)=1./(1.+EXP((EE-UE)/TK))
101     CONTINUE
        EG=1.424
        XMR=SQRT(1./((1./.063+1./.5))*9.1)*(1E-14)
        HBAR=1.054E-27
        ELECT2=(4.8E-10)**2
        C1=ELECT2/(HBAR*2*3.1416)
        C2=EG*SQRT(2.)*XMR
        DO 102, K=1,8
        DO 102, J=1,10
        DO 102, I=1,5
        C3=SQRT(XHW(I)-EG)/(XHW(I)**2)
        C4=C1*C2*C3/SQRT(1.602E-12)
        DIELE2(K,J,I)=C4*(FE(K,J,I)+FH(I,J))
        WRITE(*,*) I,J,K,DIELE2(K,J,I)
102     CONTINUE
        DO 103, I=1,5
        DO 103, J=1,10
        DO 103, K=1,8
        K1=K+2
        WRITE(3,104) K1,DIELE2(K,J,I)
104     FORMAT(1X,I2,',',F6.5)
103     CONTINUE
        STOP
        END
```

Kztr.bas

```
  DIM COUNT(1023),XSIG(1023),XREF(1023),XPR(1023),SPR(1023),SREF(1023)
  DIM B$(10),XP(1023),YSIG(511),TIME(511),Y(525),XPLOT(511)
"THIS PROGRAM ACCEPTS THE PROBE AND REFERENCE SIGNALS FROM THE TRACOR"
"SIGNAL AVERAGER IN THE PUMP AND PROBE ABSORPTION EXPERIMENT.  THIS"
"PROGRAM ACCEPTS A PREDETERMINED NUMBER OF SCANS FOR AVERAGING, PLOTS"
"THE DATA ON THE SCREEN AND ALLOWS THE OPTION OF ACQUIRING MORE DATA."
"THIS PROGRAM REJECTS ALL DATA FOR WHICH THE REFERENCE COUNTS FALLS"
"OUTSIDE THE LIMITS SET BELOW"
  INPUT"START,FIRST & SECOND RATE CHANGE POINTS";ST1,ST2,ST3
  INPUT"INITIAL,MIDDLE & FINAL UNIDEX FEED RATES";FR1,FR2,FR3
  INPUT"TRACOR DWELL TIME";DWELL
1 INPUT"NUMBER OF CYCLES OF TRACOR";ICYCLE
  INPUT"MAXIMUM AND MINIMUM COUNTS FOR REF";MAXCT,MINCT
  INPUT"ENTER DATA FILE NAME";FILE$
  FOR I=0 TO 1023
  XP(I)=0
  SREF(I)=0
  SPR(I)=0
  XSIG(I)=0
  COUNT(I)=0
  NEXT I
  FILE2$=FILE$+".TRM"
  FILE3$=FILE$+".PRB"
  FILE1$=FILE$+".REF"
  OPEN FILE2$ FOR OUTPUT AS #2
2 IF ICYCLE=1 THEN GOTO 3
  FOR ICY= 1 TO ICYCLE
  OPEN "COM1:9600,N,8,2,LF" AS #1
  PRINT "DO NOT ACTIVATE TRACOR IF AUTO LEARN MODULE IN USE"
  GOTO 4
3 OPEN "COM1:9600,N,8,2,LF" AS #1
  PRINT "ACTIVATE TRACOR OUTPUT"
4 FOR I=1 TO 3
  INPUT#1,B$(I)
  NEXT I
  FOR I=0 TO 127
  INPUT#1,ABC$
  FOR J=0 TO 7
  K=7*J+8
  AB$=MID$(ABC$,K,7)
  L=8*I+J
  XPR(L)=VAL(AB$)
  NEXT J
  NEXT I
  FOR I=0 TO 127
  INPUT#1,ABC$
  FOR J=0 TO 7
  K=7*J+8
  AB$=MID$(ABC$,K,7)
  L=8*I+J
  XREF(L)=VAL(AB$)
  NEXT J
```

```
  NEXT I
  CLOSE#1
  FOR I=0 TO 1023
  IF XREF(I)>MAXCT THEN GOTO 5
  IF XREF(I)<MINCT THEN GOTO 5
  COUNT(I)=COUNT(I)+1
  XSIG(I)=XSIG(I)+XPR(I)/XREF(I)
  SREF(I)=SREF(I)+XREF(I)
  SPR(I)=SPR(I)+XPR(I)
5 NEXT I
  IF ICYCLE=1 THEN GOTO 9
  PRINT,ICY,XSIG(10),XSIG(200),XSIG(500)
  NEXT ICY
  FOR J=0 TO 1023
  IF COUNT(J)=0 THEN GOTO 6
  COUNTA=COUNT(J)
  GOTO 7
6 COUNTA=10000
7 XP(J)=XSIG(J)/COUNTA
  IF COUNT(J)=0 THEN PRINT J
  NEXT J
  SCREEN 2
  CLS
  XPMX=0
  FOR K=0 TO 511
  K1=2*K
  XPLOT(K)=XP(K1)+XP(K1+1)
  IF XPMX<XPLOT(K) THEN XPMX=XPLOT(K)
  NEXT K
  FOR K=0 TO 511
  XPLOT(K)=199*XPLOT(K)/XPMX
  PSET(K,XPLOT(K))
  NEXT K
  INPUT"REPEAT CYCLE=1; CONT=0";IRCYC
  IF IRCYC=1 THEN GOTO 2
  FOR L=1 TO 1023
  COUNTA=COUNT(L)
  IF COUNTA=0 THEN COUNTA=10000
  SREF(L)=SREF(L)/COUNTA
  SPR(L)=SPR(L)/COUNTA
  IF COUNT(L)>0 THEN GOTO 8
  PRINT L
  XP(L)=XP(L-1)
8 NEXT L
9 INPUT"MIN & MAX CHANNELS FOR BKGD {T<0}"; ICHMN,ICHMX
  BKGD=0
  FOR J=ICHMN TO ICHMX
  BKGD=BKGD+XP(J)
  NEXT J
  BKGD=.01*BKGD/(ICHMX-ICHMN+1)
  FOR J=0 TO 1023
  XP(J)=XP(J)/BKGD
  NEXT J
  FOR J=6 TO 517
```

```
J1=2*J-12
Y(J)=.5*(XP(J1)+XP(J1+1))
NEXT J
FOR J=0 TO 5
Y(J)=Y(6)
Y(J+518)=Y(517)
NEXT J
FOR J=6 TO 517
A=.61*Y(J-1)+.37*Y(J-2)+.22*Y(J-3)+.135*Y(J-4)+.08*Y(J-5)+.05*Y(J-6)
B=.61*Y(J+1)+.37*Y(J+2)+.22*Y(J+3)+.135*Y(J+4)+.08*Y(J+5)+.05*Y(J+6)
YTEMPJ=(Y(J)+A+B)/.393
YSIG(J-6)=.1*INT(YTEMPJ)
NEXT J
CP1=(ST2-ST1)/(2*FR1*DWELL)
CP2=(ST3-ST2)/(2*FR2*DWELL)
ICP1=INT(CP1)
ICP2=INT(CP2)
FS1=FR1*DWELL/75
FS2=FR2*DWELL/75
FS3=FR3*DWELL/75
TIME(0)=ST1/150
FOR I=1 TO ICP1
TIME(I)=TIME(I-1)+FS1
NEXT I
FOR I=ICP1+1 TO ICP2
TIME(I)=TIME(I-1)+FS2
NEXT I
FOR I=ICP2+1 TO 511
TIME(I)=TIME(I-1)+FS3
NEXT I
CLS
FOR I=0 TO 511
PSET(I,YSIG(I))
NEXT I
FOR I=0 TO 511
TIME(I)=.01*(INT(TIME(I)*100))
NEXT I
OPEN FILE1$ FOR OUTPUT AS #1
OPEN FILE3$ FOR OUTPUT AS #3
FOR I=0 TO 511
I1=2*I
SREF(I)=.005*INT(100*(SREF(I1)+SREF(I1+1)))
SPR(I)=.005*INT(100*(SPR(I1)+SPR(I1+1)))
NEXT I
FOR I=0 TO 511
PRINT#2,TIME(I);YSIG(I)
PRINT#3,SREF(I)
PRINT#1,SPR(I)
NEXT I
INPUT"TERMINATE  YES=1, NO=0";TERM
CLOSE
IF TERM=0 THEN GOTO 1
END
```

Grtconv.bas

```
"This program calculates the diffracted signal from a two pulse"
"orientation grating as a function of the momentum relaxation time."
"The pulse shape is a gaussian pulse of FWHM = 460 fs."
"The integration routine uses a gaussian integration technique with"
"weighting factors read in from a file entitled weight.dat."
DIM x(20), w(20), erfc#(20), g(300), t(300), tr$(15)
tr$(1) = ".050"
tr$(2) = ".075"
tr$(3) = ".100"
tr$(4) = ".125"
tr$(5) = ".150"
tr$(6) = ".200"
tr$(7) = ".250"
tr$(8) = ".300"
tr$(9) = ".400"
tr$(10) = ".500"
tr$(11) = ".600"
tr$(12) = ".700"
tr$(13) = ".800"
tr$(14) = ".900"
tp = .27
FOR j = 0 TO 50
t(j) = -1! + .01 * j
NEXT j
FOR j = 51 TO 150
t(j) = -.5 + .005 * (j - 50)
NEXT j
FOR j = 0 TO 149
t(300 - j) = -t(j)
NEXT j
CLS
FOR ip = 1 TO 14
trr$ = RIGHT$(tr$(ip), 3)
ff1$ = "d:grta" + RIGHT$(trr$, 3) + ".dat"
ff2$ = "d:grtb" + RIGHT$(trr$, 3) + ".dat"
LOCATE 1, 60, 0: PRINT ; ff1$
tr = VAL(tr$(ip))
a1 = .34802
a2 = -.09588
a3 = .74786
p = .47047
gmax = 0!
OPEN "weight.dat" FOR INPUT AS #2
FOR i = 11 TO 20
INPUT #2, x(i), w(i)
x(21 - i) = -x(i)
w(21 - i) = w(i)
NEXT i
FOR i = 11 TO 20
20 t = 1! / (1! + p * x(i))
xf# = (a1 * t + a2 * t * t + a3 * t * t * t)
erfc#(i) = LOG(xf#) - x(i) * x(i)
```

```
xt = 2 * EXP(x(i) * x(i)) - xf#
erfc#(21 - i) = LOG(xt) - x(i) * x(i)
NEXT i
FOR j = 0 TO 300
tau = t(j)
xsum = 0
FOR i = 1 TO 20
ff1 = x(i) * tau / tp + 3! * tp * x(i) / tr
ff2 = -.75 * tau / tr - .75 * tau * tau / (tp * tp) - .75 * tp * tp / (tr *
tr)
ff = LOG(w(i)) + erfc#(i) + ff1 + ff2 + 2! * tp / tr
IF ff > 80 THEN PRINT "overflow"; i; ff; ff1; ff2; tr; tau: STOP
IF ff < -80 THEN ff = -80
xsum = xsum + EXP(ff)
NEXT i
g(j) = xsum
IF g(j) > gmax THEN gmax = g(j): jmax = j
NEXT j
OPEN ff1$ FOR OUTPUT AS 1
OPEN ff2$ FOR OUTPUT AS 3
PRINT , ff1$
IF gmax = 0 THEN gmax = 1!
gcut = 1E-35
IF gmax > 1 THEN gcut = 1E-35 * gmax
FOR i = 0 TO 300
IF g(i) < gcut THEN g(i) = 0!
g(i) = g(i) / gmax
PRINT #1, USING "##.### #.###"; t(i); g(i)
PRINT #3, USING "##.### #.###"; t(300 - i); g(i)
NEXT i
CLOSE
NEXT ip
STOP
```

Bibliography

Alfano, R. R., editor. **Semiconductors Probed by Ultrafast Laser Spectroscopy**, Vol I & II, (Academic Press, New York, NY 1984).

Alfano, R. R. and Shapiro, S. L., Scientific American **228**, 42 (1973).

Auston, D. H., McAfee, S., Shank, C. V., Ippen, E. P. and Teschke, O., Solid State Electronics **21**, 147 (1978).

Blakemore, J. S., J. Appl. Phys. **53**, R123 (1982).

Blakemore, J. S., **Semiconductor Statistics**, (Dover, New York 1983).

Casey, H. C., Jr. and Panisch, M. B., **Heterostructure Lasers**, (Academic Press, New York, 1978) Part A.

Conwell, E. M., **Solid State Physics, Supplement 9**, (Academic Press, New York 1967).

De Silvestri, S., Laporta, P., and Svelto, O., IEEE J. Quantum Electron. **QE-20**, 533 (1984).

Diels, J.-C.,, Dietel, W.,, Fontaine, J. J.,, Rudolph, W., and Wilhemli, B.,, J. Opt. Soc. Am B, **2**, 680 (1985).

Eichler, H. J., Optica Acta **24**, 631 (1977).

Eichler, H. J., Günter, P., Pohl, D. W., **Laser-Induced Dynamic Gratings**, (Springer-Verlag, Berlin 1985).

Erskine, D. J., Taylor, J. and Tang, C. L., Appl. Phys. lett. **45**, 54 (1984).

Ferry, D. K., Osman, M. A., Joshi, R., and Kann, M.-J., Solid State Electron. **31**, 401 (1988).

Fontaine, J. J.,, Dietel, W., and Diels, J.-C.,, IEEE J. Quantum Electron. **QE-19**, 1467 (1983).

Fork, R. L., Greene, B. I. and Shank, C. V., Appl. Phys. Lett. **38**, 671 (1981).

Fork, R. L., Shank, C. V., Yen, R. and Hirlimann C. A., IEEE J. Quantum Electron. **QE-19**, 500 (1983).

Gordon, J. P. and Fork, R. L., Optics Lett. **9**, 153 (1984).

Ippen, E. P. and Shank, C. V., Appl. Phys. Lett. **27**, 488 (1975).

Ippen, E. P., Shank, C. V. and Dienes, A., Appl. Phys. Lett. **21**, 348 (1972).

Kahen, K. B. and Leburton, J. P., Phys. Rev. B **32**, 5177(1985).

Kash, K., Wolff, P. A. and Bonner, W. A., Appl. Phys. Lett. **42**, 173 (1983).

Leheny, R. F., J. Shah, Fork, R. L., Shank, C. V., and Migus, A.. Solid State Comm. **31**, 809 (1979).

Lin, W. Z., Fujimoto, F. G., Ippen, E. P. and Logan, R. A., Appl. Phys. Lett. **50**, 124 (1987).

Lin, W. Z., Fujimoto, F. G., Ippen, E. P. and Logan, R. A., Appl. Phys. Lett. **51**, 161 (1987).

Lugli, P. and Ferry, D. K., Physica **117B**, 251 (1983).

Lugli, P. and Ferry, D. K., IEEE Transactions on Electron. Devices, **ED-32**, 2431 (1985).

Lugli, P., Jacoboni, C. and Reggiani, L., SPIE Proc. **793**, 102 (1987).

Migus, A., Shank, C. V., Ippen, E. P. and Fork, R. L., IEEE J. Quantum Electron. **QE-18**, 101 (1982).

Miranda, R. S., Jacobovitz, G. R., Cruz, C. H. B., and Scarparo, M. A. F., Optics Lett. **11**, 224 (1986).

Osman, M. A. and Ferry, D. K., J. Appl. Phys. **61**, 5330 (1987).

Osman, M. A. and Ferry, D. K., Phys. Rev. B **36**, 6018 (1987).

Osman, M. A. and Grubin, H. L., Solid State Electron, **31**, 471 (1988).

Osman, M. A., Grubin, H. L., Kreskovsky, J. P. and Ferry, D. L., SPIE PROC. **793**, 94 (1987).

Oudar, J. L., Migus, A., Hulin, D., Grillon, G., Etchepara, J.,and Amtonetti, A., Phys. Rev. Lett. **53**, 384 (1984).

Pankove, J. L., **Optical Processes in Semiconductors**, Dover, New York (1971).

Rosker, M. J., Wise, F. W. and Tang, C. L., Appl. Phys. Lett. **49**, 1726 (1986).

Schoenlein, R. W., Lin, W. Z., Ippen, E. P. and Fujimoto, F. G., Appl. Phys. Lett. **51**, 1442 (1987).

Seymour, R. J., Junnarkar, M. and Alfano, R. R., Solid State Comm. **41**, 657 (1982).

Shah, J., Solid State Electron, **21**, 43 (1978).

Shah, J., Deveaud,B., Damen, T. C., Tsang, W. T., Gossard, A. C. and Lugli, P., Phys. Rev. Lett. **59**, 2222 (1987).

Shank, C. V., Fork, R. L., Leheny, R. F., and Shah, J., Phys. Rev. Lett. **42**, 112 (1979).

Shank, C. V., Fork, R. L. and Yen, R. T. in **Picosecond Phenomena III**, edited by K. B. Eisenthal, R. M. Hochstrasser, W. Kaiser and A. Laubereau (Springer-Verlag, Heidleberg, 1982) P. 2.

Shank, C. V. and Ippen, E. P., **Mode-locking of Dye Lasers** in Topics in Applied Physics, Vol 1. ed. by F. P. Schäfer (Springer-Verlag Berlin 1977).

Shapiro, S. L., editor, **Ultrashort Light Pulses** (Springer-Verlag Berlin 1977).

Shen, Y. R., **The Principles of Nonlinear Optics**, (John Wiley & Sons, New York 1984) Pp 242-264.

Smirl, A. L., Boggess, T. F., Wherrett, B. S., Perryman, G. P. and Miller, A., IEEE J. Quant. Electon. **QE-19**, 690 (1983).

Smirl, A. L., Boggess, T. F., Wherrett, B. S., Perryman, G. P. and Miller, A., Phys. Rev. lett. **49**, 933 (1982).

Smirl, A. L., Moss, S. C. and Lindle, J. R., Phys. Rev. B **25**, 2645 (1982).

Taylor, A., J., Erskine, D. J.,, and Tang, C. L., J.Opt. Soc Am. B **2**, 663 (1985).

Taylor, A., J., Erskine, D. J., and Tang, C. L., Appl. Phys. Lett. **43**, 989 (1983).

Taylor, A., J. and J. M. Wiesenfeld, Phys. Rev. B, **35**, 2321 (1987).

Treacy, E. B., IEEE J. Quantum Electron. **QE-5**, 454 (1969).

Valdmanis, J. A., and Fork, R. L., IEEE J. Quantum Electron. **QE-22**, 112 (1986).

Valdmanis, J. A., Fork, R. L. and Gordon, J. P., Optics Lett. **10**, 131 (1985).

Vardeny, Z., and Tauc, J., Optics Commun. **39**, 396 (1981).

Weiner, A. M., Fujimoto, J. G. and Ippen, E. P., Optics Lett. **10**, 71 (1985).

Wherrett, B. S. and Higgins, N. A., Proc. R. Soc. Lond. **A379**, 67 (1982).

Wherrett, B. S., Smirl, A. L. and Boggess, T. F., IEEE J. Quantum Electron. **QE-19**, 680-689 (1983).

Wise, F. W., Walmsley, I. A., and Tang, C. L., Appl. Phys. Lett. **51**, 605 (1987).

Woerdman, J. P., Phys. Lett. **32A**, 305 (1970).

Woerdman, J. P., PhD Thesis (1971). J. J. Wynne, Phys. Rev. **178**, 1295 (1969).

Yariv, A., **Quantum Electronics**, (John Wiley & Sons, New York 1975).

Yoffa, E., Phys. rev. B **23**, 1909 (1981).

Yuen, S. Y., and Wolff, P. A., Appl. Phys. Lett. **40**, 457 (1982).

Yuen, S. Y., Wolff, P. A., Ram-Mohan L. R., and Logan, R. A., Solid State Commun. **56**, 489 (1985).

Zimmerman, J., Lugli, P.,and Ferry, D. K., Solid State Elect. **26**, 233 (1986).